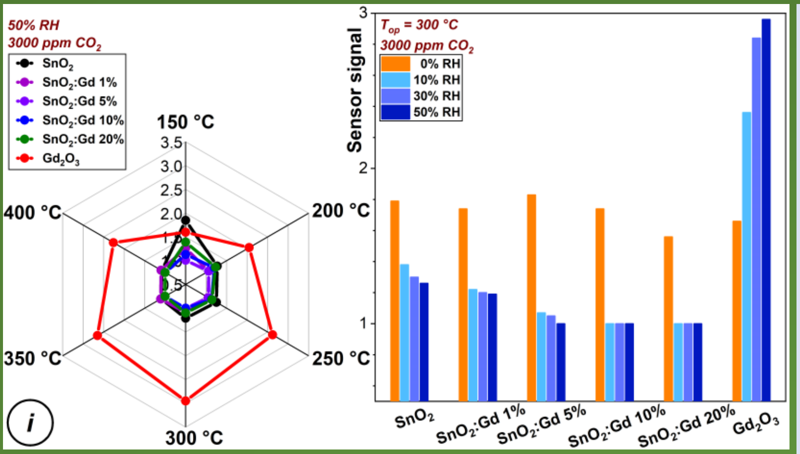

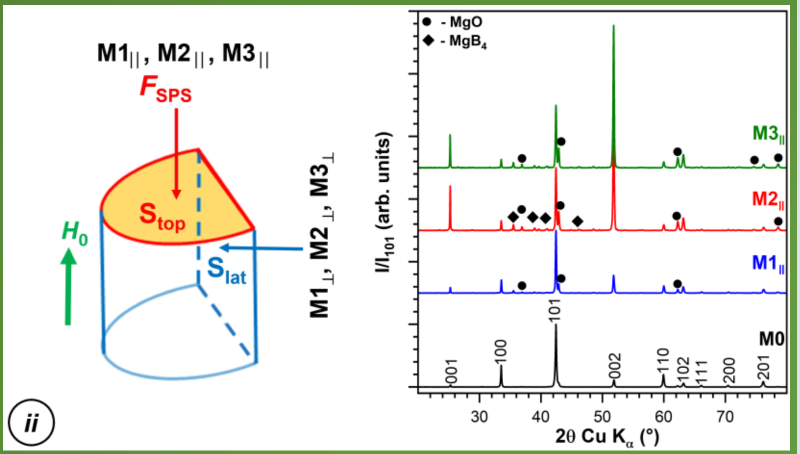

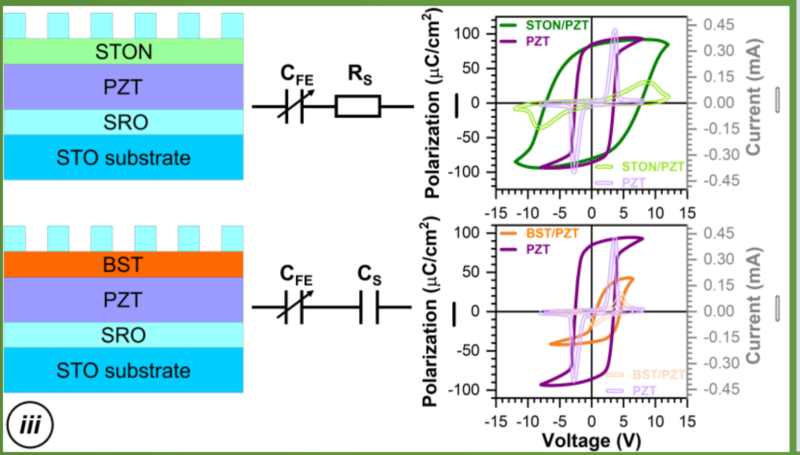

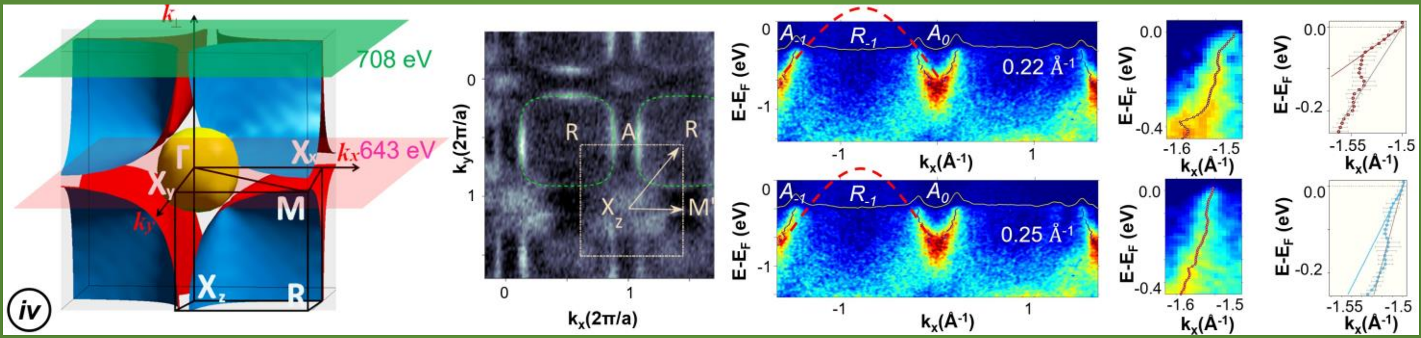

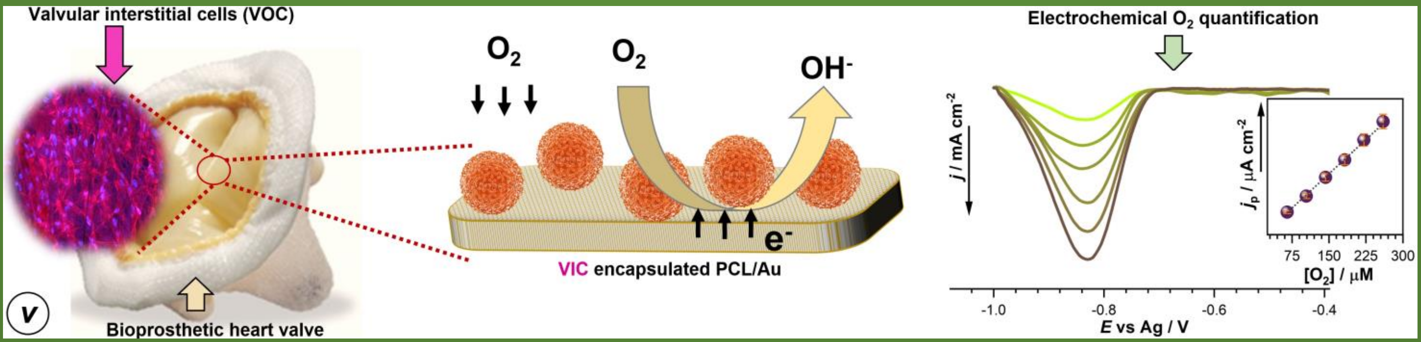

National Institute of Materials Physics

ANNUAL REPORT

2022

Ministry of Research, Innovation and Digitalization

National Institute
of
Materials Physics

ANNUAL REPORT
2022

Cover page – Figures reproduced/adapted from:

- ***i.*** C Ghica *et al.*, “Influence of relative humidity on CO_2 interaction mechanism for Gd-doped SnO_2 with respect to pure SnO_2 and Gd_2O_3”, *Sens. Actuators B Chem.* 368, 132130 (2022).
- ***ii.*** AG Boni *et al.*, “Negative-capacitance and switching dynamics control via non-ferroelectric elements”, *ACS Appl. Energy Mater.* 5, 3, 3307–3318 (2022).
- ***iii.*** MA Grigoroscuta *et al.*, “Towards high degree of *c*-axis orientation in MgB_2 bulks”, *J. Magnes. Alloy.* 10, 2173–2184 (2022).
- ***iv.*** MA Husanu *et al.*, “Ferroelectricity modulates polaronic coupling at multiferroic interfaces”, *Commun. Phys.* 5, 209 (2022).
- ***v.*** CG Sanz *et al.*, “Quantification of cell oxygenation in 2D constructs of metallized electrospun polycaprolactone fibers encapsulating human valvular interstitial cells”, *J. Electroanal. Chem.* 905, 116005 (2022).

Research Laboratories

LABORATORY 10
“Functional Nanostructures”

Head of laboratory: Dr. Silviu POLOȘAN, Senior Researcher rank 1 (silv@infim.ro)

Personnel: 32 members – 9 × SR1, 1 × SR2, 9 × SR3, 2 × SR, 9 × RA, and 1 × technician (**SR stands for Senior Researcher; RA stands for Research Assistant*).

Main research directions:

The group deals with nanostructures and nanostructured materials preparation and development of applications. Both chemical/electrochemical (chemical bath deposition, electrochemical deposition with and without a template, chemical vapor deposition) and physical (sputtering, thermal evaporation in vacuum, electrospinning and forcespinning) methods are employed for nanostructures and nanostructured materials preparation. Different types of materials are used, including here metals, metal oxides, organometallic compounds and polymers. The nanostructures developed by this approach are used as building blocks for different types of functional devices (*e.g.*, transistors or diodes, biosensors, actuators). Several specific examples follow:

- Nanostructures and devices based on nanostructures – physical and chemical methods are employed for preparing nanostructures. Electrochemical or chemical deposition is used for preparing nanowires of zinc oxide with diameters down to 10 nm. Thermal oxidation of metal foils is used for obtaining metal oxide nanowires with diameters down to 20 nm. Further, the nanowires can be employed as building blocks for electronic devices such as diodes and transistors using microlithographic (photolithography and electron beam lithography). Devices complexity can be employed (*e.g.*, core shell devices can be fabricated) by covering the nanowires with thin-films employing methods such as magnetron sputtering or thermal evaporation. Chemical vapor deposition is employed for preparing thin nanostructured films such as metal oxides or graphene.
- Materials for applications in optics, optoelectronics and photonics for devices which include diodes and transistors for light emitting applications, glasses or modular composition fibers for photonic applications.
- Biosensors and biomedical devices based on nanostructures or on devices containing nanostructures as building blocks.

Nanostructures and nanostructured materials can be exploited successfully in biosensors, mainly due to the high specific surface but also due to other specific functionalities induced by the low dimensionality. Electrochemical sensors are developed based on nanostructured materials and are functionalized with different types of biomolecules in such a way in which both the desired sensitivity and selectivity are obtained. In this context, different types of substrates and configurations of functionalization are investigated with the goal of optimizing device performances. Novel applications are considered, including wearable sensors for physiologic parameters monitoring. Several specific examples follow:

- Submicrometer fibers; biomimetic devices based on microfiber web electrodes. In our group, methods of fabricating polymer submicrometric fibers were developed namely: electrospinning and forcespinning. By further functionalization, transparent and flexible electrodes based on metal covered polymer fiber webs are obtained. These electrodes can be applied on a wide range of substrates including here materials such as textiles and paper and can become the functional element of devices such as biosensors or for applications such as artificial muscles. Functionality can be increased by covering with electroactive polymers, leading to devices with highly superior performances when compared to classic architectures.
- Biocompatible materials represent another research direction of the group, several approaches being developed, including both biopolymeric fibers (collagen or cellulose), natural membranes (eggshell membrane) or nanostructured materials such as hydroxyapatite. Further

functionalization includes covering with different compounds or nanostructures or doping and leads to multiple fields of applications, the main one being that of medical devices.

The research directions of Lab. 10 are mostly interconnected for developing devices with direct applications. Equipment for fabricating fibers by means of electrospinning and forcespinning were designed and developed in the laboratory with the support of the engineers from the application department.

Relevant infrastructure:

The activity of Lab. 10 relies on several fully-equipped chemistry and electrochemistry laboratories (dedicated to different types of applications) as well as clean room infrastructure, essential for devices fabrication:

- Electron-beam nanolithography equipment with Raith Elphy systems with laser interferometers and Hitachi S3400 and Zeiss Merlin compact electron microscopes;
- Lithography/Mask Alignment EVG®620 NT system with nanoimprint capabilities;
- CVD equipment for preparation of carbon-based nanostructures;
- CVD equipment for deposition of semiconducting materials;
- Laboratory for optical characterization including UV – Vis absorption spectrometers (Carry 5 and Perkin Elmer 35), photoluminescence spectrometers (Edinburgh and Perkin Elmer LS55), near field photoluminescence microscope, plasmonic resonance spectrometer with potentiostat;
- Liquid chromatography equipment with mass spectroscopy;
- Laboratory for cytocompatibility testing, including cell culture facilities and multi-parametric analysis methods (flow cytometry, spectrophotometry, fluorescence microscopy).

Available services:

- Scanning electron microscopy characterization of materials (micromorphology, composition);
- Optical characterization by means of optical spectroscopy;
- Development of equipment for producing micrometric and submicrometric fibers by means of electrospinning and forcespinning.

Main results:

- 15 ongoing projects (3 × PED, 1 × PTE, 4 × PCE, 1 × TE, and 6 × PD) of which 5 continue in 2023 (2 × PED, 2 × PCE, and 1× PD);
- 60 articles published in Web of Science®-indexed journals with impact factor (of which 28 with main author from Lab. 10);
- 2 OSIM awarded patents;
- 10 OSIM patent requests.

Highlights:

- Various types of sensors were developed, using nanostructures as building blocks and exploiting the reduced dimensions in improving sensitivity and selectivity [see *Biosensors, 12, 500 (2022)* & *Scientific Reports 12, 2261 (2022)* & *Current Opinions in Electrochemistry 34, 101024 (2022)* & *Analytical Chemistry 91, 1920–1927 (2018)* & *International Journal of Molecular Sciences 23, 14438 (2022)* & *Journal of Electroanalytical Chemistry 921, 116663 (2022)* & *Scientific Reports 12, 6834 (2022)* & *Materials Science in Semiconductor Processing 42, 364–372 (2016)*];
- It was found that actuators based on electrospun fibers are also capable of sensing mechanical and chemical signals and untethered actuation is possible [see *Current Opinions in Electrochemistry 34, 101024 (2022)* & *Microchimica Acta 189, 245 (2022)* & *Talanta 241, 123255 (2022)*];

- It was proved that various polymer fibers can be embedded as electrodes in functional devices, adding flexibility and opening a wide range of potential applications [see *Microchimica Acta 189, 245 (2022)* & *Talanta 241, 123255 (2022)* & *Journal of Electroanalytical Chemistry 905, 116005 (2022)*];
- Biocompatibility properties can be finely tuned by choosing specific materials or material combinations [see *Scientific Reports 12, 2261 (2022) & Polymers 14, 1826 (2022)*].

LABORATORY 20
"Complex Heterostructures and Multifunctional Materials"

Head of laboratory: Dr. George STAN, Senior Researcher rank 1 (george_stan@infim.ro)

Personnel: 33 members – 6 × SR1, 6 × SR2, 7 × SR3, 2 × SR, 7 × RA, 2 × engineers, 2 × sub-engineers, and 1 × technician.
From the members with permanent contracts, 24 possess PhD titles (in physics, chemistry, materials engineering) – including 1 PhD supervisor – and 2 are PhD students.

Main research directions:

- Ferroelectric materials and related structures for electronic, optoelectronic and sensing applications (including non-volatile memories, UV and IR detectors, piezoelectric devices);
- Materials and devices with application in microelectronics, photovoltaic conversion and light/particle detection (including field-effect transistors, hybrid perovskite and kesterite solar cells, and silicon-based particle detectors);
- Superconducting and magnetic materials, strongly correlated electron systems;
- Dielectric and ferroelectric materials for microwave devices (*e.g.*, dielectric resonators, ferroelectric varactors, filters, antennas).
- Materials for healthcare applications.

Relevant infrastructure:

Laboratory 20 possesses a noteworthy infrastructure, covering the entire technological chain from the preparation of materials in the form of powders, bulk and thin layers and their complex physico-chemical characterization, to the integration of the optimized materials into functional devices. Amongst the most important systems and equipment one can mention:

- SURFACE SCIENCE pulsed lased deposition (PLD) work station (**Fig. 20–1a**) equipped with: 2 deposition chambers, each with 4-target carousels; a KrF excimer laser with 248 nm wavelength, repetition rate of 1 – 10 Hz, and maximum energy of 700 mJ; control of laser fluence; substrate heating up to 1000 °C; control of working gases pressure; *in-situ* reflection high-energy electron diffraction (RHEED) capabilities. One reaction chamber is used to deposit ferroelectric layers based on perovskites and other metal oxides (*e.g.*, doped ZnO, HfO_2), whilst the other chamber is used to prepare superconductor thin-films.
- SURFACE SCIENCE hybrid system for thin-films synthesis from temperature-sensitive materials by (*i*) matrix assisted pulsed laser evaporation (MAPLE) and (*ii*) PLD, constituted of: a deposition chamber with *in-situ* freezing facilities for targets (*e.g.*, frozen suspensions of organic materials or inorganic nanoparticles in a support matrix); a KrF excimer laser with 248 nm wavelength, 1 – 10 Hz repetition rate, and 700 mJ maximum power; maximum heating temperature of the substrate: 500 °C – MAPLE & 700 °C – PLD.
- Multi-cathode radio-frequency (RF), direct current (DC) and pulsed direct current (p-DC) magnetron sputtering (MS) systems with various facilities: bias, etching and heating (up to 800 ° C) of substrates; vacuum load-lock for sample transfer; vacuum systems (down to ~10^{-6} Pa); computerized control and process automation. The latest MS equipment, AJA PHASE II J, purchased in 2016, is shown in **Fig. 20–1b**. Each MS system in Laboratory 20 is dedicated to a distinct class of materials: metallic contacts; semiconductor and dielectric materials; biocompatible materials.
- Chemistry laboratory for the preparation of powders, bulk materials and thin-films by chemical (wet) methods, equipped with high-temperature annealing furnaces; spin-coating systems; fume hoods, aggregate mills; weighting scales; in-house made glove-boxes; glassware; *etc.*

- Doctor blade/Slot-die MTI system for large area deposition equipped with 100 mm width adjustable micrometer applicator, a slot-die head and an adjustable speed syringe pump. Additionally, two in-house built Doctor blade/Slot-die systems are also available.
- Professional Glove-box MBraun with two chambers (3 and 4 gloves), with integrated spin-coater and closed cycle gas purification system capable of maintaining an atmosphere with H_2O and O_2 under 0.1 ppm and with a solvent filter.
- Laboratory for the preparation of piezoelectric and superconducting materials, polycrystals and single crystals.
- Ceramic materials 3D printing laboratory, equipped with a NORDSON EFD, EV series, robocasting (direct ink writing) printing system, with Ultimus V dispenser (**Fig. 20–2a**); an ANTON PARR MCR302e modular rheometer (**Fig. 20–2b**); and a THINKY ARE-250 ceramic mixing & degassing machine.

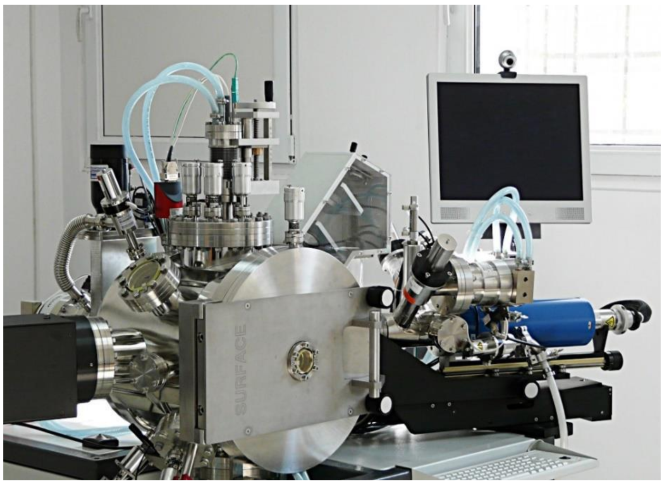

Fig. 20–1a PLD workstation assembly, SURFACE SCIENCE, for the deposition of ferroelectric thin-films.

Fig. 20–1b RF, DC and p-DC magnetron sputtering system, AJA PHASE II, for the deposition of semiconductor thin-films.

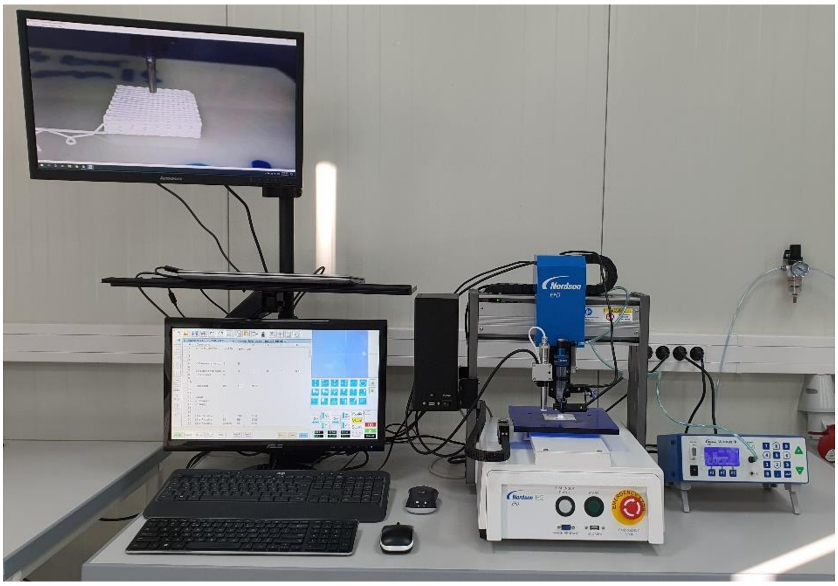

Fig. 20–2a 3D printing system by robocasting (direct ink writing) technology, NORDSON EFD, EV series, with Ultimus V dispenser.

Fig. 20–2b ANTON PARR MCR302e modular rheometer.

- X-ray diffraction systems for structure analysis of thin-films (a RIGAKU SmartLab 3 kW/2017 from room-temperature to 1100 °C – **Fig. 20–3a** and a BRUKER D8 Advance/2006) and powders (ANTON PAAR XRDynamic500 – from 600 °C to –180°C and a BRUKER D8 Advance/2007).

- Optical and structural characterization systems, including a (*i*) variable angle spectroscopic ellipsometer (WOOLLAM) with wavelength range 200 – 1700 nm (6.2 – 0.73 eV), angle of incidence (35 – 90°), automated sample translation stage (for mapping) 150 mm × 150 mm, and an Instec temperature control stage (-160 – 600 °C) and (*ii*) a near infrared (NIR), infrared (midIR) and far infrared (farIR) Fourier transform infrared (FTIR) JASCO spectrometry platform, encompassing the 12000 – 50 cm^{-1} spectral range (**Fig. 20–3b**). VASE Woollam can be used in the following modes: (*i*) reflection ellipsometry on semiconductor/dielectric thin-films or multilayers (inferred sample parameters: thicknesses, refractive index, extinction coefficient, absorption coefficient, dielectric function, band gap, critical point energies, electrical parameters for degenerate semiconductors – resistivity/conductivity, carrier density, scattering time, carrier mobility, phase transition in the temperature range -160 – 600 °C); and (*ii*) transmission ellipsometry on uniaxial/biaxial crystals, glasses and glass ceramics (derived sample parameters: linear birefringence and linear dichroism, Verdet constant/ Faraday rotation).
- Surface investigation by scanning probe microscopy (SPM) in contact or non-contact mode with piezoelectric (PFM), magnetic (MFM) or conductive (C-AFM) response.


Fig. 20–3a RIGAKU SmartLab 3 kW high-resolution XRD system for thin-films analysis.

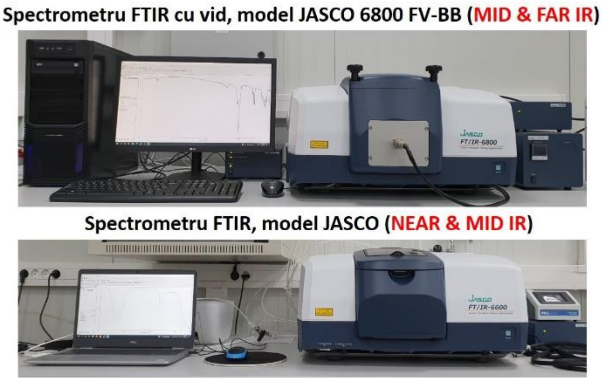
Spectrometru FTIR cu vid, model JASCO 6800 FV-BB (MID & FAR IR)

Spectrometru FTIR, model JASCO (NEAR & MID IR)

Fig. 20–3b FTIR spectroscopic platform with extended NIR – MID – farIR spectral range, 12000 – 50 cm^{-1}.

- Electrical measurements laboratory (see **Fig. 20–4**), including: 2 LAKE SHORE cryo-probers for electrical measurements in the temperature range of 10 – 400 K; one with vertical magnetic field up to 2.5 T, and one with horizontal magnetic field up to 1.5 T, each with at least 3 micro-manipulated arms with contact needles allowing electrical measurements from liquid helium to 400 K under various electric/magnetic fields and illumination conditions; 4 cryostats, covering a temperature range between 10 – 800 K; DLTS (deep-level transient spectroscopy) and TSC (thermally stimulated current) systems for the investigation of electrically active defects (charge carrier traps) in materials and MOS-like structures; set-up for pyroelectric measurements; ferritesters; various instruments for measuring currents, resistances and voltages (electrometers, nanovoltmeters, Lock-In amplifiers); voltage and current sources; RLC bridges; and impedance analyzers. These facilities are used to perform complex characterization of electrical (hysteresis loops; CV and I-V characteristics; impedance spectroscopy; defect spectroscopies; *etc*.) and superconductive properties (electron transport, thermodynamics, magnetic-field penetration depth measurements); determination of the d_{33} piezoelectric coefficient.
- Solar cells testing laboratory (**Fig. 20–5**), with two Newport LED solar simulators (aperture 50 mm × 50 mm), VeraSol-2 AAA Class and a MiniSol ABA Class), with AM 1.5G solar spectrum and adjustable power coupled with a Keithley source 2601. A system for measuring

the Quantum Efficiency (EQE and IPCE) with accessories, working in the 250 – 2500 nm spectral range, is available.

- Microwave dielectric materials and devices testing laboratory, including:
  - Vector Network Analyzer PNA 8361A from Agilent (0.01 – 67 GHz) for two-ports complex S parameters. It uses electronic calibrator Agilent N4694-60001 in the range of 0.01 – 67 GHz. For access, 1.9 mm, 2.9 mm, 2.4mm, 3.5 mm, SMA or N connectors or adaptors are used.
  - Vector Network Analyzer PNA-X N5245A from Agilent (0.1 – 50 GHz standalone) with 4 ports and dual sources. It allows measurements of the S and X non-linear parameters. By using the millimeter wave extensions, the system covers a wide frequency band up to 500 GHz. Each extension pair allows the measurement of the two-ports parameter of waveguide devices. The millimeter wave extensions are from Agilent/OML (N5260A V10 VNA2, WR-10, 75-110 GHz; N5260A V06 VNA2, WR-06, 110-170 GHz; N5260A V05 VNA2, WR-05, 140-220 GHz; N5260A V03 VNA2, WR-03, 220-325 GHz; N5260A V02.2 VNA2, WR-02.2, 325-500 GHz).
  - Anechoic chamber with internal dimensions 3040 mm × 4100 mm × 2800 mm, for antenna characterizations (*e.g.*, directivity parameter) in the range of 0.9 – 40 GHz.
  - Microprobe station for direct *on-wafer* measurements of two-ports in the frequency range 0.1 – 67 GHz by using GSG probes with 150 µm and 100 µm pitches.
  - THz-TDS spectrometer from AISPEC Pulse IRS 2000 Pro, operating in the range of 200 GHz – 5 THz.

- In the framework of collaborative research activities, Laboratory 20 can access other NIMP infrastructures, such as: TEM and SEM equipment; XPS characterization (including at Elettra Synchrotron Trieste); magnetic measurements (SQUID, PPMS); other optical spectroscopy techniques (Raman, UV-Vis-NIR, luminescence); clean-room (photolithography, dry etching); and *in-vitro* preliminary biological testing of materials.

Fig. 20–4 Laboratory for electrical characterization of dielectric, ferroelectric and semiconductor materials.

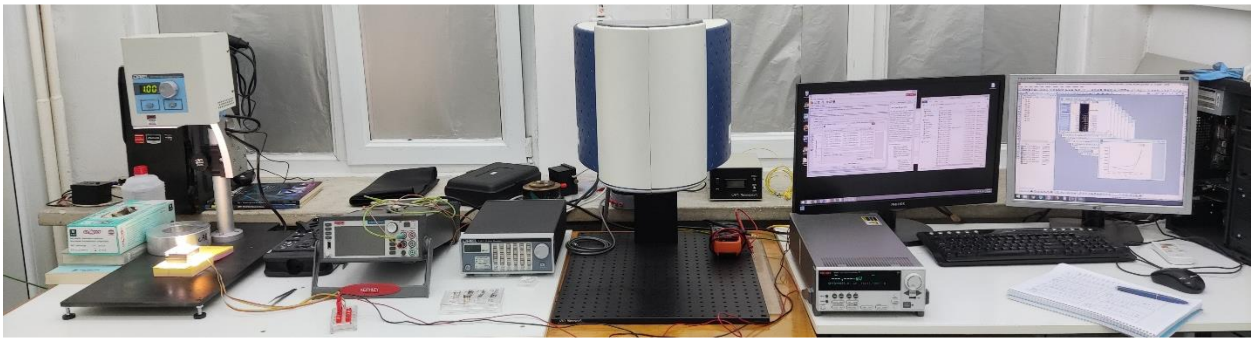

Fig. 20–5 Solar cells testing laboratory.

Available services:

- Preparation of materials (nano-powders; bulk ceramics; fabrication of thin-films by various techniques, including chemical methods, CVD and PVD techniques);
- Investigation of charge carrier traps by DLTS and TSC;
- Electric characterization of materials in a wide temperature range, under electric and magnetic fields;
- Investigation of pyroelectric properties;
- Fabrication and characterization of materials by electrochemistry;
- Fabrication and characterization of perovskite solar cells;
- Fabrication and characterization of microelectronic devices (*e.g.*, FET, MOS);
- Characterization of microwave, millimeter waves and terahertz materials and devices;
- Antenna characterization (antenna directivity) in anechoic chamber in the frequency band from 900 MHz to 40 GHz;
- Electromagnetic design for microwaves devices/structures by using high accuracy software packages such as CST Studio Suite, Ansoft HFSS, and Ansoft Designer;
- Deposition of biocompatible (ceramic and glass) coatings on metallic implants;
- Characterizations by (*a*) reflection ellipsometry on semiconductor/dielectric thin-films or multilayers (thicknesses, refractive index, extinction coefficient, absorption coefficient, dielectric function, band gap, critical point energies, electrical parameters for degenerate semiconductors – resistivity/conductivity, carrier density, scattering time, carrier mobility, phase transition in the temperature range -160 – 600 °C); and (*b*) transmission ellipsometry on uniaxial/biaxial crystals, glasses and glass ceramics (optical constants, linear birefringence and linear dichroism, Verdet constant/ Faraday rotation).
- XRD characterizations for crystalline phase identification and their quantitative analysis; determination of the lattice parameters, average size of crystallites, macro- and micro-strains, preferred orientation, *etc*; analysis of homo- and hetero-epitaxial structures; X-ray reflectometry analyzes for inferring the thickness, density and roughness of the surface and interfaces of amorphous and crystalline layers and multi-layers; *etc*.
- FTIR spectroscopy analyses in transmission, specular reflectance (including at grazing incidence), attenuated total reflectance – ATR (RT – 180 °C), diffuse reflectance – DRIFT (RT – 500 °C) and integrating sphere modes.
- Morpho-compositional analyses by HR-SEM – EDXS;
- Surface characterization of materials by AFM, PFM, MFM and C-AFM.

Main results:

- 18 ongoing projects (2 × PCCF, 1 × CERN, 1 × SEE, 6 × PED, 1 × PTE, 1 × PCE, 3 × TE, and 3 × PD) of which 6 continue in 2023 (1 × CERN, 1 × SEE, 1 × PED, 1 × PTE, 1 × PCE, and 1 × PD);
- 47 articles published in Web of Science®-indexed journals with impact factor (of which 14 with main author from Lab. 20);
- 3 OSIM awarded patents;
- 8 OSIM patent requests.

Highlights:

- Successful implementation of the economical contract with the Swarm European Services, tackling researches in the field of memristors for cryptographic key applications (the collaboration continues in 2023);
- Synthesis of *n*- (Nb) and *p*- (Fe) doped PZT epitaxial layers and highlighting of the significant effect of doping, even at a concentration of 1 at.%, on the electrical properties (*e.g.*, polarization; coercive field) of PZT [see *Scientific Reports 12, 9131 (2022)*], allowing for the

control over the as-grown polarization orientation (up- or down-), with important implications for developing ferroelectric *p-n* homojunctions;

- Synthesis of quaternary chalcogenide films for photovoltaics, obtained *via* electrodeposition and underlining the in-depth concentration gradients [*see Journal of Alloys and Compounds 906, 164379 (2022)*], or *via* spray pyrolysis and the method to suppress the CoS_2 secondary phase [see *Ceramics International 48 (21), 32418-32426 (2022)*];
- Identification of new silica- and phosphate-based bioactive glass systems, substituted with copper and/or gallium, followed by their successful implementation in implant-type coatings with a marked antimicrobial effect [see *Journal of Materiomics 8, 893–905 (2022)* and *Bioactive Materials 8, 325–340 (2022)*];
- EEA-Norway funded project, targeting the fabrication of large-area perovskite solar cells and their assembly into mini-solar panels.

LABORATORY 30
“Magnetism and Superconductivity”

Head of laboratory: Dr. Victor KUNCSER, Senior Researcher rank 1, Habil. (kuncser@infim.ro)

Personnel: 33 members – 5 × SR1, 5 × SR2, 10 × SR3, 3 × SR, 4 × RA, 1 × technological development engineer (*TDE), and 3 × technicians.
Except for the scientific activity, the group is also involved in educational and training activities. There are 3 PhD advisers coordinating 2 to 3 PhD students yearly as well as master and undergraduate students performing their scientific training.

Main research directions:

- Fundamental and applied research in the field of magnetic and magneto-functional materials for actuator and sensoristic applications as well as in the field of superconductivity, mainly targeting materials with superconducting properties with potential for practical applications. The research process covers all stages, from preparation (bulk materials, thin-films or nanostructures) to structural and electronic characterization, completed with a deep analysis of the magnetic and superconducting properties, respectively.
- Related to the magnetic behavior, mainly the functionalities mediated by magnetic reconfiguration controlled by temperature, magnetic and electric fields, applied or from interface interactions, are envisaged. The research is focused especially on the study of 0D, 1D and 2D nanostructures. In the case of magneto-functional structures, magnetic systems of nanoparticles, thin-films and multilayers, materials for colossal magnetoresistance (CMR), giant magnetoresistance (GMR) and tunneling magnetoresistance (TMR), soft and hard magnetic materials, Heusler compounds with spin polarization, heterogeneous multiferroic systems, magneto-caloric materials, diluted magnetic oxides/semiconductors, thermo-electric systems, *etc* are envisaged. In addition, bulk materials, advanced hybrid systems and composites / nanocomposites destined to operate in extreme conditions such as the ones in fusion and fission reactors, particle accelerators and in space, are investigated. Interactions at the interface and functionalities induced by them in nanostructured hybrid systems such as soft magnet / hard magnet (exchange-spring), ferromagnet/antiferromagnet (exchange-bias), ferromagnet-ferroelectric (magneto-electric coupling) represent other fields of interest related to fundamental and applicative aspects of smart multi-functional systems. In specific cases, the experimental studies are completed by theoretical studies approaching electronic configurations based on Density Functional Theory (DFT) and magnetic configurations based on finite-element simulation programs.
- Related to the superconducting behavior, studies of vortex matter, dynamics and pinning and nano-engineering of artificial pinning centers for high-magnetic field applications are envisaged. Exploration of fields of applicability of these materials and related ones considering, beyond superconductivity, other that may be important for applications, such as mechanical, biological, optical are also considered. The studied materials are mainly cuprate high temperature superconductors Y (rare earth) $Ba_2Cu_3O_7$ (RE123) with nano-engineered pinning centers, Bi- and La- based superconducting cuprates, MgB_2 (with various additions for increasing pinning properties), iron-based pnictide and chalcogenide multicomponent superconductors and low temperature (classic) metallic and intermetallic superconductors. Other materials of interest are CeO_2, $SrTiO_3$, LiPdPtB, PdO, boron/carbide composites, selected steels, and archaeological ceramic materials. Most of the materials are obtained in the laboratory in various forms: powders, polycrystalline bulk samples, single crystals, wires/tapes, nanostructures, heterostructures and nanocomposites. The group uses advanced techniques for obtaining or processing materials: conventional powder synthesis in controlled atmosphere, cryochemistry or energy milling, crystal growth in flux or by melting zone,

growth of thin-films by laser ablation, sintering by spark plasma, lamination, arc melting, *etc*. Advanced analysis of superconducting properties aims in particular to determine vortex phase diagrams vortex dynamics and vortex pinning. Temperature dependence of magnetization and resistivity, isothermal hysteresis magnetization and magnetic relaxation, current-voltage characteristics, bulk pinning force and pinning potential, *etc* are analyzed within the existing theoretical models or using recognized practical and theoretical methodologies developed by some members of the group, for example pinning potential determined from frequency-dependent AC susceptibility response, or the use of normalized magnetic relaxation rate to determine the cross-over between elastic and plastic vortex creep, and various field- and temperature-dependent creep exponents.

Relevant infrastructure:

Amongst important research equipment, considering preparation facilities as well as characterization ones, the following can be listed:

- Spark plasma sintering, hot pressing sintering, microwave sintering (**Fig. 30–1**);
- Melt-spinning and various ball mills;
- Nanoparticle preparation systems by hydrothermal / solvothermal synthesis in autoclave and centrifugation for separation by sizes);
- RF/DC sputtering deposition system for magnetic thin-films and multilayers with 4 sources and base pressure in the range of 10^{-9} mbar;
- Facility for inducing thermal transfer in radiofrequency magnetic field to determine specific absorption rates in dispersed nanoparticle systems;
- Thermogravimetric and differential scanning calorimetry systems;
- Vibrating Sample Magnetometry system in magnetic fields up to 9 Tesla;
- Mossbauer spectrometers with different accessories to perform measurements at variable temperatures (4.5 K – 1000 K) and in applied fields, *via* the detection of gamma radiation / X- rays / conversion electrons (the only group in Romania active in Mossbauer Spectroscopy) (**Fig. 30–1**);
- Complex system for measurements of physical properties (PPMS) with magnetic fields up to 14, DynaCool System in up to 9 T and a SQUID type magnetometer (**Fig. 30–1**) working in 7 T down to 2 K from Quantum Device with the corresponding facility for liquid He production (18 L /24 h);
- Magnetic texturing of thin-films is investigated by vectorial MOKE magnetometry;
- For high temperature domain, the laboratory possesses a Laser Flash Analyzer system that allows the determination of thermal diffusivity, specific heat and thermal conductivity of the volume materials or multilayers (3 layers, including liquids) in the range 25 – 1100 °C, a dilatometer (Netzsch 402 C, 2015) to determine thermal expansion coefficients (25 – 1600 °C) and an equipment (Netzsch, Nemesis 2015) to determine electrical conductivity and Seebeck coefficient (25 – 800 °C);
- In order to determine the composition in bulk / powder systems, an X-ray fluorescence device is available, while for very low concentrations/quantities the group possesses an inductively coupled plasma mass spectrometer (ICP-MS) (**Fig. 30–1**), with an extension for thin film analysis by laser ablation (LA), the last one being acquired in 2019;
- Mechanical properties are determined in quasistatic regime up to 1700 °C, using a recently-acquired equipment (INSTRON).

Fig. 30–1 ICP-MS with LA for thin-films (upper left), Mossbauer spectrometers with closed circuit He cryostats (lower left) and SQUID device – Quantum Design, of high sensitivity (middle). Spark plasma sintering plant (FCT Systeme GmbH) used to obtain high density bulk materials (right).

Available services:

- Preparation of metallic and intermetallic compounds in the geometry of thin-films, ribbons or bulk;
- Synthesis of materials that are important for applications using state-of-the-art powder metallurgy techniques;
- Lyophilization from frozen materials;
- Treatment of powders and thin-films at high pressures and temperatures in non-corrosive gas atmosphere (hydrogen, nitrogen, methane, carbon dioxide, helium) and measurement of the formation kinetics and thermodynamics of the materials obtained by gas-solid reaction;
- High sensitivity magnetometry to characterize the magnetic properties of the elements (bulk, powders and nano-powders, ribbons and nanocomposites, 0-, 1- and 2-dimensional nanostructures);
- Characterization of the thermodynamic and transport properties (thermal, electric) of the materials in a large temperature domain;
- Determination of the Debye temperature, specific heat and entropy variation of solid materials in the temperature range of 2 – 300 K and in a magnetic field between 0 and 14 T;
- Determination of thermal conductivity of solid materials in the temperature range of 2 – 300 K and in a magnetic field between 0 and 14 T;
- Complex characteristics and specific properties of materials with iron evidenced by powerful nuclear gamma resonance investigation methods (Mossbauer spectroscopy);
- Specific temperature-dependent properties evidenced by modern differential thermal analysis methods, differential calorimetry and mass spectrometry;
- Atomistic simulation within the DFT of the materials for advanced applications and finite element micromagnetic modelling;
- Preparation / processing by various techniques of powders, single-crystals, thin-films / heterostructures / nanostructures, bulks, composites;
- Magnetic and transport measurements on superconducting materials;
- Analysis of experimental data obtained on superconductors with the determination and modeling of critical parameters (critical temperature, critical current density, irreversibility field, pinning force and pinning mechanisms, trapped field, vortex pinning energies, Debye temperature, and others);
- Mechanical measurements in quasistatic regime up to 1700 °C (bending / compression of hard materials);

- Analysis of mechanical properties and correlation with fractography aspects;
- Targets fabrication for thin-layer deposition.

The group also develops materials and technologies for a number of applications: superconducting thin layers and coated conductors from high critical temperature cuprates containing nano-engineered pinning centers; superconducting MgB_2 wires/tapes in metallic sheath; MgB_2-based magnetic storage devices, magnetic concentrators and magnetic shieldings; MgB_2-based powders, coatings and bulks for biomedical applications; boron-based super-hard materials for tools and extreme high temperature applications, integrated multifunctional devices.

Main results:

- 19 ongoing projects (1 × SOL, 1 × SEE, 4 × EURATOM, 7 × PED, 1 × PTE, 1 × PCE, 2 × TE, and 2 × PD) of which 13 continue in 2023 (1 × SOL, 1 × SEE, 4 × EURATOM, 4 × PED, 1 × PCE, 2 × TE);
- 49 articles published in Web of Science®-indexed journals with impact factor (of which 29 with main author from Lab. 30);
- 1 OSIM awarded patent;
- 7 OSIM patent requests.

Highlights:

- First comprehensive physico-chemical characterization of Roman ceramics and pottery vessels found in Romania (*e.g.*, XRF, XRD, FTIR, SEM/EDX, XRT, DTA-TG, laser calorimetry, Mossbauer spectroscopy, magnetometry, colorimetry and mechanical properties results were corroborated proving the performances of ancient Roman technologies in fabrication of smart materials [see *Scientific Reports 12, 15864 (2022)*];
- Detailed investigations related to applications of MgB_2 in superconductivity, either as textured bulk, high density material or in configuration of hybrid superconductor-ferromagnet shield [see *Ceramics International 48, 31914 (2022)* or *Superconductor Science and Technology 35, 044002 (2022)*];
- Nano-engineering of artificial pinning centers of high-temperature YBCO superconducting films and their use in novel architecture of hybrid superconductor/ferromagnetic heterostructures [see *Nanomaterials 12, 1713 (2022)* and *Materials 15, 2345 (2022)*] and detailed theoretical and experimental investigation of the pinning potential in highly performing $CaKFe_4As_4$ superconducting monocrystals [see *Scientific Reports 12, 19132 (2022)*];
- Comprehensive research on nanosized simple and complex hydrides for advanced solid-state hydrogen storage applications [see *International Journal of Molecular Sciences 24, 143 (2022)*];
- Experimental investigations of temperature- and gas-driven effects in multiple phase alloys including MAX [see *Nanomaterials 12, 4136 (2022)*] and nano-nitride reinforced Fe-Cr alloys for nuclear energy applications [see *Journal of Materials Research and Technology 20, 2293 (2022)*];
- Engineering and complex investigation of multifunctional ferromagnetic shape memory ribbons with magnetocaloric, magnetoresistive and magnetostrictive effects [see *Nanomaterials 12, 3367 (2022)*];
- Tuning types of magnetic order and magnetic anisotropies by induced organization of magnetic nanoclusters in solids [see *Nanomaterials 12, 1176 (2022)* and *Coatings 12, 1366 (2022)*] and liquids [see *Nanoscale 14, 4386 (2022)*];
- Engineering of thermo-electric figure of merit in materials with applications at medium and high temperatures [see *Journal of Alloys and Compounds 893, 162400 (2022)*].

LABORATORY 40

“Surface and Interface Science”

Head of laboratory: Dr. Cristian Mihail TEODORESCU, Senior Researcher rank 1, Habil. (teodorescu@infim.ro)

Personnel: 23 members – 2 × SR1, 4 × SR2, 6 × SR3, 1 × TDE3, 2 × SR, 6 × RA, and 2 × technicians.

Main research directions:

- Surface and interface analysis by photoelectron spectroscopies (XPS–ESCA, ARUPS, spin-resolved PES, PED) *in situ* electron diffraction (LEED, RHEED), AES, scanning tunneling microscopy and spectroscopy STM–STS, photoelectron spectromicroscopy, low energy and photoemission electron microscopy (LEEM–PEEM);
- Surfaces, thin-films and heterostructure preparation by molecular beam epitaxy (MBE);
- Theoretical aspects of ferroic systems.

New subjects:

- Analysis of ferroelectric surfaces, band bending in heterostructures;
- Molecular reactions at ferroelectric surfaces;
- In plane conduction properties of 2D systems on ferroelectric surfaces;
- ‘2D nanoreactors', molecular reactions with reactants stabilized between graphene layers and substrates;
- Spin asymmetry in band structure of 2D systems
- Photocatalysts with internal junctions
- Multiferroic structures with indirect exchange or coupling through charge accumulation
- Theoretical developments in the area of ferroic thin-films (ferroelectric, ferromagnetic)
- Development of new devices operating in ultrahigh vacuum (effusion cells, evaporators, manipulators)
- Development of software packages for data analysis.

Relevant infrastructure:

- A complex cluster for surface and interface science (Specs, **Fig. 40–1**), composed by: (*i*) a chamber for photoelectron spectroscopy (XPS, ESCA, UPS, AES); (*ii*) a molecular beam epitaxy (MBE) chamber with *in situ* follow-up by low energy electron diffraction (LEED) and reflection high energy electron diffraction (RHEED) and residual gas analysis; (*iii*) a chamber for scanning tunneling microscopy and spectroscopy (STM/STS); (*iv*) load-lock and storage of samples in ultrahigh vacuum;
- An installation for X-ray photoelectron spectroscopy with possibilities of restricted area analyses (lateral resolution 2 µm) and automated change of samples / measuring areas, coupled to a reaction cell at high pressures and temperatures (Kratos, **Fig. 40–2**);
- A complex cluster for surface and interface science (Specs, **Fig. 40–3**), delocalized actually on the SuperESCA beamline at the Elettra synchrotron radiation facility in Trieste (Combined Spectroscopy and Microscopy on a Synchrotron – CoSMoS), composed by: (*i*) a chamber for photoelectron spectroscopy (XPS, ESCA, UPS, AES) with angle and spin resolution (ARPES, XPD, ARUPS, SR-UPS); (*ii*) a molecular beam epitaxy (MBE) chamber with *in situ* follow-up by low energy electron diffraction (LEED) and reflection high energy electron diffraction (RHEED) and residual gas analysis; (*iii*) a chamber for scanning tunneling microscopy and spectroscopy (STM/STS); (*iv*) load-lock and storage of samples in ultrahigh vacuum. This installation has allocated each semester from Elettra 5 days of „in-house research” beamtime and 6 days of beamtime allocated based on research projects, reserved only from projects from Romania. In addition to synchrotron radiation beamtime, photoelectron spectroscopy using

laboratory sources, or other experiments STM/STS, LEED, RHEED, Auger, *etc* are possible at any time, provided the personnel is able to travel at Elettra;

- An installation for low energy and photoemission electron microscopy: LEEM – PEEM, micro LEED, micro ARUPS (Specs). The installation is able to perform simultaneous imaging (*i.e.*, without scanning) of surfaces by using low energy electrons or photoelectrons produced by UV radiation. In the LEEM mode, the lateral resolution is about 5 nm, and in the PEEM mode about 50 nm. The advantages of using this installation are: (*i*) the possibility to record immediate imaging, to realize movies, to follow-up in real-time surface modifications; (*ii*) the fact that one uses low energy electrons makes this method suitable for delicate surfaces, which otherwise would be damaged by high energy electrons such as the ones used in scanning electron microscopy (SEM); (iii) one may obtain structural or electronic structure (densities of states, dispersion laws) information on nanometer scale.

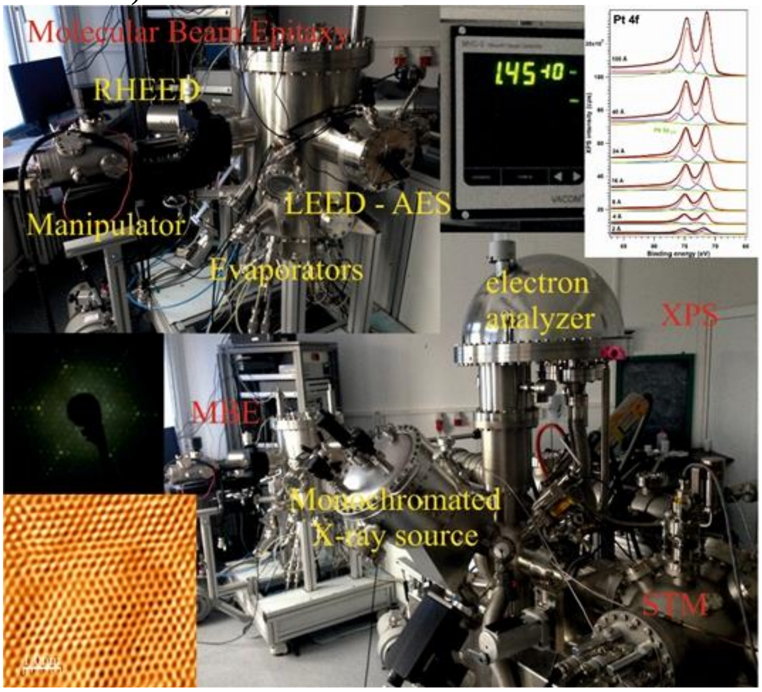

Fig. 40–1 The first cluster of surfaces and interfaces (the “multi-method system” coupled to MBE), located at NIMP. With red, the principal components are denoted (XPS, STM, MBE). With yellow, the main devices. Other photographs from this panel plot the working pressures, the quality of XPS spectra, LEED and STM images. Produced by Specs, Berlin, Germany.

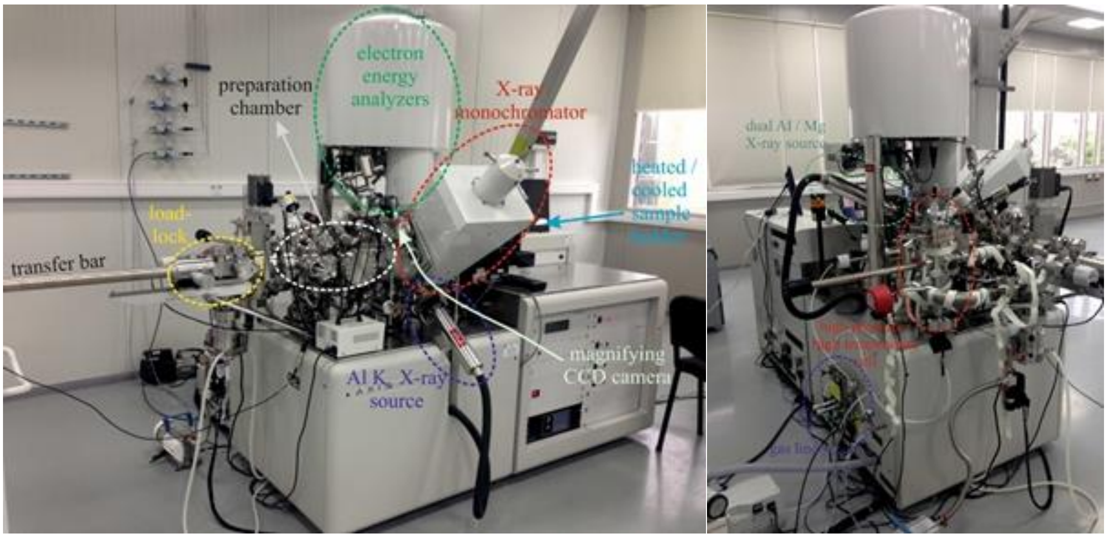

Fig. 40–2 The installation for photoelectron spectroscopy with possibilities of analysis on micrometer areas and provided with a cell for sample treatment at elevated pressures and temperatures (4 bar / 1000 °C). Produced by Kratos, Manchester, United Kingdom.

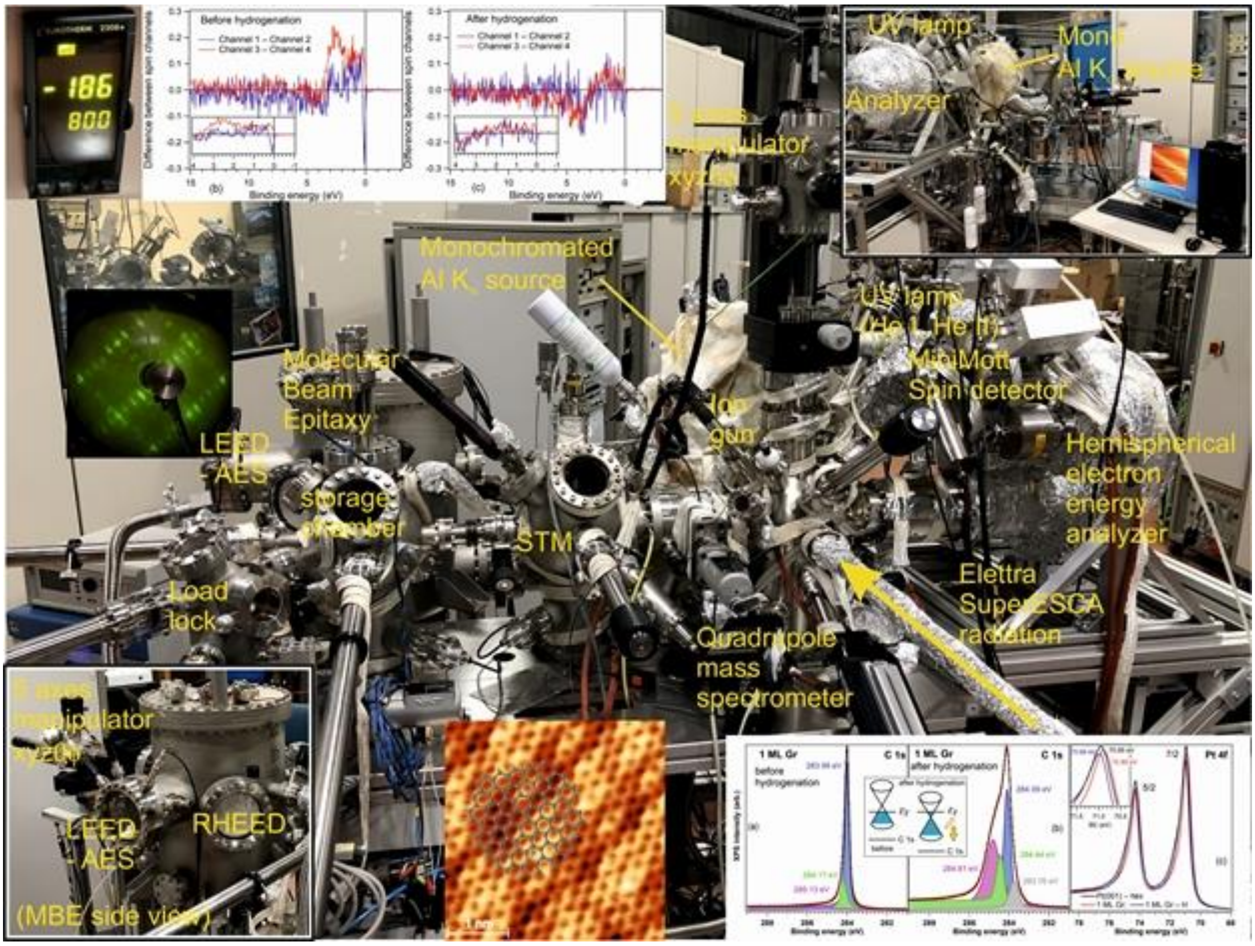

Fig. 40–3 The CoSMoS (combined spectroscopy and microscopy on a synchrotron) cluster coupled to the SuperESCA beamline at Elettra, Trieste. Produced by Specs, Berlin, Germany.

- Setup for extended X-ray absorption fine structure (EXAFS). Excitations: Mo $K_{\alpha 1}$ (17479.34 eV), W $L_{\alpha 1}$ (8397.6 eV), power 3 kW (40 kV, 75 mA); Ge(220), Ge(400), Ge(840) monochromators; detectors: proportional counters, scintillation detectors; measurement in transmission or fluorescence; simulation and analysis software. Produced by Rigaku, Tokyo, Japan.
- Installation for positron annihilation-induced Auger electron spectroscopy, CNCAN certification in process.

Available services:

- Photoelectron spectroscopy-based techniques: X-ray photoelectron spectroscopy (XPS) and diffraction (XPD), ultraviolet photoelectron spectroscopy (UPS), angle-resolved UPS (ARUPS), spin-resolved ARUPS;
- Auger electron spectroscopy (AES) and diffraction (AED);
- Low energy electron diffraction (LEED) and reflection high energy electron diffraction (RHEED) characterization of surfaces;
- Scanning tunneling microscopy (STM) and spectroscopy (STS) at variable temperature.
- Sample depth-profiling by ion sputtering assisted by XPS or AES;
- Surface cleaning and synthesis of epitaxial thin-films by molecular beam epitaxy (MBE);
- Thermally-programmed desorption of molecules from surfaces by residual gas analysis (RGA);
- Low energy electron microscopy (LEEM) and photoemission electron microscopy (PEEM), micro-LEED and micro-ARUPS;
- Extended X-ray absorption fine structure (EXAFS);

- Positron annihilation-induced Auger electron spectroscopy (PAES), CNCAN authorization pending.

Main results:

- 7 ongoing projects (1 × PCCF – as principal investigator of team T1, 1 × PCE, 2 × TE, 1 × PD, 1 × ELI, and 1 × Installation of National Interest) of which 4 continue in 2023 (1 × PCE, 1 × TE, 1 × ELI, and 1 × Installation of National Interest);
- 38 articles published in Web of Science®-indexed journals with impact factor;
- 3 OSIM awarded patents;
- 4 OSIM patent requests.

Highlights:

- The first report of the experimental band structure of $Pb(Zr,Ti)O_3$, correlated with the polarization state of the thin film. Experimental measurements are compared with theoretical determinations by ab initio methods. The nature of stabilizing charges for the ferroelectric state near the surfaces was also identified [see *Advanced Science 10, 2205476 (2023)*];
- Polaronic coupling in $LaSrMnO_3$ is modulated by a ferroelectric film interfacing the manganite. The polarization of the ferroelectric thin film modulates the density of 2D holes and 3D electrons and influences their coupling with the lattice, by formation of high Fröhlich polarons which diminish the mobility of charge carriers [see *Communications Physics 5, 209 (2022)*];
- The solid Earth's inner core has ferromagnetic properties. This finding results from the application of a new model for band ferromagnetism, which explains, on one hand, all properties of 3D ferromagnetic metals (stable structures, occurrence of ferromagnetism, Curie temperatures, coercive fields) and, on the other hand, predicts the occurrence of re-entrant ferromagnetism at extremely high temperatures (see *Physics of the Earth and Planetary Interiors 326, 106856 (2022)*];
- Microscopic model for ferroelectricity with variable dielectric constant, derived self-consistently from mean field theory. This model extends the microscopic model for ferroelectricity proposed last year, where charges accumulated at surfaces and interfaces of a ferroelectric thin film are considered as stabilizing charges for the ferroelectric state. The permittivity of the ferroelectric was considered an external parameter of the model, while in the case of this last work the permittivity is self-consistently derived starting from the equation of state resulting from statistical physics applied to the microscopic model [see *Physical Chemistry Chemical Physics 24, 5419–5430 (2022)*];
- Nanoscopic correlations and interpretations from multifit analysis of photoelectron spectromicroscopy data of ferroelectric surfaces. By ultrafast fitting of all spectra from a data cube produced by spectro-microscopic measurements using synchrotron radiation on a ferroelectric material, one analyzes correlations between fitting parameters and quantifies separately charging effects with respect to band bending effects inherent to the state with out-of-plane polarization; one determines also the evolution of a ferroelectric state at the expense of the other and also the distribution of the band bending at surface [see *Results in Physics 36, 105436 (2022)*];
- Electron localization in graphene nanodots with lifetime controlled by circularly polarized light. This localization takes place in spite of the Klein tunneling; the lifetime of these localized states can be controlled by the light intensity and by the application of a magnetic field perpendicular on the graphene quantum dot [see *Physical Review B 105, 125408 (2022)*].

LABORATORY 50
“Theoretical Physics and Computational Modeling”

Head of laboratory: Dr. Valeriu MOLDOVEANU, Senior Researcher rank 1 (valim@infim.ro)

Personnel: 7 members – 1 × SR1, 1 × SR2, 3 × SR3, 1 × SR, 1 × RA, and 1 × PhD student.

Main research directions:
- Topological and transport properties of 2D materials and lattices;
- Hybrid quantum systems for nano-electronics and nano-optomechanics;
- Correlation effects in 2D lattices and artificial molecules.

Main results:
- 1 ongoing project (PD);
- 10 articles published in Web of Science®-indexed journals with impact factor (of which 3 with main author from Lab. 50, and 5 in collaboration with experimental groups).

Highlights:
- Characterization of the spectral and quantum transport properties of two-dimensional heterostructures based on topological materials with different topology, specifically the Chern-type topological insulator and the Weyl semimetal. The calculations were performed in the Landauer–Büttiker formalism, with a focus on the changes in the energy spectrum and edge states distribution in the presence of interfaces. The results show that the combined action of the two types of edge states in the presence of interfaces gives rise to unexpected features in the quantum Hall effect, such as the zero-value plateau, lack of negative plateaus, and asymmetric fractional plateaus. These effects are observed mainly in certain heterostructures, while the system Chern insulator/semimetal/Chern insulator shows a robust anomalous quantum Hall effect. The findings suggest that metamaterials could be a good platform for experimentally observing such effects [see *Applied Surface Science 587, 152769 (2022)*];
- Theoretical studies on quantum interference in physical systems described by discrete nonsingular Hamiltonians and submitted to external perturbations [see *Physical Review B 105, 155303 (2022)*];
- Improved calculation of eigenvalues and eigenfunctions for hybrid quantum system in the ultrastrong qubit-photon coupling regime [see *Physical Review A 105, 023704 (2022)*].

LABORATORY 60
“Optical Processes in Nanostructured Materials”

Head of Laboratory: Dr. Mihaela BAIBARAC, Senior Researcher rank 1, Habil. (barac@infim.ro)

Personnel: 29 members – 5 × SR1, 4 × SR2, 2 × SR3, 7 × SR, 10 × RA, and 1 × technician.
From the 29 members, 18 possess PhD titles in physics. 1 PhD supervisor and 6 PhD students are involved in educational activities.

Main research directions:

- Optical properties of composite materials based on macromolecular compounds and carbon nanoparticles (graphene, including graphene oxide and reduced graphene oxide, carbon nanotubes, fullerene) and phosphorene, respectively, for applications in the field of eco-nanotechnologies, health and energy storage (supercapacitors, rechargeable batteries);
- Photoluminescence of 2D inorganic materials (including dichalcogenides) and their applications in information technology, sensors and energy storage;
- Optical properties of plasmonic materials, quantum dots and their applications in the fields of eco-nano-technologies and the pharmaceutical field;
- Optical properties of the inorganic micro/nano-particles for applications in the fields of heritage and optoelectronics.

Relevant infrastructure:

- An UV-VIS-NIR spectrophotometer, Lambda 950 model, from Perkin Elmer;
- A FTIR spectrophotometer, Vertex 80 model, from Bruker;
- A FT-Raman spectrophotometer, MultiRam model, from Bruker (**Fig. 60–1**);
- A Fluorolog FL-3.2.2.1 model with upgrade for the NIR range, from Horiba Jobin Yvon;
- A triple Raman spectrophotometer T64000 model, from Horiba Jobin Yvon, equipped with the lasers for the excitation in visible range;
- A FTIR imaging microscope SPOTLIGHT 400 from Perkin Elmer;
- A thermoluminescence reader Harshaw TLD 3500;
- A system for photoconductivity and I–V characteristics;
- A Scanning Near Field Optical Microscope (Multiview 4000 SNOM/SPM system from Nanonics) coupled with Atomic Force Microscope (AFM);
- A Fluoromax 4P with quantum efficiency and colorimetry options, for luminophores characterization, o system to measure surface/interfacial tension, contact angle and density;
- A Langmuir-Blodgett instruments, KSV 2000 system and KSV 5003 model;
- A potentiostat/galvanostat, Voltalab 80, from Radiometer Analytical;
- A multi-channel potentiostat/galvanostat, Origaflex model, from Origalys;
- An equipment for deposition by vacuum evaporation of organic materials;
- A broadband dielectric spectroscopy system from Novocontrol;
- An infrared spectro-microscope, Carry 600, from Agilent Scientific;
- A surface plasmons resonance (SPR) equipment from Reichert (**Fig. 60–2**);
- A hybrid Magnetron Sputtering – Pulsed Laser Deposition equipment for thin-films (**Fig. 60–3**);
- A physical Vapor Transport equipment for transition metal dichalcogenides (**Fig. 60–4**).

Available services:

- Development of composite materials based on the conducting and insulating polymers and carbon nanoparticles of the type carbon nanotubes, graphene oxide, reduced graphene oxide, graphene quantum dots, fullerene and carbon nanohorns;

- Development of organic/inorganic hybrid materials based on conducting polymers and inorganic nanoparticles of the type ZnO, ZnS, CdS, TiO_2;
- Chemical and electrochemical functionalization of 2D materials (reduced graphene oxide, phosphorene, *etc*) with the organic and macromolecular compounds;
- Synthesis of transition metal dichalcogenides (TDMs) of the type MoS_2, WS_2, *etc*;
- The preparation of the surface-enhanced Raman scattering (SERS) supports of the type of rough metallic (Ag, Au, Cu) films, the colloidal suspensions of the metallic nanoparticles and the graphene sheets decorated with metallic nanoparticles;
- Deposition of thin layers using magnetron sputtering and Langmuir Blodgett;
- Realization of organic/organic and organic/inorganic structures by vacuum evaporation and from solution;
- Controlled crystallization of thin-films in various atmospheres;
- Functionalization of metallic surfaces for development of optical sensors *via* surface plasmons resonance;
- Analyzes by the UV-VIS-NIR and IR absorption spectroscopy, Raman scattering, surface-enhanced Raman scattering (SERS), surface-enhanced infrared absorption (SEIRA) spectroscopy, photoluminescence, atomic force microscopy and broad-band dielectric spectroscopy;
- Structural characterization and phase identification in crystalline materials;
- Contact angle analysis for assessment of hydrophobic/hydrophile properties;
- Measurements of surface/interface tension and of the density of liquids;
- Colorimetry and quantum yield measurements for the characterization of phosphors;
- Calculated absorption coefficient of inorganic and macromolecular chain with density-functional theory (DFT);
- Electrochemical analysis by cyclic voltammetry, chronoamperometry, chronopotentiometry, electrochemical impedance spectroscopy, Tafel polarizations;
- Surface nano-patterning by UV Nano Imprint lithography (UV-NIL);
- Characterization of organic heterostructures for opto-electronic devices;
- Galvanostatic charge-discharge measurements for the testing nanomaterials as electrode active materials in supercapacitors and rechargeable batteries;
- The preparation of electrodes with the application in the field of the electrochemical sensors;
- Analysis concerning the stability of the drugs in the presence of UV light and various chemical agents by UV-VIS spectroscopy, photoluminescence, Raman scattering and FTIR spectroscopy.

Fig. 60–1 MultiRam FT-Raman spectrophotometer from Bruker.

Fig. 60–2 Surface Plasmon Resonance equipment from Reichert.

Fig. 60–3 Hybrid Magnetron Sputtering – Pulsed Laser Deposition equipment for thin-films.

Fig. 60–4 Physical Vapor Transport equipment for transition metal dichalcogenides.

Main results:

- 7 ongoing projects (1 × SEE, 1 × M-ERA NET, 1 × POC-G, 1 × POC-TI, 2 × PED, and 1 × PCE), all ongoing in 2023; in addition, Lab. 60's team is involved in 2 COST actions.
- 37 articles published in Web of Science®-indexed journals with impact factor (of which 19 with main author from Lab. 60);
- 4 OSIM awarded patents;
- 7 OSIM patent requests.

Highlights:

- The highlighting photodegradation pathways of pharmaceutical compounds of the: pantoprazole sodium- [see *Scientific Reports 12, 9515 (2022)*], ampicillin- [see *Pharmaceuticals 15, 415 (2022)*], losartan potassium-, [see *Pharmaceutics 14, 2419 (2022)*], and azathioprine-type [see *International Journal of Molecular Sciences 23, 3975 (2022)*];
- Development of a new memristor with ultra-low power consumption based on 2D chalcogenide materials [see *Applied Surface Science 599, 153983 (2022)*] and thin-films for photovoltaic cells [see *ACS Omega 7, 23800–23814 (2022)* and *Scientific Reports 12, 7958 (2022)*];
- Development of transparent glassy nanocomposites doped with broad-band luminescence rare-earth ions ($Eu^{2+)}$ and high efficiency, for various applications: X-ray storage phosphor for digital imaging, scintillators, particles detectors, dosimetry white light sources [see *Nanomaterials 12, 3016 (2022)*];
- The molecular mobility of two alkyl phenyl benzoates was investigated by broadband dielectric spectroscopy over a large frequency and temperature range for both bulk materials and composites with aerosil A380 [see *Journal of Molecular Liquids 359, 119374 (2022)*].
- Fabrication of metalens by UV-NIL and tunable metalens for sensors with application in detection of different types of plastic (see *project EEA-RO-NO-2018-0438: Elastomeric tunable metasurfaces for efficient spectroscopic sensors for plastic detection*);
- Realization of organic heterostructures with bulk heterojunction based on arylenevinylene polymers donors and perylene diimide acceptor on surfaces nanostructured by UV-NIL [see *project PCE 66 din 08/02/2021: Waterproof deformable hybrid solar cells* & *see Nanomaterials 12, 4230 (2022)*];
- Chemical and electrochemical functionalization of phosphorene with diphenylamine and poly(diphenylamine) [see *Polymers 14, 4479 (2022)*].

LABORATORY 70
“Atomic Structures and Defects in Advanced Materials”

Head of laboratory: Dr. Corneliu GHICA, Senior Researcher rank 1 (cghica@infim.ro)

Personnel: 35 members – 5 × SR1, 7 × SR2, 6 × SR3, 2 × SR, 11 × RA, 3 × engineers, and 1 × technician.

Main research directions:

- Atomic scale structure-functionality correlations in advanced materials (nanostructures, thin-films, ceramics and special alloys);
- Paramagnetic point defects, either intrinsic or induced by impurities or radiations in insulators and wide-bandgap semiconductors;
- Investigation of the physical-chemical mechanisms underpinning the detection process in nanostructured materials for gas sensing applications;
- Dielectric and semiconductor thin-films for microelectronic applications of interest for environment, security, space, biomedicine, food safety;
- Cellular and non-cellular *in vitro* interactions and biomedical applications of inorganic nanomaterials and hybrid nanostructures.

Main research infrastructure:

- Aberration-corrected analytical transmission electron microscope (HRTEM/HRSTEM) provided with EDS and EELS microanalytical facilities for sub-Ångström resolution imaging and atomic-resolution elemental mapping;
- High-resolution analytical electron microscope for electron tomography, *in situ* and *operando* experiments by specimen heating/cooling/electrical biasing;
- SEM-FIB dual analytical system used for morpho-structural and microanalytical investigations (SEM, EDS, EBSD) as well as for ion beam micro- and nano-processing;
- Continuous wave (cw) X-band (9.8 GHz) EPR spectrometer with variable temperature (VT) accessories in the 80 – 500 K range; cw Q-band (34 GHz) EPR spectrometer with ENDOR (Electron-Nuclear Double Resonance) and VT accessories (5 – 300 K);
- Pulse X-band (9.7 GHz) EPR spectrometer equipped with pulse ENDOR, pulse ELDOR (Electron-Electron Double Resonance) and VT accessories (5 – 300 K);
- Automatic liquid He plant completed with a helium recovery system; computer-controlled gas mixing station and associated electrical measurements chains for materials testing under controlled atmosphere;
- Chemical reactor and autoclave for hydrothermal and co-precipitation chemical synthesis;
- Magnetron sputtering installation for thin-films deposition, with *in situ* characterization/monitoring by Auger electron spectroscopy (AES), low-energy electron diffraction (LEED) and ellipsometry;
- Installation for rapid thermal annealing, oxidation and nitriding; horizontal furnace with 3 temperature zones for thermal treatments and physical vapor deposition (PVD);
- Measurement chains for electrical, ferroelectric and photoelectric characterization, Hall effect and magnetoresistance measurements.

Fig. 70–1 (a) Bruker EPR spectrometer in X band (9.7 GHz) in pulsed regime with ENDOR accessories; (b) Bruker EPR spectrometer in CW Q-band with ENDOR accessory;(c) Setup for electrical measurements under controlled atmosphere gas mixing station; (d) JEM 2100 high-resolution analytical transmission electron microscope; (e) Tescan Lyra III analytical SEM-FIB dual system;(f) Magnetron sputtering installation for thin-films deposition, provided with in situ AES, LEED and ellipsometry; (g) Installation for rapid thermal processing (RTA, RTO, RTN), horizontal furnace with 3 temperature zones for thermal treatments and PVD; (h) Measurement chains for electrical, ferroelectric and photoelectric characterization, Hall effect and magnetoresistance measurements.

Available services:

- SEM morphological characterization of advanced materials;
- TEM characterization of nanostructured materials, thin-films, ceramics, alloys;
- Chemical elemental composition and elemental mapping by SEM-EDS and STEM-EDS;
- Multifrequency EPR characterization of bulk and nanostructured insulating and semiconductor materials: nature, concentration, localization, formation mechanism and stability of the paramagnetic centers in materials; chemical processes, structural or magnetic transitions;
- Controlled simulation of toxic and explosive gas environments (CO, CH_4, NO_2, H_2S, NH_3, SO_2) for gas sensors testing and calibration; temperature-voltage calibration for the optimization of power consumption for substrates and gas sensors.
- Growth of thin-films and multilayers by magnetron sputtering;
- Rapid thermal annealing (RTA) and controlled oxidation (RTO) at temperatures within 200 – 1250 °C, heating rates up to 200 °C/s in gas flow (N_2, O_2, Ar, H_2) and thermal treatments using the horizontal furnace with 3 temperature zones up to 1200 °C in vacuum or flow of Ar, N_2;
- Electrical characterization under dark/illumination conditions, Hall effect measurements and modelling of experimental curves current-voltage (I–V) at varying temperature, in DC and AC, capacity-voltage (C–V), capacity-frequency (C–f), capacity-time (C–t), polarization-voltage (P–V), I–T and R–T; spectral characteristics of the photocurrent (I–λ) in modulated and continuous illumination; Hall measurements: V–I curves as a function of current, magnetic field and temperature.

LASDAM operates as Partner Facility within CERIC-ERIC (https://www.ceric-eric.eu/) on behalf of NIMP, the Romanian Representing Entity in the consortium along with research institutes and universities in Austria, Croatia, Czech Republic, Hungary, Italy, Poland, Slovenia.

Main results:

- 13 ongoing projects (1 × PCCF, 2 × PED, 3 × PCE, 1 × M-ERA.NET, 4 × TE, 1 × PD, and 1 POC) of which 10 continue in 2023 (1 × PED, 3 × PCE, 1 × M-ERA.NET, 4 × TE, and 1 POC);
- 47 articles published in Web of Science®-indexed journals with impact factor (of which 8 with main author from Lab. 70);
- 2 OSIM awarded patents;
- 3 OSIM patent requests.

Highlights:

- Exploration of new materials for CO and CO_2 detection: the sensing mechanism in chemosensors based on NiO and Gd-doped SnO_2 as an interplay between ionosorption processes and the nanomorphology of the gas-sensitive material [see *Sensors and Actuators B: Chemical 368, 132130 (2022)*; *Chemosensors 10, 191 (2022)*; and *Chemosensors 10, 466 (2022)*];
- Elucidation of the role played in the photocatalytic activity by the crystalline structure and distribution of the Ti^{3+} defects in nanocrystalline TiO_2 polytypes [see *Nanomaterials* 12, 2563 (2022)];
- New chemical routes for the synthesis of multipurpose iron oxide-TiO_2 magnetic nanocomposites with engineered morpho-structural, AC magnetic heating, ROS photogeneration and biocompatibility properties for biomedical and environment-related applications [see *Scientific Reports* 12, 6887 (2022)];
- In-depth characterization of impurities in dark cubic boron nitride (cBN): morphology, crystal structure, composition, and conduction electron properties of quasi-spherical α-Sn nanoprecipitates with unstrained diamond cubic structure, analyzed by correlated analytical HRTEM/STEM and multifrequency ESR investigations [see *ACS Omega* 7, 41981–41996 (2022)];
- MOS-like trilayer structures for non-volatile memories including floating gates based on doped high-k oxide thin films: SiGeSn quantum dots embedded in HfO_2 and Zr-doped ZrO_2 [see *Coatings* 12, 348 (2022) and *Coatings* 12, 1369 (2022)].

LABORATORY 80

“Catalytic Materials and Catalysis”

Head of laboratory: Dr. Mihaela FLOREA, Senior Researcher rank 1, Habil. (mihaela.florea@infim.ro)

Personnel: 8 members – 2 × SR1, 1 × SR 2, 1 × SR3, 1 × SR, and 3 × RA.

Main research directions:

- Development of heterogeneous catalytic and photocatalytic materials (preparation and characterization);
- Catalytic reactions: selective oxidation reactions, hydrogenation reactions, synthesis of polymers from renewable/alternative resources, depolymerization of plastics, reduction of volatile organic compounds;
- Photocatalysis: water splitting, photocatalytic CO_2 transformation and artificial photosynthesis;
- Energy: synthesis of materials used as electrocatalysts in fuel cells.

Relevant infrastructure:

Lab. 80 has an infrastructure covering various methods of catalytic material preparation and physico-chemical characterization. Among the important infrastructures one can mention:

- Chemistry laboratory (**Fig. 80–1**) equipped with all necessary small equipment’s for catalytic materials synthesis (ovens working in air or vacuum, rotavapors, magnetic stirrers, autoclaves for hydrothermal treatments, chemical niche, apparatus for milliQ water production, centrifuge, balances) and catalytic reactors (in house reactors for solid-gas phase and liquid-solid phase reactions);
- Thermo-programmed desorption and reduction equipment (TPD-TPR) – for determining the adsorption capacity and redox properties (**Fig. 80–2**);
- Spectroscopy analysis: UV-Vis and Raman portable (**Fig. 80–2**);
- Thermal analysis – to study the relationship between a sample property and its temperature as the sample is heated or cooled in a controlled manner (**Fig. 80–2**)
- Analysis of the reaction products – gas chromatograph with three detectors (TCD, FID, and BID) gas chromatograph coupled with mass spectrometer (**Fig. 80–2**).

The group has access to other infrastructures located at NIMP, through collaborative research activities, such as: SEM; TEM; XPS; optical spectroscopies (Raman, UV-Vis-NIR, FTIR); X-ray diffraction; ICP-MS; photoluminescence.

Fig. 80–1 Chemistry laboratory.

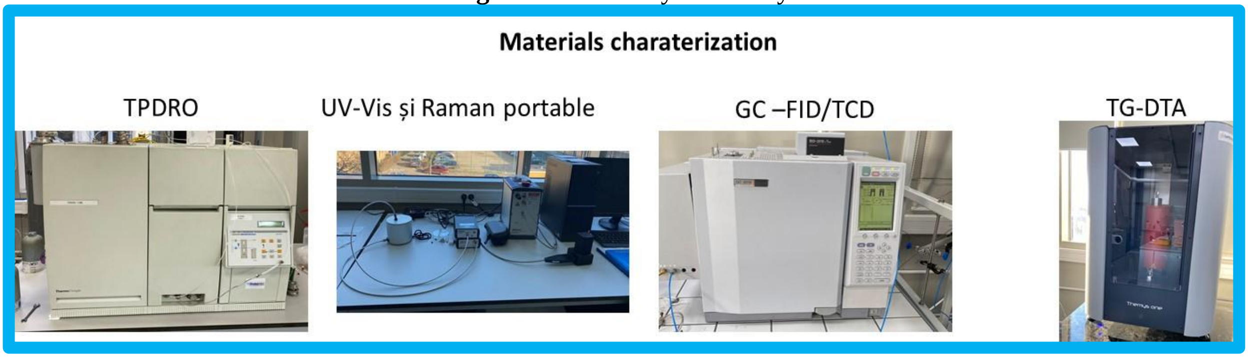

Fig. 80–2 Equipment for materials characterization and analysis.

Available services:

- Catalytic materials preparation;
- Gas-solid and gas-liquid catalytic reaction;
- Water splitting;
- Surface characterization;
- Structural and textural characterization of the catalytic materials;
- Investigation of acid-base and redox properties.

Main results:

- 5 ongoing projects (1 × ERC-like, 1 × M-ERA.NET, 1 × PTE, 1 × PCE, and 1 × TE) of which 3 continue in 2023 (1 × ERC-like, 1 × PTE, and 1 × PCE);
- 6 articles published in Web of Science®-indexed with high-impact factor (of which 2 with the main author from Lab. 80);
- 1 Patent Cooperation Treaty with Drexel University (U.S.A.).

Highlights:

- The studies supported by the TE project have resulted in the creation of a modified acid MXenes that can depolymerize PET to its monomers (terephthalic acid and ethylene glycol) with a yield of up to 70% from various sources like plastic bottles, T-shirts, and green plastic bottles;

- Making 1D filaments of materials containing Ti, C, and O to split water under photocatalytic conditions and create H_2 gas is a straightforward, low-cost, and economically viable strategy thanks to a collaboration with a team of researchers at Drexel University headed by Prof. M. Barsoum (The partnership will continue into 2023 as well);
- The primary objective of the ERC-like project is to use surface-modified MAX-phase with various metal oxides to produce methanol *via* selective oxidation of methane;
- New photocatalytic systems based on *i*-MXene-semiconductor composites for hydrogen production *via* photocatalytic water splitting reaction are the main focus of the PCE-funded project.
- The development of new 2D hybrid perovskites to be used as an adsorber layer in solar cell devices.

Materials modeling, preparation and characterization

Electrochemical Deposition of ZnO Nanowires on CVD-Graphene/Copper Substrates

Issam Boukhoubza[a], Elena Matei[b], Anouar Jorio[a], Monica Enculescu[b], Ionut Enculescu[b]
[a]Group of Nanomaterials and Renewable Energies, Laboratory of Solid State Physics, Faculty of Sciences Dhar El Mahraz, Sidi Mohammed Ben Abdellah University, 30000 Atlas Fez, Morocco
[b]Laboratory of Functional Nanostructures, National Institute of Materials Physics, 405A Atomistilor, 077125 Magurele, Romania

ZnO nanowires (NWs)/graphene (G) hybrids can be developed to enhance the performance of optoelectronic devices [1], including sensors, light-emitting diodes, and photodetectors. In this work [2] ZnO NWs/G hybrids were synthesized by a two-step process (Figure 1a, b). In the first step, the graphene-covered electrodes were obtained by chemical vapor deposition (CVD) on Cu substrates. Secondly, the ZnO NWs were deposited onto the graphene surface by using electrochemical deposition [3].

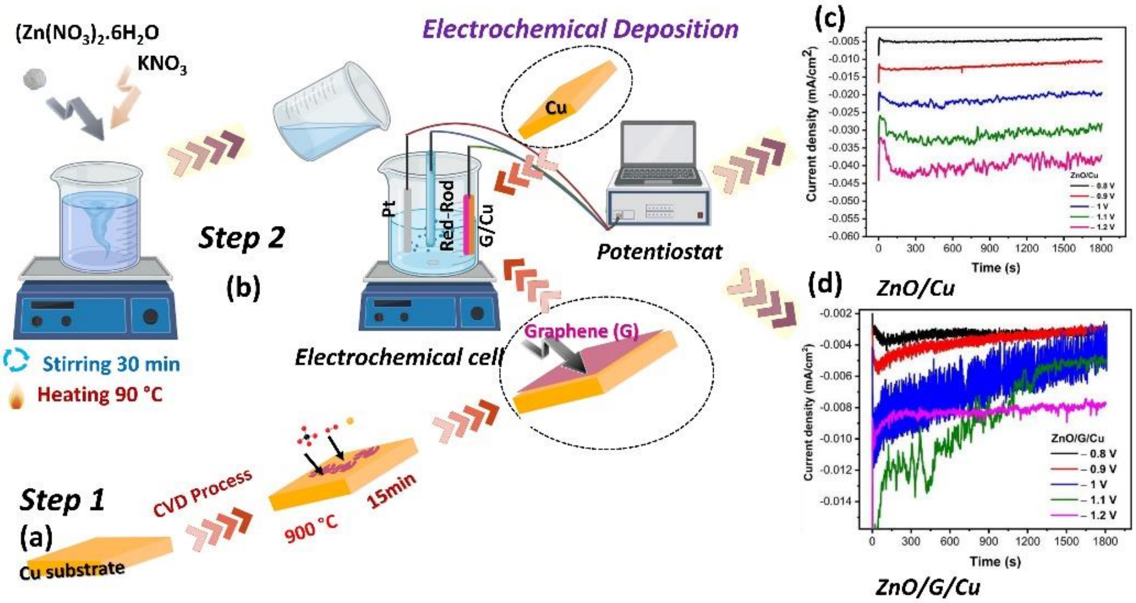

Fig. 1 Synthesis process of (a) CVD-G/Cu and (b) ZnO/G/Cu and deposition curves at different applied potentials for (c) ZnO/Cu and (d) ZnO/G/Cu.

Based on the electrochemical measurements conducted in this study, it was found that a higher current density was observed for the pristine copper electrodes compared to graphene covered electrodes during the ZnO NWs electrodeposition process. Further, the deposition on graphene covered electrodes occurred at more electronegative potentials. In both cases, the process was observed to follow a nucleation/growth mechanism, with a higher nucleation rate observed for copper substrates. The XRD measurements indicated the formation of the hexagonal wurtzite structure of ZnO, the high texture coefficient of (002) planes in ZnO NWs/G/Cu samples confirms that ZnO nanowires exhibit a preferential orientation growth along the *c*-axis.

The high-resolution SEM images showed that the growth process on both simple and graphene covered Cu electrodes lead to dense and homogeneous ZnO NWs with well-crystallized material. ZnO nanowires with hexagonal and planar faces were observed at their top in the potential range of −0.8 V to −0.9 V (Figure 2a,b), while pyramid-faced nanowires were observed in the potential range of −1 V to −1.2 V (Figure 2c–e). In the case of CVD-graphene/Cu electrodes, a high density of wires was observed at electrode potentials of −0.8 V to −1.1 V (Figure 2g–k), decreasing at −1.2 V (Figure 2j), this trend being consistent with a nucleation growth model and a diffusion rate-limited process. Cross-section SEM image (Figure 2l) confirmed the formation of ZnO NWs with a length of 1.5–2 μm on the graphene/Cu substrate at −0.9 V. The average diameter distribution was determined by measuring ZnO NWs from SEM images using Image J software (Figure 2f). The results indicated that the NWs had an average size which depends on electrode potential and ranges between 20 and 300 nm.

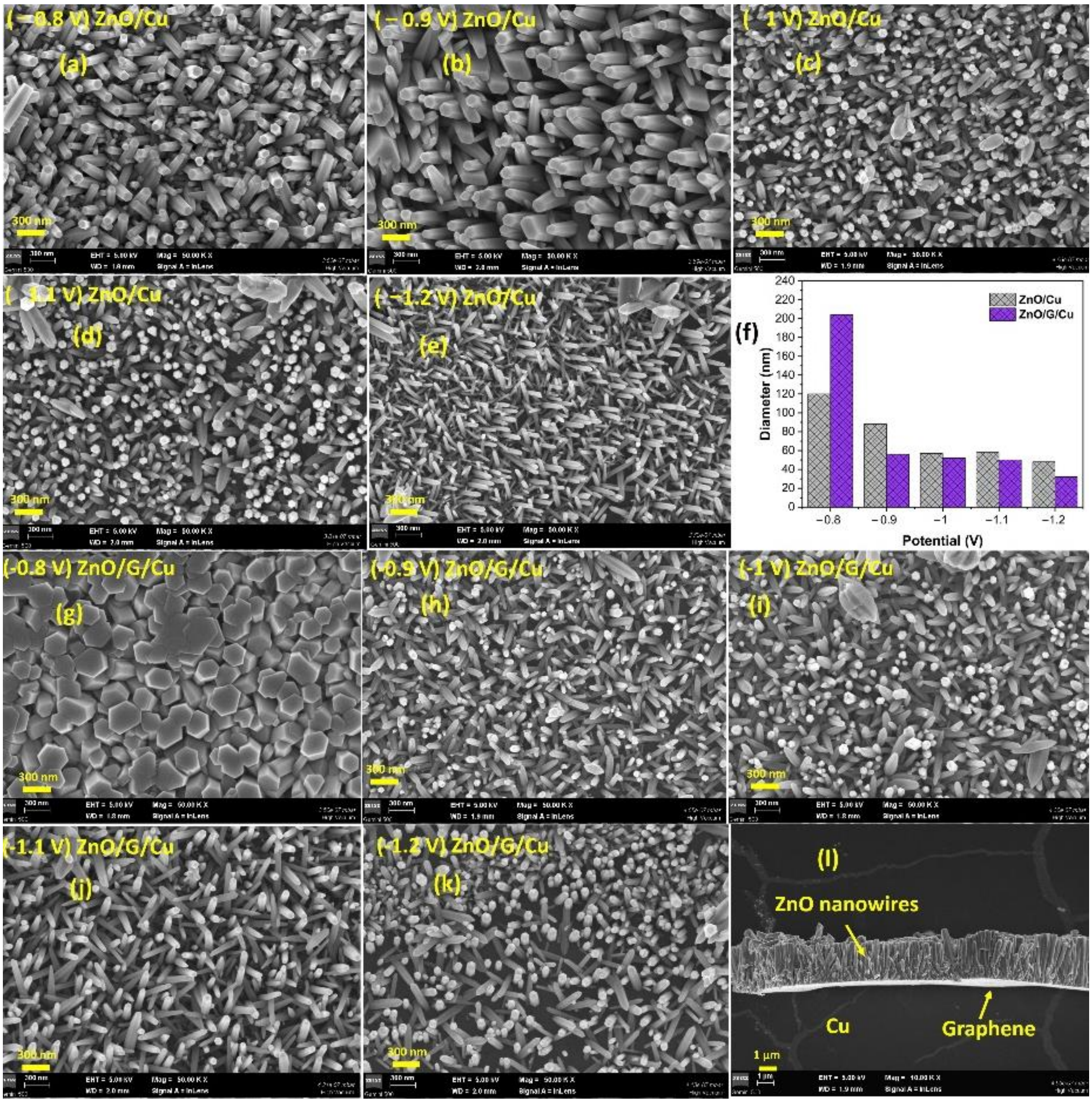

Fig. 2. SEM images of ZnO nanowires grown on (a─e) Cu and (g─k) G/Cu at different potentials *vs.* RE. (l) Cross-section of ZnO/G/Cu obtained at −0.9 V *vs.* RE. (f) Average diameter size of ZnO nanowires as function of deposition potential for both types of electrodes.

Based on the reflectance spectra, it was found that the band gap of ZnO/Cu (3.15 eV) was slightly less than the band gap of ZnO/G/Cu (3.21 eV). This difference in band gap value was attributed to the interaction between ZnO nanowires and the graphene layer, as well as to the concentration of point defects in the material.

The photoluminescence (PL) spectra (Figure 3a) showed that, in all cases, the wires grown on graphene presented a more intense excitonic peak compared to ZnO nanostructures grown directly on copper at the same electrode potential. This observation was attributed to a lower concentration of defects, which was also correlated to the results obtained from the diffraction measurements. The concentration of defects was also found to be related to the deposition potential, with the luminescence of the exciton peak being more intense for the samples grown at less electronegative potential. For the samples grown at the most electronegative potential, the excitonic peak almost disappeared, being dwarfed by the defect-related bands. The chromaticity diagram showed a shift in emission from yellow-orange obtained for ZnO/G/Cu to greenish-yellow of Zn/Cu.

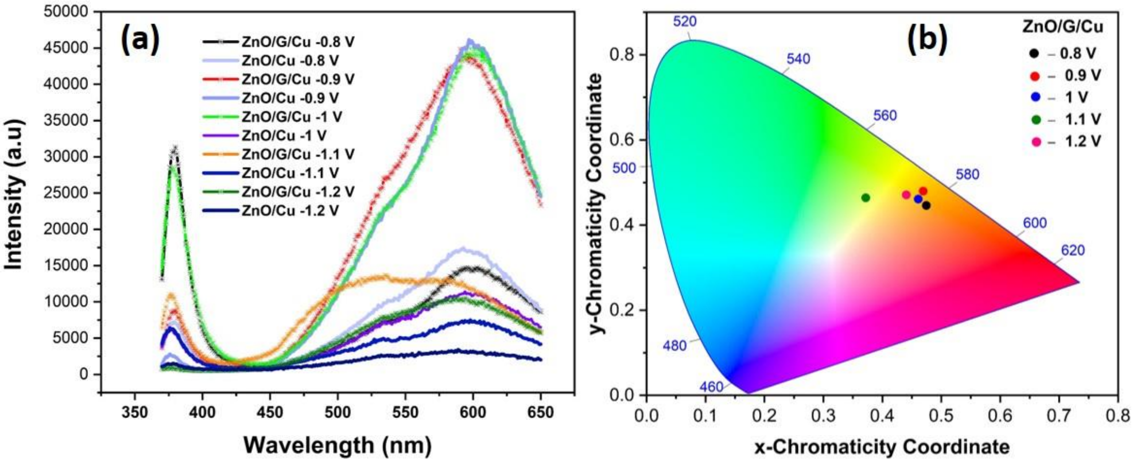

Fig. 3. (a) PL spectra and (b) CIE chromaticity diagram of ZnO/G/Cu prepared at different applied potentials.

References

1. L George, S Thomas, S Nalini, MK Jayaraj, "Electrodeposition of ZnO nanostructures on graphene for optoelectronic applications", *AIP Conference Proceedings* 2162, 020014 (2019).
2. I Boukhoubza, E Matei, A Jorio, M Enculescu, I Enculescu, "Electrochemical deposition of ZnO nanowires on CVD-graphene/copper substrates", *Nanomaterials* 12, 2858 (2022).
3. E Matei, A Costas, C Florica, M Enculescu, I Pintilie, L Pintilie, I Enculescu, "Electrical properties of templateless electrodeposited ZnO nanowires", *Materials Science in Semiconductor Processing* 42, 364–372 (2016).

Functionalization of Flax Fibers by ZnO Electroless Deposition: Approach for Tailoring the Interphase in the Natural Fiber-Reinforced Epoxy Resin Composites

Nicoleta Preda[a], Andreea Costas[a], Francesca Sbardella[b], Maria Carolina Seghini[b], Fabienne Touchard[c], Laurence Chocinski-Arnault[c], Jacopo Tirillo[b], Fabrizio Sarasini[b]
[a]Laboratory of Functional Nanostructures, National Institute of Materials Physics, 405A Atomistilor, 077125 Magurele, Romania
[b] Department of Chemical Engineering Materials Environment, Sapienza-Università di Roma & UdR INSTM, 18 Via Eudossiana, 00184 Roma, Italy
[c] Département Physique et Mécanique des Matériaux, ENSMA, Institut PPRIME, CNRS—ENSMA—Université de Poitiers, 1 Av. Clément Ader, B.P. 40109, CEDEX, 86961 Poitiers, France

Natural fiber-reinforced epoxy resin are the most used composite materials in the automotive and construction industries, the interfacial adhesion between the fibers and matrix playing the key role in achieving the required mechanical performance. In our study [1], flax fibers were coated by ZnO electroless deposition in order to develop a ZnO nanostructured interphase, which can improve the interphase between the fibers and epoxy resin in their composites. A surface functionalization technique, ZnO electroless deposition allows the coverage of complex geometries and non-conductive substrates such as fabrics with ZnO nanostructures.

The XRD patterns of the ZnO-coated flax fibers (Figure 1) showed: (*i*) two narrow peaks at 15° and 17° and one sharper intense peak at 23° related to the cellulose I phase from higher plant cellulose and (*ii*) sharp, narrow and intense diffraction peaks assigned to ZnO hexagonal wurtzite phase.

The FESEM images of the ZnO-coated flax fibers (Figure 2) emphasize that the ZnO electroless deposition leads to a relatively uniform coating of fibers on large areas. The size and morphology of ZnO nanostructures is not influenced by the sample geometry (fabric or yarn), the surface of the fibers being covered by a continuous, homogeneous and densely packed array of ZnO well faceted hexagonal prisms having a base diameter of ~500 nm and the height of ~100 nm.

The wettability of the flax fabrics before and after ZnO electroless deposition was assessed (Figure 3). The pristine flax fabric absorbs instantly the water droplet placed on its surface (hydrophilic behavior) while the water droplet seems “to rest” on the ZnO-coated flax fabrics, immediately after its placement on the surface, the surface revealing an apparent contact angle of ~140° (hydrophobic behavior). This particular behavior can be related on one hand to the decrease of the space between the flax fibers due to their covering with ZnO nanostructures and to the hydrophobic behavior of the ZnO synthesized by the electroless deposition approach and on the other hand to the capillary wicking, phenomenon that usually occurs in the porous structure of the fabrics.

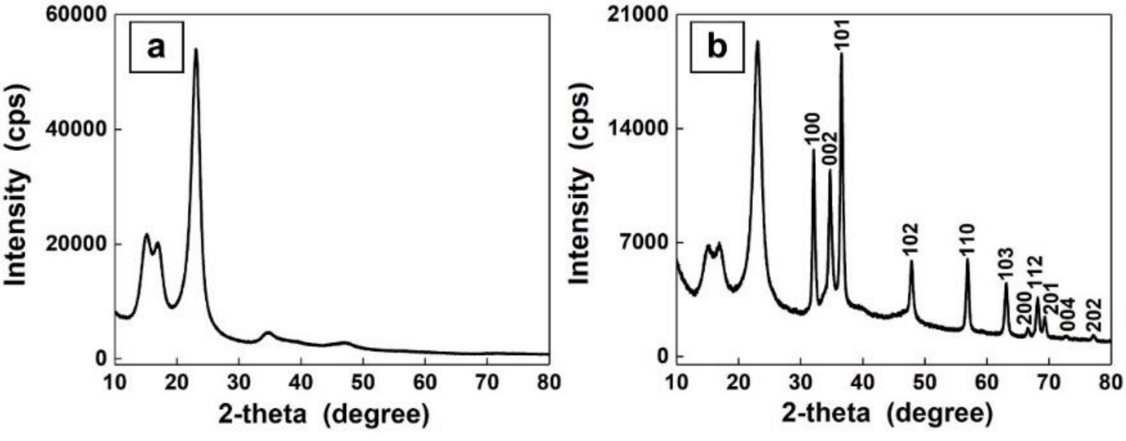

Fig. 1 XRD patterns of (a) flax fibers and (b) ZnO-coated flax fibers.

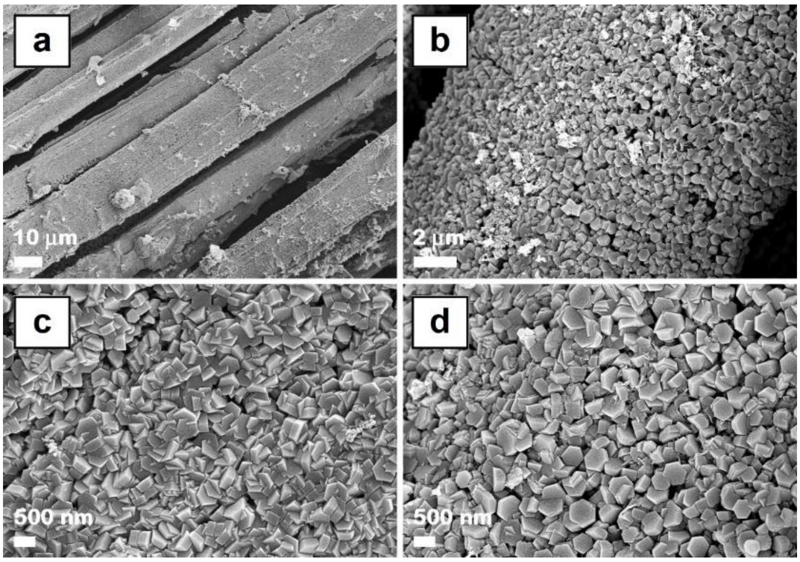

Fig. 2 FESEM images of ZnO-coated flax fibers as (a, c) fabrics and (b, d) yarns.

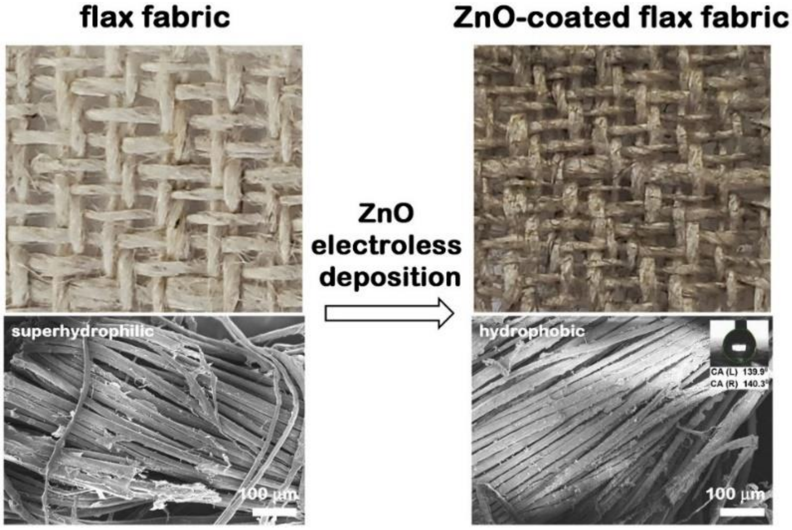

Fig. 3 Optical images and FESEM images of flax fabrics and ZnO-coated flax fabrics. In the inset is shown the optical photograph of the water droplet shape on the hydrophobic surface of ZnO-coated flax fabrics and the water contact angles for the corresponding sample.

The single yarn fragmentation tests revealed that the presence of ZnO nanostructures on the surface of the flax fibers leads to a notable increase in the interfacial adhesion with an epoxy matrix, reductions of 36% and 9% in debonding and critical length values being measured compared to those of the pristine flax yarns, respectively. Thus, the ZnO nanostructured interphase allows a smoother transition between the flax yarns and the epoxy resin matrix in terms of mechanical properties for a better load transfer and mechanical interlocking.

The functionalization of flax fibers by ZnO electroless deposition opens new opportunities for tailoring the mechanical performance of the composites based on natural fibers and synthetic matrices in order to meet a wide range of requirement necessary for expanding their potential range of applications.

References

1. N Preda, A Costas, F Sbardella, MC Seghini, F Touchard, L Chocinski-Arnault, J Tirillo, F Sarasini, “Hierarchical flax fibers by ZnO electroless deposition: tailoring the natural fibers/synthetic matrix interphase in composites”, *Nanomaterials* 12, 2765 (2022).

Novel Dextran Coated Cerium Doped Hydroxyapatite Thin Films

Carmen Steluta Ciobanu[a], Ionela Cristina Nica[b,c], Anca Dinischiotu[c], Simona Liliana Iconaru[a], Patrick Chapon[d], Bogdan Bita[e], Roxana Trusca[f,g], Andreea Groza[e], Daniela Predoi[a]

[a]Laboratory of Functional Nanostructures, National Institute of Materials Physics, 405A Atomistilor, 077125 Magurele, Romania

[b]Department of Biochemistry and Molecular Biology, Faculty of Biology, University of Bucharest, 91–95 Splaiul Independentei, 050095 Bucharest, Romania

[c]Research Institute of the University of Bucharest-ICUB, University of Bucharest, 050657 Bucharest, Romania

[d]HORIBA Jobin Yvon S.A.S., 6-18, Rue du Canal, CEDEX, 91165 Longjumeau, France;

[e]National Institute for Laser, Plasma and Radiation Physics, 409 Atomistilor, 077125 Magurele, Romania,

[f]Faculty of Applied Chemistry and Materials Science, Department of Science and Engineering of Oxide Materials and Nanomaterials, University "Politehnica" of Bucharest, 060042 Bucharest, Romania

[g]Centre for Micro and Nanomaterials, University "Politehnica" of Bucharest, 060042 Bucharest, Romania

Studies regarding the production and characterization of hydroxyapatite materials in various chemical structures represent effervescent research topics due to medical and biological applications of these compounds. Natural hydroxyapatite (HAp) is the major mineral constituent extensively present in bones and teeth (enamel and dentine) and largely used in reconstruction engineering. It can contain cations such as: Mg^{2+}, Na^{2+} or anions such as CO_3^{2-}, OH^- [1,2]. Nevertheless, synthetic hydroxyapatite $Ca_{10}(PO_4)_6(OH)_2$ is widely used for repair and regeneration of bone hard tissue considering its biocompatibility, non-toxicity and osteoconductive properties [1–5]. HAp can also encourage the growth and adherence of osteoblast and osteoclast cells as well as their proliferation [3–5]. In the present work [5], we report for the first time our results regarding the morphology, composition, structure and biocompatibility of dextran coated cerium doped hydroxyapatite ($Ca_{10-x}Ce_x(PO_4)_6(OH)_2$), thin films with x=0.05 (5CeHAp-D) and x=0.1 (10CeHAp-D) obtained by radio frequency magnetron sputtering (RF-MS) technique. The powders of 5CeHAp-D and 10CeHAp-D were obtained in agreement with our previous studies [6] where the (Ca+Ce)/P molar ratio was 1.67. Then, the dextran coated cerium doped hydroxyapatite composite layers have been deposited on silicon substrates by RF-MS. Firstly, sputtering targets of 5CeHAp-D and 10CeHAp-D in cylindrical shapes were obtained. Then, by turn, each sputtering target was placed inside the magnetron source for deposition of 5CeHAp-D and respectively 10CeHAp-D layers [5]. Atomic Force Microscopy was used to obtain information about the surface morphology of the 5CeHAp-D and 10CeHAp-D composite thin films. The results depicting the AFM 2D surface topographies as well as their 3D representation are presented in Figure 1a–d. The 2D AFM micrographs and their 3D representation of the surface of 5CeHAp-D and 10CeHAp-D composite thin films suggested the obtaining of a continuous and uniformly deposited layer in the case of both samples. Moreover, the AFM topographies of the 5CeHAp-D and 10CeHAp-D composite thin films' surfaces highlighted that the layers do not present any unevenness, fissures or any other type of discontinuities. The root means square roughness (R_{RMS}) parameters determined from the AFM topographies were $R_{Rms} = 37.98$ nm for 5CeHAp-D and $R_{Rms} = 15.07$ for 10CeHAp-D. The values obtained for the root mean square roughness implies that the surface topography of both samples is homogenous and does not present a significant roughness. On the other hand, the 2D AFM topographies as well as their 3D representation highlighted that the surface of the thin film is composed of nanostructured conglomerates, whose size decreased with the increase of the cerium ions concentration [5]. Figures 1e,f present the depth profiles of the 5CeHAp-D and 10CeHAp-D composite thin films obtained by GDOES. Thus, the distribution of elements contained in the 5CeHAp-D and 10CeHAp-D layers, namely: Ca, P, O, C, H and Ce was revealed starting from the layer surface (t= 0 s) to the substrate interface as function of the sputtering time. Due to the changes of sputtering rate during the GDOES depth profiling analysis, mainly at layer/substrate interfaces, the conversion of sputtering time into sputtered depth is not accurate and not recommended [7]. In Figure 1e,f, the layer/substrate interfaces are marked by the simultaneous decreasing of the intensities of the depth profile curves of the elements contained in the layer (Ca, P, C, O, H, Ce) and increasing of the intensities of the depth profile curves of the element characteristic to the substrate (Si).

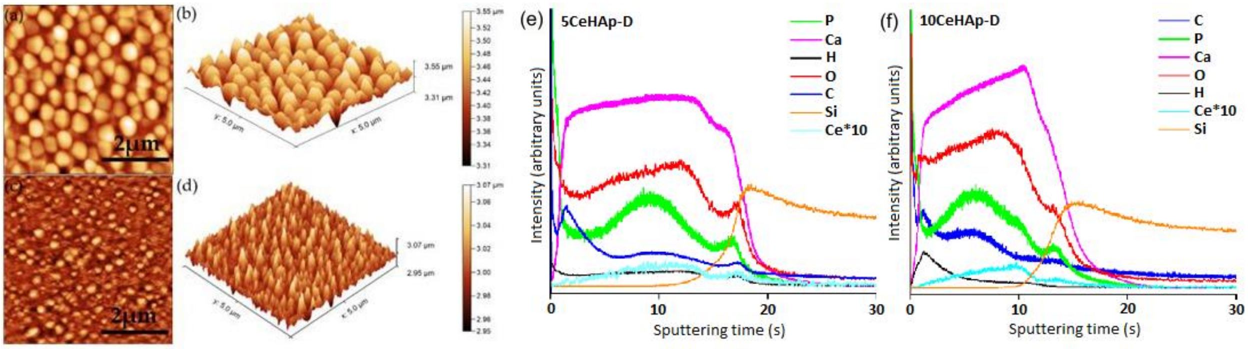

Fig. 1 Typical 2D AFM images of surface topography obtained on (a) 5CeHAp-D and (c) 10CeHAp-D composite thin films and their (b,d) 3D representation. Compositional depth profiles of the (e) 5CeHAp-D and (f) 10CeHAp-D composite coatings obtained by GDOES [5].

The temporal evolution of Ca, P and Ce depth profile curves are similar (see Figure 1e,f), even at layer/substrate interface where can be observed some humps/peaks. These suggest the diffusion/implantation of Ca, P and Ce elements into the Si substrates as well as their linkages. Additionally, the sputtering time for 10CeHAp –D sample is shorter than in the case of 5CeHap-D sample, indicating a thinner 10CeHAp –D layer. These data are in good agreement with SEM, AFM and metallographic microscopy analysis that shows a more compact structure of 10CeHAp –D layer than of 5CeHap-D layer. The depth profile curves of C, O and H, which represent the chemical elements characteristic to dextran are also observed in the graphs from Figure 1e,f. Their intensities are higher at shorter sputtering times (0-5s) indicating the presence of polymer mainly at sample surfaces [5]. The AFM topographies of the thin films' surfaces after being exposed with normal gingival fibroblasts were acquired at room temperature in normal atmospheric conditions on a surface of $20 \times 20\ \mu m^2$ (Figure 2 a–f). The 2D AFM topographies emphasized that on the surface of the investigated samples, could be seen typical patterns of the cellular morphology of normal gingival fibroblasts cells having typical flattened and elongated shapes [8]. Both the 2D AFM topographies and their 3D representations highlighted that after an exposure of 24 h, the normal gingival fibroblasts exhibited a good adherence to the 5CeHAp-D and 10CeHAp-D composite thin film's surfaces and also there is clear evidence of their spread all over the thin films' surfaces. On the other hand, the cells also adhered to the uncoated Si discs but the AFM topographies revealed that they did not spread on the entire Si disc's surface [5]. The AFM results demonstrated that normal gingival fibroblasts cells spread equally and formed a monolayer exhibiting characteristic elongated fibroblastic morphology on the surface of 5CeHAp-D and 10CeHAp-D composite layers. For a more in-depth characterization of the biological response induced by these modified Si surfaces in gingival fibroblasts, the morphology and actin cytoskeleton dynamics were also evidenced by fluorescence microscopy (Figure 2 g–l).

Thus, it was shown that the human cells maintained their specific elongated morphology and established numerous focal adhesions after 24 h of incubation, which confirmed that the behavior of gingival fibroblasts and their proliferative capacity was not disturbed in the presence of CeHAp-D composite coatings. These bioactive surfaces were harmless to the human gingival fibroblasts, proving a good biocompatibility. The AFM results are in good agreement with the viability assays conducted and suggest that the CeHAp-D composite thin films do not exhibit any cytotoxic effect against the normal gingival fibroblasts after 24 h of exposure, making them suitable for the future development of biomedical devices [5].

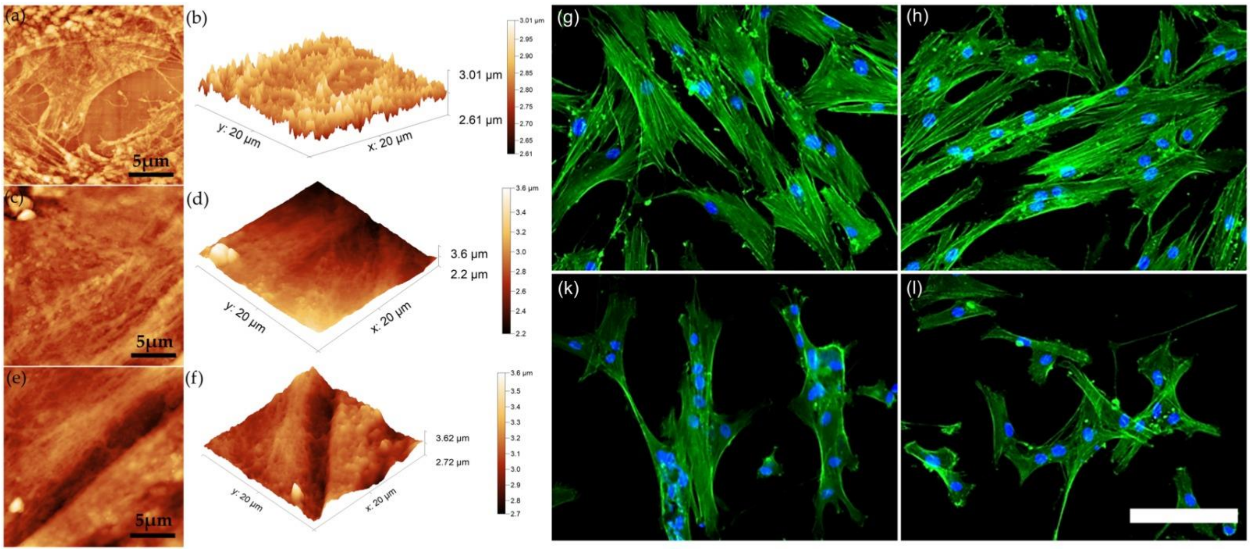

Fig. 2 2D AFM topography of gingival fibroblasts after 24 h of incubation with (a) uncoated Si substrates, (c) 5CeHAp-D and (e) 10CeHAp-D composite thin films and their (b,d,f) 3D representation. Actin cytoskeleton organization of gingival fibroblasts after 24 h of incubation with (h) uncoated Si substrates, (k) 5CeHAp-D and (l) 10CeHAp-D coatings. F-actin (green) was labeled with phalloidin-phalloidin-fluorescein isothiocyanate (FITC) and nuclei (blue) were counterstained with 4′,6-diamidino-2-phenylindole dihydrochloride (DAPI). Scale bar: 20 μm [5].

References

1. T Tite, AC Popa, LM Balescu, IM Bogdan, I Pasuk, JM Ferreira, GE Stan, “Cationic substitutions in hydroxyapatite: Current status of the derived biofunctional effects and their in vitro interrogation methods”, *Materials* 11, 2081 (2018).
2. N Eliaz, N Metoki, “Calcium phosphate bioceramics: A review of their history, structure, properties, coating technologies and biomedical applications”, *Materials* 10, 334 (2017).
3. LE Sima, GE Stan, CO Morosanu, A Melinescu, A Ianculescu, R Melinte, J Neamtu, SM Petrescu, “Differentiation of mesenchymal stem cells onto highly adherent radio frequency-sputtered carbonated hydroxylapatite thin films”, *Journal of Biomedical Materials Research Part A* 95, 1203–1214 (2010).
4. P Wang, L Zhao, J Liu, MD Weir, X Zhou, HH Xu, “Bone tissue engineering via nanostructured calcium phosphate biomaterials and stem cells”, *Bone Research* 2, 14017 (2014).
5. CS Ciobanu, IC Nica, A Dinischiotu, SL Iconaru, P Chapon, B Bita, R Trusca, A Groza, D Predoi, “Novel dextran coated cerium doped hydroxyapatite thin films”, *Polymers* 14, 1826 (2022).
6. D Predoi, SL Iconaru, MV Predoi, “Dextran-coated zinc-doped hydroxyapatite for biomedical applications”, *Polymers* 11, 886 (2019).
7. A Groza, A Surmeian, C Diplasu, C Luculescu, P Chapon, A Tempez, M Ganciu, “Physico-chemical processes occurring during polymerization of liquid polydimethylsiloxane films on metal substrates under atmospheric pressure air corona discharges”, *Surface and Coatings Technology* 212, 145–151 (2012).
8. D Predoi, A Groza, SL Iconaru, G Predoi, F Barbuceanu, R Guegan, MS Motelica-Heino, C Cimpeanu, “Properties of basil and lavender essential oils adsorbed on the surface of hydroxyapatite”, *Materials* 11, 652 (2018).

Negative-capacitance and Switching Dynamics Control *via* Non-ferroelectric Elements

Andra Georgia Boni[a], Roxana Patru[a], Lucian Dragos Filip[a], Cristina Florentina Chirila[a], Iuliana Pasuk[a], Ioana Pintilie[a], Lucian Pintilie[a].

[a]Laboratory of Complex Heterostructures and Multifunctional Materials, National Institute of Materials Physics, 405A Atomistilor, 077125 Magurele, Romania

The unique property of ferroelectricity to change polarization state using an external electric field has led to the development of many applications such as FERAM and FEFET electronic devices. The dynamic of polarization switching plays an important role in determining important parameters for binary digital devices. Intermediate polarization states can also be exploited for memories with multiple states and analog or neuromorphic computing. The negative capacitance property present in the FE layer integrated into the gate stack of field-effect transistors has been a hot topic in the last decade, as it can lead to a substantial decrease in subthreshold slope and reduction of power consumption. The main focus for new applications is the ability to control the switching dynamic by changing the electrostatic conditions for the ferroelectric element using several methods. However, there is a limited number of studies focusing on understanding the complex relationship between polarization switching dynamics in ferroelectrics and external electrostatic conditions.

This study discusses the impact of the electric properties of non-ferroelectric components of a device on its ferroelectric properties, specifically for thin-film ferroelectric capacitors [1]. The hysteresis loops for polarization-voltage (P-V) and current-voltage (I-V) measurements were measured for different series resistors and capacitors, and it was found that increasing the resistance leads to an increase in the coercive voltage and wider current peaks associated with polarization switching, while decreasing the capacitance leads to a stronger imprint towards positive voltages. The apparent coercive voltage is determined by the resistivity of the non-ferroelectric component, and the presence of a series capacitor does not necessarily suppress polarization, but rather induces an internal electric field in the ferroelectric component, inversely proportional to the value of the series capacitance. Further two bilayer structures were prepared to investigate the effects of adding a high-resistivity layer (STON) and a high-capacitance layer (BST) to a ferroelectric (PZT) capacitor (Figure 1). The hysteresis characteristics of the PZT/STON structure were found to be similar to those of a series-connected PZT capacitor with a range of resistances between 10 kΩ and 50 kΩ, while the PZT/BST structure exhibited similar behavior to a PZT capacitor connected in series with a high-capacitance capacitor. However, the remnant polarization of the PZT/BST structure was lower than that of a simple PZT capacitor, possibly due to changes in electrostatic conditions during the deposition process and a discharge of the paraelectric BST layer during cool-down. The bilayer structure may exhibit high leakage currents due to a decrease in the ferroelectric resistivity or tunneling through the thin paraelectric layer.

The second part of the our examined the voltage drop on circuit components during polarization switching for a series connection between the FE capacitor and a non-FE component. The results of high amplitude positive triangular voltage pulses for R_S=50 kΩ showed that in the in the first part, the voltage on the FE capacitor follows the applied voltage, then remaining constant during switching, and then abruptly increasing towards the applied voltage. Hysteresis loops for a C_S=4 nF for different voltage polarities of the measurement pulse were also studied and the results showed that the orientation of the apparent imprint is changeable in the case of a series capacitor. The voltage drop on the FE is measured during two switching situations and found to be constant, with the necessary voltage for switching is insensitive to external contribution. The governing mechanism involves an impedance adaptation of the circuits to stabilize the new polarization state by redistributing the available voltage on other circuit components. Figure 2 illustrates the hysteresis relationship between V_{FE} and V_{app} for the cases of C_S and R_S, as well as the charge conservation law that dictates this non-linear behavior. For time steps 1, 2, and 3, the dependence of V_{FE} on V_{app} is similar in both cases, but differences arise after switching is completed and V_{app} returns to 0V. In the case of C_S, V_{FE} shows a clockwise dependence on V_{app}, while for R_S there is an anticlockwise variation. The resulting polarization and free energy for a series connection with a capacitor and various resistors are also shown in Figure 2. In the case of C_S, only one direction of polarization is stable, and switching in the other direction places the system in a state close to the NC regime, which is unstable and evolves towards the initial stable state while passing through the NC regime again.

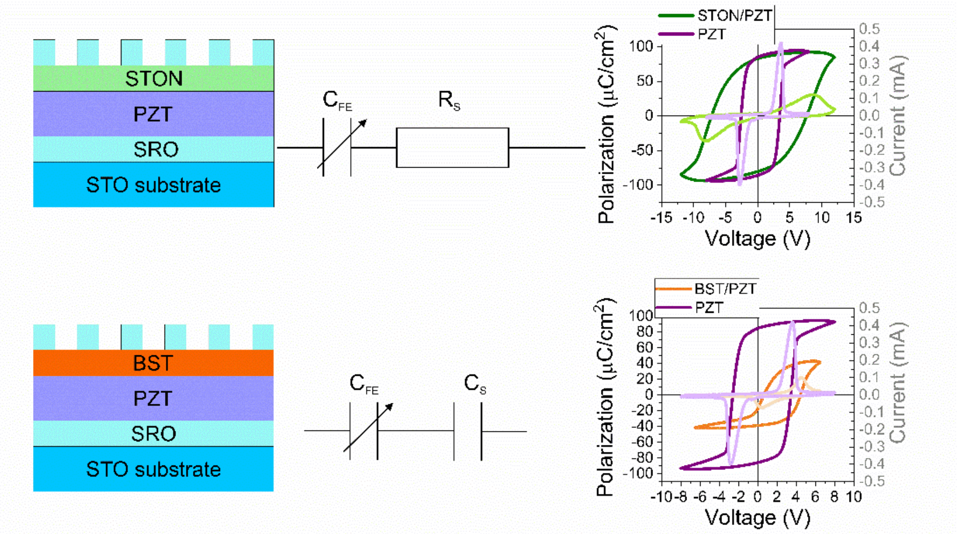

Fig. 1 Illustration of the architecture of the multilayered structures of PZT/STO and PZT/BST, with the equivalent electronic circuit, and the resulting hysteresis measurements compared to a simple PZT layer.

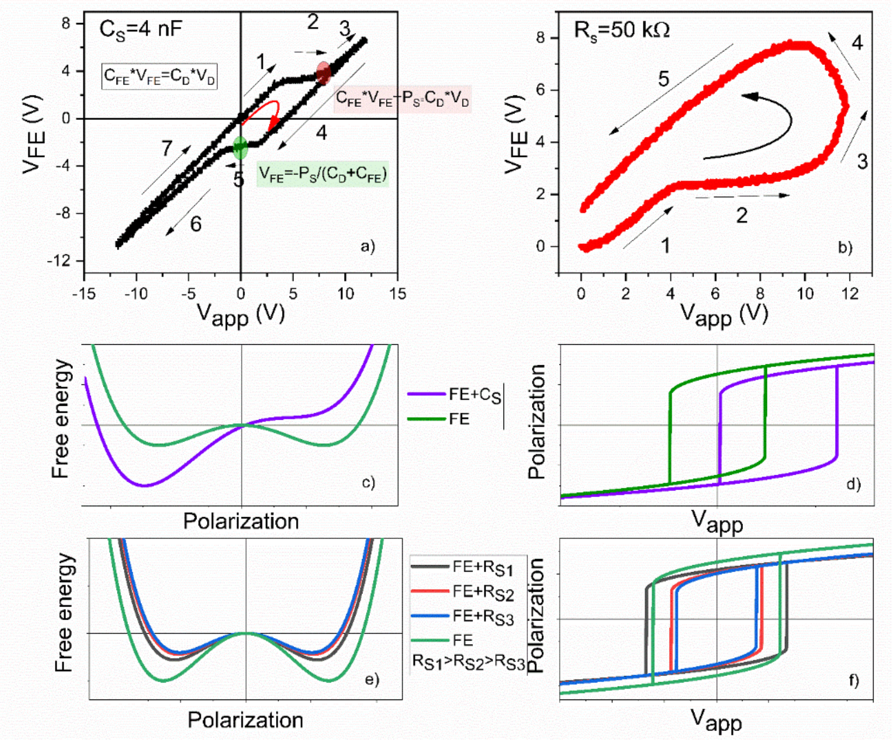

Fig. 2 The difference between electrostatic changes given by the non-FE element explained by hysteresis dependence of V_{FE} as function of V_{app} and by the thermodynamic picture. The dependence of drop of voltage on FE as a function of applied voltage for a) Cs=4nF and for b)Rs=50kΩ. c) The free energy representation of a FE series connected with a Cs and comparison with a simple FE $C_{FE}\ /\ C_S\ = 0.01$. d) Comparison between theoretical hysteresis loop of a simple FE capacitor and a FE series connected with a Cs.e) The free energy representation of a FE series connected with different Rs and comparison with a simple $FE\ C_{FE}\ /\ C_D\ = 0.01$, 0.1 and 0,5. f) Comparison between theoretical hysteresis loop of a simple FE capacitor and a FE series connected with an Rs.

This study highlights the impact of different non-ferroelectric (non-FE) elements, such as resistors and capacitors, in series with ferroelectric (FE) layers on the hysteresis behavior of FE devices. Although the hysteresis characteristics may appear similar, the switching behavior and voltage distribution between components are drastically different for a resistor-series (R_S) or capacitor-series (C_S) connection. Delaying polarization compensation during switching leads to unstable states associated with negative capacitance (NC). The study suggests that the C_S configuration is useful for reducing hysteresis in FE NCFET for computing applications, while the R_S configuration can obtain intermediate polarization states for multi-bit memory or neuromorphic computing. Obtaining a good capacitance ratio or purely resistive or capacitive behavior in multilayer thin films is challenging but necessary for further developing FE-based devices.

References

1. AG Boni, R Patru, LD Filip, C Chirila, I Pasuk, I Pintilie, L Pintilie, “Negative-capacitance and switching dynamics control via non-ferroelectric elements”, *ACS Applied Energy Materials* 5, 3, 3307–3318 (2022).

Controlling Polarization Direction in Epitaxial Pb($Zr_{0.2}Ti_{0.8}$)O_3 Films through Nb (n-type) and Fe (p-type) Doping

Cristina Florentina Chirila[a], **Viorica Stancu**[a], **Georgia Andra Boni**[a], **Iuliana Pasuk**[a], **Lucian Trupina**[a], **Lucian Dragos Filip**[a], **Cristian Radu**[a], **Ioana Pintilie**[a], **Lucian Pintilie**[a]
[a]National Institute of Materials Physics, 405A Atomistilor, 077125 Magurele, Romania

Pb(Zr,Ti)O_3 (PZT) material is used in bulk or thin film form in a wide variety of applications due to its numerous functional properties, such as spontaneous polarization that can be controlled by an electric field, temperature, mechanical stress, and light, as well as a tunable dielectric constant, birefringence, and more. Although doping in ferroelectrics has been the subject of numerous articles, the conduction type in ferroelectric films is still up for debate. One way to tailor the PZT properties for certain purposes is through doping. The percentage of doping is generally greater than 1% and often significantly higher in reported studies. Some studies on the impact of low doping concentration on the properties of PZT were performed on ceramic-like samples, disregarding the fact that the effect of doping should be studied on samples of very good crystalline structure, preferably close to a single crystal. It is difficult to grow PZT single crystals because PbO is volatile during the growth process. However, for this study, high-quality epitaxial thin films were grown using pulsed laser deposition (PLD) on the single-crystal substrate $SrTiO_3$ (STO), with $SrRuO_3$ (SRO) serving as a buffer layer and bottom electrode.

The aims of this study were (1) to examine the impact of 1% Fe and Nb doping on the electrical characteristics of epitaxial PZT films and (2) to investigate whether changing from n-type (Nb) to p-type (Fe) doping may influence the polarization orientation in the as-grown layers.

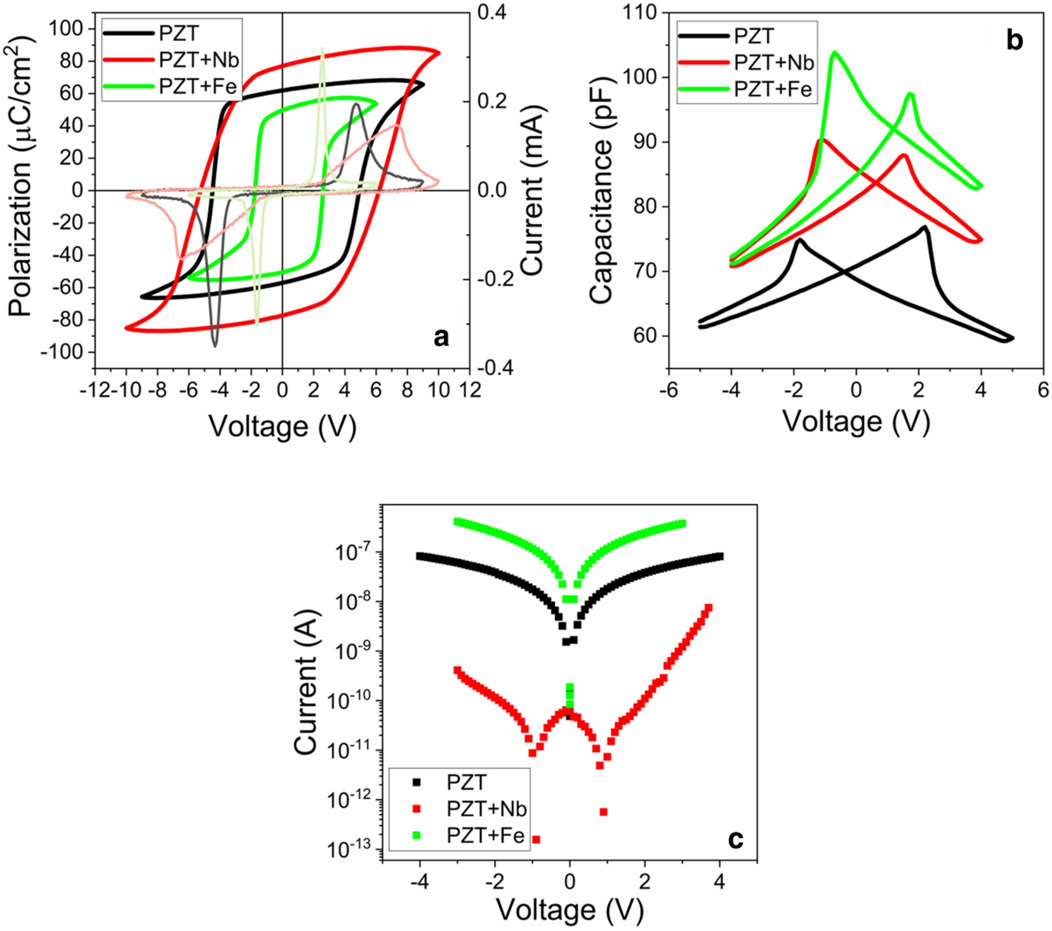

Fig. 1 (a) The hysteresis P–V and I-V characteristics recorded at RT for 1 kHz frequency of high amplitude pulse; (b) The capacitance–voltage characteristics recorded at RT with 0.2 V a.c. signal and at 100 kHz frequency. (c) The current–voltage characteristics recorded for totally saturated polarization at RT.

The films were deposited from Fe and Nb doped targets, respectively, using PLD, which is a method that transfers the target stoichiometry into the deposited films. The SRO and PZT layers grew epitaxially on the STO (001) substrate, as confirmed by XRD and TEM analyses, with the relationships (001)PZT||(101)SRO||(001)STO and (010)PZT||(010)SRO||(010)STO.

The electrical properties of Fe and Nb doped PZT were found to be significantly different from each other: the coercive field was smaller in Fe-doped PZT, the height of the potential barrier at the interface with $SrRuO_3$ (SRO) electrodes was almost three times larger in Nb-doped PZT, the concentration of charge carriers was slightly higher in Fe-doped PZT, and the leakage current was about two orders of magnitude larger in Fe-doped PZT. These differences are explained by the modifications made to the electrical characteristics of PZT by the two dopants. Additionally, it was found that the polarization direction changes depending on the type of doping, with PZT-Nb having an upward dominant polarization and PZT-Fe having a downward dominant polarization. Figure 1 displays the findings of common electrical experiments carried out at room-temperature. Both the percentage of *a*-domains (and domain walls) and the quantity of strained *c*-domains, as determined by XRD, do not correlate with the considerable differences in the electric properties of the three samples. Therefore, it can be said that these differences are caused by the effects of doping on the characteristics of the "relaxed" PZT volume, which makes up the majority (approximately 95%) of the sample. Whether PZT-Fe is p-type and PZT-Nb is n-type cannot be determined solely by electrical measurements. PFM investigations were carried out to gain some insight.

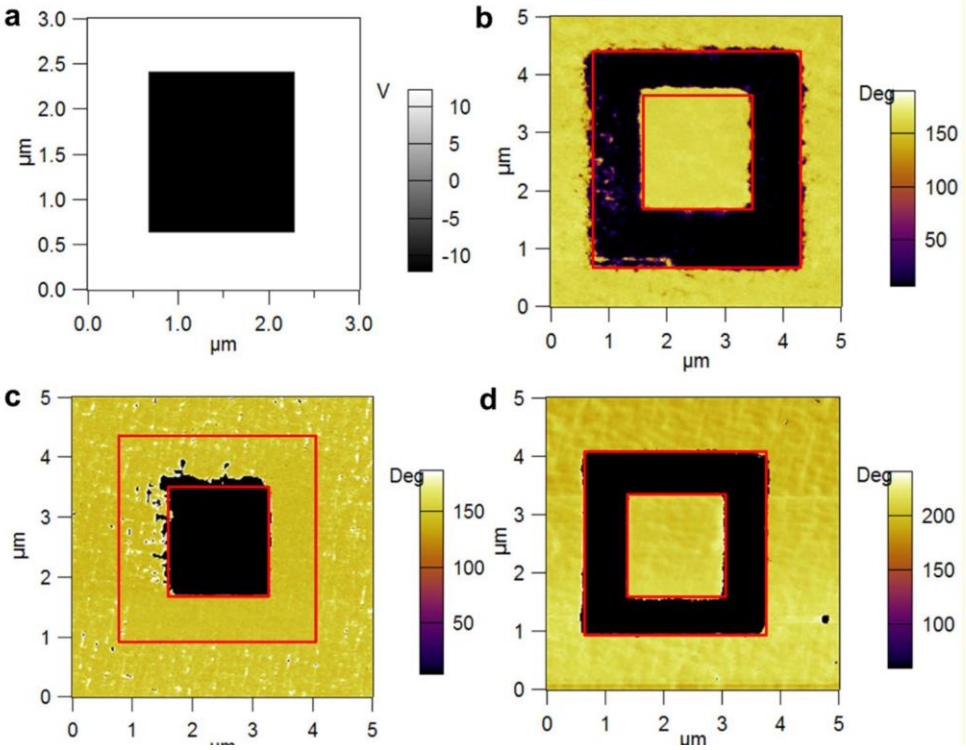

Fig. 2 (a) Poling map applied for polarization switching; Piezoresponse phase images after domain writing according to the poling map on: (b) PZT-Nb; (c) PZT-Fe; (d) un-doped PZT thin films.

The PFM results showed that the polarization orientation in the epitaxial PZT films can be controlled by the type of doping used. The PZT-Nb film, which is assumed to be n-type, exhibited an upward polarization in its as-grown state, whereas the PZT-Fe film, assumed to be p-type, showed a downward polarization orientation. The undoped sample behaved similarly to PZT-Nb, suggesting intrinsic n-type doping due to the presence of oxygen vacancies. These results are consistent with previous studies that have shown that the polarization orientation in PZT can be manipulated by changes in the chemistry of the PZT layer or the conduction type of the bottom electrode.

Figure 2 shows the PFM phase pictures for the three samples, which were obtained using box-in-box poling. The PZT-Nb film exhibited an upward polarization, as seen from the same phase contrast in the inner and outer boxes. In contrast, the PZT-Fe film showed a phase contrast similar to that of the outer box, indicating a downward polarization orientation. These observations suggest that the type of doping affects the polarization orientation in the as-grown state of the PZT film. Figure 3 provides a possible explanation for the observed PFM results. In PZT-Nb, the n-type doping creates electron carriers, which compensate for the depolarization field, resulting in an upward polarization orientation. In contrast, in PZT-Fe, the p-type doping creates hole carriers, which do not compensate for the depolarization field, leading to a downward polarization orientation. The undoped sample exhibited n-type behavior due to the presence of oxygen vacancies, which created electron carriers that compensate for the depolarization field, resulting in an upward polarization orientation.

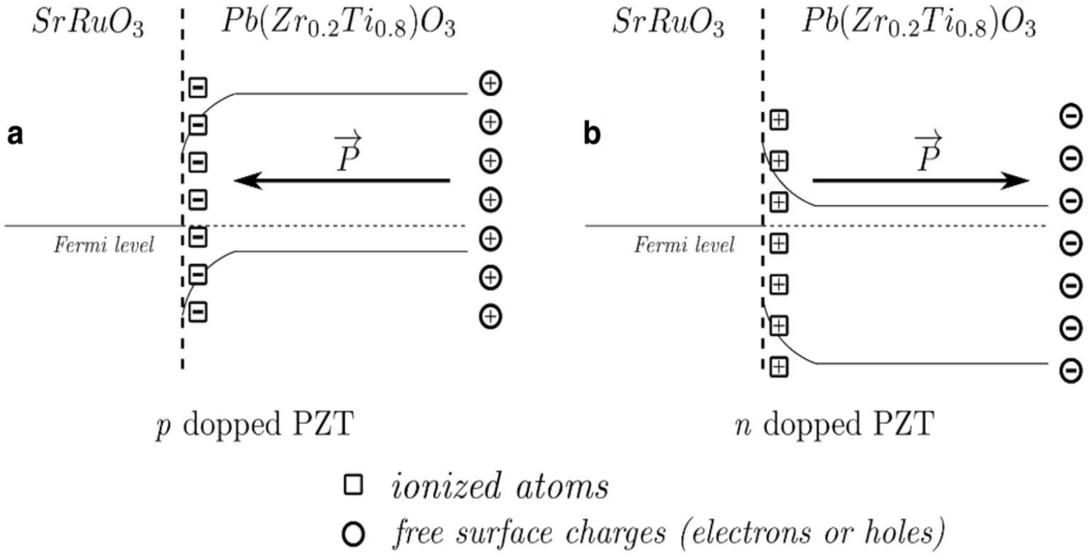

Fig. 3 Band alignment sketch for the two doping cases, with the preferred polarization direction in the PZT.

However, based on the information provided, it seems that the squares and circles may represent the distribution of charges at the interface and surface of the PZT films, respectively. The ionized atoms in the interface region (squares) are likely responsible for compensating the polarization charges, while the free surface charges (circles) may play a role in determining the overall polarization orientation of the films. The study shows that even low doping concentrations of Fe and Nb can significantly affect the electrical properties of the PZT films, with Fe acting as an acceptor and Nb acting as a donor. Additionally, the study demonstrates that the type of doping (n-type or p-type) can influence the polarization orientation of the PZT layer, which could have important implications for developing ferroelectric p-n homojunctions. Overall, this study provides new insights into the effects of doping on the properties of epitaxial PZT films.

References

1. CF Chirila, V Stancu, GA Boni, I Pasuk, L Trupina, LD Filip, C Radu, I Pintilie, L Pintilie, "Controlling polarization direction in epitaxial $Pb(Zr_{0.2}Ti_{0.8})O_3$ films through Nb (n-type) and Fe (p-type) doping", *Scientific Reports* 12, 9131 (2022).

Quaternary Chalcogenide Films for Photovoltaics

Outman El Khouja[a,b], Khalid Nouneh[b], Constantin Catalin Negrila[c], Elena Matei[d], Victor Kuncser[e], Aurelian Catalin Galca[a]

[a]Laboratory of Complex Heterostructures and Multifunctional Materials (HeCoMat), National Institute of Materials Physics, 405A Atomistilor, 077125 Magurele, Romania

[b] Laboratory of Materials Physics and Subatomic (LPMS), Faculty of Sciences, Ibn Tofail University, Campus Universitaire, 14000 Kenitra, Morocco

[c]Laboratory of Surface and Interface Science, National Institute of Materials Physics, 405A Atomistilor, 077125 Magurele, Romania

[d]Laboratory of Functional Nanostructures, National Institute of Materials Physics, 405A Atomistilor, 077125 Magurele, Romania

[e]Laboratory of Magnetism and Superconductivity, National Institute of Materials Physics, 405A Atomistilor, 077125 Magurele, Romania

$Cu_2ZnSnS(Se)_4$ [CZTS(Se)] is amongst the materials considered for emerging photovoltaic cells. Several reasons were mentioned for the low experimental photo-conversion efficiency of CZTS(Se) based solar cells: the co-existence of detrimental secondary phases such as CuS, SnS and/or ZnS, the intrinsic vacancy defects (*e.g.*, V_{Zn}, V_{Sn}, and V_{Cu}), the two oxidation states (Sn^{2+} and Sn^{4+}) of tin, antisite defects (Cu_{Zn}, Cu_{Sn}, and Sn_{Zn}), defect complexes or clusters ([Zn_{Sn} + $2Zn_{Cu}$], [V_{Zn} + Sn_{Zn}], [V_{Cu} + Zn_{Cu}]), the co-existing polymorphism (kesterite, stannite and disordered phase).

The synthesis of these materials in thin form is a two-step process, the film (or multilayer) obtained by various techniques being subsequently annealed in controlled atmosphere to finally obtain the kesterite/stannite phase. Thus, the post-annealing plays a crucial role. However, the composition and other properties of the pre-annealed structures are also important.

Since Zn related defects are considered detrimental to solar cells performances, the substitution of Zn^{2+} with other cations with the same valence can be explored; the quaternary class of materials, Cu_2MSnS_4 being lately under investigation. Cu_2CoSnS_4 (CCTS) and Cu_2FeSnS_4 (CFTS) are regarded as CZTS alternatives, keeping in the same time the requirements (eco-friendly, earth abundant elements, and good optical and electrical properties) of promising p-type materials for solar cells.

Co-electrodeposition, a low-cost and reliable method, can be used to obtain quaternary chalcogenides (here selected results on CFTS [1][2] being presented). Along with the metal salts (usually sulfates), $Na_2S_2O_3$ is also used during electrodeposition to provide a source of sulphur, but in the same time to act as complexing agent.

Spray pyrolysis is a promising deposition technique to cover large surfaces at lower cost. As example, to obtain CCTS [3], water solution of $CuCl_2$, $CoCl_2$, $SnCl_2$, and thiourea are sprayed over heated substrate, where, as a result of chemical reactions and thermal decomposition, the quaternary chalcogenide is obtained.

The X-ray diffraction (Figure 1a) indicated for both materials, CFTS and CCTS, a stannite structure (tetragonal space group I-42m), the experimental data matching well with the corresponding ICDD-PDF cards no. 00-044-1476 and no. 04-014-3403, respectively. The most intense observed diffraction lines at $2\theta = 28.5°$, $32.8°$, $47.5°$, and $56.5°$ correspond to *112*, *200/004*, *220/204*, and *312/116* reflections of stannite. The *101* diffraction line of the tetragonal lattice at $2\theta \sim 18.4°$ is a particular feature of tetragonal structure, this peak being absent in the case of perfect cubic symmetry. Moreover, considering that the most intense peak of the secondary hexagonal SnS_2 phase is at $2\theta = 14.7°$ (ICDD-PDF no. 00-023-0677), it is recommended to do measurements also below $2\theta = 20°$.

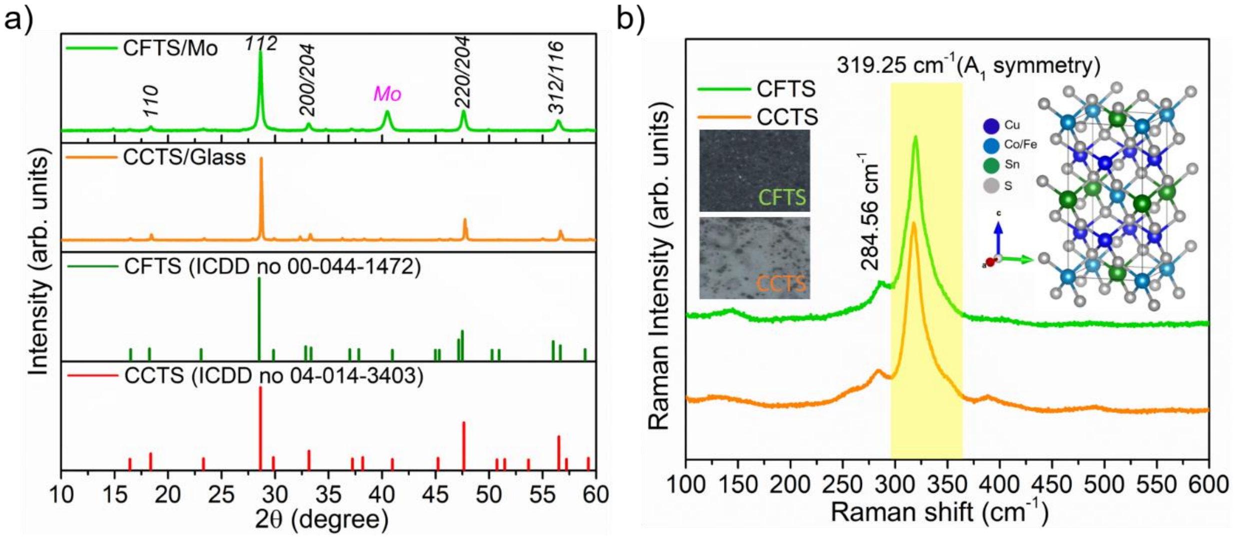

Fig. 1 (a) XRD patterns, and (b) Raman spectra of CCTS and CFTS sulfurized films.

In the case of CCTS films, the minor peaks at 2θ = 27.8°, 32.3°, 36.3°, 46.3°, and 54.9° corresponded to the CoS_2 (PDF card no 00-041-1471), a phase which was unveiled also by Raman spectroscopy (Figure 1b). Raman spectroscopy confirmed the presence of stannite as main phase, by the presence of significant peaks around 318 – 334 cm^{-1}, 284 - 290 cm^{-1}, and 390 -396 cm^{-1}. The most intense CCTS peak found between 318 and 334 cm^{-1} is associated to A_1 symmetry of the CCTS stannite structure, this vibration mode arising from the mobility of S anions around the mono-valent Cu and tetravalent Sn cations. The Raman shift of these peaks depends not only on the stoichiometry but also on any internal deformation induced by strain. Secondary phases which can be formed might be visible in Raman, for example SnS_2 with a characteristic Raman peak at 314 cm^{-1}, and CoS_2 with distinct signature at 476 – 490 cm^{-1}.

Tin loss *via* SnS evaporation is one of the technological issues which can occur during the annealing process. When the thermal treatment is done in the sealed ampoule/graphite box, the SnS partial pressure suppresses the evaporation of SnS. Please note that this is not the case of the presented works, where SnS and Sn vapors are reaching the film surface, where some reacts with the sulfur atmosphere and finally SnS_2 solid phase is formed.

By X-ray photoelectron spectroscopy (XPS) (Figure 2a) in the case of CFTS, the Fe $2p_{1/2}$ and Fe $2p_{3/2}$ are overlapped by the most intense Sn 3p3/2 peak. The spectra acquired before and after removing the contaminated surface using light-weight argon direct current sputtering (3 keV / 10 min) are merely the same, suggesting a very Sn rich surface. When the Fe 2p core levels are hidden, it is recommended to inspect the less intense Fe 3p X-ray photoelectron spectrum. In the presented case sodium (Na 2s) is also observed. After partially removing the top surface, two F e3p components are revealed, the one at 54.60 eV corresponding to Fe from CFTS, while the peak at 56.84 eV being assigned to oxidized Fe (or sulfoxide) or the CFTS, iron being in a different coordination or valence state.

High resolution ^{57}Fe Conversion Electron Mössbauer spectrum (Figure 2b) evidenced 2 doublet patterns, a less split one with a relative spectral area of 78%, Fe^{3+} in tetrahedral sites of paramagnetic stannite structure, and a larger split one of only 22% relative contribution, Fe^{2+} ions in the analyzed sample, the Fe^{2+} ions being in more distributed atomic configurations.

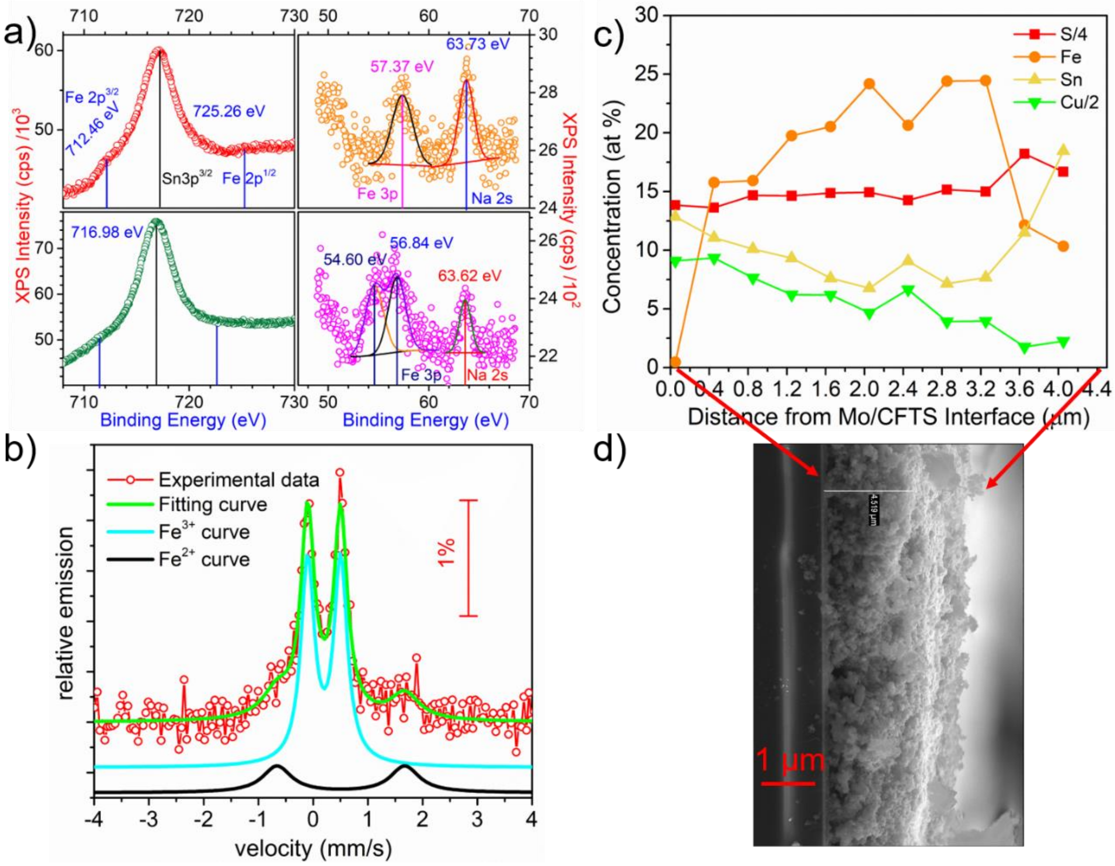

Fig. 2 (a) X-ray photoelectron spectroscopy results of CFTS film (Fe 2p, Na 2s, and Fe 2p, Na 2s after removing the contaminated layer from the film surface; (b) ^{57}Fe Conversion Electron Mössbauer spectrum of a CFTS with the corresponding fitting components; (c) in-depth relative atomic concentrations of the CTFS elements; and (d) cross-section scanning electron micrograph of the CFTS film.

In-depth relative atomic fill fractions (Figure 2c) of CFTS components (Cu, Fe, Sn, and S) for a sample sulfurized at 550 °C, determined by energy-dispersive X-ray spectroscopy, showed that the concentration of tin toward and at the surface is higher than in the rest of the film, while a larger amount was probed also at the Mo/CFTS interface. Thus, the melting/vaporization/diffusion/solidification processes of the Sn and SnS are responsible for the final atomic composition and the respective in-depth gradients. Also, the very low concentration of Fe toward the surface explains the weak signature measured by XPS. In the same time, copper concentration decreased monotonously and slightly toward the surface. The cross-section scanning electron micrograph (Figure 2d) of the same sample, showed relatively large grains along with a high porosity of the film.

References

1. O El Khouja, AC Galca, K Nouneh, MY Zaki, M Ebn Touhami, M Taibi, E Matei, CC Negrila, M Enculescu, L Pintilie, "Structural, morphological and optical properties of Cu–Fe–Sn–S thin films prepared by electrodeposition at fixed applied potential", *Thin Solid Films* 721, 138547 (2021).
2. O El Khouja, I Assahsahi, K Nouneh, M Ebn Touhami, M Secu, A Talbi, Y Khaaissa, E Matei, V Stancu, A Galatanu, AC Galca, "Structural and transport properties of Cu_2CoSnS_4 films prepared by spray pyrolysis", *Ceramics International* 48 (21), 32418-32426 (2022).
3. O El Khouja, CC Negrila, K Nouneh, M Secu, M Ebn Touhami, E Matei, V Stancu, M Enculescu, V Kuncser, AC Galca, "Bulk and surface characteristics of co-electrodeposited Cu_2FeSnS_4 thin films sulfurized at different annealing temperatures", *Journal of Alloys and Compounds* 906, 164379 (2022).

Polymorphic Absorber Layers for Thin-Film Solar Cell Application Prepared by Magnetron Sputtering

Mohamed Yassine Zaki[a], Florinel Sava[a], Iosif Daniel Simandan[a], Angel Theodor Buruiana[a,b], Claudia Mihai[a], Alin Velea[a,*], Aurelian Catalin Galca[a]
[a]National Institute of Materials Physics, 405A Atomistilor, 077125 Magurele, Romania
[b]Faculty of Physics, University of Bucharest, 405 Atomistilor, 077125 Magurele, Romania

Ternary, quaternary and quinary chalcogenide materials have emerged recently as promising absorber layers for thin film solar cells. The main advantages of these semiconductors are their ecofriendly composition, excellent optoelectronic properties and promising power conversion efficiency. Cu_2SnS_3 (CTS), Cu_2ZnSnS_4 (CZTS) and $Cu_2ZnSn(S,Se)_4$ (CZTSSe) are the most famous emerging thin-film absorber layers [1]. CTS has gathered considerable attention because to its potential usage as tiny band semiconductors for infrared photodetectors as well as photocatalytic, optoelectronic, and supercapacitor applications. It is also regarded as a starting precursor for the synthesis of CZTS compound [2]. Various physical and chemical techniques have been employed to synthesize CTS semiconductors [3]. Here we report a magnetron co-sputtering approach to produce CTS films using two different stacking orders (SLG\Cu\$SnS_2$ and SLG\$SnS_2$\Cu) and annealed at different temperatures using two atmospheres (S or Sn+S) as shown in Figure 1a,b.

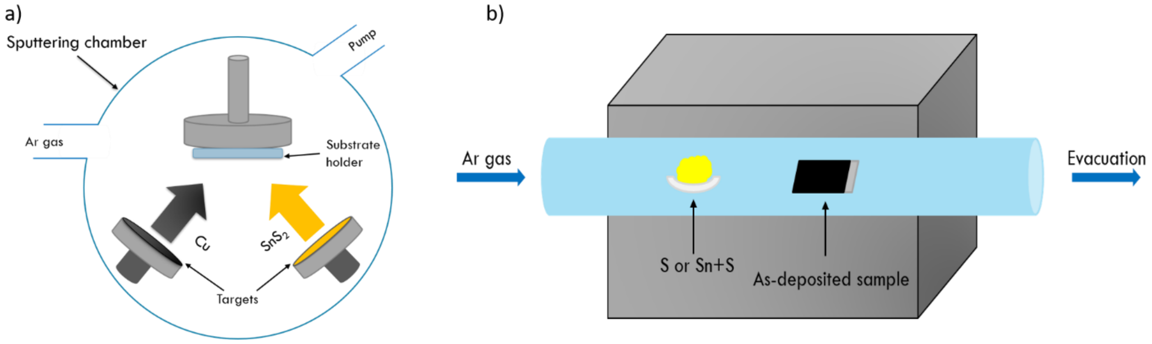

Fig. 1 Illustration of (a) the schematic diagram of the deposition chamber and (b) the annealing process.

Raman spectroscopy for the sulfurized samples showed that all samples in the SLG\Cu\$SnS_2$ annealed under sulfur atmosphere stack are polymorphic. The SLG\$SnS_2$\Cu stack annealed in S, on the other hand, has a tetragonal dominating structure in the film annealed at 350 °C, whereas the sulfurized films at higher temperatures are polymorphic with a greater proportion of monoclinic CTS peaks. In both stacks sulfurized at 300 °C, according to the GIXRD measurements, the hexagonal CuS secondary phase formed; however, starting at 350 °C, this phase is present only in trace amounts independent of the stacking sequence. Due to SnS evaporation from the top layer, the sulfurized SnS_2-capped samples show poor surface morphology with many voids (SEM not shown). The progressive drop in Sn and S concentration seen in the EDS study supported this. The copper-capped films, on the other hand, have nearly stoichiometric compositions, and uniform and homogenous surfaces. The band gap of the SnS_2-capped samples annealed in S, ranged between 1.14 and 1.48 eV, while for the Cu-capped ones annealed in the same atmosphere, it ranged between 0.98 and 1.45 eV, according to optical measurements.

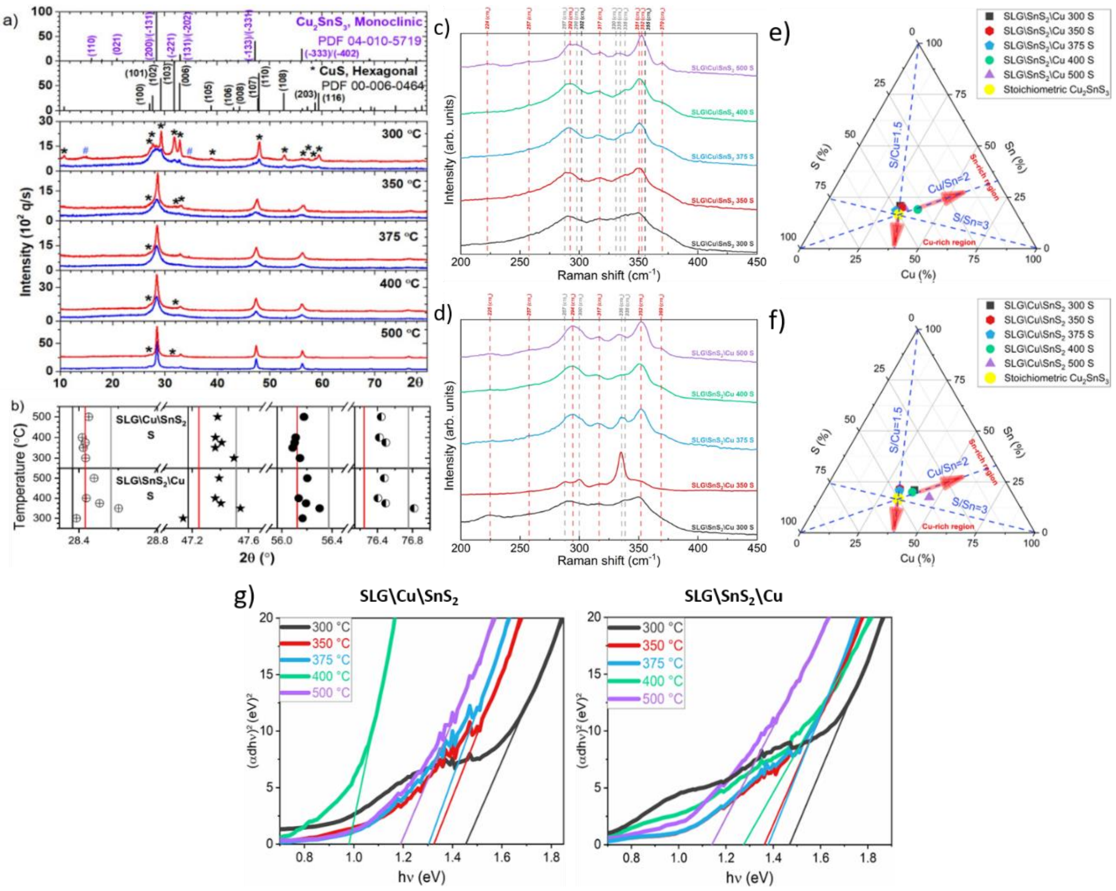

Fig. 2 Structural, compositional and optical properties of films annealed in S at different temperatures: (a) GIXRD diagrams of SLG\Cu\SnS$_2$ and SLG\SnS$_2$\Cu stacks; (b) Angular positions of the most intense peaks in relation to the ICDD cards of tetragonal (gray), cubic (black) and monoclinic (red) structures; (c,d) Raman spectra of the SLG\Cu\SnS2 and SLG\SnS2\Cu; (e,f) EDS results of both stacks; and (g) Tauc plots of the two stacks.

The SLG\Cu\SnS$_2$ samples with SnS$_2$ as the capping layer contain very little of the hexagonal CuS secondary phase, as inferred from GIXRD and Raman spectroscopy, for the annealing under Sn + S atmosphere at different temperatures. Due to the Sn + S annealing conditions, a non-uniform surface is visible in SEM images (not shown), and a slight increase in the Sn and S content is noted. The optical band gap energy ranges from 1.18 to 1.37 eV. On the other hand, the SLG\SnS$_2$\Cu stack, has the overall best characteristics after being annealed at various temperatures in a Sn + S atmosphere. The film was annealed at 350 °C and the GIXRD analysis revealed a CTS phase with peaks orientated toward the tetragonal structure. Raman spectroscopy detected high signal at 335 cm^{-1} corroborated this. The samples annealed at 500 and 550 °C are polymorphic and with the most prominent peaks corresponding to the monoclinic CTS structure. All films have dense and compact surfaces (SEM not shown), and their elemental compositions are the closest to stoichiometry with band gaps between 1.06 and 1.30 eV depending on the structural properties of each film.

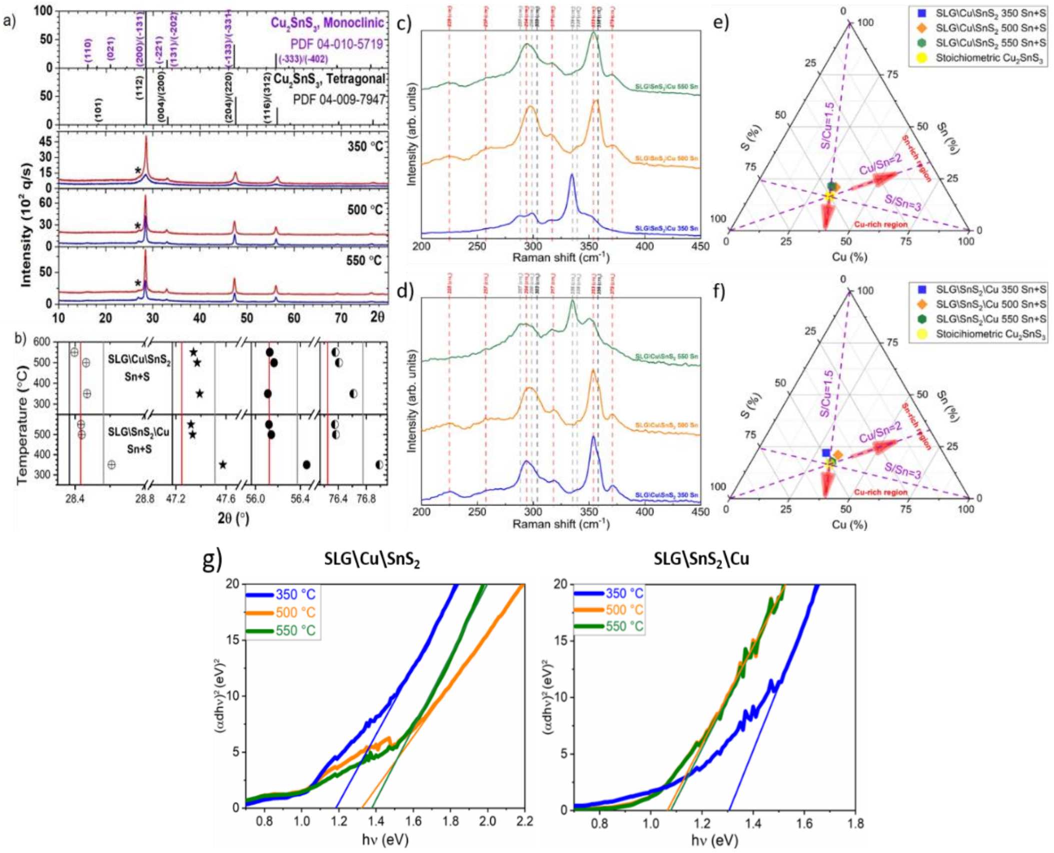

Fig. 3 Structural, compositional and optical properties of films annealed in Sn + S at different temperatures: (a) GIXRD diagrams of SLG\Cu\SnS$_2$ and SLG\SnS$_2$\Cu stacks; (b) Angular positions of the most intense peaks in relation to the ICDD cards of tetragonal (gray), cubic (black) and monoclinic (red) structures; (c,d) Raman spectra of the SLG\Cu\SnS2 and SLG\SnS2\Cu; (e,f) EDS results of both stacks; and (g) Tauc plots of the two stacks.

Cu_2SnS_3 films can be produced using two alternative stacking configurations using Cu and SnS_2 sputtering targets, according to this new synthesis technique. A Cu-capped layer can be used to improve the surface morphology in order to prevent SnS evaporation, the structural parameters can be adjusted by changing the temperature in order to achieve the desired crystalline phase, and Sn + S annealing is showed to be advantageous in order to prevent SnS losses and achieve the desired stoichiometry. These results are beneficial for the solid reaction of an additional ZnS layer on top of CTS films to create CZTS films [4].

References

1. MY Zaki, F Sava, ID Simandan, AT Buruiana, C Mihai, A Velea. AC Galca, “Cu_2SnSe_3 phase formation from different metallic and binary chalcogenides stacks using magnetron sputtering,” *Materials Science in Semiconductor Processing* 153, 107195, (2023).
2. MY Zaki, F Sava, ID Simandan, AT Buruiana, C Mihai, A Velea. AC Galca, “Effect of the stacking order, annealing temperature and atmosphere on crystal phase and optical properties of Cu_2SnS_3,” *Scientific Reports* 12, 7958, (2022).
3. MY Zaki, F Sava, ID Simandan, AT Buruiana, N Becherescu, AC Galca, C Mihai, A Velea, “Synthesis and characterization of Cu_2ZnSnS_4 thin films obtained by combined magnetron sputtering and pulsed laser deposition,” *Nanomaterials* 11, 2403, (2021).
4. MY Zaki, F Sava, ID Simandan, AT Buruiana, I Stavarache, AE Bocirnea, C Mihai, A Velea, AC Galca, “A two-step magnetron sputtering approach for the synthesis of Cu_2ZnSnS_4 films from Cu_2SnS_3\ZnS stacks,” *ACS Omega* 7, 23800–23814, (2022).

Capacitive and Inductive Effects in Perovskite Solar Cells: The Different Roles of Ionic Current and Ionic Charge Accumulation

Nicolae Filipoiu[a], Amanda Teodora Preda[a], Dragos-Victor Anghel[a], Roxana Patru[b], Rachel Elizabeth Brophy[c], Movaffaq Kateb[c], Cristina Besleaga[b], Andrei Gabriel Tomulescu[b], Ioana Pintilie[b], Andrei Manolescu[c], George Alexandru Nemnes[a]
[a] University of Bucharest, Faculty of Physics, 405 Atomistilor, 077125 Magurele, Romania
[b]Laboratory of Complex Heterostructures and Multifunctional Materials, National Institute of Materials Physics, 405A Atomistilor, 077125 Magurele, Romania
[c]Department of Engineering, Reykjavik University, IS-102 Reykjavik, Iceland

The perovskite solar cells (PSCs) represent a promising alternative to the well-established technologies like silicon-based and thin-film solar cells, due to the significant power conversion efficiency (PCE), obtained at comparatively lower fabrication costs. However, the most problematic aspect which still hinders the commercialization concerns the stability of the PSCs and therefore the possible degradation mechanisms are at the forefront of the current research. The hysteretic effects known to occur in the J-V characteristics of PSCs impacted early studies by the uncertainty in the evaluation of PCE, while currently, potential links to degradation mechanisms are in the focus. In addition to these capacitive effects, a peculiar large inductive behavior was evidenced in some PSCs by small-signal analyses performed with electrochemical impedance spectroscopy (EIS) technique. The reported large capacitive and inductive effects created controversies with respect to the underlying mechanisms, yielding essentially two classes of models based on: (*i*) giant accumulation capacitances and generic inductances (CA) [1,2] – a model easy to be applied by experimentalists; (*ii*) ionic modulation of the collected current (CC), properly addressing the microscopic reasons [2] however, too complex to be routinely employed for analyzing the experimental data. In this context, we developed a comprehensive equivalent circuit model (see Figure 1), able to reproduce both capacitive and inductive effects while providing a bridging point between the CA and CC classes of models. The backbone of our circuit model is composed from standard elements such as the current source corresponding to the photogenerated current I_{ph}, the diode element introducing a recombination current I_d, the shunt resistance R_{sh}, accounting for a recombination current I_{sh}, and the series resistance R_s plus a small geometrical capacitance C_0, counting for the hysteretic effects. We have also introduced two essential parts, namely the R-C circuit blocks for the two interfaces of the halide perovskite with the hole transporter layer (HTL) and the electron transporter layer (ETL), in series with the perovskite absorber ionic resistance R_a and the additional current source corresponding to the ionic modulated recombination current, I_{rec}. The corresponding charges (Q_1 and Q_2) for the capacitors C_1 and C_2, with instantaneous applied voltages $V_1(t)$ and $V_2(t)$, describe the ionic charge accumulation at the two interfaces. The R_1 and R_2 resistances account for the electron or hole-ion charge neutralization at the two interfaces. The current I_c denotes the ionic current flowing inside the perovskite absorber layer. The central assumption of the model is that the recombination current I_{rec} is modulated by both ion charge accumulation and ionic current, using the following Ansatz:

$$I_{\text{rec}} = I_{\text{rec}0} + \sum_{i=1}^{2} a_i Q_i + b I_c, \qquad (1)$$

Thus, I_{rec} depends on the ionic charge (Q_i), where i=1,2 relates to the interface with ETL and HTL, respectively, and on the ionic current (I_c). The term I_{rec0} represents a reference recombination current, in the absence of the ionic influence, which simply regauges the photogenerated current, while a_i and b parameterize the inductive and capacitive recombination current contributions. These contributions to the recombination current are associated with capacitive and inductive effects, respectively, and we corroborate the numerical simulations with EIS measurements showing the role of the recombination currents of photogenerated carriers in producing both capacitive and inductive effects as the illumination is varied [4]. Thus, starting with the large signal analysis, we recover known dynamical effects, such as the current bump in the reverse scan under positive poling (see Figure 2a), inverted hysteresis under negative poling and tuning of the hysteretic effects under illumination and bias scan rate, correlated with the relatively large time scales involved in the ion migration processes [4]. Inductive effects may appear at low frequencies and can be produced by defect-induced recombination controlled by ionic accumulations at the interfaces, introduced by the $a \times Q_C$ term in Eq. (1). In Figure 2b we assess the changes in the Nyquist plot and the frequency dependence of the measured apparent capacitance (C_{app}) when increasing the a-parameter. Small values of a still produce a capacitive behavior, while larger ones make the inductive effect visible at low frequencies, eventually overcoming the capacitive behavior.

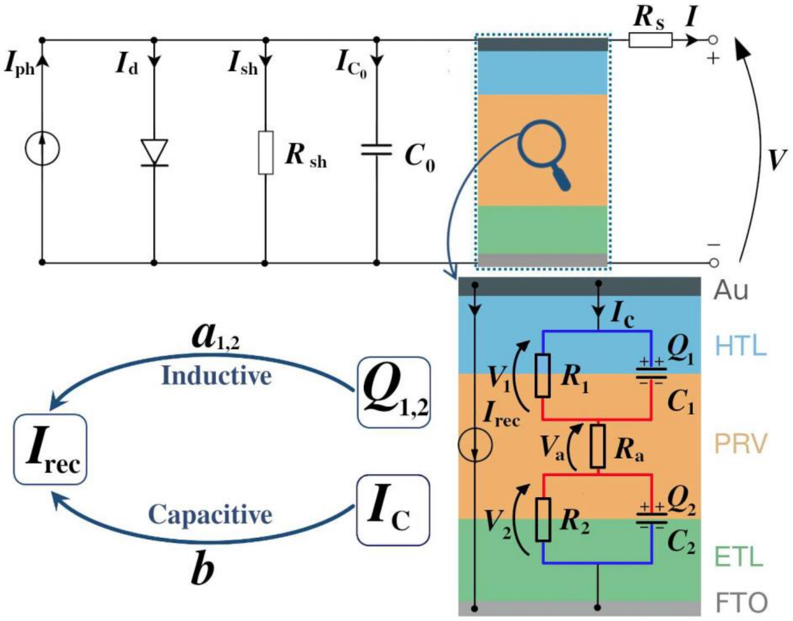

Fig. 1 The equivalent circuit model employed for describing capacitive and inductive effects. The colorful sections represent the PSC elements in standard configuration with FTO and gold electrodes.

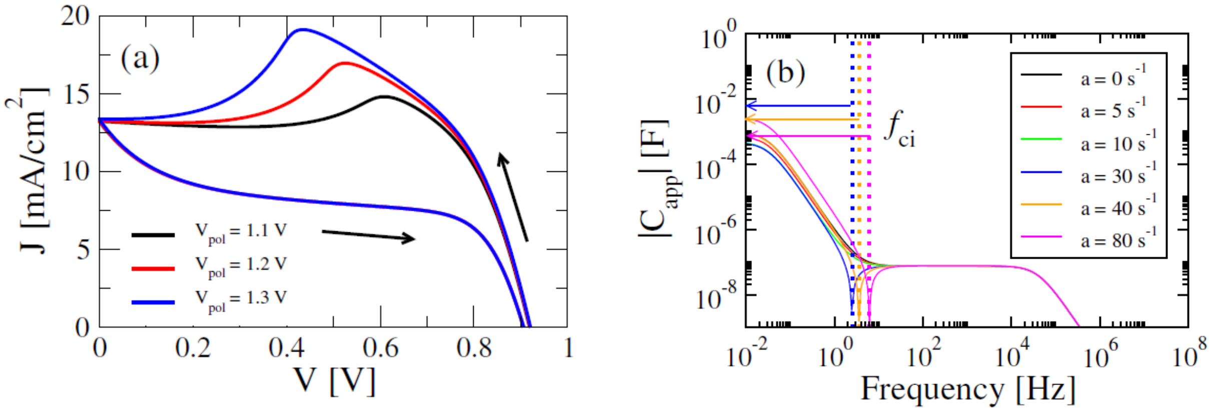

Fig. 2 (a) J-V characteristics for $V_{pol} > V_{oc}$ poling conditions; (b) Inductive behavior produced by ion-defect induced recombination. Increasing the parameter a the recombination current is enhanced leading to significant inductive effects. The threshold frequency f_{ci} marks the transition between the capacitive and inductive behavior.

The phasor diagrams shown in Figure 3 are a perfect representation of the capacitive and inductive behavior for the current components in the small signal analysis regime. When applying a small signal of 1 mV, the measured current i is dephased by the two different recombination mechanisms.

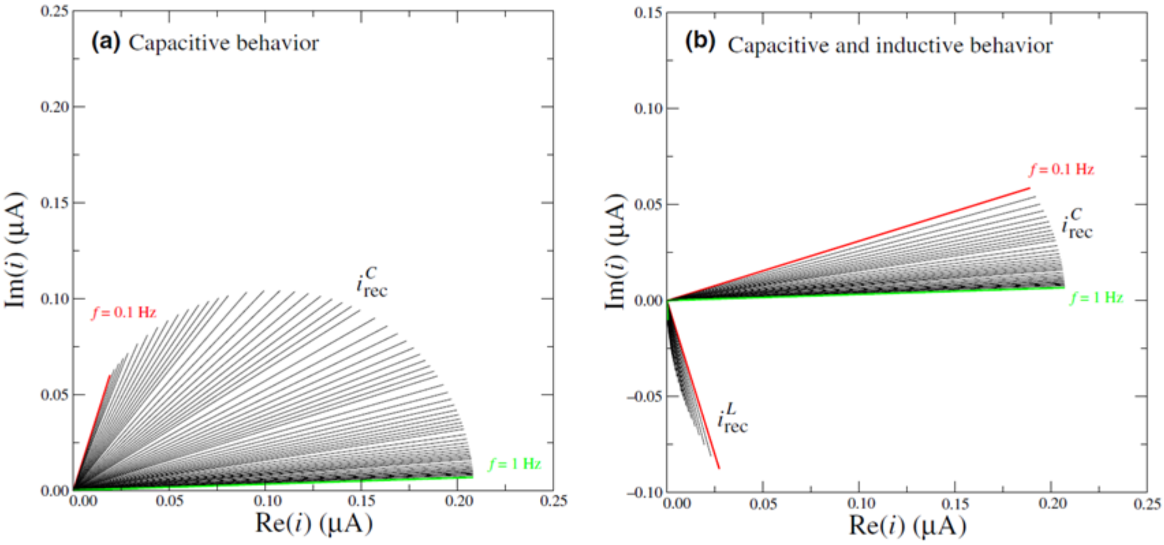

Fig. 3 Phasor diagrams showing the dephasing of the recombination currents in the frequencies range of f = 0.1–1 Hz for two types of PSCs, with: (a) capacitive effects only (a = 0, b = 100) and (b) capacitive and inductive effects (a = 30 s−1, b = 100) showing the π/2 dephasing between I^{c}_{rec} and I^{L}_{rec}.

We show that there is a connection between capacitive and inductive effects, as the former depends on the ionic current, $I_c = \partial Q_c/\partial t$, while the latter is connected to the ionic charge accumulations, Q_i. The recombination current is, in general, a sum of these two components and the parameters *a* and *b*, which are sample specific, will establish one of the two behaviors. The experimental results confirm the assumption concerning the voltage dependence of the capacitance, which is essential for describing the J-V hysteresis and reinforce the connection between the capacitive and inductive effects, both being linked to the recombination of photogenerated carriers. The strong variation of the inductive effects with illumination is indicative for a mechanism based on the recombination of photogenerated carriers, emerging from ionic accumulations. This complements the other recombination mechanisms based on local electric fields in the absorber, which is responsible for the capacitive effects.

In conclusion, the introduced equivalent circuit model is not only able to reproduce both capacitive and inductive effects but gives the experimentalists a framework of investigating the defect states based on the observed inductive effects, aiding further the mitigation of the degradation effects in PSCs.

References

1. K Seki, “Equivalent circuit representation of hysteresis in solar cells that considers interface charge accumulation: Potential cause of hysteresis in perovskite solar cells”, *Applied Physics Letters* 109, 033905 (2016).
2. GA Nemnes, C Besleaga, AG Tomulescu, I Pintilie, L Pintilie, K Torfason, A Manolescu, “Dynamic electrical behavior of halide perovskite based solar cells”, *Solar Energy Materials and Solar Cells* 159, 197–203 (2017).
3. W Tress, N Marinova, T Moehl, SM Zakeeruddin, MK Nazeeruddin, M Gratzel, “Understanding the rate-dependent *J–V* hysteresis, slow time component, and aging in $CH_3NH_3PbI_3$ perovskite solar cells: the role of a compensated electric field”, *Energy & Environmental Science* 8, 995–1004 (2015).
4. N Filipoiu, AT Preda, DV Anghel, R Patru, RE Brophy, M Kateb, C Besleaga, AG Tomulescu, I Pintilie, A Manolescu, GA Nemnes, “Capacitive and Inductive effects in perovskite solar cells: The different roles of ionic current and ionic charge accumulation”, *Physical Review Applied* 18, 064087 (2022).

Boosting the Bio-functionality of Silica- and Phosphate-based Bioactive Glasses by the Standalone and Combined Incorporation of Therapeutic CuO and Ga_2O_3 Elements

George E. Stan[a], Teddy Tite[a], Adrian-Claudiu Popa[a], Maria Iuliana Chirica[a], George Adrian Lungu[a], Dan Macovei[a], Cristina Bartha[a], Bryan W. Stuart[b], Hugo R. Fernandes[c], Lucian Albulescu[d], Cristiana Tanase[d], Sultana Nita[e], Nicoleta Rusu[e], David M. Grant[b], José M.F. Ferreira[c]

[a]National Institute of Materials Physics, 405A Atomistilor, 077125 Magurele, Romania
[b]Advanced Materials Research Group, Faculty of Engineering, University of Nottingham, University Park, NG7 2RD, Nottingham, United Kingdom
[c]Department of Materials and Ceramics Engineering, University of Aveiro, 3810-193 Aveiro, Portugal
[d]National Institute of Pathology "Victor Babes", 050096 Bucharest, Romania
[e]National Institute for Chemical Pharmaceutical Research and Development, 031299 Bucharest, Romania

Bioactive glasses (BGs) gained prominence in the orthopedic and dentistry fields for preventing the failure of the bioinert metallic implants, by making them able to overcome their deficient bone bonding ability, as well as capable to tackle post-surgery bacterial infections [1]. Recently, the individual incorporation of antimicrobial agents (*e.g.*, silver, zinc, copper, or gallium) in BGs has been explored as a new attractive strategy for boosting even further their bio-functionality [2]. In this study, copper (Cu) and gallium (Ga) were selected for their proficient antimicrobial activity, and incorporated separately and concurrently into silica- (SBG), phosphate-(PBG)-based bioactive glass formulations. The interlinked structural/physico-chemical properties and the *in vitro* biological effects of these new glass compositions were investigated for the first time. A special attention was dedicated to the understanding of the structural role of Ga in SBGs and PBGs, not yet elucidated, furthermore as this will govern the predictability of the biological performance of these materials.

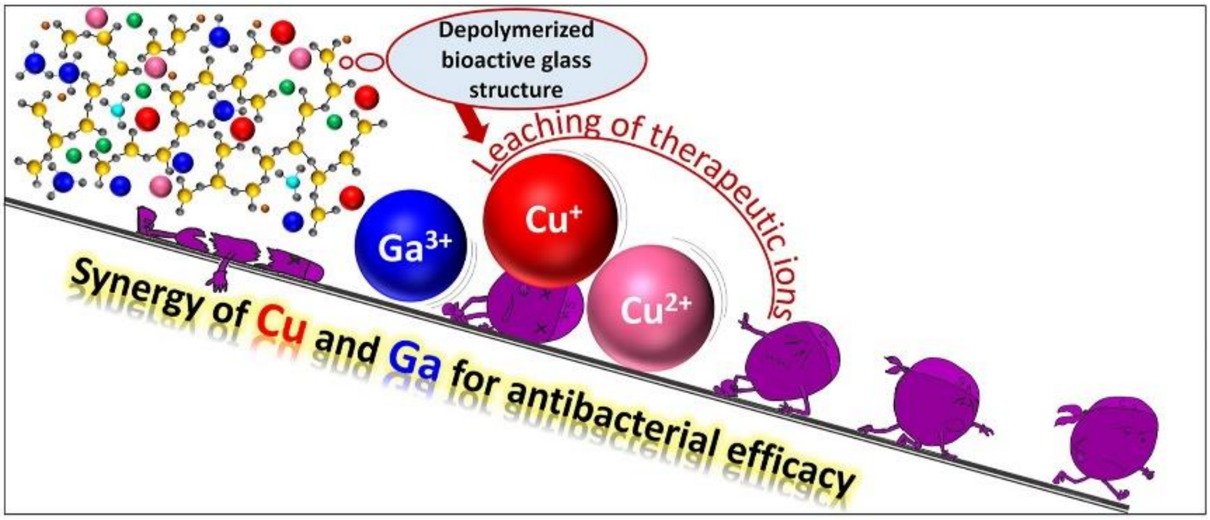

Illustration of the synergy between Cu and Ga leached ions from BGs against bacterial stains.

Specifically, ten formulations of SBGs (based on the FastOsBG® system) and PBGs (derived from the P_2O_5-CaO-Na_2O-Fe_2O_3 compositional system) were prepared by melt-quenching [1]. Their expected and experimental oxide concentrations (in mol%) and the corresponding codes of these BGs are presented in Table 1. CuO partially substituted CaO (in both SBG and PBG systems), whilst Ga_2O_3 partially replaced MgO (for SBGs) or Fe_2O_3 (for PBGs), both network intermediates. A good match between the expected and experimental oxide compositions was inferred by energy dispersive X-ray spectroscopy (EDXS), within the experimental errors (Table 1).

Table 1 The oxide concentration (in mol%) – theoretical (the.) and experimentally determined (exp.) by EDXS as arithmetic means ± standard deviation (n=3) and thermal parameters (extracted from TG-DSC measurements) of the as-synthesized SBG and PBG materials.

Sample code		Oxide concentration (mol %)							Thermal properties		
SBG series		SiO_2	CaO	P_2O_5	MgO	CaF_2*	CuO	Ga_2O_3	T_g (°C)	T_c (°C)	T_m (°C)
C0G0	the.	38.5	36.1	5.6	19.2	0.6	–	–	715	912	>1200
	exp.	39.3 ± 0.2	36.7 ± 0.6	5.0 ± 0.1	19.0 ± 0.3	–	–	–			
C5G0	the.	38.5	31.1	5.6	19.2	0.6	5.0	–	694	881	1161
	exp.	38.7 ± 0.5	32.2 ± 0.4	5.1 ± 0.1	18.4 ± 0.2	–	5.6 ± 0.9	–			
C3G2	the.	38.5	33.1	5.6	17.2	0.6	3.0	2.0	657	897	>1200
	exp.	38.6 ± 0.3	33.9 ± 1.0	5.2 ± 0.1	16.8 ± 05	–	3.6 ± 0.5	1.9 ± 0.1			
C2G3	the.	38.5	34.1	5.6	16.2	0.6	2.0	3.0	721	895	>1200
	exp.	38.7 ± 0.3	34.7 ± 0.7	5.1 ± 0.1	16.1 ± 0.4	–	2.6 ± 0.4	2.8 ± 0.1			
C0G5	the.	38.5	36.1	5.6	14.2	0.6	–	5.0	800	938	>1200
	exp.	39.6 ± 0.4	36.6 ± 0.8	5.0 ± 0.2	14.0 ± 0.2	–	–	4.8 ± 0.1			
PBG series		P_2O_5	CaO	MgO	Na_2O	Fe_2O_3	CuO	Ga_2O_3	T_g (°C)	T_c (°C)	T_m (°C)
C0G0	the.	50.0	35.0	–	10.0	5.0	–	–	561	686	811
	exp.	49.8 ± 0.4	33.7 ± 0.2	–	12.3 ± 0.3	4.2 ± 0.1	–	–			
C5G0	the.	50.0	30.0	–	10.0	5.0	5.0	–	530	680	804
	exp.	48.9 ± 0.1	29.3 ± 0.2	–	11.4 ± 0.1	4.8 ± 0.1	5.6 ± 0.1	–			
C3G2	the.	50.0	32.0	–	10.0	3.0	3.0	2.0	440	688	790
	exp.	48.4 ± 0.1	31.7 ± 0.2	–	11.6 ± 0.4	3.0 ± 0.1	3.2 ± 0.2	2.1 ± 0.1			
C2G3	the.	50.0	33.0	–	10.0	2.0	2.0	3.0	518	684	785
	exp.	50.0 ± 0.2	32.2 ± 0.4	–	10.0 ± 0.4	2.0 ± 0.1	2.2 ± 0.1	3.6 ± 0.3			
C0G5	the.	50.0	35.0	–	10.0	–	–	5.0	457	609	1185
	exp.	50.5 ± 0.1	34.4 ± 0.2	–	9.9 ± 0.2	–	–	5.2 ± 0.1			

The glass crystallization (T_c) and melting (T_m) temperatures of SBGs were higher than the ones of PBGs, denoting the better structural thermal stability of the former. The incorporation of Cu was found to decrease the glass transition (T_g) for both SBGs and PBGs, suggesting its role as network modifier (expanding and weakening the glass network). In contrast, Ga augmented and reduced the T_g of SBGs and PBGs, respectively, advocating for its a role as network former in SBGs (strengthening the glass network) and as modifier for PBGs. These first results offered the first clues that Ga plays dissimilar structural roles in SBGs and PBGs.

The X-ray diffraction analyses has shown a broad halo centered at 2θ≈29° and 25° for SBGs and PBGs, respectively, indicative of their amorphous structure. The halo was less intense and broader for PBGs suggesting an increased structural disorder with respect to SBGs. The downshift of the PBGs' halo exposed a lower packing density of the glass network. Furthermore, the FTIR spectroscopy revealed that the incorporation of Ga in PBGs was accompanied by the emergence of the asymmetric stretching P–4NBO bonds (Q_P^0 band at ~1003 cm^{-1}), which testified for a local de-polymerization of these glasses. Likewise, the X-ray photoelectron spectroscopy measurements showed that Cu had a similar chemical state in both SBG and PBG systems, whilst Ga was found in a richer oxygen chemical environment in PBGs with respect to SBGs. Definite evidences on the role of Ga in SBGs and PBGs were extracted by extended X-ray absorption fine structure (EXAFS) spectroscopy. The EXAFS results evidenced a four-fold coordination of Ga in SBG and six-fold coordination in PBG, emphasizing that Ga acts as network former in SBG and as network modifier in PBG. The structural disorder of the short-range environment of Ga was three times larger in the PBG in comparison to SBG, unveiling much more ordered GaO_4 clusters in the SBG than in the case of the GaO_6 ones in PBG. Taken together, the structural and physico-chemical analysis indicated that Cu acted as network modifier irrespective of type of glass, whilst Ga had a prominent glass network former role in SBGs, and a network modifier one in PBGs.

Consequently, the SBGs and PBGs fostered different ion leaching patterns, with Cu ions being released in similar concentrations (ranging from 10 to 35 ppm at BG doses of 5 mg/mL) for both type of glasses, whilst the Ga ions were leached with 1–2 orders of magnitude lower in the case of SBGs (*i.e.*, 0.2–3.2 ppm) compared to PBGs (*i.e.*, 9–27 ppm) (Figure 1a,b). Interestingly, the antibacterial efficiency was accentuated by the coupled release of Cu and Ga ions from SBGs and their synergetic complementary action (Figure 1c,d). The *in vitro* cell proliferation (MTS) (Figure 1e,f) and death (LDH) (Figure 1g,h) assays (in NIH/3T3 mouse fibroblast cell cultures) revealed no cytotoxic effects at a dose of 5 mg/mL of BG powder, irrespective of composition. The most promising SBG candidate materials was constituted by the "C2G3" formulation: $38.5SiO_2-34.1CaO-5.6P_2O_5-16.2MgO-0.6CaF_2-2.0CuO-3.0Ga_2O_3$ (mol%). SBG- C2G3 led to moderate Cu and Ga ion release, excellent cytocompatibility and noteworthy antibacterial efficacy against the *Staphylococcus aureus* strain.

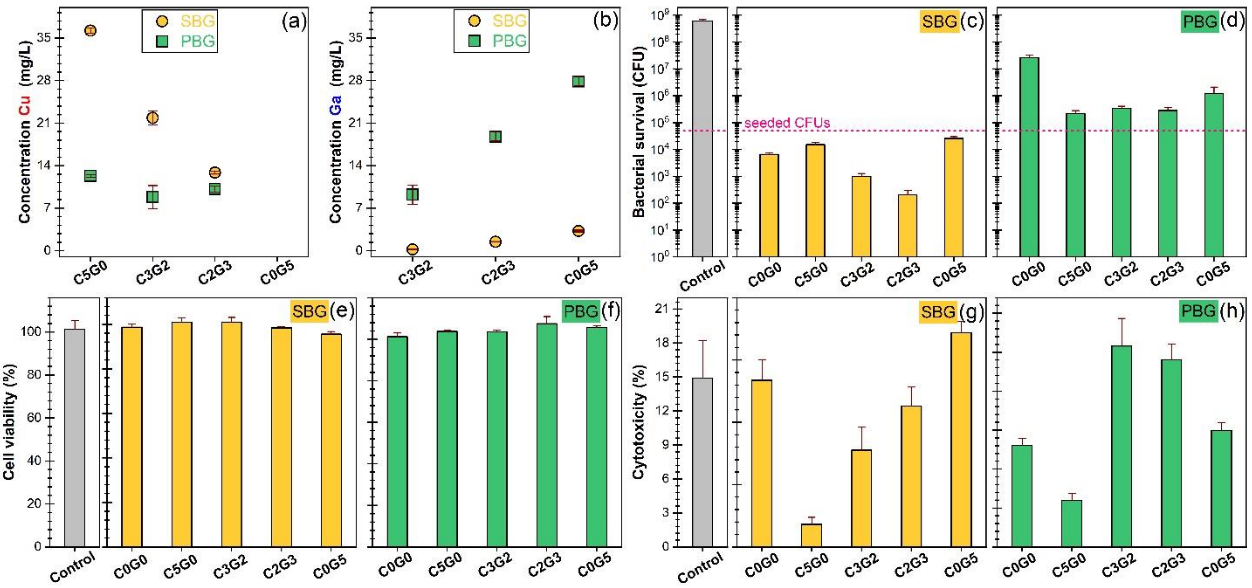

Fig. 1 (a,b) The concentrations of (a) Cu and (b) Ga therapeutic ions released by SBGs and PBGs (tested at doses of 5 mg/mL) after immersion in the complete cell culture medium for 24 h, as determined by ICP-MS; (c–h) Bar charts representation of the (c,d) antibacterial activity and (e–h) cytocompatibility of the SBG and PBG materials. The antimicrobial activity at 24 h (represented in log-scale) of the (c) SBG and (d) PBG materials (at powder doses of 5 mg/mL) against the *S. aureus* bacterial strain. The NIH/3T3 (ATCC® CRL−1658™) mouse fibroblast (e,f) cell viability/proliferation (evaluated by the MTS assay) and (g,h) cytotoxicity (inferred by the LDH test) at 24 h of the (e,g) SBG and (f,h) PBG materials, at powder mass-to-medium volume ratios of 5 mg/mL.

References

1. L Drago, M Toscano, M Bottagisio, “Recent evidence on bioactive glass antimicrobial and antibiofilm activity: A mini-review”, *Materials* 11, 326 (2018).
2. T Tite, AC Popa, BW Stuart, HR Fernandes, IM Chirica, GA Lungu, D Macovei, C Bartha, L Albulescu, C Tanase, S Nita, N Rusu, DM Grant, JMF Ferreira, GE Stan, “Independent and complementary bio-functional effects of CuO and Ga_2O_3 incorporated as therapeutic agents in silica- and phosphate based bioactive glasses”, *Journal of Materiomics* 8, 893–905 (2022).

Advanced Characterization of Roman Ceramic from Romula

Petre Badica[a], Andrei Alexandru-Dinu[a], Mihai A. Grigoroscuta[a], Viorel Sandu[a], Gheorghe V. Aldica[a], Iuliana Pasuk[a], Mihail Burdusel[a], Cristina Bartha[a], Victor Kuncser[a], Andrei Kuncser[a], Monica Enculescu[a], Silviu Polosan[a], Andrei Galatanu[a], Claudiu Locovei[a], Ioana Porosnicu[b], Ion Tiseanu[b], Marilena Ferbințeanu[c], Mircea Negru[d], Nicolae-Dan Batalu[e], Ionuț Săvulescu[f], Nicolae Cruceru[g]

[a]National Institute of Materials Physics, 405A Atomistilor, 077125 Magurele, Romania
[b]National Institute of Laser, Radiation, and Plasma Physics, 409 Atomistilor, 077125 Magurele, Romania
[c]Faculty of Chemistry, University of Bucharest, 90 Panduri, 050663 Bucharest, Romania
[d]CICSA, Faculty of History, University of Bucharest, 4 – 12 Bd. Regina Maria, 030167 Bucharest, Romania
[e]University Politehnica of Bucharest, 313 Splaiul Independentei, 060042 Bucharest, Romania
[f]Faculty of Geography, University of Bucharest,1 Bd. Nicolae Balcescu, 010041 Bucharest, Romania
[g]Institute of Speology "Emil Racovita", Romanian Academy, 13 Calea 13 Septembrie, 050731 Bucharest, Romania

Romula was the largest Roman city in Dacia Inferior (Malvensis) that played an important military, administrative, trade, production, and cultural role. The archaeological site of Romula (today Reșca village, near Caracal, the Olt County, Romania) extends over 3.06 km^2 and it is located between the Carpathian Mountains and the Lower Danube River. It was built by Romans as a fortress during the First War with Dacians (101–102 AD). Romula received the title of municipium (123–124 AD), and, later, of colonia in 248 AD or in the time of Emperor Septimius Severus, 193–211 AD). It was abandoned in 271–275 AD in the time of Emperor Aurelian or even earlier, 253–268 AD, in the time of Emperor Gallienus. In the Northern Quarter were identified eight pottery workshops and 25 pottery kilns as evidence for an industrial-level fabrication of ceramic. Therefore, Romula was one of the largest production centers of ceramic in the Lower Danube area, the discoveries of Roman ceramics being the reference for this region: the ceramic artefacts excavated in the site are building items (bricks, tiles, pavement pieces, and others), terracotta lamps, and pottery (amphorae, kitchen pottery, others). About 5 of the mentioned kilns were dedicated for the production of bricks and tiles and they were dated to the first decades of the third century AD.

Bricks are old building materials (~8000 BC for mudbricks and ~3000 BC for burnt bricks, Mesopotamia) and they are still in use nowadays, mostly for facades and walls between structural concrete elements, but on a significantly lower scale than in the ancient times when buildings were entirely made of bricks. This may induce the idea that the ancient bricks are obsolete and deprecated. This is not the case since the ancient bricks proved to intrinsically incorporate modern concepts such as sustainability, durability, green and environment friendly materials and buildings, materials reuse/recycling. The high quality and durability of the bricks was also recognized in the middle ages and burnt bricks from Romula were reused about 1000 years later, e.g. for building of churches and towers [1]. Therefore, ancient bricks may unveil unexpected know-how forgotten technologies and concepts. Studies of ancient bricks from different periods, geographical locations, and cultures can also provide other valuable information: on one side the knowledge about ancient bricks and technologies is needed for appropriate restoration and conservation of the heritage constructions, and on the other side it can promote a better understanding of the regional development and society. Bricks through their archaeological availability and spreading, while being typically specific for the local production can be also viewed as convenient reference ceramic materials to compare with. For example, other ceramic artefacts such as amphorae, kitchen and storage ware are prone to trade activities, and comparison with local brick materials can provide and demonstrate different details of the commercial routes as well as other aspects of daily life. To do so, advanced and complex investigations of the ancient ceramic materials are required.

Sesquipedalian mud and burnt bricks (second to third century AD) were excavated from the Roman city of Romula. Excavation of mud bricks in the northern Roman provinces is an unexpected and surprising discovery. Along with local soils, bricks were investigated by petrographic analysis, X-ray fluorescence (XRF), X-ray diffraction (XRD), Fourier transformed infrared spectroscopy (FT-IR), electron microscopy (SEM/EDX), X-ray microtomography (XRT), thermal analysis (DTA-TG), laser calorimetry, Mössbauer spectroscopy, magnetometry, colorimetry, and mechanical properties assessment [2]. The results are useful for conservation/restoration purposes. Based on them, the material replicating the one of the ancient burnt bricks was produced in the lab. from the local raw materials extracted near the Romula site, and a patent request was submitted [3]. Remarkably, our study and comparison with literature data indicate the possible control and wise optimization by the ancient brickmakers through the recipe, design (size, shape, and micro/ macrostructure), and technology of the desired physical–chemical–mechanical properties. Roman bricks can be viewed as materials that adapt to external factors, similar, to some extent, to modern "smart" or "intelligent" materials. These features can explain their outstanding durability to changes of weather/climate and mechanical load induced by landslides, earthquakes, and so on. The criteria for the fabrication of durable Roman bricks were revealed and they can be summarized as follows: (*i)* Raw materials for fabrication of mud and burnt bricks are a mixture of ~ 40 wt.% clay and 60 wt.% sand with a relatively small particle size (< 2 mm); (*ii*) The amount of alkali metals such as Na, K should be relatively low, ~ (3–5) wt.% (oxide representation). This is required to avoid excessive melting during thermal processing and, thus, to limit the formation of a high amount of the hard, but brittle glassy phase. The glassy phase impacts microstructure (pores size and distribution) and further the weathering and mechanical behavior of the burnt brick; (*iii*) Separation of Fe from the aluminosilicates, clusterization, and oxidation were revealed. Iron has a complex behavior and role in controlling the stability and decomposition of silicates. Its interplay with calcium is especially important, but more research is needed to understand the details considering each silicate type and mixtures. The relative amount of Fe (represented as oxide in XRF results) takes values in the 6–10 wt.% range; (*iv*) The amount of calcium is relatively high in both mud and burnt bricks from Romula. For the burnt brick, calcium represented as oxide in XRF is around 6–8 wt.%, while in the mudbrick it is even higher, around 15–19 wt.%. The amount of calcium (and of calcium carbonate in particular) in the bricks should be optimum to contribute pores development or, more general, the microstructure formation and control during processing (drying and burning). Calcium plays a key role in the reversible long-term chemical processes of the brick interaction with the environment with a strong effect on cracks and pores behavior. Other mechanisms of the brick-environment interaction should also consider silicates crystal chemistry during processing and during their long-term use; (*v*) The amount of Mg (represented as oxide in XRF results) in mud and burnt bricks should be relatively low (1–2 wt.%), significantly lower than that of calcium. A high amount negatively impacts cracks and pores behavior during processing and long-term interaction of the brick with the environment; (*vi*) The special flat shape and size of the burnt brick, the small distributed pores and reinforcement particles (large pores or particles are only about 3–3.5 vol.%) in the aluminosilicates matrix and the lack of a high amount of brittle glassy phase in the matrix are essential for mechanical properties. Although these burnt bricks are classified as soft, they can withstand large compressive mechanical loads, and more important, large load variations, adapting and preserving their integrity; (*vii*) Burning temperature of the bricks is optimized to ensure previous criteria. For the burnt brick from Romula the temperature is slightly above 800 °C and below 850 °C.

Pottery vessels made of kaolin clay from the Roman Period (2nd, 3rd centuries AD) found in Romula were investigated by petrographic, X-ray diffraction, X-ray fluorescence, thermal analysis, electron microscopy, and mechanical tests [4]. Our results are compared with available data on kaolin clays and pottery vessels from other sites located along the lower course of Danube river and near the Black Sea, namely in Moesia Superior, Moesia Inferior, and Thracia. Archeological and geographical contexts are addressed. Results of our analysis suggest a local production of ceramics in Romula, by using raw materials from the north of Lower Danube, in opposition to the idea that kaolin ware was imported from the provinces south of the Danube.

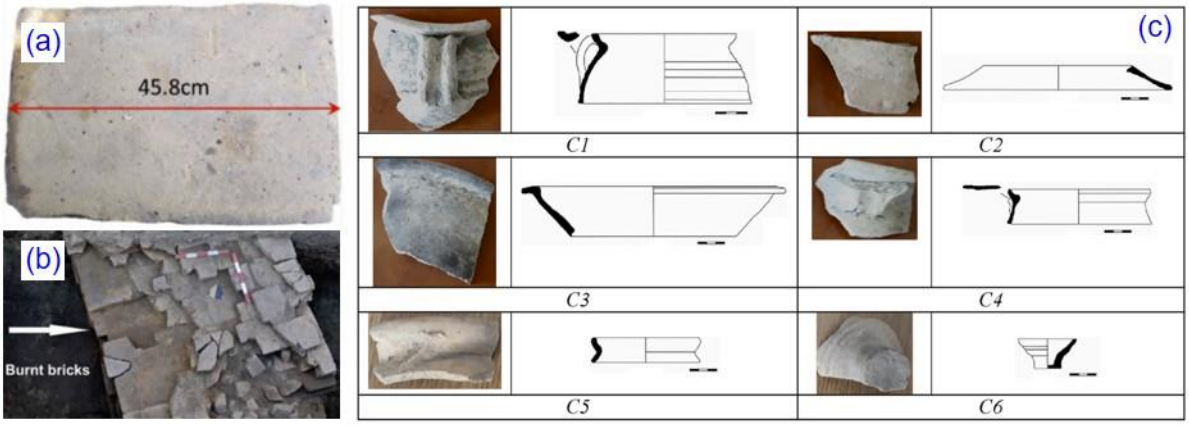

Fig. 1 (a) The burnt brick from a wall (b) built in the last decade of the second century to first third of the third century AD in Romula (from ref. [2]); (c) Kaolin pottery fragments from Romula and schematic drawings of the ware shapes (from ref. [4]).

References

1. M Negru, D Batalu, P Badica, F Mihu, I Poll, “Recycling of Roman bricks from Romula”, *HERITAGE* – Proceedings of 6th International Conference on Heritage and Sustainable Development, 2018, 12 – 15 June, Granada, Spain, p. 1451-1462, e-ISBN 978-84-338-62, ISSN: 2712-0554.
2. P Badica, A Alexandru-Dinu, MA Grigoroscuta, M Burdusel, GV Aldica, V Sandu, C Bartha, S Polosan, A Galatanu, V Kuncser, M Enculescu, C Locovei, I Porosnicu, I Tiseanu, M Ferbinteanu, I Savulescu, M Negru, ND Batalu, “Mud and burnt Roman bricks from Romula”, *Scientific Reports* 12, 15864 (2022).
3. P Badica, D Batalu, MA Grigoroscuta, I Savulescu, M Negru, “Fabrication and ceramic material for bricks replicas of the Roman ones”, *OSIM patent request* A/00740 (2018).
4. P Badica, A Alexandru-Dinu, M Grigoroscuta, C Locovei, A Kuncser, C Bartha, G Aldica, M Negru, D Batalu, N Cruceru, I Savulescu, “Kaolin clay pottery discovered in the Roman city of Romula (Olt county, Romania)”, *Journal of Archaeological Science: Reports* 36, 102899 (2021).

MgB_2 Superconductor: High Density, Textured Bulks and Hybrid Superconductor-Ferromagnet Shields

Petre Badica[a], Mihai A. Grigoroscuta[a], Viorel Sandu[a], Gheorghe V. Aldica[a], Iuliana Pasuk[a], Mihail Burdusel[a], Andrei Kuncser[a], Alina M. Ionescu[a], Lucian Miu[a], Oleg Vasylkiv[b], Tohru S. Suzuki[b], Laura Gozzelino[c], Michela Fracasso[c], Andrea Napolitano[c], Roberto Gerbaldo[c], Gianluca Ghigo[c], Francesco Laviano[c], Daniele Torsello[c], Mykola Solovyov[d], Fedor Gömöry[d], Dan Batalu[e]

[a]National Institute of Materials Physics, 405A Atomistilor, 077125 Magurele, Romania
[b]National Institute for Materials Science, 1-2-1 Sengen, 305-0047 Tsukuba, Ibaraki, Japan
[c]Department of Applied Science and Technology, Politecnico di Torino, 10129 Torino, Italy
[d]Institute of Electrical Engineering, Slovak Academy of Sciences, 841 04 Bratislava, Slovakia
[e]University Politehnica of Bucharest, 313 Splaiul Independentei, 060042 Bucharest, Romania

MgB_2 is a practical superconductor. However, in the last 10 years MgB_2 became a material of great interest for emergent applications, such as propellants, batteries, and catalysis, as a source material to obtain 2D borophene-like materials (*e.g.*, BH borophane), in the biomedical field (taking advantage of its promising antimicrobial, antitumoral, biodegradable, and biocompatible features), heritage and ecology being the latest trends [1]. These new directions place MgB_2 as a material well integrated with nature cycles that can promote the concept of one eco- and health-friendly material, with many envisioned practical purposes. This type of material is at the core of a clean and sustainable economy promoting new developments, boosting the older ones (e.g. superconductivity) and minimizing the costs for the transition to new and modern materials and technologies.

To fulfill the potential, in some applications including the superconducting ones, high density bulks are needed. Polycrystalline MgB_2 bulk samples were produced by *ex-situ* spark plasma sintering (SPS) using the oxygen-free preceramic polymer additive poly(dimethylsilane) as a source for carbon doping and as a sintering aid [2]. Two major effects were identified. One is the significant enhancement of the densification kinetics during sintering for all tested compositions. The second one is the improvement of the high field critical current density for a certain level of the poly(dimethylsilane) addition.

Superconducting applications require high critical current densities, J_c. Critical current density can be enhanced by stronger vortex pinning and higher connectivity. Different approaches are applied in this regard.

Nano-structuring is effective in promoting enhancement of the density of grain boundaries. Grain boundaries and interfaces are recognized as efficient pinning centers. Introduction of additives with the purpose to modify the grain boundaries or the electronic structure through chemical substitutions of B or Mg in the crystal lattice of MgB_2 is another method that can be successful. In our recent report [3], high density (94–98% of the theoretical density) MgB_2 samples added with $C_6H_{10}Ge_2O_7$ and cubic BN with compositions $(MgB_2)_{1-x}(Ge_2C_6H_{10}O_7)_{0.0028}(cBN)_x$ ($x = 0.003, 0.005, 0.007, 0.01$) and $(MgB_2)_{1-y}(Ge_2C_6H_{10}O_7)_y(cBN)_{0.005}$ ($y = 0.0014, 0.0028, 0.005, 0.0075$) were obtained by spark plasma sintering technique. For optimum doped samples with $x = 0.005–0.007$ and $y = 0.0028–0.005$, a weak enhancement of zero-field critical current density J_{c0}, irreversibility field H_{irr}, and volume pinning force $F_{p,max}$ was determined. This behavior is very different from similar samples added with a single additive for which H_{irr} has a large enhancement. Consequently, it suggests the presence of opposite structural and microstructural effects induced by the additives. These effects, on the one hand, are discussed to decrease the sensitivity of MgB_2 superconducting properties in the co-added samples comparative to samples added with $C_6H_{10}Ge_2O_7$, and, on the other hand, they contribute to anomalies that were found when assessing the pinning force–related parameters by the universal scaling law.

Another possibility to enhance J_c is to take advantage of the MgB_2 anisotropy. The crystal structure of MgB_2 is composed of alternate stacked layers of B and Mg. The *in-plane* flow of the supercurrent is favored. Hence, textured MgB_2 materials are of interest for practical purposes. Our article [4] presents fabrication and characterization of spark plasma sintered textured (001) MgB_2 with a record degree of orientation of about 40% and 16% by high-energy ultra-sonication and slip casting in high magnetic field (12 T) and 0 T magnetic field, respectively (Figure 1). Structural characterization was performed by X-ray diffraction, and electron microscopy. The analysis revealed unexpected preferred orientation also in the MgO secondary phase due to the epitaxial growth of (111) MgO on (001) MgB_2. The influence of oriented microstructure on the superconducting characteristics such as critical current density (J_c), irreversibility field (H_{irr}), and on the pinning properties were assessed. High anisotropy versus sample orientation in applied magnetic field, H, was observed for J_c (Figure 2), H_{irr}, pinning activation energy (U^*) extracted from relaxation measurements. The zero-field critical current, J_{c0} and $F_{p,max}$ are weakly or not dependent on the direction of H, while the other indicated parameters are significantly influenced. Results enable control of superconducting parameters by further optimization of microstructure through MgB_2 texturing as a novel and viable strategy for development of bulk MgB_2 with enhanced properties when taking advantage of its anisotropy.

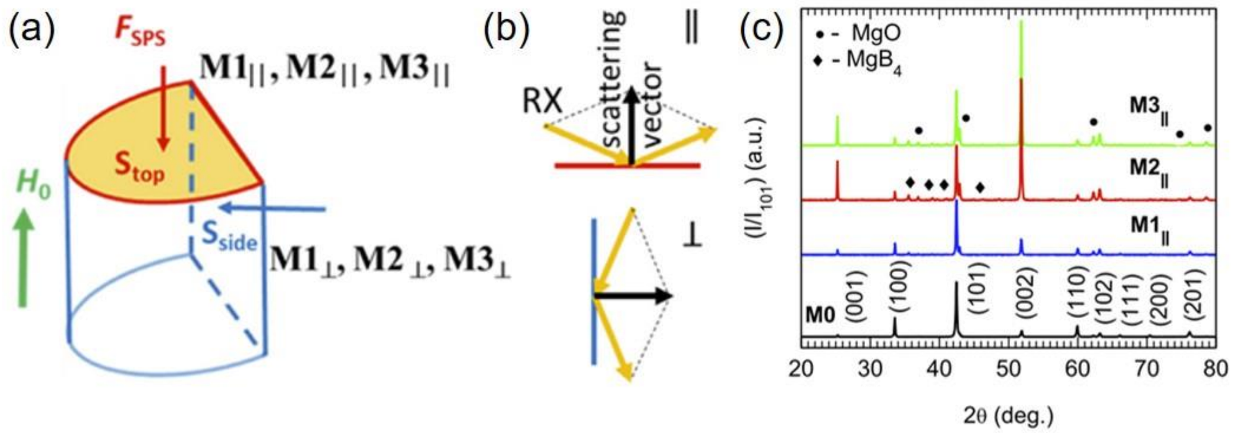

Fig. 1 (a, b) Schematic drawing (from ref. [4]) showing the as-prepared discs of MgB_2 by using slip casting under a high magnetic field H_0 = 12 T and subsequent spark plasma sintering (SPS); (c) XRD patterns on S_{top} of the samples M0 (raw powder of MgB_2), M1 (bulk sample, orientation degree 16.1 %, fabricated by SPS in vacuum), M2 (bulk sample, orientation degree of 40.5 %, fabricated by slip casting in 12 T and SPS in vacuum), and M3 (bulk sample, orientation degree of 39.6 %, fabricated by slip casting in 12 T and SPS in N_2). All bulk samples were prepared from MgB_2 raw powder processed under high energy ultrasound sonication (600 W). Note (00l) texture of MgB_2 phase (follow the lines labeled (hkl).

MgB_2 superconductor (SC) shows promising results as a key material for low-frequency magnetic-field passive-shielding. A cylinder and a cup were fabricated from machinable MgB_2 added with 10 wt. % hexagonal BN and shielding ability was investigated experimentally and by 3D numerical simulation for each indicated part or for a hybrid configuration with a ferromagnetic (FM) ring (Figure 3) [5]. Due to the small aspect-ratio of the SC parts, a strong decrease of the shielding capability emerges when the applied field is tilted away from to the shield's axis. The solution is to use a hybrid SC-FM configuration (excellent results are obtained for the cup) even when the external field is rotated by a few degrees away of the cup's axis.

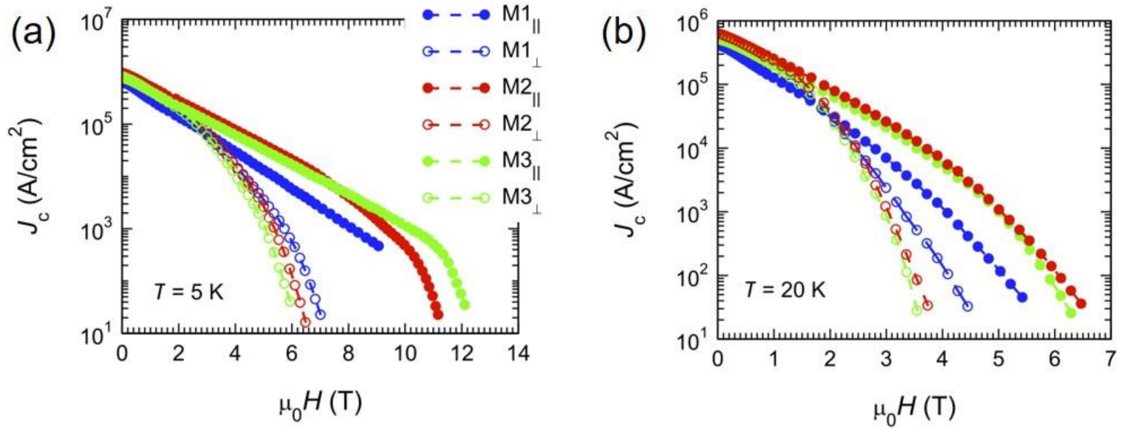

Fig. 2 Critical current density at (a) – 5K and at (b) – 20 K of samples M1-3 measured with applied field *H* parallel and perpendicular to Stop (see Fig. 1) (from ref. 4). Note higher values of J_c when the applied magnetic *H* is parallel to normal of S_{top} plane (see Fig. 1a).

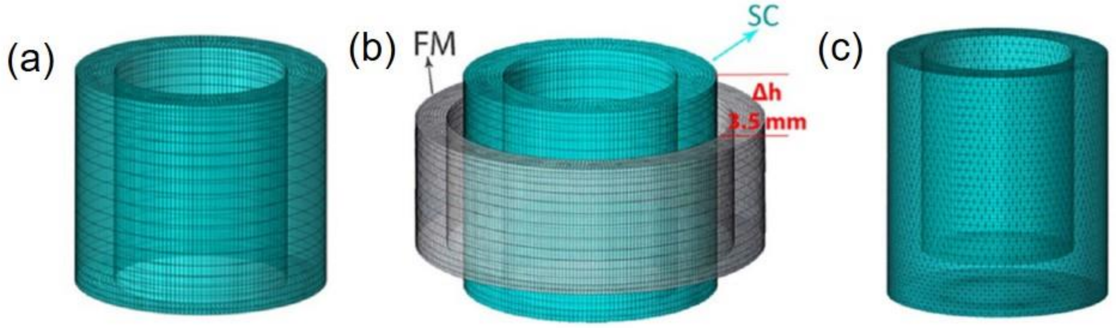

Fig. 3 (a)- superconducting tube; (b)- superconducting and ferromagnetic coaxially mounted tubes (hybrid shield); (c)- superconducting cup (from ref. 5).

References

1. P Badica, D Batalu, "Beyond superconductivity towards novel biomedical, energy, ecology, and heritage applications of MgB_2", *Green Chemistry Letters and Reviews 15*, 646–657 (2022).
2. V Sandu, GV Aldica, MA Grigoroscuta, M Burdusel, I Pasuk, YC Ching, AM Ionescu, P Badica, "Effect of polysilane addition on spark plasma sintering and superconducting properties of MgB_2 bulks" *Ceramics International* 48, 31914–31922 (2022).
3. AM Ionescu, GV Aldica, S Popa, M Enculescu, V Sandu, I Pasuk, M Burdusel, MA Grigoroscuta, L Miu, P Badica, "MgB_2 with addition of cubic BN and $Ge_2C_6H_{10}O_7$ obtained by spark plasma sintering technique", *Journal of Superconductivity and Novel Magnetism* 35, 3467–3476 (2022).
4. MA Grigoroscuta, GV Aldica, M Burdusel, V Sandu, A Kuncser, I Pasuk, AM Ionescu, TS Suzuki, O Vasylkiv, P Badica, "Towards high degree of *c*-axis orientation in MgB_2 bulks", *Journal of Magnesium and Alloys* 10, 2173–2184 (2022).
5. L Gozzelino, M Fracasso, M Solovyov, F Gömöry, A Napolitano, R Gerbaldo, G Ghigo, F Laviano, D Torsello, MA Grigoroscuta, GV Aldica, M Burdusel, P Badica, "Screening of magnetic fields by superconducting and hybrid shields with circular cross-section", *Superconductor Science and Technology* 35, 044002 (2022).

Nanosized Simple and Complex Hydrides for Advanced Solid-State Hydrogen Storage

Cezar Comănescu[a,b], **Petru Palade**[a], **Radu Cristian**[a]
[a]National Institute of Materials Physics, 405A Atomistilor, 077125 Magurele, Romania,
[b]Faculty of Physics, University of Bucharest, 405 Atomistilor, 077125 Magurele, Romania

The world energy crisis has affected mankind in many ways, ramping up the energy prices and nearing us even closer to the complete depletion of fossil fuels (coal, gas and oil), estimate to be all extinct by 2090. On one hand, replacement of fossil fuel may be a forced transition, but one that ensures a clean energy production while minimizing environment pollution and associated greenhouse effect. Simple metal hydrides and complex hydrides (borohydrides, alanates) have the potential to offer a safe, solid-state storage of hydrogen, with a theoretical gravimetric capacity exceeding DOE's target for 2025 (5.5 wt.%) [1–3]. A variety of hydrogen storage options exist, ranging from physisorption to chemisorption alternatives (Figure 1) [1]. While the theoretical hydrogen storage capacity is high (up to 20.7 wt.% for $Be(BH_4)_2$), very few of them are actually used as hydrogen storage materials.

Some important drawbacks must be overcome: high dehydrogenation enthalpies, high dehydrogenation temperature onset, slow dehydrogenation / rehydrogenation kinetics, and side-reactions occurring during a/d cycling, making complete rehydrogenation still elusive [1–3]. Various strategies for improvement of thermodynamic features of hydrides have been pursued [3]. With high structural versatility and high applicability potential, nanoporous materials can be tailored to accommodate suitably-sized compounds, such as metal hydrides. Among these porous materials, many examples have been explored recently as scaffolds: MOFs, carbon nanomaterials, graphene derivatives, MXenes, TM oxides, siloxanic materials, ordered mesoporous carbon OMC, metal scaffolds for microencapsulation (Mg, Al), polymers and nitrides (Figure 2) [3]. Machine learning was recently employed for predicting the hydrogen release of systems based on lithium borohydride $LiBH_4$.

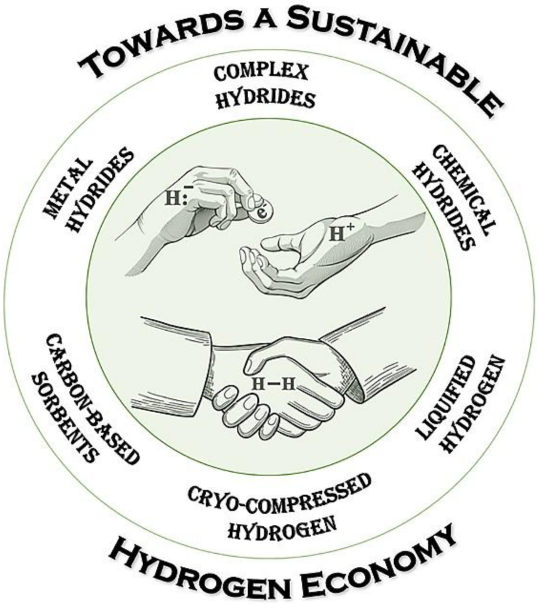

Fig. 1 Convergence of storage methods towards a sustainable hydrogen economy [1].

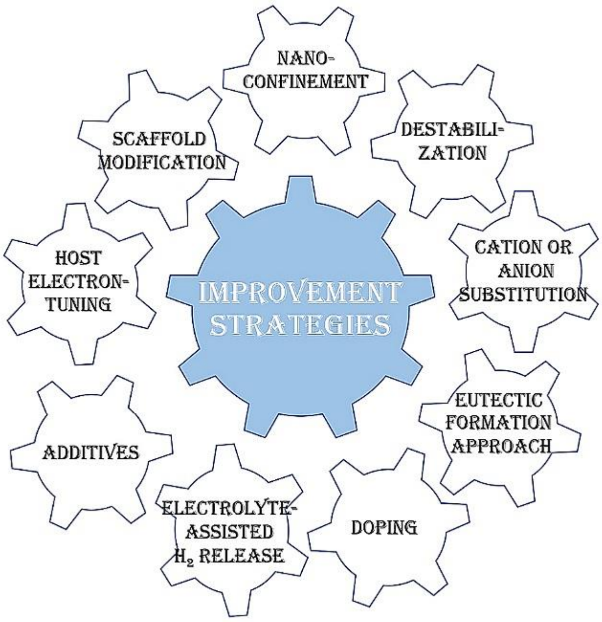

Fig. 2 Improvement avenues in hydride systems [3].

A recent report combines nanoconfinement strategy of $LiBH_4$ with ferrite additive compounding (MFe_2O_4, M=Co, Ni) [4]. Melt-impregnation of $LiBH_4$ in a ferrite-catalyzed nanosupport

MFe_2O_4@Graphene afforded an effective reduction in decomposition temperature, without altering the decomposition pathway. First group metal borohydrides are some of the most ionic and stable complex hydrides, but they are air- and moisture-sensitive, hence they must be handled under inert atmosphere (N_2/Ar), or nanoconfined in a support that would limit their exposure to atmosphere. The lightest borohydride, $LiBH_4$ has one of the highest gravimetric storage capacity (18.4 wt.%), however only 13.8 wt.% is accessible via thermal decomposition at ~400 °C in LiH, B and H_2 (reaction 1) [4].

$$\boldsymbol{o-LiBH_{4\,(s)} \xrightarrow{108-112°C} h-LiBH_{4\,(s)} \xrightarrow{275°C} LiBH_{4\,(l)} \xrightarrow{400-600°C} LiH_{(s)} + B_{(s)} + \frac{3}{2}H_2\uparrow} \qquad \text{(reaction 1)}$$

The reversibility of the system is not trivial: it requires extreme conditions (70–350-bar H_2, $t > 600$ °C) and will not proceed to completion, leading to continual decrease in hydrogen capacity with absorption/desorption cycling (reaction 2).

$$\boldsymbol{LiH_{(s)} + B_{(s)} + \frac{3}{2}H_2 \xrightarrow{690°C, 197.4\ atm\ H_2} LiBH_{4\,(s)}} \qquad \text{(reaction 2)}$$

In order to overcome the sluggish kinetics and high energetic barriers, five nanocomposites have been synthesized with 15 wt.% ferrite catalyst in the graphene support: (*i*) $LiBH_4$-graphene; (*ii*) $LiBH_4$-($NiFe_2O_4$/graphene catalyst heat treated in Ar flow); (*iii*) $LiBH_4$-($NiFe_2O_4$/graphene catalyst heat treated in H_2Ar flow); (*iv*) $LiBH_4$-($CoFe_2O_4$/graphene catalyst heat treated in Ar flow); (*v*) $LiBH_4$-($CoFe_2O_4$/graphene catalyst heat treated in H_2Ar flow) (Figure 3). It becomes apparent that thermal decomposition of metal salt precursors of corresponding metal ferrite catalysts follows a different course during treatment in Ar *vs* H_2/Ar, and the resulting active catalyst has subtle but clear influence on H_2 release activation energy. Figure 3 represents the X-ray diffractograms of $LiBH_4$ mixed with $CoFe_2O_4$ (CFO) and $NiFe_2O_4$ (NFO) catalysts supported on graphene (G). The samples were extracted after five cycles of hydrogen absorption/desorption being in final re-hydrogenated (absorbed) state. During measurements the samples were covered with polymeric foil in order to avoid oxidation. The dominant contribution from the XRD pattern belongs to graphene, however the presence of Li_3BO_3 peaks points out to a certain degree of surface oxidation.

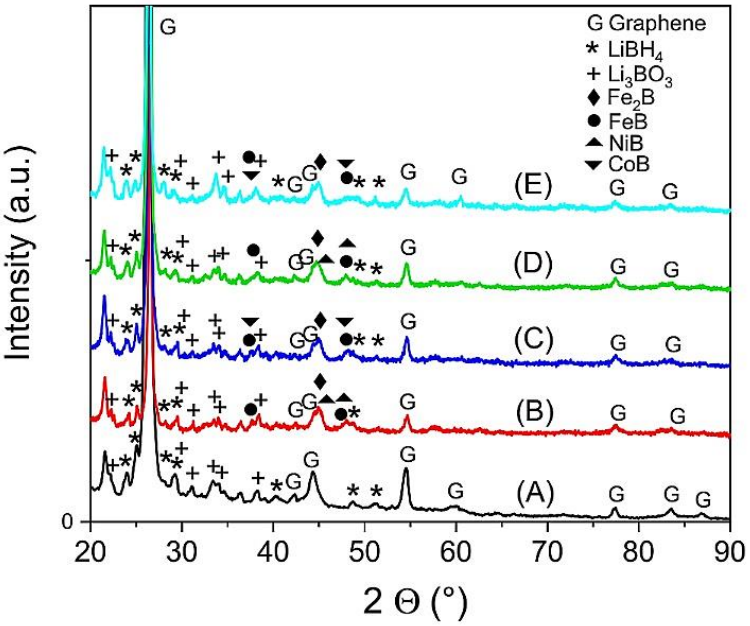

Fig. 3 X-ray diffraction data for synthesized mixtures of $LiBH_4$ with catalysts supported on graphene after re-hydrogenation: (A) $LiBH_4$-graphene, (B) $LiBH_4$-NFO-G-Ar, (C) $LiBH_4$-CFO-G-Ar, (D) $LiBH_4$-NFO-G-H_2Ar, (E) $LiBH_4$-CFO-G-H_2Ar [4].

One can observe that even though the first $LiBH_4$-G decomposition is the fastest among all samples, the same sample behaves worst after 5 a/d cycles. This confirmed the catalytic role of $NiFe_2O_4$ and $CoFe_2O_4$ addition to graphene, which improves the hydrogen desorption process. Hydrogen desorption with temperature ramp rate of 2 °C/min up to 450 °C was allowed longer time at the final temperature, to ensure complete nanocomposite dehydrogenation. (Figure 4).

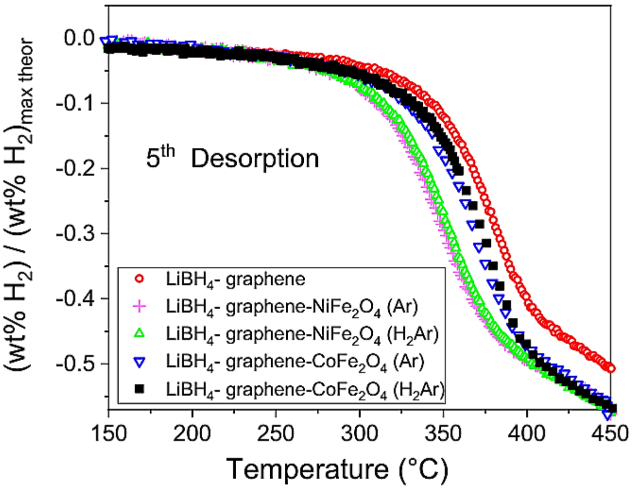

Fig. 4 Thermal programmed desorption (TPD) measurements with temperature ramp rate (2 °C/min) after 5 a/d cycles.

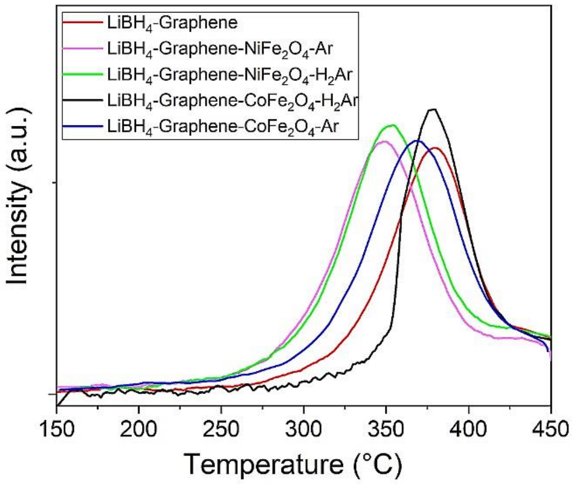

Fig. 5 Desorption peak temperature for samples: $LiBH_4$-graphene, $LiBH_4$-NFO-G-Ar, $LiBH_4$-CFOG-Ar, $LiBH_4$-NFO-G-H_2Ar, $LiBH_4$-CFO-G-H_2Ar [4].

The peak desorption temperatures were deduced from TPD measurements, after 5 a/d cycles, and the normalized released amount values corresponding to complete desorption at the final temperature of 450 °C showed improved behavior of $LiBH_4$-NFO-G-Ar. The desorption peak temperature is lower for $LiBH_4$-NFO sample compared with $LiBH_4$-CFO sample for catalysts treated both in Ar and H_2Ar flow (Figure 5).

This study highlights the evolution of catalyst phases during cycling, and confirms the positive role of boride species FeB, Fe_2B, NiB and CoB on the rehydrogenation process. The desorption temperature peak for $LiBH_4$-NFO-G-Ar (lithium borohydride mixed with $NiFe_2O_4$ supported on graphene heat treated in Ar flow) is the lowest among all samples, with a hydrogen desorption activation energy of 127 kJ/mol, significantly lower than that of bulk $LiBH_4$ (146 kJ/mol–170 kJ/mol, lit.), which again confirms the catalytic role of nanosized metal ferrites synthesized [4].

References

1. C Comanescu, “Complex metal borohydrides: From laboratory oddities to prime candidates in energy storage applications”, *Materials* 15, 2286 (2022).
2. C Comanescu, “Recent development in nanoconfined hydrides for energy storage”, *International Journal of Molecular Sciences* 23, 7111 (2022).
3. C Comanescu, “Paving the way to the fuel of the future - nanostructured complex hydrides”, *International Journal of Molecular Sciences* 24, 143 (2022).
4. P Palade, C Comanescu, C Radu, “Synthesis of nickel and cobalt ferrite – Doped graphene as efficient catalysts for improving the hydrogen storage kinetics of lithium borohydride”, *Materials* 16, 427 (2023).

Nanostructures and Heterostructures Based on $YBa_2Cu_3O_{7-x}$ Superconducting Films Grown by Pulsed Laser Deposition

Ion Ivan[a], Alina M. Ionescu[a], Claudiu Locovei[a,b], Melania Onea[a,b] Daniel N. Crisan[a], Andreea Andrei[c], Armando Galluzzi[d], Massimiliano Polichetti[d], Jesus Mosqueira[e], Soltan Soltan[f,g], Gisela Schütz[f], Joachim Albrecht[h], Adrian Crisan[a]

[a]National Institute of Materials Physics, 405A Atomistilor, 077125 Magurele, Romania
[b]Faculty of Physics, University of Bucharest, 405 Atomistilor, 077125 Magurele, Romania
[c]National Institute for Laser, Plasma & Radiation Physics, 409 Atomistilor, 077125 Magurele, Romania
[d]Department of Physics, University of Salerno, 132 Via Giovanni Paolo II, 84084 Fisciano, Italy
[e]Universidade de Santiago de Compostela, 15706 Santiago de Compostela, Spain
[f]Max Planck Institute for Intelligent Systems, 3 Heisenbergstraße, D-70569 Stuttgart, Germany
[g]Department of Physics, Faculty of Science, Helwan University, 11792 Cairo, Egypt
[h]Research Institute for Innovative Surfaces FINO, Aalen University, 1 Beethovenstraße, D-73430 Aalen, Germany

For high-field power applications of high-temperature $YBa_2Cu_3O_{7-x}$ (YBCO) superconductors, it became obvious in recent years that nano-engineered artificial pinning centers (APCs) are needed for increasing the critical current and pinning potential. As opposed to the artificial pinning centers obtained by irradiation with various particles, which is a quite expensive approach, we have studied superconducting samples having self-assembled defects, created during the sample fabrication, that act as effective pinning centers. A comprehensive review on various types of pinning centers in various superconductors, using various approaches and various architectures can be found in Ref. [1]. In addition, the search for ***magnetic*** APCs gave rise to various superconductor/ferromagnetic nanostructures and heterostructures hybrids. In brief, the nano-engineered superconducting films were grown by Pulsed Laser Deposition (PLD) on $SrTiO_3$ (STO) single-crystal substrates using a KrF excimer laser with 248 nm wavelength with pulse duration of 30 ns, repetition rate of 3–8 Hz, laser energy density of 0.7–1.7 J/cm^2, laser energy between 240 and 266 mJ, and target–substrate distance of 5–6 cm, in a PLD chamber with computer-controlled multi-target carousel allowing sequential depositions from several targets. As for the $CaRuO_3$/YBCO ferromagnetic/superconductor heterostructures, they were also grown by PLD, first 200 nm YBCO and then 130 nm CRO, with or without a 5 nm STO buffer layer. For a fast investigation of the pinning potential of APCs, we introduced a simple, straight-forward method of estimating the frequency-dependent critical current density by using AC susceptibility measurements, in fixed temperatures and DC magnetic fields at many fixed frequencies, from the positions of the maxima in the dependence of the out-of-phase susceptibility on the amplitude of AC excitation magnetic field. Frequency-dependent critical current density was estimated from the out-of-phase (imaginary) AC susceptibility χ'' response as function of the AC field amplitude h_{ac}, at fixed temperatures T (77 K and 65 K) and fixed applied DC magnetic fields H_{DC} (between 3 and 14 T, in steps of 1 T), measured on a *Quantum Design* Physical Properties Measurement System PPMS in $\mu_0 H_{DC}$ up to 14 T, AC field amplitude h_{ac} up to 16 Oe, and AC field frequency f between 47 and 9997 Hz. At a given temperature, for several H_{DC}, $\chi''(h_{ac})$ dependence may show a peak in the experimental window of our measurements, its position h^* representing the AC field of full penetration of the perturbation in the center of the sample, which can be correlated with the critical current density of the specimen: $J_c = h^*/\alpha d$, where d is the film thickness and α a constant around 0.9. In Figure 1 is shown an example of $\chi''(h_{ac})$ dependence for various AC field frequencies, at 77 K and 7 T (left), and, respectively, the frequency dependence of the critical current density (right-hand side), lines representing fits with various models.

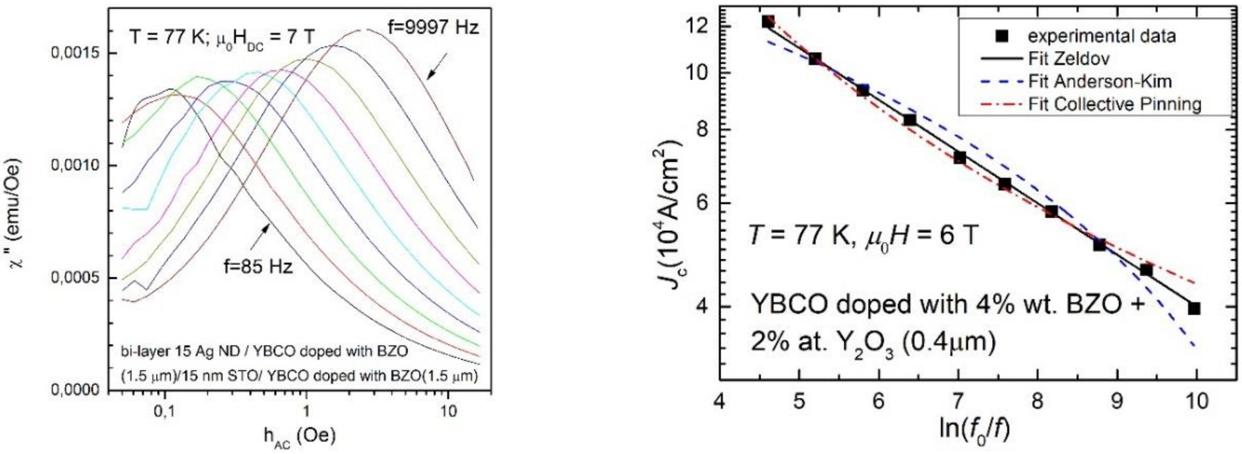

Fig. 1 AC field amplitude dependence of the out-of-phase susceptibility (*left*) and frequency dependence of the critical current density (*right*) for one of the studied nanostructures.

The data in the right-hand side of Figure 1 were analyzed in the framework of Kim-Anderson model (that predicts a linear dependence of the pinning potential on the probing current), and Collective Pinning model (that predicts a power law dependence of the pinning potential on the probing current), which are the two most used classical models of pinning. However, as can be seen in the figure, our experimental data are better described by using a logarithmic dependence of the pinning potential on the probing current, proposed by Zeldov, which we have shown [2] to lead to a linear dependence of the experimental data in the double-logarithmic plot in Figure 1. Furthermore, we completed the theoretical approach [2] to relate the slope b in the fit (black full line) in Figure 1 with the pinning potential $U_0 = k_B T(1+1/b)$.

Similar excellent fits were obtained for all the investigated samples (See ref. 2), and in all DC fields where the maxima in $\chi''(h_{ac})$ could be registered (please note that the maximum AC field amplitude in our equipment is 16 Oe). Figure 2 shows such dependencies for two of the investigated samples, in DC field amplitudes for which our experimental window allows the recording of maxima in $\chi''(h_{ac})$ for at least 6-7 frequencies.

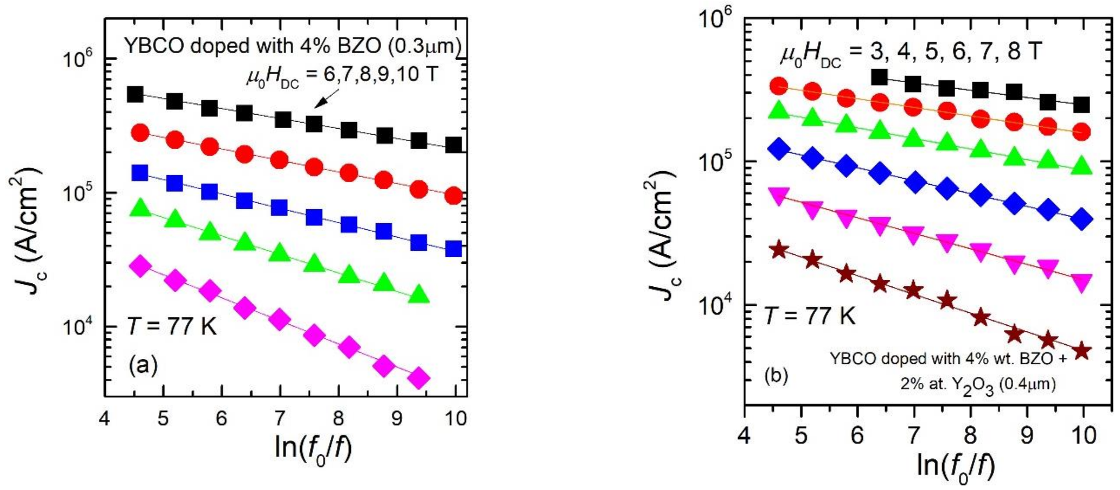

Fig. 2 Frequency dependence of the critical current density of the two samples (YBCO doped with 4 wt.% BZO – *left* & YBCO doped with 4 wt.% BZO + 2 at.% Y_2O_3 – *right*), at 77 K in DC magnetic fields. All the dependences are very well-described by straight lines in the double-logarithmic plot.

In this work we have investigated 6 samples, with various types of APCs, and in all cases the results were also well described by our model. In all cases, from the slopes b, we determined the pinning potentials $U_0(H_{DC}) = k_B T(1+1/b)$, in K ($k_B = 1$), which are between 750 K in 3 T and 150 K in larger fields, at 77 K, and sample-dependent (due to different thickness, APCs material(s), various nanostructuring architecture and technique), as can be seen in Figure 3.

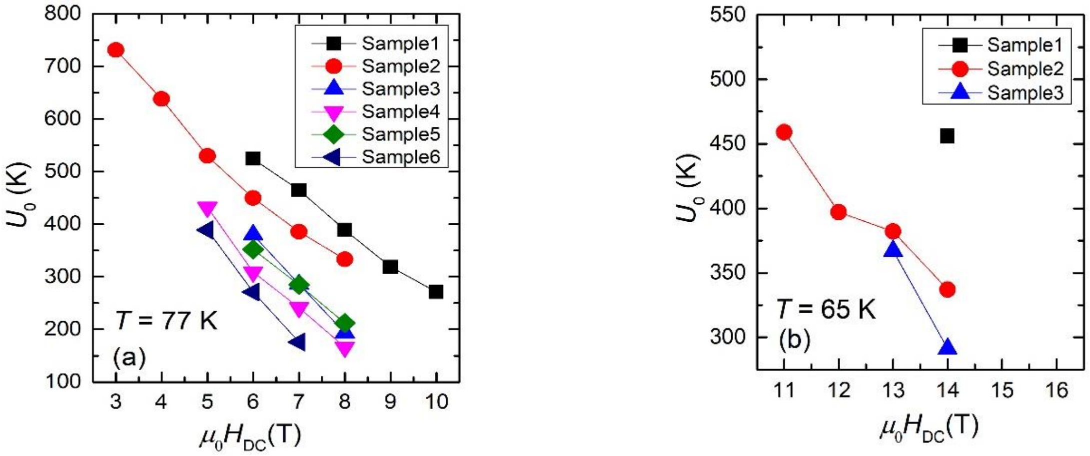

Fig. 3 Estimated values of the pinning potentials $U_0(H_{DC})$, in K ($k_B = 1$), at (a) 77 K and (b) 65 K.

As for the CRO/YBCO ferromagnetic/superconductor hybrid, the influence of CRO on YBCO and vice versa has been studied by SQUID magnetometry [3]. Detailed measurements of the magnetic moment of the heterostructures as a function of temperature, magnetic field and relaxation time have been performed. A large ferromagnetic signal has been found in case of direct deposition of CRO on YBCO, while in case of layers separated by the STO buffer, the magnetization is reduced. Furthermore, we observe a strong suppression of superconductivity after the direct deposition of the CRO film. A subsequent oxidation process shows that the superconducting properties are partially recovered, most likely due to an efficient oxygen diffusion through the STO barrier. The materials´ structure has been investigated by XRD analysis, which identified the mechanical strain to be the origin for the formation of a ferromagnetic state in CRO. The highest magnetization has been obtained when the thin layer CRO layer was deposited directly on YBCO, without further oxygenation. Although CRO proved to be not suitable as magnetic pinning center for increasing the critical current density, such hybrid heterostructures can find useful applications in hybrid spintronic devices.

References

1. P Mele, A Crisan, MI Adam, "Pinning-engineered $YBa_2Cu_3O_x$ thin films", in: *Vortices and Nanostructured Superconductors*; Adrian Crisan Ed., Springer: Berlin/Heidelberg, Germany, 15–63 (2017).
2. I Ivan, AM Ionescu, DN Crisan, A Andrei, A Galluzzi, M Polichetti, J Mosqueira, A Crisan, "Pinning potential of the self-assembled artificial pinning centres in nanostructured $YBa_2Cu_3O_{7-x}$ superconducting films", *Nanomaterials* 12, 1713 (2022).
3. AM Ionescu, I Ivan, C Locovei, M Onea, A Crisan, S Soltan, G Schütz, J Albrecht, "Ferromagnetism and superconductivity in $CaRuO_3$/$YBa_2Cu_3O_{7-\delta}$ heterostructures", *Materials* 15, 2345 (2022).

Pinning Potential in Highly Performant $CaKFe_4As_4$ Superconductor

Alina M. Ionescu[a], Ion Ivan[a], Daniel N. Crisan[a], Armando Galluzzi[b], Massimiliano Polichetti[b], Shigeyuki Ishida[c], Akira Iyo[c], Hiroshi Eisaki[c], Adrian Crisan[a]
[a]National Institute of Materials Physics, 405A Atomistilor Str., 077125 Magurele, Romania
[b]Department of Physics "E.R. Caianiello", University of Salerno, 132Via Giovanni Paolo II, , 84084 Fisciano, Italy
[c]Research Institute for Advanced Electronics and Photonics, National Institute of Advanced Industrial Science and Technology (AIST), 1-1-1 Umezono, Tsukuba, Ibaraki 305-8568, Japan

Among the newly-discovered iron-based superconductors (IBS), superconductors based on $AEFe_2As_2$ (AE being alkali-earth metal Ca, Sr, Ba) parent compound, the so-called 122 system, became the most popular materials for both physical explorations and wire applications because of their T_c as high as 38 K, very high upper critical fields μ_0H_{c2} (> 70 T) and low anisotropies γ (<2), attracting substantial attention in comparison with other IBSs that have been reported in the literature. Superconductivity in $AEFe_2As_2$ is primarily induced by alkali metal (A = Na, K, Rb, Cs) substitution at AE sites. More recently, a new type of IBSs has been reported, having a new structure, abbreviated as AEA1144, namely $CaAFe_4As_4$ (A = K, Rb, Cs) and $SrAFe_4As_4$ (A = Rb, Cs). In these cases, because A does not mix with AE due to the large difference in atomic radii, AEA1144 crystallizes through alternate stacking of the AE and A layers across the Fe_2As_2 layer, changing the space group from *I4/mmm* to *P/4 mmm*, the compounds being superconductors with T_c values between 31 and 36 K. The most studied compound in this new type of IBS is $CaKFe_4As_4$ (CaK1144) due to its excellent superconducting properties. From the point of view of potential applications, the behavior of the critical current density, and the structure and type of defects that act as effective pinning centers in high magnetic fields are of paramount importance.

Up until now, the strength of the various types of pinning centers, which are responsible for the excellent properties of this new material in terms of critical current density and very steep irreversibility line (crucial for high-field applications) were studied as bulk pinning force from DC magnetic hysteresis loops. In this work [1], we investigated the pinning potential of the nanoscale defects (pinning centers) in CaK1144 single crystals from magnetic relaxation measurements.

$CaKFe_4As_4$ single crystals were synthesized via the self-flux method using FeAs, and the samples used in this study are thin square discs, having the typical dimensions $a \approx 1.2$ mm, $b \approx 1.2$ mm and $c \approx 0.04$ mm. Standard (zero-field cooling, ZFC) DC magnetic hysteresis curves and the magnetization relaxation were registered with a commercial Quantum Design Magnetic Property Measurement System (MPMS). Well below T_c and above the field for the first full vortex penetration (in increasing H), or at any H in decreasing field, the irreversible magnetic moment is identified with the measured moment m. In all the experiments reported here, the DC applied field is parallel to the c-axis (perpendicular to the largest plane a-b) of the single crystal.

It is now well established that the use of DC magnetic relaxation measurements can provide very useful information regarding the type of vortex creep (elastic or plastic), the pinning potential (activation energy), and the vortex creep exponent p in the current density J dependence of the pinning potential. The vortex exponent has well established theoretical values for various collective (elastic) vortex creep regimes: 1/7 in the single vortex collective creep domain, 3/2 or 5/2 in the case of the creep of small vortex bundles, and 7/9 for large vortex bundles. In a disordered vortex phase the creep process involves plastic vortex deformations, and p is negative ($p = -0.5$ for dislocation-mediated plastic creep). The DC magnetic relaxation results are well described in terms of thermally activated flux creep. After the application of a DC external magnetic field H, with the parameterization of the pinning potential U and the general vortex creep relation, the $U[J(t), T]$ dependence is expressed as

$$U[J(t), T] = (U_c/p)[(J_{c0}/J)^p - 1] = T\ln(t/t_0), \quad (1)$$

where $U_c(T)$ is a characteristic pinning energy, $J_{c0}(T)$ is the creep-free critical current density, and t_0 is the macroscopic time scale for creep ($\sim 10^{-6} - 1$ s), varying weakly with $J(t)$. The analysis is simplified by determining a normalized relaxation rate $S = -d\ln(|m_{\mathrm{irr}}|)/d\ln(t) = -d\ln(J)/d\ln(t)$ and the corresponding normalized pinning potential $U^* = T/S$. At constant H and T, when the overall J relaxation is not pronounced, p and t_0 can be considered constant, leading to

$$U^*(J) = U_{\mathrm{c}}(J_{\mathrm{c0}}/J)^p = U_{\mathrm{c}}(|m_0|/|m_{\mathrm{irr}}|)^p. \qquad (2)$$

With the above relations, one obtains $U^* = U_{\mathrm{c}} + pT\ln(t/t_0)$. For a fixed, moderate, window time for averaging t_{w}, $\ln(t/t_0) \sim \ln(t_{\mathrm{w}}/t_0) \sim$ constant, resulting in $U^*(T) \sim U_{\mathrm{c}} + pT\ln(t_{\mathrm{w}}/t_0)$,
where U_{c} for collective (elastic) pinning is lower than the characteristic pinning energy for plastic pinning (when the pinning structure accommodates vortices). The creep exponent can be accurately determined from magnetic relaxation and Eq. (2), with the assumption that $\ln(U_{\mathrm{c}})$ and $\ln(J_{\mathrm{c0}})$ are weakly temperature dependent, which is true for a relatively large T interval at fixed DC fields. From the magnetization relaxation measurements, we have estimated the values of S at various temperatures, in the three applied DC fields, which are shown in Figure 1a, while the temperature dependence of the normalized pinning potential $U^* = T/S$ is shown in Figure 1b.

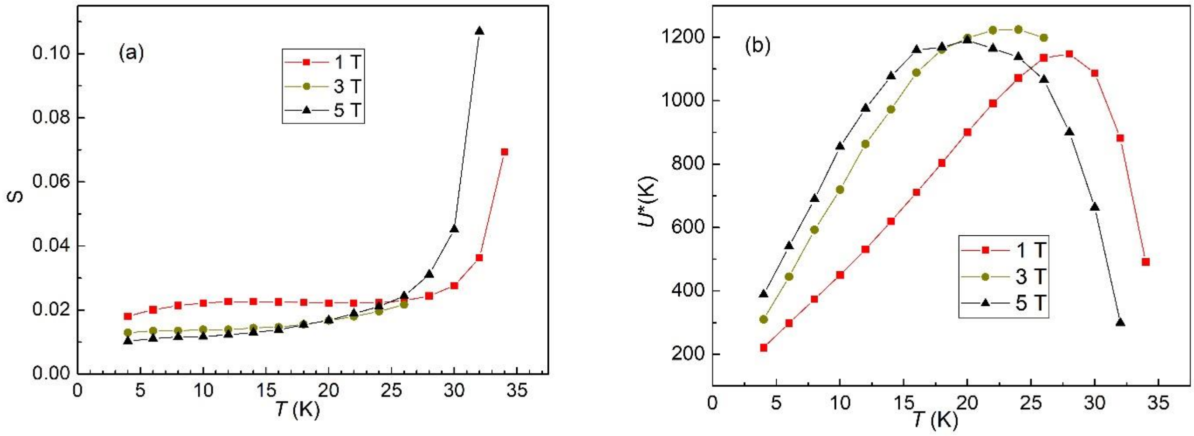

Fig. 1 Temperature dependence (a) of the normalized relaxation rate $S = -\mathrm{d}\ln(|m|)/\mathrm{d}\ln(t)$; and (b) of the normalized pinning potential $U^* = T/S$.

As can be seen in Figure 1b the temperature dependence of the normalized pinning potential has a maximum that separates the elastic creep at lower temperatures from plastic creep at higher temperatures, situated between 28 K in 1 T and 20 K in 5 T, which is very important in respect with practical applications in high magnetic fields at liquid hydrogen temperatures (20 K) in the future hydrogen economy. Another important issue is the very high values of U^*, up to 1200 K at peak position. Considering that the vortex creep is in principle a thermally-activated Arrhenius process, the probability of a thermally-activated flux jump (flux creep) out of the potential well associated with the pinning centers is inversely-proportional to the exponential of U^*/T (U^* in K, $k_{\mathrm{B}}=1$), which, for 5 T at 20 K (where $U^* \approx 1200$ K), is $\exp(-1200/20) = \exp(-60) \approx 9\times10^{-27}$, an extremely low value. For the lower values of U^* (between 200 and 400 K at lowest temperature of 4 K, liquid helium temperature, the above-mentioned probabilities are $\exp(-200/4) = \exp(-25) \approx 10^{-11}$, and, respectively, $\exp(-400/4) = \exp(-100) \approx 4\times10^{-44}$.

When a large current is passed through the superconductor in an applied magnetic field the resulting Lorentz force induces flux movement. It is clear that this is the case for high-field applications, and, consequently, the dependence of the pinning potential due to variation of current (at given applied fields) is very important. Eq. (2), which represents the pinning potential at fixed temperature and magnetic field as function of the current density $J \propto |m|$, allows the estimation of the creep exponent p. Making use of the experimental data for each temperature and field and of Eq. (2) rewritten as $\ln(U^*) = p[\ln(1/|m_{\mathrm{irr}}|) + const]$, the plot $\ln(U^*)$ *vs* $\ln(1/|m_{\mathrm{av}}|) = \ln(1/J_{\mathrm{av}})$, shown in Figure 2, provides the needed information regarding the dependence of the normalized vortex creep activation energy (pinning potential) on the current density, in various DC magnetic fields and reveals a crossover between elastic creep (left-hand side of the graph) and plastic creep (right-hand side). As can be seen from eq. (2), the slopes in Figure 2 (where $\ln(U^*)$ *vs* $\ln(1/|m_{av}|)$ dependence is linear) represent the vortex creep exponent *p*, which is positive for elastic creep and negative for plastic creep (– 0.35 in 1 T, – 0.54 in 5 T, in good agreement with theoretical predictions $p = -0.5$ for dislocation-mediated plastic creep).

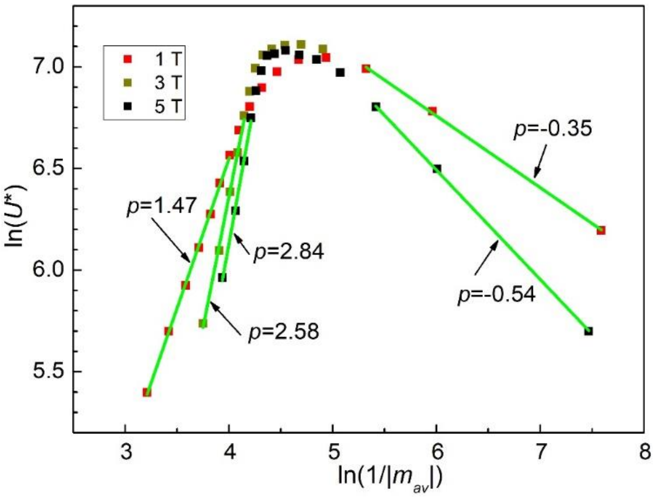

Fig. 2 Dependence of the normalized pinning potential U^* on the inverse of irreversible magnetization averaged over t_w, in double logarithmic plot, for the three DC magnetic fields indicated in the figure. The slopes of the straight lines in the figure represent the vortex creep exponent *p* in eq. (2).

The values of the vortex creep exponents in the elastic creep regime are also in striking agreement with theoretical predictions: in 1 T $p = 1.47$ is practically 3/2 as predicted by the elastic creep of small vortex bundles, while in higher fields, 3 and 5 T, *p* values of 2.58 and, respectively, 2.84 are comparable with the theoretical prediction from the elastic manifold theory in the small vortex bundle creep regime $p = 5/2$.

References

1. AM Ionescu, I Ivan, DN Crisan, A Galluzzi, M Polichetti, S Ishida, A Iyo, H Eisaki, A. Crisan, “Pinning potential in highly performant $CaKFe_4As_4$ superconductor from DC magnetic relaxation and AC multi-frequency susceptibility studies”, *Scientific Reports* 12, 19132 (2022).

Phase Evolution, Temperature- and Gas-Driven Effects in Multiple Phase Alloys and Films

Alina D. Crisan[a], Nirina Randrianantoandro[b], Valentina Mihalache[a], Iuliana Pasuk[a], Ionel Mercioniu[a], Ovidiu Crisan[a]
[a]National Institute of Materials Physics, 405A Atomistilor, 077125 Magurele, Romania
[b]Institut des Molécules et Matériaux du Mans, Université du Maine, 72085 Le Mans, France

The temperature-driven effects in alloys and films are illustrated by a couple of examples where it can be seen that drastic change or improvement of magnetic or electronic performances can be expected under influence of external conditions. First example is the hard-ternary compounds of Cr-Al-C [1], under scrutiny for their amazing property of being both of ceramic and of metallic character in the same time. In order to analyze the formation of phases of interest and their evolution with temperature, thin films of the proper Cr_2AlC composition were subjected to Raman analysis under the two laser irradiation regimes: low laser power (LLPD – 2.5 to 4 mW/cm^2) and high laser power (HLPD – 4 mW/cm^2). The Raman scattering spectra have been recorded between 120 – 2000 cm^{-1} for 30 min (Figure 1). It is known that the Cr-Al-C phase structure can be assigned to the D46h space group, presenting 4 optical modes, 3 being Raman-active, while the fourth is both infrared-active and Raman-active.

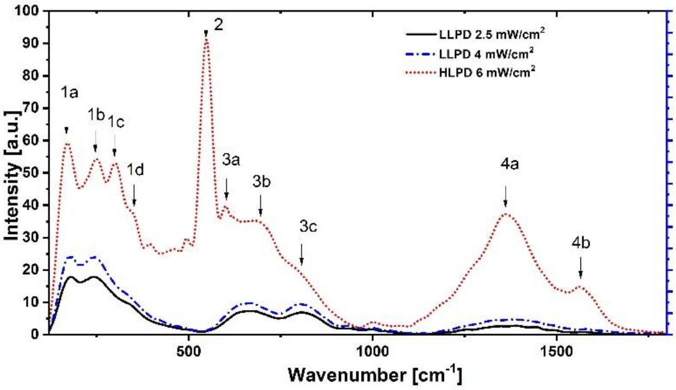

Fig.1 Raman spectra of Cr-Al-C film under low (LLPD) and high (HLPD) laser irradiation regime.

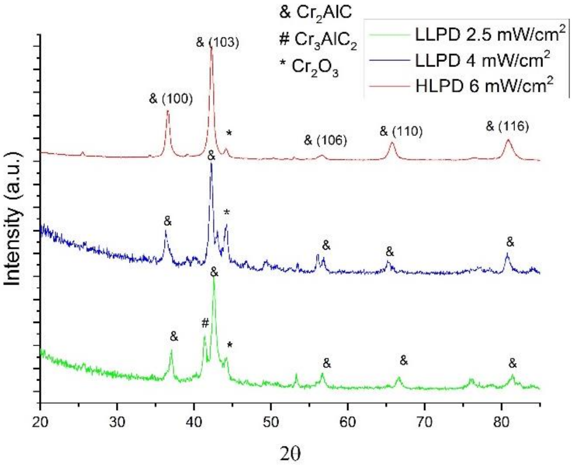

Fig.2 XRD patterns of Cr-Al-C film after low (LLPD) and high (HLPD) laser irradiation regime.

We discovered thus that the Raman spectrum can be separated into 3 spectral regions: the low (0 – 500 cm^{-1}), the intermediate (500 – 1000 cm^{-1}) and the high (1000 – 1800 cm^{-1}) regions. It is worthwhile noting that in the previous literature, not more than only one or two of these regions are customarily investigated, therefore our study is the first one presenting such a large Raman range. It has been shown that the low spectral region encompasses Raman peaks that are attributable to M_2AX phases. Since 211 structures have as parent the $D_{46}{}^{h}$ space group, the three optic modes, Raman-active, are due to A_g+2E_{2g} levels and the fourth infrared and Raman-active is due to E_g level. These 4 peaks are denoted in the Figure.1 as *1a* to *1d* peaks. It can be seen that the low spectral region has some large, convoluted Raman peaks in the case of the LLPD recorded spectra, very large but with smaller intensity Raman peaks in the intermediate spectral region, and almost no Raman peaks in the high spectral region. This aspect is drastically changed in the case of the HLPD Raman experiment at 6 mW/cm^2. In this case, much more intense and sharp Raman peaks are observed. The sharp peaks observed in the low spectral region have larger intensities than in the case of LLPD mode and they are sharper. The presence of these peaks appearing in the low spectral region, labelled *1a-1d* peaks, constitute the signature of the occurrence of the crystalline MAX phases. In the intermediate spectral region for wavenumbers between 500 and 1000 cm^{-1}, MAX phase materials show customarily two broader peaks of lower intensity, labelled *3a-3b*. Apart these modes, a very intense peak appears at cca. 548 cm^{-1}. In agreement with the other work [2] this quite intense and sharp peak has been assigned to the occurrence of chromium oxides, notably Cr_2O_3. The high spectral region shows quite intense and very broad Raman peaks that are attributed to the D- and G-bands of carbon, typical for carbon bonding in nanocrystalline alloys. This temperature-driven effect induced by the laser irradiation of the Cr-Al-C film, of inducing the presence of MAX phases embedded into carbon-rich disordered phase has been documented for the first time and has been confirmed by XRD analysis (Figure 2). The XRD of the LLPD at 2.5 and 4 mW/cm^2 sample present formation of a mostly crystalline pattern, as proven by quite well-formed, sharp and intense Bragg peaks. Here, most of the identified Bragg peaks have been assigned to the hexagonal Cr_2AlC phase, except for few low intensity satellite lines. The XRD pattern for the HLPD at 6 mW/cm^2 sample is however different. Here the Bragg lines are better defined and narrower, moreover all the other satellite peaks not belonging to the main 211 M_2AX phase have disappeared. Exception makes the small Bragg peak attributable to the hexagonal Cr_2O_3 phase. The existence of the chromium oxide Bragg peak in the XRD pattern confirms well the results obtained in the Raman analysis.

Another temperature-driven effect on the phase evolution in alloys has been documented in [3]. Here, it has been shown that in the case of Fe-Pt-Nb-B alloys. The magnetic behavior of the annealed samples evolves with increasing the annealing temperature (Figure 3), its property being governed by the competing role between anisotropy energy and the exchange coupling between grains. The coercive field has been shown to exhibit a maximum for the annealing at 700 °C (Figure 4), which in turns proves to be optimal annealing temperature for acquiring good magnetic properties correlated with well refined nanocrystalline structure.

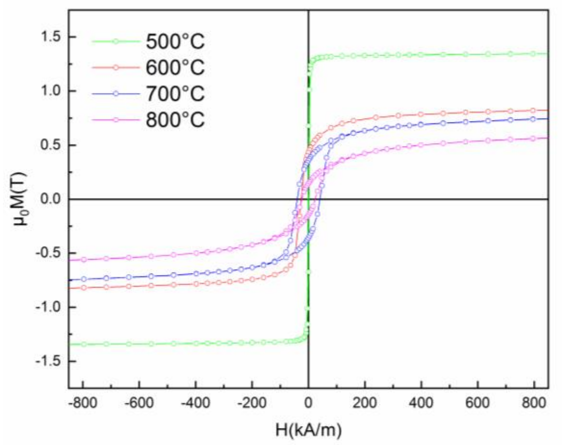

Fig. 3 Hysteresis loops of annealed Fe-Pt-Nb-B sample.

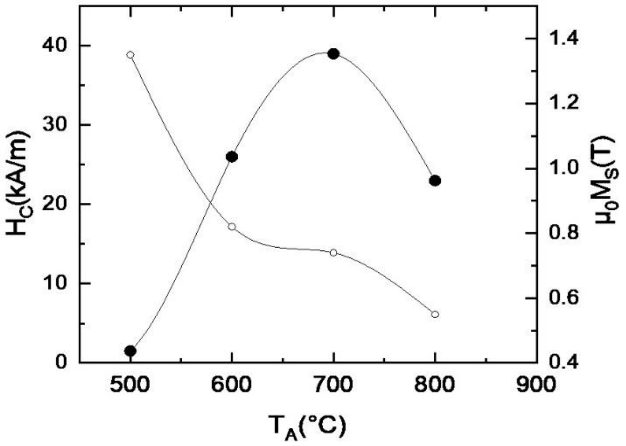

Fig. 4 Coercivity and saturation vs annealing T.

The temperature-driven effect is even more compelling when detailing the Mössbauer results (Figure 5). The Mössbauer spectrum for the as-cast sample, top graphs in Figure 5, recorded at 77 K, exhibit broad magnetic sextets, typical of distributed Fe environments encountered in Fe-rich amorphous ribbons. The hyperfine field B_{hf} distributions derived from the fitting of the Mössbauer spectra show a bimodal-type feature, typical for disordered Fe environment encountered in amorphous-like alloys, with two main chemical environments for Fe. It has been shown that the annealing at 500 °C to 600 °C promotes formation of two main metastable nanocrystalline phases: fcc A1 (FePt-based) and FeB-rich phase in the primary crystallization stage, dominated by nucleation of crystallites. Further annealing at 700 °C and 800 °C promotes formation of fcc Fe_3Pt and fct Fe_2B crystalline phases, in the secondary crystallization stage, dominated by grain growth processes and poly-crystals formation, as determined from the fitting. A surprising para to ferromagnetic transition has been observed for the fcc A1 disordered FePt-based phase, this phase being proven to be paramagnetic at 300 K and ferromagnetic at 77 K.

A third example is that of the gas-driven effects recorded in the mechanically alloyed $Fe_{14}Cr$ alloys [4]. Nano-nitride reinforcement of Fe–Cr alloys are under intense investigations, since it can produce materials for nuclear energy applications. Here, the structural and magnetic characterization has proven that the ferrite that has been supersaturated with nitrogen during the mechanical alloying shows a strong decrease in grain size and saturation magnetization, an increase in lattice parameters, its microstrain as well as in its coercive field. These improvements have been associated with features of discontinuous precipitation reaction of coherent nitride precipitates, involving a new α”-phase within the expanded lattice, as a result of the temperature-driven effect in the austenite phase field. Such microstructure refinement accompanied by gas-driven effect represented by the supersaturation with nitrogen produces thus a strengthening of $Fe_{14}Cr$ alloys which can be achieved on powders milled for much less time as compared to previously reported strengthening of $Fe_{14}Cr$–W–Ti ferritic steels.

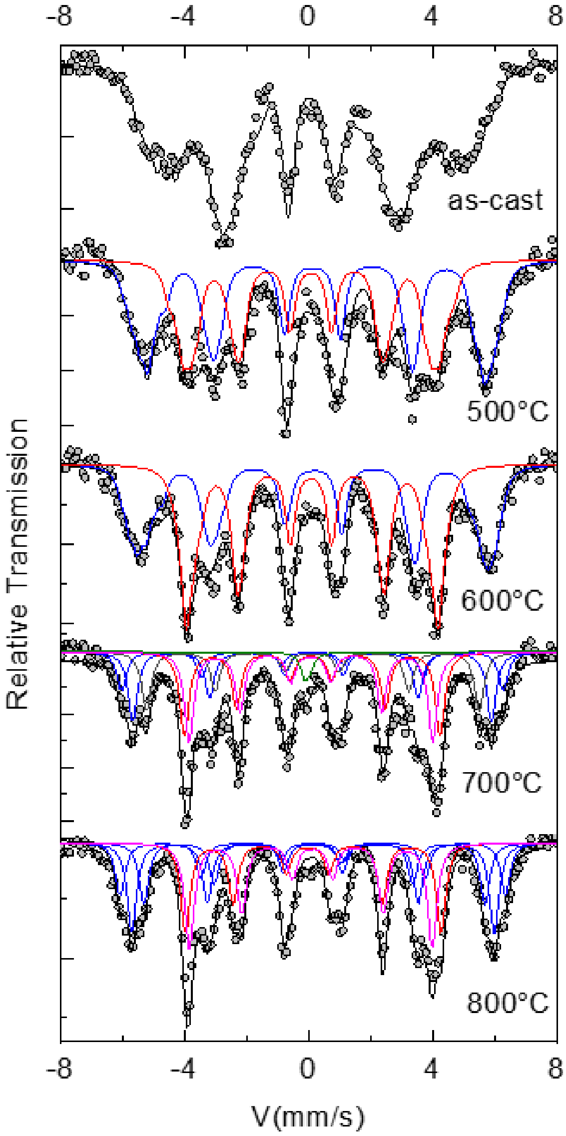

Fig. 5 300 K Mössbauer spectra of annealed samples.

References

1. O Crisan, AD Crisan, “Microcrystallization effects induced by laser annealing in Cr-Al-C ion-beam-sputtered films”, *Nanomaterials* 12, 4136 (2022).
2. AD Crisan, O Crisan, “Morpho-structural investigations and carbon nanoclustering effects in Cr-Al-C intermetallic alloys”, *Nanomaterials* 12, 3225(2022).
3. O Crisan, AD Crisan, N Randrianantoandro, “Temperature-dependent phase evolution in FePt-based nanocomposite multiple-phased alloys”, *Nanomaterials* 12, 4122 (2022).
4. V Mihalache, I Pasuk, I Mercioniu, “Effect of the supersaturation with nitrogen on the structure refinement and magnetic properties of mechanically alloyed and heated $Fe_{14}Cr$ ferritic alloys”, *Journal of Materials Research and Technology* 20, 2293–2308 (2022).

Tuning Types of Magnetic Order and Magnetic Anisotropies by Induced Organization of Magnetic Nanoclusters

Victor Kuncser[a], Claudiu Locovei[a], Anda-Elena Stanciu[a], Bogdana Borca[a], Andrei Kuncser[a], Nicusor Iacob[a], Cristian Radu[a], Aurel Leca[a], Gabriel Schinteie[a]
[a]National Institute of Materials Physics, 405A Atomistilor, 077125 Magurele, Romania

Most of the modern spintronic applications demand nanosized systems in the form of thin films and multilayers, nanowires and nanoparticles, that should satisfy several conditions regarding the magnetic properties and magnetic anisotropy. Tuning the magnetic anisotropy can be achieved via a series of different preparation methods and conditions. However, both the magnetic dimensionality and magnetic anisotropy can be even more widely tuned by assembling simple magnetic nanoentities under different morphological configurations. In this regard, the simplest unit is the magnetic nanoparticle. Finding a way to induce the desired auto-organization of magnetic nanoparticles, which in addition can be formed under different shapes (spherical, ellipsoidal, cubic etc.), would be an important achievement to control the magnetic properties of the system with respect to envisaged high technological applications. The organization of the magnetic entities can take place either in a fluid media or in a solid matrix. In the first case, specific ferrofluids can be formed with wide applications from civil engineering to bio-medicine [1]. In the second case, the matrix can not only intermediate the magnetic interactions among the clusters, but also influence their shape and configuration. In turn, the auto-organization of the clusters can change the crystalline structure of the hosting matrix. Two examples will be presented in the following on the way that the organization of magnetic nanoclusters inside the thickness of a metallic film or on the surface of a metallic film can lead to a large variety of magnetic dimensionalities and types of the magnetic anisotropy in the overall complex system.

The first example deals with the organization of Fe nanoclusters in the hosting Au matrix of a thin Au_xFe_{1-x} thin film [2].

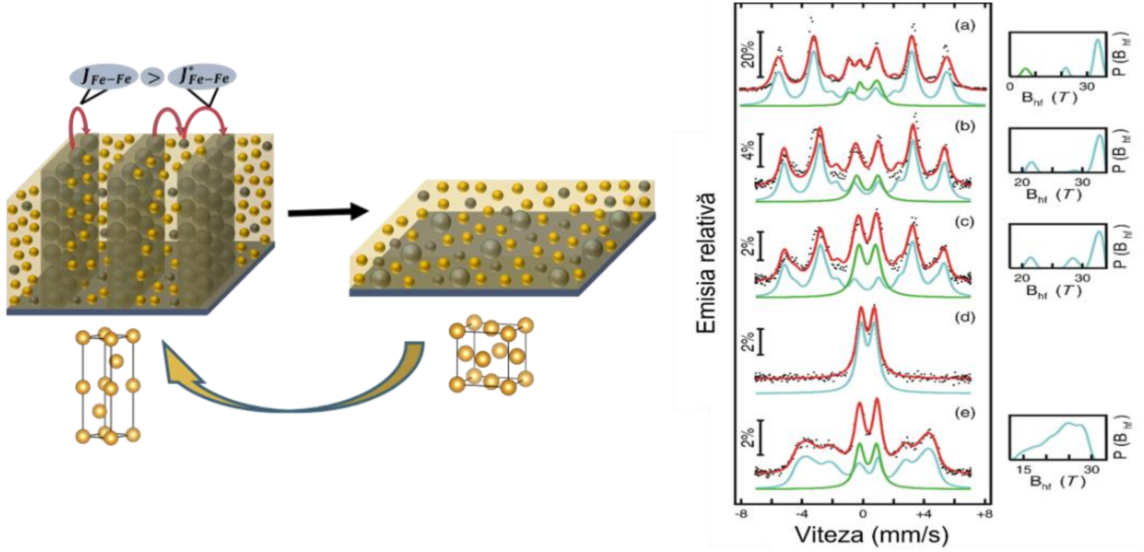

Fig. 1 Representation of the lamellar organization of Fe clusters (gray spheroids) in the Au matrix. By decreasing the film thickness toward the cluster diameter, a more disordered filiform-like organization of the magnetic clusters is obtained. On the right hand are represented the room temperature 57Fe CEM spectra which prove the formation of metallic Fe clusters which strongly interact inside the lamellar structure as well as the inert-lamellar superparamagnetic clusters with thickness (b,c,d) and concentration (a,b,e) dependent relative spectral area contributions.

Au_xFe_{1-x} nanophase thin films with compositions ranging from x = 20 to x = 80 at. % and thicknesses ranging from 6 to 70 nm were obtained by co-deposition magnetron sputtering and further investigated with respect to their morpho-structural and magnetic properties by X-ray Diffraction, cross-section Transmission Electron Microscopy, Selected Area Electron Diffraction, Magneto Optical Kerr Effect, Superconducting Quantum Interference Device magnetometry and Conversion Electron Mössbauer Spectroscopy. It was proven that depending on the preparation conditions, different configurations of defect α-Fe magnetic clusters (about 4 nm in diameter), i.e., randomly distributed or auto-assembled in lamellar or filiform configurations, can be formed in the Au matrix. A close relationship between the Fe clustering process and the type of the crystalline structure of the Au matrix was underlined, with the stabilization of the unusual hexagonal phase (hcp 4H) at a composition close to 70 at. % of Au, where thickness dependent lamellar configurations of the Fe clusters perpendicular to the film plane are formed (Figure 1). However, always a small fraction of Fe clusters of similar size are randomly distributed in between the formed lamellar structures and mediate the inter-lamellar magnetic interactions between clusters. A competition between the inter-lamellar and intra-lamellar interaction is achieved at low temperature, leading to a dominant 3D Ising type magnetic structure in case of the 70 nm thick film. Here, more fragmented lamellar structures are formed, with all the 3 components of the exchange integral present and only one spin component, due to the orientation of the Fe macro-spin along the lamella length. A 2D Ising type magnetic structure is achieved at low temperature for the 17 nm thick film, due to the formation of the lamellar structure accompanied by a higher fraction of inter-lamellar clusters which behave superparamagnetic, as evidenced by magnetic measurements. 2D Ising type magnetic structures are evidenced at room temperature for both films by vectorial MOKE magnetometry, with the best formed uniaxial anisotropy (narrowest angular distribution of easy axis) evidenced in the 70 nm thick film (Figure 2).

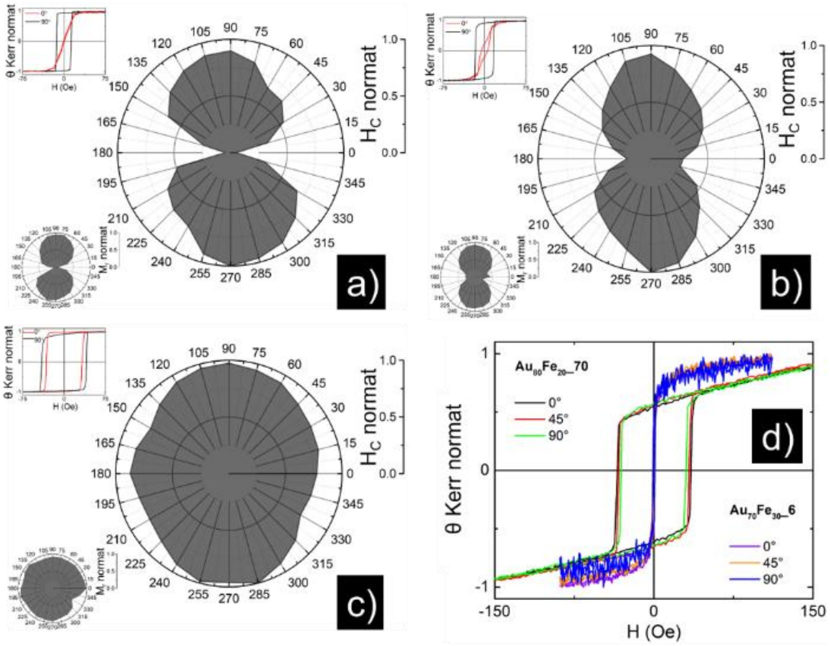

Fig. 2 Polar graphical representation of normalized Hc obtained from MOKE hysteresis curves acquired at different azimuthal angles (inset shows the normalized M_r in function of recording azimuthal angles and the hysteresis loops corresponding at 0° and 90°) for sample (a) $Au_{70}Fe_{30}$_70, (b) $Au_{70}Fe_{30}$_17 and (c) $Au_{20}Fe_{80}$_70; the hysteresis loops from (d) were obtained on sample $Au_{80}Fe_{20}$_70 and $Au_{70}Fe_{30}$_6.

At the smallest thickness of 6 nm, the Fe clusters present a superparamagnetic behavior at room temperature and the film thickness impose a rather narrower particle size distribution as reflected in the sharpest reaching of the blocking temperature at about 70 K. Above 70 K, the ZFC magnetization decreases very slowly, showing that a higher number of magnetic clusters are still interacting. The involved type of interactions among such clusters can be deduced from the very high coercive field which characterizes them at the low temperature of 20 K. This clearly suggests a high uniaxial anisotropy and presence of magnetic order specific to only a 2D Ising type of magnetic system, in agreement with only one layer of Fe magnetic clusters distributed in the film plane, especially along linear chains. Such magnetic chains interact also laterally via the interstitial Fe clusters of similar size, which enter into the magnetic frozen regime below the blocking temperature of 70 K, therefore providing the 2D magnetic character (exchange interactions in the two directions of the film) of the overall system.

The second example consists in nanostructured undulated thin films of Fe and FeCo prepared on linearly trenched Mo templates. Inhomogeneous undulated thin films consisting of low size (5 nm average size) oblate islands and larger prolate islands with the magnetic easy axis along the trenches were obtained in all cases by specific sputtering conditions [3]. The geometrical parameters, relative fraction and surface distribution of the magnetic clusters can be widely tuned by the preparation conditions and hence the type of magnetic order and associated anisotropy of the system. In specific conditions, the prolate nanoparticles are mainly formed on the trench valley whereas the finer oblate ones are more distributed on the hills and intermediate the inter-chain magnetic interactions at low temperature (Figure 3).

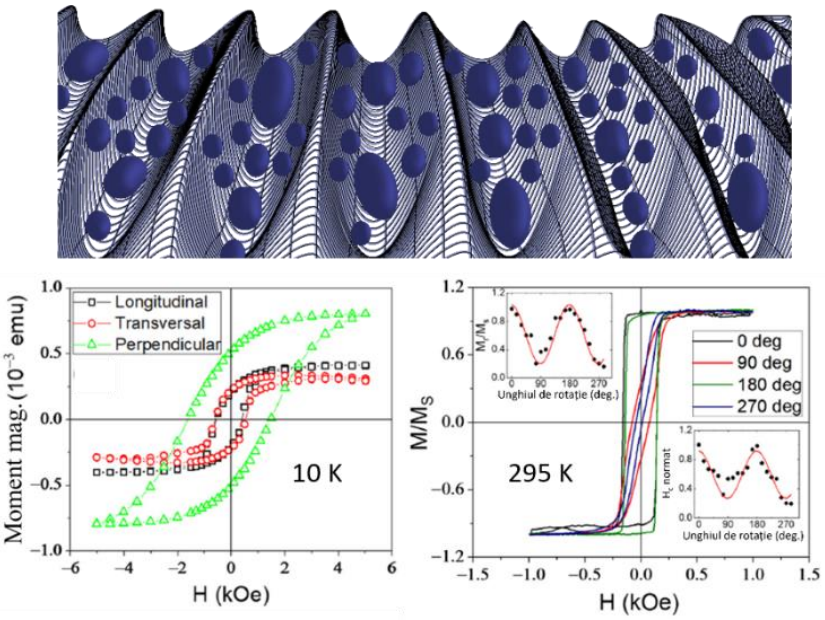

Fig. 4 Schematic distribution of the Fe-Co fine oblate magnetic clusters and larger prolate magnetic clusters on Mo trenches. The low temperature hysteresis loop (bottom-left) evidence the 2D XY type of magnetic order with in plane distribution of the easy axis whereas the room temperature vectorial MOKE loops (bottom- right) evidence in plane uniaxial anisotropy along the trenches.

By increasing the temperature, the low-size oblate nanoparticles become superparamagnetic and cut off the long-range inter-chain interactions among the larger prolate nanoparticles. Hence, at room temperature, the magnetization reversal is specific to an assembly of non-interacting oblate ellipsoidal nanoparticles which behave as nanowires with the easy axis of magnetization oriented along the trenches. The uniaxial anisotropy of the system at room temperature and the complex anisotropy at low temperature can be controlled by induced specificities of trenches, thickness, and composition of the magnetic material. The obtained results open new paths for the extension of the studies concerning the adjustment of magnetic properties on various non-homogeneous systems formed by cluster organization inside or at surface of thin films.

References

1. V Socoliuc, MV Avdeev, V Kuncser, R Turcu, E Tombacz, . Vekas, “Ferrofluids and bio-ferrofluids: looking back and stepping forward”, *Nanoscale* 14, 4386 (2022).
2. C Locovei, C Radu, A Kuncser, N Iacob, G Schinteie, A Stanciu, S Iftimie, V Kuncser, “Relationship between the formation of magnetic clusters and hexagonal phase of gold matrix in Au_xFe_{1-x} nanophase thin films”, *Nanomaterials* 12, 1176 (2022).
3. AE Stanciu, G Schinteie, A Kuncser, C Locovei, L Trupina, N Iacob, A Leca, B Borca, V Kuncser, “Magnetic properties of nanosized Fe and FeCo Systems on trenched Mo templates”, *Coatings* 12, 1366 (2022).

Enhancement of Thermo-Electric Figure of Merit for Materials with Application at Medium and High Temperatures

Bogdan Popescu[a], Ilhame Assahsahi[a,b], Magdalena Galatanu[a], Monica Enculescu[a], Gabriel Constantinescu[c], Andrei Kovalevsky[c], Andrei Galatanu[a]
[a]National Institute of Materials Physics, 405A Atomistilor, 077125 Magurele, Romania
[b]ISA Laboratory, ENSA, Ibn Tofail University, 14000 Kenitra, Morocco
[c]Department of Materials and Ceramic Engineering, CICECO—Aveiro Institute of Materials, University of Aveiro, 3810-193 Aveiro, Portugal

The characteristic of thermoelectric (TE) materials to convert electricity into heat and vice versa has a great potential for applications such as energy conversion of waste heat into electricity, and solid-state heating and cooling. The efficiency of conversion for a material is defined by the dimensionless figure of merit $ZT = S^2T/\rho\kappa$, where S is the Seebeck coefficient, ρ the electrical resistivity, κ thermal conductivity, and T the temperature of operation. A good TE material should have a high value of the ZT, which can be obtained by maximizing the power factor (PF), defined by S^2/ρ, and by concomitantly decreasing the thermal conductivity. Unfortunately, according to the Wiedemann-Franz law, it is difficult to decouple the electronic contributions to thermal conductivity and the electrical conductivity. Some strategies to overcome this problem have been already suggested decades ago, among them being those that can decrease independently the phonon contributions to the thermal conductivity like nano-structuring the material, or involving the soft mode phonons like those induced by weakly bonded atoms in the so-called cage structured compounds. Another important issue for large scale applications (like waste heat harvesting) is to have TE materials easily produced and with reasonable costs from abundant raw materials. In this view we have approached some suitable TE material candidates and investigated routes to further enhance their TE efficiency.

Filled skutterudites have captured much attention as good materials for heat-to-electric power conversion, due to their structure which forms cages able to accommodate various types of weakly bonded elements, scattering more efficiently the heat carrying acoustic phonons and thereby decrease the lattice thermal conductivity. In our work [1], two types of ceramic carbide nanoparticles, β-SiC – a wide band gap semiconductor (2.2 eV), and α-WC with semimetal properties, are dispersed into the double filled $In_{0.2}Yb_{0.2}Co_4Sb_{12}$ skutterudite matrix.

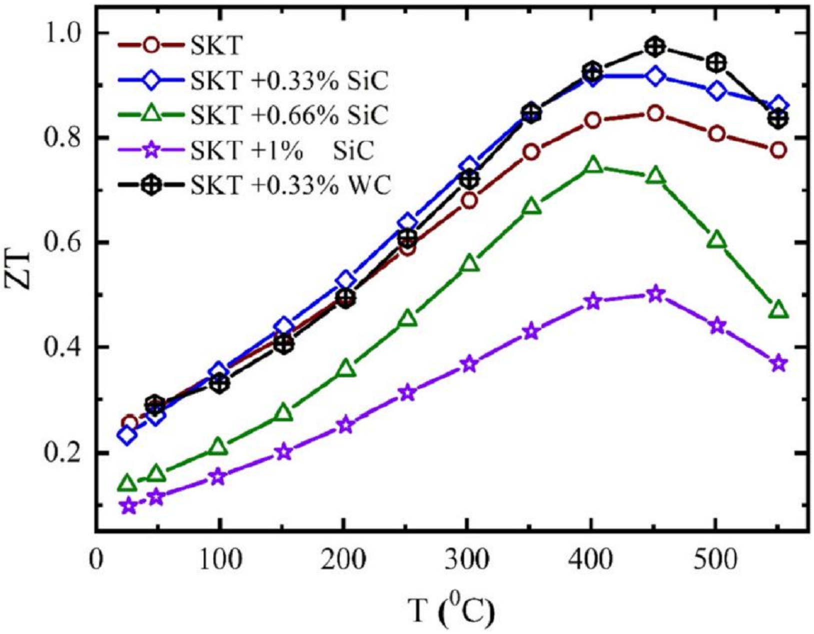

Fig. 1 Temperature dependence of the dimensionless figure of merit ZT for nanostructured composites produced from nanometric β-SiC and α-WC dispersed into the double filled $In_{0.2}Yb_{0.2}Co_4Sb_{12}$ matrix.

In Figure 1 the figure of merit for nanostructured composites fabricated from nanometric powders of β-SiC and α-WC dispersed into the double filled $In_{0.2}Yb_{0.2}Co_4Sb_{12}$ matrix is displayed. In both cases, the addition of only 0.33 v% of SiC or WC causes a notable enhancement of the power factor but influence differently the thermal conductivity. The 0.33 v% SiC/SKT composite displays a reduction of the thermal conductivity due to the increase of phonon scattering at SiC/SKT interfaces and grain boundaries, leading to an enhancement of the figure of merit over the entire temperature domain. The tungsten carbide inclusions, although increasing the thermal conductivity by a higher electronic contribution, compensate this inconvenience by attaining a high-power factor, which result in a 15% improvement of the maximum value of the figure of merit, *i.e.*, 0.97 at 450 °C.

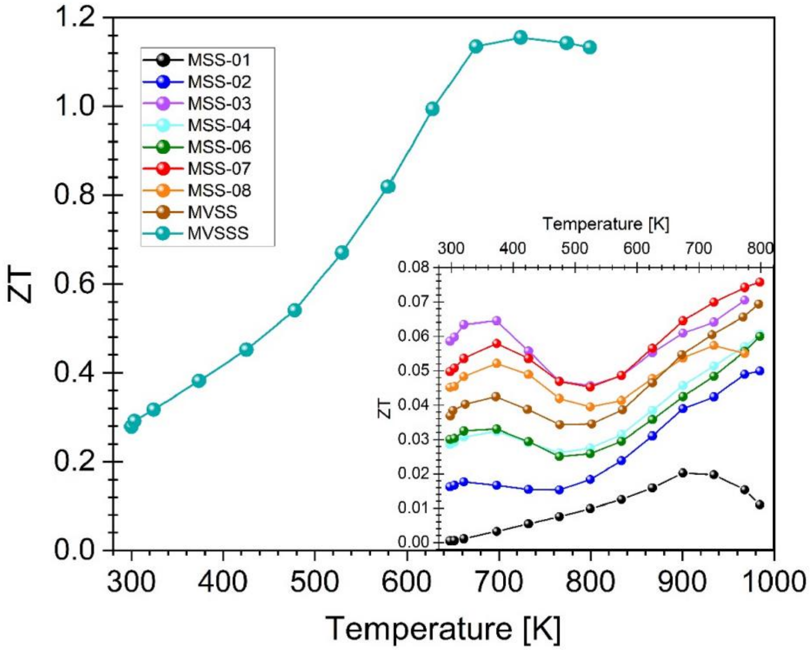

Fig. 2 Temperature dependence of the dimensionless figure of merit *ZT* for $Mg_2Si_{0.4}Sn_{0.6}$ materials. Inset: optimizing the processing parameters for undoped (MSS-01 to MSS-08) and V-doped (MVSS) materials and the double V and Sb doped material, $Mg_{1.98}V_{0.02}Si_{0.385}Sn_{0.6}Sb_{0.015}$, (main figure).

Another thermoelectric material family that attracted sustained attention for medium temperature applications is the Mg_2IV (IV = Si, Ge and Sn) silicides, characterized by relatively high thermoelectric performance, abundance and availability of raw materials, environmental compatibility and cost-efficient production. These materials also provide additional possibilities to enhance their performance via alloying and solid solution synthesizing methods, relying on the isostructural characteristic of Mg_2Si and Mg_2Sn, and the formation of solid solutions between these two compounds. Moreover, doping with Bi and Sb elements is an effective route to tune the charge carrier concentration and thus to improve the power factor of $Mg_2(Si,Sn)$ compounds. In this context, the alloys are attractive for industrial applications, and therefore simple and reliable synthesis methods are needed. However, it is rather difficult to get stoichiometric and single phase $Mg_2Si_{1-x}Sn_x$ materials by the melting method due to the miscibility gap in their pseudo-binary phase diagram.

In our work [2], $Mg_2Si_{0.4}Sn_{0.6}$ samples were prepared by a method involving the melting of the constitutive elements in a closed graphite crucible inserted into an evacuated quartz tube, followed by the spark plasma sintering of the milled ingots. Structural and morphological investigations show that the samples are mostly dual phase with the main phase close in composition to $Mg_2Si_{0.4}Sn_{0.6}$ and the other, $Mg_2Si_{1-x}Sn_x$, with a high Si content. Increasing the sintering temperature, the volume fraction of the secondary phase is diminished, while a longer dwell-time favors its solubility into the main phase. The interplay between the two phases affects the number of their interface boundaries, which, in turn, influence the carries scattering effects and further the transport properties of the samples. The optimal SPS conditions that yield the best thermoelectric performance, ZT~0.75 at around 800 K, were holding 15 min at 750 °C under a pressure of about 50 MPa, as shown in the inset of Figure 2. Following the same method, samples with a more elaborated composition, $Mg_{1.98}V_{0.02}Si_{0.385}Sn_{0.6}Sb_{0.015}$, were produced, showing a two-orders of magnitude increase of their carrier concentration, and thus of the electrical conductivity, which generate a further enhancement of the power factor. Although the thermal conductivity has a higher electronic contribution than $Mg_2Si_{0.4}Sn_{0.6}$, at high temperatures, its values are reduced. Overall, the thermoelectric figure of merit of the doped samples is improved and, as depicted in the main Figure 2 reaches a maximum value $ZT \cong 1.15$ at 723 K. This is a 20-times increase over the best undoped materials.

Improvements in the TE performance by fine tuning the material processing conditions can be also obtained on other class of materials, like different oxides, which benefit of a very good thermal stability at high temperatures. Ceramic samples with the stoichiometry $Zn_{0.995}Al_{0.005}O$ prepared using alumina and metallic Al by the standard solid-state route [3] revealed only minor differences between the sintered samples, mainly related to the inhomogeneous distribution of Al. A significant 2-3-fold increase in electrical conductivity at temperatures above 850 K is observed for the samples prepared using metallic aluminum, affecting the charge carrier concentration and mobility. A high Seebeck coefficient was measured for ceramics prepared using metallic Al micro powder. The precursor type was found to have almost no effect on the thermal conductivity of the ceramic samples. As a result, the maximum power factor values and dimensionless figure of merit of 700 $\mu Wm^{-1}K^{-2}$ and 0.14 at 1173 K, respectively, were obtained for $Zn_{0.995}Al_{0.005}O$ ceramics, prepared using metallic aluminum micrometric powder and marking almost a two-time increase as compared to the sample processed using a conventional Al_2O_3 precursor.

References

1. B Popescu, M Galatanu, M Enculescu, A Galatanu, "The inclusion of ceramic carbides dispersion in In and Yb filled $CoSb_3$ and their effect on the thermoelectric performance", *Journal of Alloys and Compounds* 893, 162400 (2022).
2. I Assahsahi, B Popescu, M Enculescu, M Galatanu, AC Galca, R El Bouayadi, D Zejli, A Galatanu, "Influence of the synthesis parameters on the transport properties of $Mg_2Si_{0.4}Sn_{0.6}$ solid solutions produced by melting and spark plasma sintering", *Journal of Physics and Chemistry of Solids* 163, 110561 (2022).
3. G Constantinescu, A Galatanu, D Tobaldi, S Mikhalev, D Suarez, T Paulino, K Zakharchuk, S Sergiienko, D Lopes, A Kovalevsky, "Enhancement of thermoelectric performance of donor-doped ZnO ceramics by involving an in situ aluminothermic reaction during processing", *Crystals* 12, 01562 (2022).

Ferromagnetic Shape Memory Ribbons with Magnetocaloric, Magnetoresistive and Magnetostrictive Effects as Multifunctional Materials

Mihaela Sofronie[a], Bogdan Popescu[a], Monica Enculescu[a], Mugurel Ţolea[a], Felicia Ţolea[a]
[a]National Institute of Materials Physics, 405A Atomistilor, 077125 Magurele, Romania

Ferromagnetic shape memory alloys (FSMA) are a specific type of shape memory alloys (SMA) that can change their shape when exposed to a magnetic field, in addition to the normal thermal shape memory effect of SMAs. Unlike the thermal shape memory effect, which requires a phase transition of martensite to austenite and back, the magnetic shape memory effect occurs in the martensite phase. The magnetic-field-induced strains in FSMA can be orders of magnitude higher than in other magnetostrictive materials as well as (electrically induced) piezoelectric materials and are on a faster timescale than the thermal shape memory effect. In addition to applications for SMA such as mini actuators, seismic control, aerospace, medical or automobile applications, FSMA can thus have further use for sensors, smart materials, biomedical devices and actuators [1,2]. The improved ductility of the off-stoichiometric Heusler-type FSMA is caused by the existence of a secondary face-centered cubic phase γ phase, which forms during the heat treatments necessary for sample structural ordering. Using suitable preparation techniques, like melt spinning, it may be controlled and the obtained ribbons preserve a relatively good sample malleability. Another approach, for improving the magnetic and mechanical properties of Heusler-type FSMA is by substituting with Rare Earth (RE) elements [3]. Thus, in Ni-Mn-Ga and Ni-Fe-Ga alloys, various substitutions have been tested to improve their magnetic anisotropy and ductility. In addition, it is assumed that the thin melt-spun ribbons assure a more efficient heat transfer, which is desirable in magnetocaloric applications.

The Heusler non-stoichiometric $Ni_{55}Nd_{2}Fe_{18}Ga_{25}$ alloy prepared by the electric arc melting and melt spinning method was investigated. The effects of the thermal treatments on the phase composition, morphology, magneto-caloric and magneto-transport properties of the nanostructured ribbons have been examined and compared with the bulk samples. Rapidly quenched ribbons of about 15-16 µm thickness and 2-3mm width were obtained and denoted AQ ("as-quenched"). The AQ ribbons were thermally annealed in evacuated quartz ampoules followed by a direct quenching of the sample in ice water. The samples were annealed for 2 h at 673 K, and for 2 minutes at 1173 K and denoted T400 and T900, respectively.

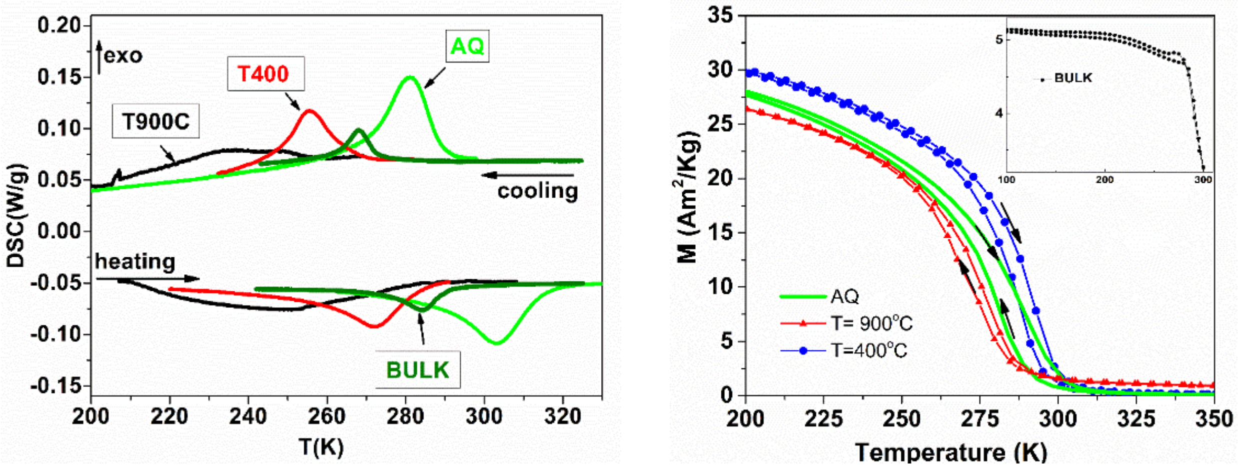

Fig. 1 *Left* – The calorimetric signals for Bulk and AQ, T400 and T900 ribbons. *Right* – Temperature dependence of magnetization for AQ, T400 and T900 ribbons and Bulk in the inset.

The thermal treatments produce, besides atomic ordering, the segregation of the γ phase, which depletes the austenitic matrix in 3d elements, hence influencing the thermal positioning of the martensitic transformation and the magnetic ordering, as shown by the calorimetric measurements.

Connect the magnetic measurements (Figure 1–right) with the calorimetric ones (Figure 1–left) is remark the Curie temperatures increase for the ordered structure, while the martensitic temperatures decrease with the rising thermal treatment temperature. The bulk samples show consecutive phase transformations with the magnetic transition at a higher temperature than the structural transition (see Figure 1–right and Table 1). Interestingly, however, the as-quenched ribbons show a concomitant magneto-structural transition in the room temperature range.

Table 1 DSC transformation temperatures (Ms, Mf, As, Af), thermodynamic equilibrium temperature T_0, the Curie temperatures and magnetic entropy change ΔS_m (at 5 T) for studied samples. Tc_A is determined by cooling and Tc_M is determined by heating.

Sample	Ms (K)	Mf (K)	As (K)	Af (K)	T_0 (K)	Tc_M (K)	Tc_A (K)	$-\Delta S_m$ (J/KgK)
Bulk	274	262.6	275.6	290	282	300	291	4.58
AQ	291	269	290	318	304.5	282.6	290	5.41
T400	267	246	261	285	276	291.6	296	4.25
T900	258	204	210	281	269.5	271	275	3.46

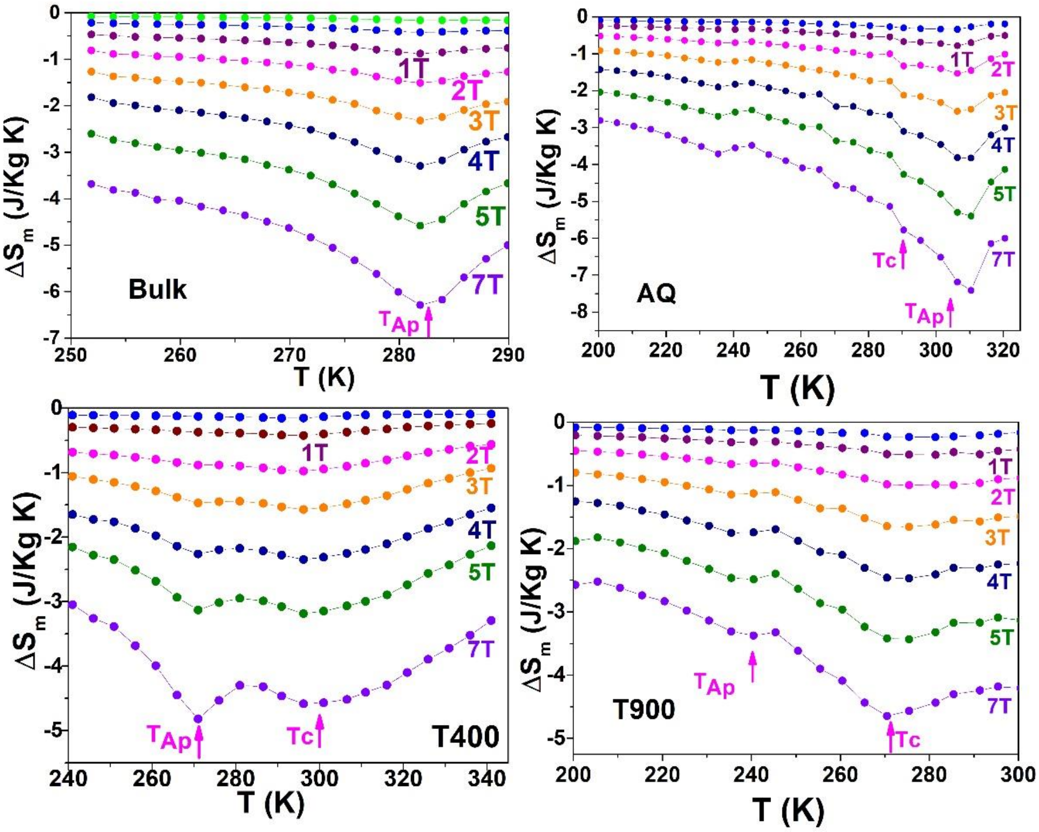

Fig. 2 Magnetic entropy variationΔS_m versus temperature on heating for Nd2 samples as Bulk and AQ, T400 and T900 ribbons.

The magnetocaloric effect (MCE) is defined as the heating or cooling of a magnetic material, isolated adiabatically when a magnetic field is applied. The Curie temperature and the martensitic one can be modified by slight changes in the composition and using proper thermal treatments. Thus, the structural transformation can overlap with the magnetic one so that the alloy has a magnetostructural transformation. We evaluated the magnetic entropy changes (ΔS_m) in $Ni_{55}Fe_{18}Nd_2Ga_{25}$ alloy with concomitant or sequential structural and magnetic phase transition prepared as bulk and as ribbons in a as quenched state or subjected to thermal treatments (Figure 2). A commonly indirect measurement technique to assess MCE is used. Magnetization was measured as a function of increasing temperature for applied magnetic field values between 0.02T and 7T, and depending on the measurement accuracy an error of only 3 – 10% for the magnetic entropy change may be achieved. From the temperature dependence of the magnetization in an applied constant magnetic field, the magnetic entropy variation is calculated using the Maxwell equation for discrete data points. As a consequence of concomitant magneto-structural transition in the RT range, the AQ ribbons have the highest value of the magnetic entropy variation from all measured samples, of -5.41 J/KgK at 310K (see Figure 2). For the thermally treated ribbons, the magnetic and structural transitions are separated, and two maxima are occurring in the thermal dependence of the magnetic entropy variation in connection with the martensitic transformation and Curie temperature.

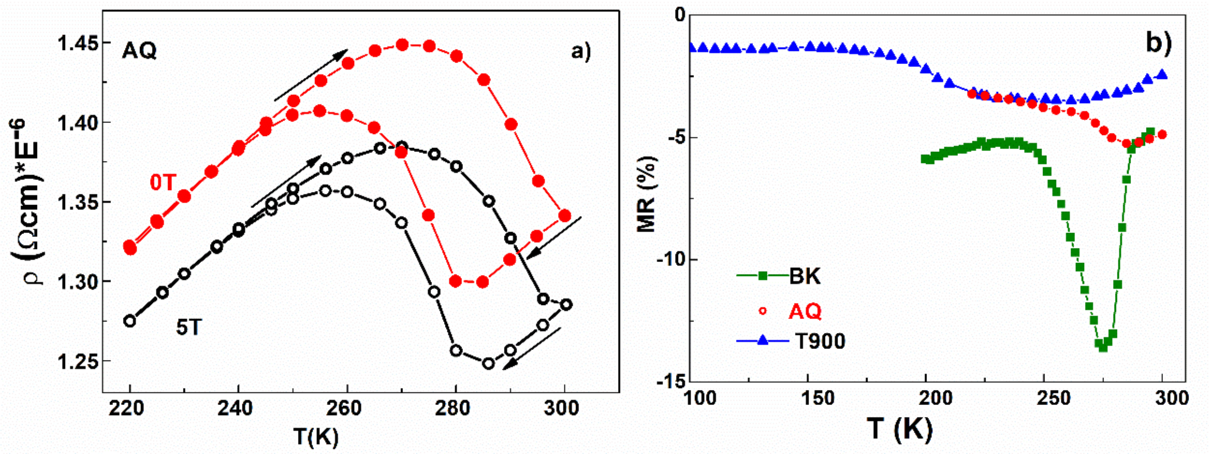

Fig. 3 (a) Temperature dependence of resistivity versus temperature in H=0T and H=5T (open symbols) for AQ ribbons; (b) Thermal variation of magnetoresistance in 5T.

To characterize the magnetoresistive effect, the variation of electrical resistivity was measured as a function of temperature, in the temperature range specific to the martensitic transformation of each sample, without an applied magnetic field (0 T) and respectively in a magnetic field of 5T (see Figure 3a). A remarkable magnetoresistive effect of 13.5% at 275 K was recorded in the bulk sample (Figure 3b), which is much higher than in the ribbons (5.23% at 285K and 3.42% at 235 K for the AQ ribbons and T900 sample, respectively).

References

1. M Sofronie, F Ţolea, M Enculescu, I Pasuk, B Popescu, “Microstructure, magnetic and magnetostrictive behavior in rapidly quenched off-stoichiometric Ni-Mn-Ga ferromagnetic shape memory alloys”, *Romanian Reports in Physics* 74, 503 (2022).
2. A Nan, R Turcu, C Tudoran, M Sofronie, A Chiriac, “Analysis of functionalized ferromagnetic memory alloys from the perspective of developing a medical vascular implant”, *Polymers* 14, 1397 (2022).
3. M Sofronie, B Popescu, M Enculescu, M Ţolea, F Ţolea, “Processing effects on the martensitic transformation and related properties in the Ni$_{55}$Fe$_{18}$Nd$_2$Ga$_{25}$ ferromagnetic shape memory alloy”, *Nanomaterials* 12, 3367 (2022).

In-situ Continuous Hydrothermal Synthesis of TiO_2 Nanoparticles on Conductive N-doped MXene Nanosheets for Binder-Free Li-ion Battery Anodes

Uthman Alli[a], Kieran McCarthy[b,c], Ioan-Alexandru Baragau[a,d], Nicholas P. Power[e], David J. Morgan[f], Steven Dunn[a], Seamus Killian[b,c], Tadhg Kennedy[b,c], Suela Kellici[a]
[a]School of Engineering, London South Bank University, 103 Borough Road, London SE1 0AA, United Kingdom
[b]Department of Chemical Sciences, University of Limerick, Limerick V94 T9PX, Ireland
[c]Bernal Institute, University of Limerick, Limerick V94 T9PX, Ireland
[d]National Institute of Materials Physics, 405A Atomistilor, 077125 Magurele, Romania
[e]School of Life Health & Chemical Sciences, Open University, Walton Hall, Milton Keynes MK7 6AA, United Kingdom
[f]Cardiff Catalysis Institute, School of Chemistry, Cardiff University, Park Place, Cardiff CF10 3AT, United Kingdom

Developing new materials and technologies for energy storage applications is an essential task for delivering the next generation of batteries. Lithium-ion batteries (LIBs) have emerged as the worldwide dominant current energy storage technology due to their high charge density and unprecedented cycling performances. Lithium has low atomic weight and volume being highly suitable for ions-intercalation into layered materials (such as graphite and MXene), thereby showing high volumetric energy density [1]. Despite these exciting properties exhibited by LIBs, they are limited by power performance, costs, safety, and environmental concerns from the toxicity of its components and lithium mining [2]. The materials involved in anode production are important in Li-ion energy storage technology and a key in determining the energy density, cyclability and of life recyclability; there remains a challenge to produce Li-ion anode materials that are binder free and poses energy storage characteristics that match the current carbon-based electrodes [3].

MXenes are 2D metallic carbides with a high surface area and rich surface chemistry. Due to their chemical nature, their electrochemical properties can be tuned, and they can be integrated into batteries as anode material without a need for polymeric binders or hazardous chemicals that pose a challenge to recycling Li-ion batteries [4,5].

The current study [6] reports the synthesis of [N-doped MXene-TiO_2] hybrid anode materials using an aqueous route. The synthetic procedure involves a two-step chemical process: (*i*) the HF etching of the Ti_2AlC MAX phase followed by physical process delamination (ultrasonication) of Ti_2CT_x MXene (see Figure 1a), and (*ii*) a CHFS treatment in ammonia (NH_4OH) solution of delaminated Ti_2CT_x, in which the nitrogen-doping of MXene was achieved, and the TiO_2 nanoparticles decorating the MXene nanosheets surface were in-situ generated, resulting in a single step continuous hydrothermal process (see the CHFS schematic in Figure 1b) to synthesize [N-doped MXene-TiO_2] hybrid nanocomposites.

The as-synthesized materials were integrated as a free-binding anode in Li-ion batteries, and the capacity tests indicate an improvement from the initial specific energy capacity of 305 $mAhg^{-1}$ to 369 $mAhg^{-1}$ after 100 cycles at a charge rate of 0.1 C and a Coulombic efficiency of 99.7%. This compares to 252 $mAhg^{-1}$ for the unmodified MXene, which exhibited a significant capacity fade to 140 $mAhg^{-1}$.

The current study reveals the ability to manufacture a Li-ion anode that does not require toxic chemicals for processing into an electrode and exhibits good energy storage characteristics in a binder-free system, and it is a significant step forward for energy storage applications. The CHFS method offered an environmentally friendly synthetic approach and demonstrated the capability to engineer MXene-related nanocomposites as promising Li-ion anode materials.

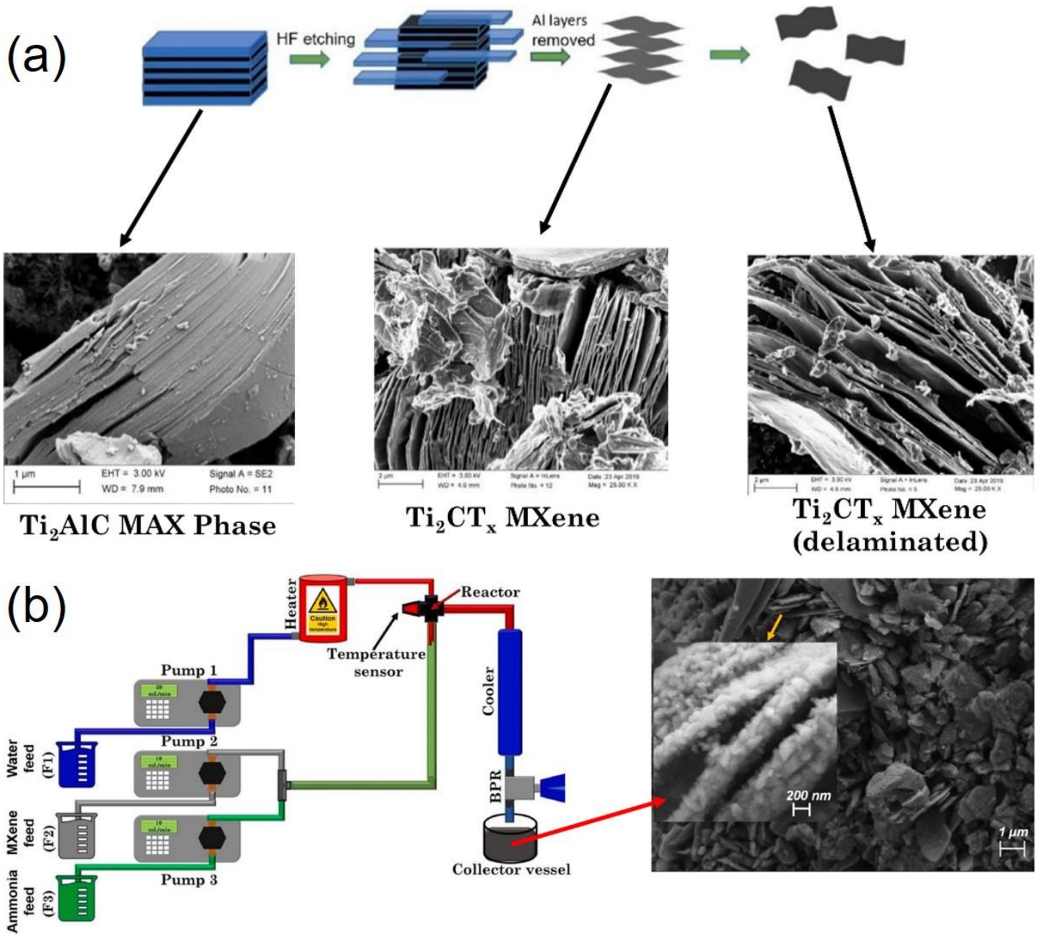

Fig. 1 (a) Schematic of the synthetic procedure of delimited Ti_2CT_x MXene via HF etching and ultrasonication and (b) the schematic of continuous hydrothermal flow synthesis reaction setup used to produce [N-doped Ti_2CT_x MXene-TiO_2] hybrid.

References

1. J Xie, YC Lu, “A retrospective on lithium-ion batteries”, *Nature Communications* 11, 9–12 (2020).
2. ZM Konz, BD McCloskey, “Lithium quantified, dead or alive”, *Nature Energy* 7, 1005–1006 (2022).
3. YP Wu, E Rahm, R Holze, “Carbon anode materials for lithium-ion batteries”, *Journal of Power Sources* 114, 228–236 (2003).
4. ANG Ravuri Syamsai, JR. Rodriguez, VG. Pol, Q Van Le, KM Bato, SF Adil, S Pandiaraj, MR Muthumareeswaran, EH Raslan, “Double transition metal MXene ($Ti_xTa_{4-x}C_3$) 2D materials as anodes for Li-ion batteries”, *Scientific Reports* 11, 688 (2021).
5. G Ma, H Shao, J Xu, Y Liu, Q Huang, PL Taberna, P Simon, Z Lin, “Li-ion storage properties of two-dimensional titanium-carbide synthesized via fast one-pot method in air atmosphere”, *Nature Communications* 12, 1–6 (2021).
6. U Alli, K McCarthy, IA Baragau, NP Power, DJ Morgan, S Dunn, S Killian, T Kennedy, S Kellici, “*In-situ* continuous hydrothermal synthesis of TiO_2 nanoparticles on conductive N-doped MXene nanosheets for binder-free Li-ion battery anodes”, *Chemical Engineering Journal* 430, 132976 (2022).

Deconvolution of Spectro-Microscopic Data from Ferroelectrics: Physical Insight of the Correlations Between Fitting Parameters

Laura E. Abramiuc[a], **Liviu C. Tănase**[a], **Alexei Barinov**[b], **Cristina F. Chirilă**[a], **Cristian M. Teodorescu**[a]
[a]National Institute of Materials Physics, 405A Atomistilor, 077125 Magurele, Romania
[b]Elettra Sincrotrone Trieste, Strada Statale 14, km 163,5 in AREA Science Park, 34149 Basovizza, Trieste, Italy

Since during the last decade it was proven that photoelectron spectroscopy is a reliable technique to derive surface charge accumulation, interface dipoles and, generally, band bending at surfaces, these findings were immediately applied to photoelectron spectro-microscopy of ferroelectric surfaces, being then able to detect charge compensated or uncompensated regions of ferroelectrics [1], to assess the ferroelectric domain structure with binding energy contrast [2] or to detect in real time surface modifications, such as surface reduction and polarization changes [3]. The above works treated conventionally photoelectron images taken at a given kinetic energy, or photoelectron spectra emerging from a limited region, sometimes assessing also their time evolution [1,3]. However, photoelectron spectro-microscopy data are far richer, since for any point on the sample surface a complete spectrum is recorded, therefore the data are (at least) in the form of 3D "data cubes". When time-evolution is involved, the dimensionality of the data would be 4D; when also the emission angle is recorded simultaneously, the bare data are 4D and with the time evolution 5D. However, up to now there was no available software package to analyze completely such multidimensional data. For photoelectron spectromicroscopy, this implies that one has to define a fast and reliable curve fitting procedure to be applied to any individual spectrum for a pixel from the sample surface. This was developed and tested in the framework of this work. The software was freely distributed to all known teams performing photoelectron spectro-microscopy or Nano-ESCA using synchrotron radiation.

Photoelectron spectro-microscopy data cubes with sub-micrometer spatial resolution from a lead zirconate titanate thin film obtained at the SpectroMicroscopy beamline from the synchrotron radiation facility Elettra (Trieste) are fitted with three components in each spatial point for several areas investigated, and correlations between the results of the fitting parameters are established, enabling one to suggest that surface band bending manifests also in the case of samples with multiple polarization states. These surface band bendings may be used for preliminary assessment of polarization states by using the contrast in binding energy. Hence, in the case of multicomponent fitting, one may derive maps of binding energies and amplitudes, as represented in Figures 1 and 2. The individual curve fitting of each spectrum and the analysis of correlations between the derived parameters (binding energies and amplitudes, see Figure 3) yields results of deeper significance in deriving the distribution of band bending [4]. In particular, points representing formally the same 'component' in the curve fitting procedure were found to belong to different polarization states, as can be seen from Figure 3b,c. This allows one to determine the *distribution* of band bending on the sample surface. It is found that the major part of the investigated areas consist in regions with outwards polarization and without out-of-plane polarization ($P^{(+)}$ and $P^{(0)}$), with the presence of some isolated metal Pb clusters. From Figure 3d one infers that the small Pb clusters are insulated and their binding energy is shifted by the value of the surrounding band bending. From Figure 3e it seems that some Pb clusters situated on areas with polarization outwards become negatively charged, to screen for effects of the depolarization field. The E2 *vs.* E3 plots (Figure 3f) might be interpreted as being the superposition of two distributions, one with higher binding energies for E2 and lower binding energies for E3 representing the case where E2 and E3 refers to the same component ($P^{(+)}$), whereas the other distribution represents the case where the two components are indeed attributed to different polarization states, reinforcing the attribution discussed above for Figure 3b,c. The linear decrease in the distribution of A2 *vs.* A3 (Figure 3i) is in line with the constancy of the overall signal. The amplitude related to Pb clusters seems not to be correlated with the relative weight of $P^{(0)}$ and $P^{(+)}$ areas (Figure 3g,h).

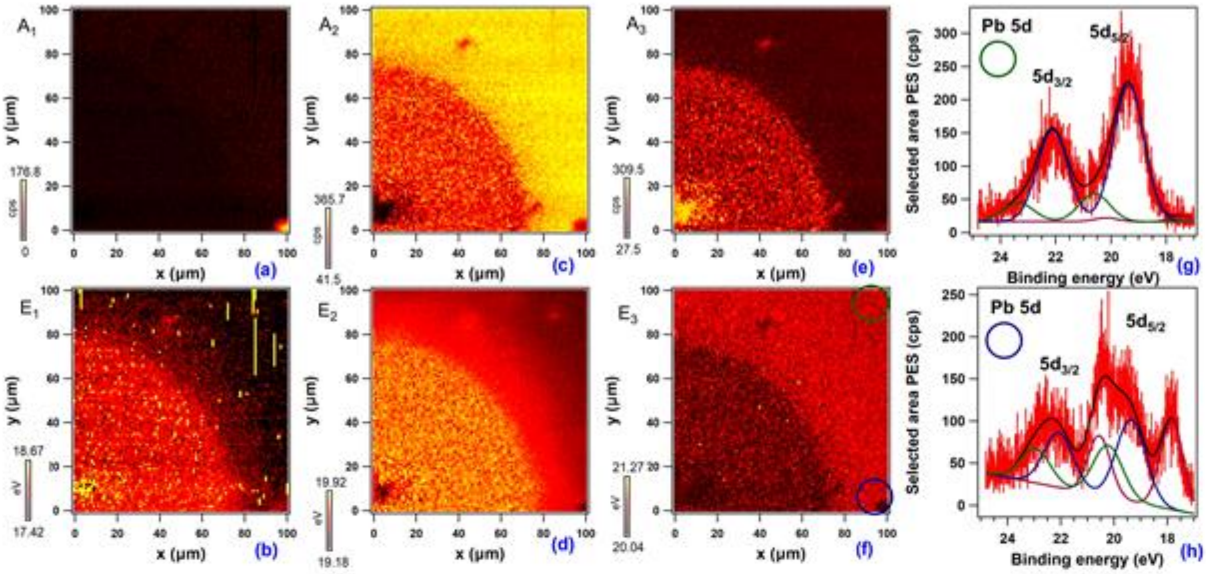

Fig. 1 Results of the individual fitting of spectro-microscopic data for a first region of the 50 nm PZT(001) film. (a, b) represents maps of amplitudes and Pb $5d_{5/2}$ binding energies for the first component; (c, d) the same for the second component; (e, f) the same for the third component. The components are numbered in order of increasing binding energy. In (f) the two (green and blue) circles designate in their centers the region where the spectra represented in (g) and (h) were extracted. In (g) and (h) also the corresponding fits with three Gaussian doublets are represented.

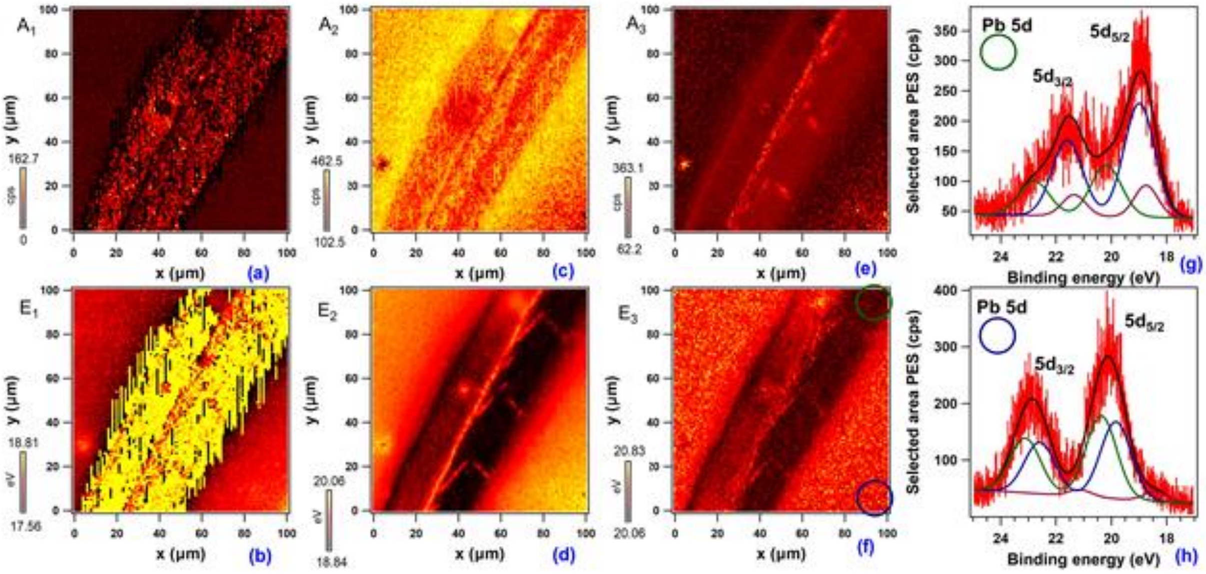

Fig. 2 The same as the previous Figure, but for another region of the sample.

The above correlations are just examples from a single data cube; in Ref. [4] other correlations for several regions of the sample have been derived. The conclusion with most physical insight is that surface band bending in the case of free ferroelectric surfaces seems to manifest even in the case of surface inhomogeneities, and sometimes there are subtle correlations between areas representing different polarization states of the material. Photoelectron spectro-microscopy is less invasive for the sample with respect to other methods used to analyze the polarization distribution at nanoscopic level, such as piezoresponse force microscopy.

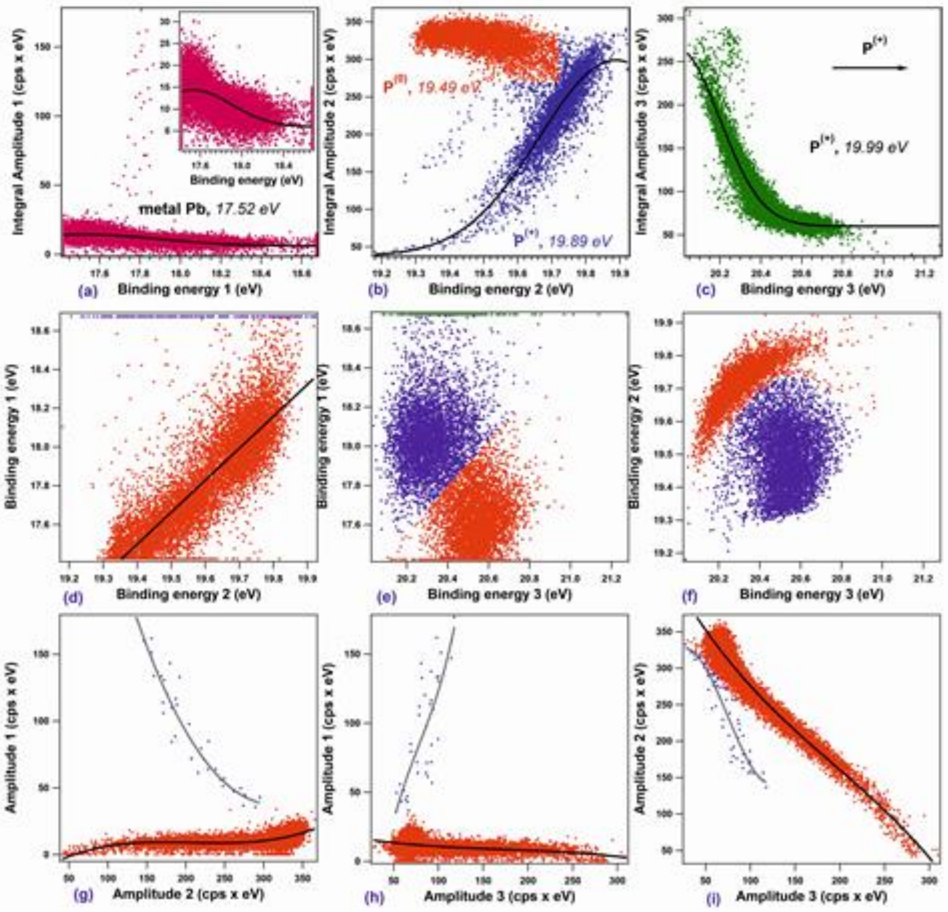

Fig. 3 Correlations between fitting parameters extracted from the analysis of data cubes corresponding to Zone 1, whose maps are represented in Figure 1a–f. E1, E2, E3 are Pb 5d$_{5/2}$ binding energies and A1, A2, A3 integral Pb 5d amplitudes for different components used in curve fitting. (a) A1 *vs.* E1; (b) A2 *vs.* E2; (c) A3 *vs.* E3; (d) E1 *vs.* E2; (e) E1 *vs.* E3; (f) E2 *vs.* E3; (g) A1 *vs.* A2; (h) A1 *vs.* A3; (i) A2 *vs.* A3.

References

1. DG Popescu, MA Huşanu, L Trupină, L Hrib, L Pintilie, A Barinov, S Lizzit, P Lacovig, CM Teodorescu, "Spectro-microscopic photoemission evidence of charge uncompensated areas in Pb(Zr,Ti)O$_3$(001) layers", *Physical Chemistry Chemical Physics* 17, 509–520 (2015).
2. MA Huşanu, DG Popescu, CA Tache, NG Apostol, A Barinov, S Lizzit, P Lacovig, CM Teodorescu, "Photoelectron spectroscopy and spectro-microscopy of Pb(Zr,Ti)O$_3$(111) thin layers: imaging ferroelectric domains with binding energy contrast", *Applied Surface Science* 352, 73–81 (2015).
3. LE Abramiuc, LC Tănase, A Barinov, NG Apostol, C Chirilă, L Trupină, L Pintilie, CM Teodorescu, "Polarization landscape effects in soft X-ray-induced surface chemical decomposition of lead zirco-titanate, evidenced by photoelectron spectromicroscopy", *Nanoscale* 9, 11055–11067 (2017).
4. LE Abramiuc, LC Tănase, A Barinov, CF Chirilă, CM Teodorescu, "Nanoscopic correlations from curve fitting of photoelectron spectromicroscopy data cubes of lead zirconate titanate films", *Results in Physics* 36, 105436 (2022).

Experimental Band Structure of Pb(Zr,Ti)O_3: Mechanism of Ferroelectric Stabilization

Dana G. Popescu[a], Marius A. Husanu[a], Procopios Christou Constantinou[b], Lucian D. Filip[a], Lucian Trupina[a], Cristina I. Bucur[a], Iuliana Pasuk[a], Cristina Chirila[a], Luminita M. Hrib[a], Viorica Stancu[a], Lucian Pintilie[a], Thorsten Schmitt[b], Cristian M. Teodorescu[a], Vladimir N. Strocov[b]

[a]National Institute of Materials Physics, 405A Atomistilor, 077125 Magurele, Romania
[b]Swiss Light Source, Paul Scherrer Institute, 5232 Villigen-PSI, Switzerland

Pb(Zr,Ti)O_3 (PZT) is the best known and the most common ferroelectric (FE) material, widely used in solid-state technology with application in non-volatile memories [1], sensors [2], transducers [3], catalysis [4] and photovoltaics [5]. Its most fundamental properties are encoded in the electronic band structure, which, however, to the date was still missing. Our recent study [6] reveals for the first time the intrinsic electronic structure of PZT depending on the FE state. The results have been obtained in soft-X-ray angle-resolved photoelectron spectroscopy (SX-ARPES) measurements performed at the ADRESS beamline of the Swiss Light Source synchrotron facility, which allows sharp definition in the out-of-plane momentum k_z, thus, recording of the 3D band structure with high resolution in full **k** momentum. The problem of sample charging due to the inherently insulating nature of the samples is solved by using thin-films, which due to self-doping push PZT in a highly doped regime. Furthermore, the SX-ARPES experiments deliver the FE-polarization dependent electrostatic potential profile across the PZT film deposited on $SrTiO_3$ and $La_xSrMn_{1-x}O_3$ substrates as well. The negative charges near the surface, required to stabilize the FE state pointing away from the sample (P+), denoted as UP sample, were identified as oxygen vacancies creating localized in-gap states below the Fermi energy. For the opposite polarization state (P−), denoted DW, the positive charges identified near the surface derive from cation vacancies developing in the PZT film with FE polarization pointing downwards, as deduced from quantitative XPS measurements.

The two PZT samples with thickness of 5 nm were grown by pulsed laser deposition on LSMO buffered TiO_2-terminated (001) STO substrate (DW) and on TiO_2-terminated (001), Nb-doped STO (Nb:STO) (UP). In Figure 1a, the photon energy $h\nu$ is varied between 350 and 520 eV at constant $k_{\|}$. The resulting iso-energy (iso-E) map in the XΓZ plane of the bulk Brillouin zone (BZ), presented in Fig. 1a, identifies the valence band maximum (VBM) in the X point at a binding energy (BE) of 2.2 eV relative to the Fermi level. The (k_x-k_y) iso-E map recorded on UP sample in the XΓM plane at the VBM using $h\nu$ = 520 eV (Figure 1b) derives from the square-like symmetry of the PZT in the *ab* plane in accordance with the iso-E surface derived from DFT calculations for the tetragonal u.c of PZT. (Figure 1c). The iso-E map recorded in the ZAR plane 0.5 eV below VBM with $h\nu$ = 465 eV (Figure 1d) also shows the DFT-predicted feature centered in the Z point for the tetragonal u.c. (Figure 1e).

The mechanism of band alignment at the interface of the PZT samples with the substrate and at the surface depending on their FE state is given in the sketched in Figure 2a. It shows the variation of the potential inside the FE film going from the surface towards the interface with the substrate and is deduced by correlating the surface sensitive ARPES data with more bulk sensitive results of the core levels, which extend the probing region down to the interface with the substrate. The dashed line represents the potential profile when opposite charges accumulate into the FE film close to the interfaces for screening the depolarization field (DF). With full lines are qualitatively traced the potentials *V*(z) inside our FE films, for both UP and DW samples, derived from the experimental data. The relative BE shift of 1.25 eV between the UP and DW samples identified in the ARPES measurements and the sharp band dispersions is compatible with the small band bending close to the surface and with the observed FE-induced band offset over the first ~ 1-2 nm close to the surface.

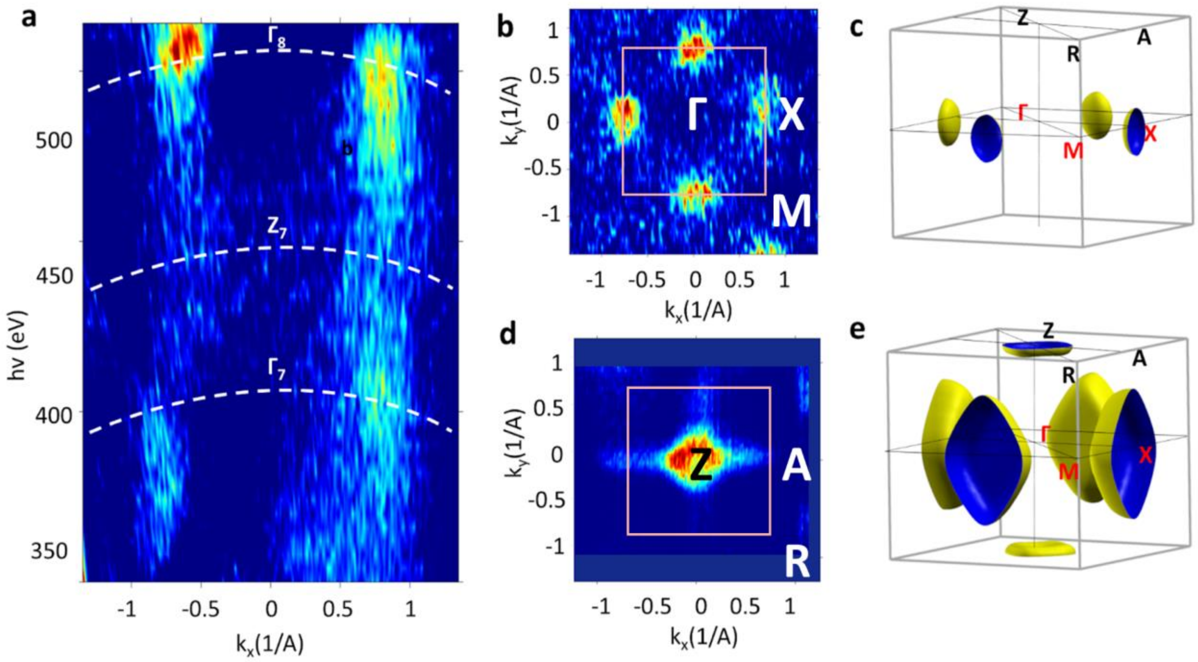

Fig. 1 Out-of-plane iso-energy (iso-E) maps of PZT recorded by varying hv between 350 eV and 520 eV while keeping the $k_{||}$ in the XΓZ plane of the bulk Brillouin zone (a). (k_x-k_y) Iso-E in the ΓMX plane at the VBM (b) and in the ZAR plane at 0.5 eV below the VBM (d). The calculated iso-E surface at VBM (c) and 0.5 eV below VMB (e) [6].

V(z) in Figure 2b describes the positive charging into Nb:STO close to the interface to compensate the FE polarization pointing away from the substrate (P+), while a negatively charged LSMO interface stabilizes the FE state pointing toward the substrate (P−). The substrate-induced band bending at the bottom interface is an essential condition for the stabilization of the FE state, facilitating the accumulation of negative/positive charge sheets at the surface/bottom interface to stabilize the P+/P− FE polarization. In the measurements performed at RT, presented in Figure 2d,e for Pb 4*f*, respectively Ti 2*p*, the same trend is identified, featured however by a smaller band offset at the PZT surface, Λ= 0.7 eV deduced from the ARPES measurements, ΔBE_{Pb} = 0.6 eV and ΔBE_{Ti} = 0.3 eV. Since W_f should not depend on temperature, this implies that the decrease of Λ and ΔBEs relates to changes in the FE nature of PZT. Indeed, in Figure 2d we identify the development of an additional component at lower BEs in the Pb 4*f* spectra indicating the clustering of metallic Pb resulted from broken Pb-O bonds, accompanied by formation of oxygen vacancies (OVs) in the UP sample. The absence of such a component in the DW sample indicates that the OVs and the accompanying negative charges developing into the UP sample are a requirement to compensate for the DF and stabilize the P+ FE state. They accumulate close to the PZT surface to create a negative charge sheet, which screens the fixed, polarization charges. In the DW sample featured by P− FE state on the other hand, the DF generated by the fixed negative polarization charges at the PZT surface and positive at the bottom interface with LSMO are screened by the creation of CVs (Pb and Ti).

The observed effect of doping with anion and cation vacancies induced by the FE polarization can be employed for tuning the electronic structure of ferroelectrics for energy conversion, where creating localized electron energy levels is a way to enhance absorption of light in the visible range. Furthermore, the energy levels of the oxygen vacancies (V_Os), if in ferromagnetic clusters and properly aligned in energy, can be used for spin injection in FE heterostructures.

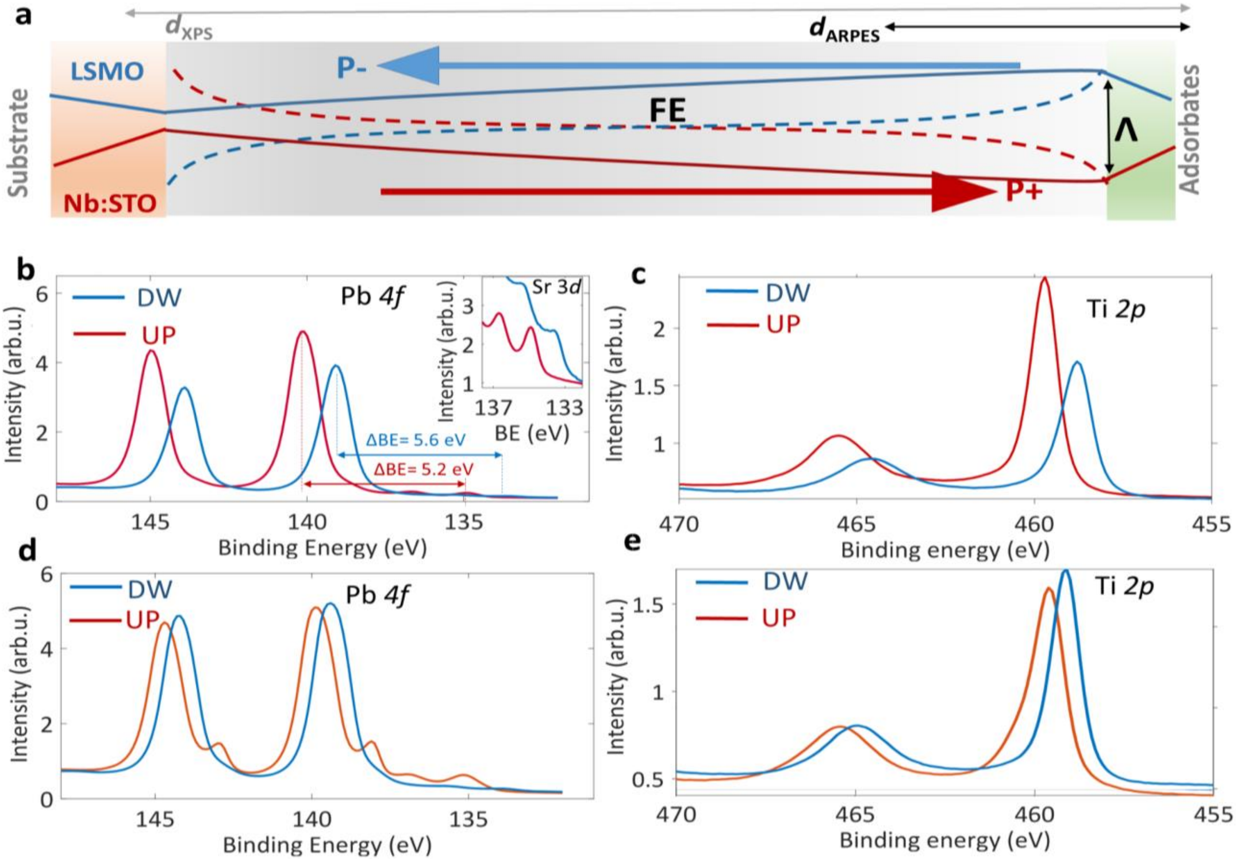

Fig. 2 Band bending mechanism from the core levels. Band bending at the PZT surface as a function of the FE state. (a) Sketch of the band bending potential along the UP and DW samples. (b,c) Pb *4f* and Ti *2p* core level spectra of DW (blue) and UP (red) - samples recorded at 12 K and after 20 mins of continuous exposure to the X-ray beam. The same spectra recorded at room-temperature are presented in (d,e) [6].

References

1. V Garcia, S Fusil, K Bouzehouane, S Enouz-Vedrenne, ND Mathur, ABarthélémy, M Bibes, "Giant tunnel electroresistance for non-destructive readout of ferroelectric states", *Nature* 460, 81–84 (2009).
2. Y Lee, J Park, S Cho, YE Shin, H Lee, J Kim, J Myoung, S Cho, S Kang, C Baig, H Ko, "Flexible ferroelectric sensors with ultrahigh pressure sensitivity and linear response over exceptionally broad pressure range", *ACS Nano* 12, 4045–4054 (2018).
3. J Bernstein, K Houston, L Niles, S Finberg, H Chen, LE Cross, K Li, K Udayakumar, "Micromachined ferroelectric transducers for acoustic imaging", *Proceedings of International Solid State Sensors and Actuators Conference*, 1, INSPEC Accession Number: 5751726, pp. 421–424 (1997)
4. D Li, MH Zhao, J Garra, AM Kolpak, AM Rappe, DA Bonell, JM Vohs,"Direct in situ determination of the polarization dependence of physisorption on ferroelectric surfaces", *Nature Materials* 7, 473–477 (2008).
5. SY Yang, J Seidel, SJ Byrnes, P Shafer, CH Yang, MD Rossell, P Yu, YH Chu, JF Scott, JW Ager III, L W Martin, R Ramesh, "Above-bandgap voltages from ferroelectric photovoltaic devices", *Nature Nanotechnology* 5, 143–147 (2010).
6. DG Popescu, MA Husanu, PC Constantinou, LD Filip, CI Bucur, L Trupina, I Pasuk, CChirila, LM Hrib, L Pintilie, T Schmitt, CM Teodorescu, VN Strocov, "Experimental band structure of Pb(Zr,Ti)O_3: mechanism of ferroelectric stabilization", *Advanced Science* 10, 2205476 (2023).

Ferroelectricity Modulates Polaronic Coupling at Multiferroic Interfaces

Marius A. Husanu[a], Dana G. Popescu[a], Federico Bisti[b], Luminita M. Hrib[a], Lucian D. Filip[a], Iuliana Pasuk[a], Raluca Negrea[a], Marian C. Istrate[a], Leonid Lev[c], Thorsten Schmitt[b], Lucian Pintilie[a], Andrey Mishchenko[d], Cristian M. Teodorescu[a], Vladimir N. Strocov[b]
[a]National Institute of Materials Physics, 405A Atomiştilor 405A, 077125 Magurele, Romania
[b]Swiss Light Source, Paul Scherrer Institute, 5232 Villigen-PSI, Switzerland
[c]Moscow Institute of Physics and Technology, 9 Institutskiy lane, 141700, Dolgoprudny, Russia
[d]RIKEN Center for Emergent Matter Science (CEMS), 2-1 Hirosawa, Wako, 351-0198, Saitama, Japan

The proximity of the hole-doped manganite $La_{0.7}Sr_{0.3}MnO_3$ (LSMO) and a ferroelectric (FE) material with a well-defined orientation of the FE polarization (**P**), provides a local tuning of the doping level close to the interface. Charge modulation in the interfacial region of LSMO occurs in order to compensate for the unscreened depolarizing field due to the discontinuity in the ferroelectric polarization, with its spatial localization related to the Thomas-Fermi screening length. An electrostatic picture of compensating the FE polarization assumes a charge depletion in LSMO when **P** points towards the interface, and a charge accumulation when it points in the opposite direction. However, the final picture of the interface-altered electronic structure extends beyond such simplifying electrostatic-derived arguments.

Our study [1] uses soft X-ray ARPES, whose probing depth matches the interfacial region and whose sharp intrinsic resolution in the out-of-plane momentum k_z allows precise sampling of the 3D **k**-space, to access electronic properties of the LSMO interface buried under thin FE layers of BTO and PZT, which propagate the hole-depletion state into the joining LSMO region. We reveal aspects, which so far remained hidden due to either the extreme surface sensitivity and consequently large k_z broadening of conventional ultra-violet ARPES.

We establish the coexistence of hole-coupled 2D and electron-coupled 3D Fröhlich polarons (FP) in LSMO. Addressing the impact of polaronic coupling on the interface electronic structure is experimentally challenging since most spectroscopic techniques, by probing the whole heterostructure depth, can rarely isolate the contribution of the contact region only. One way of extracting such information is from the spectral function, $A(\mathbf{k},\omega)$, which contains the effect of all many-body (electron-electron and electron-boson) interactions. It is directly accessed by angle-resolved photoelectron spectroscopy (ARPES), with the EPI signature being a dip-hump structure of $A(\mathbf{k},\omega)$ accompanying the quasiparticle peak (QP) at low band filling and kinks in the experimental band dispersion at large occupations of the conduction band. Here, we demonstrate how the polaronic-coupling strength can be tuned by the FE polarization through the preferential occupation of the $e_g(3z^2\text{-}r^2)$ orbitals vs $e_g(x^2\text{-}y^2)$ ones. Such altered orbital occupation modifies in turn the relative electron/hole density and changes their contribution at the screening of the electron-phonon coupling. In addition, our study resolves the subtle balance between hole depletion and electron accumulation which stabilize the well-defined polarization state of the FE top layer in multiferroic heterostructures.

The images in Fig. 1a, b, recorded with 708 eV, represent band dispersions within the cube-like hole pocket of the Brillouin zone (BZ) for bare LSMO (Figure 1a) and for the PZT|LSMO interfaces (Figure 1b). Superimposed on top are the fits of the momentum distribution curves (MDC) maxima through the binding energies (traced by blue dotted line) and the MDCs at E_F (yellow line) whose gradient indicates the Fermi momentum k_F.

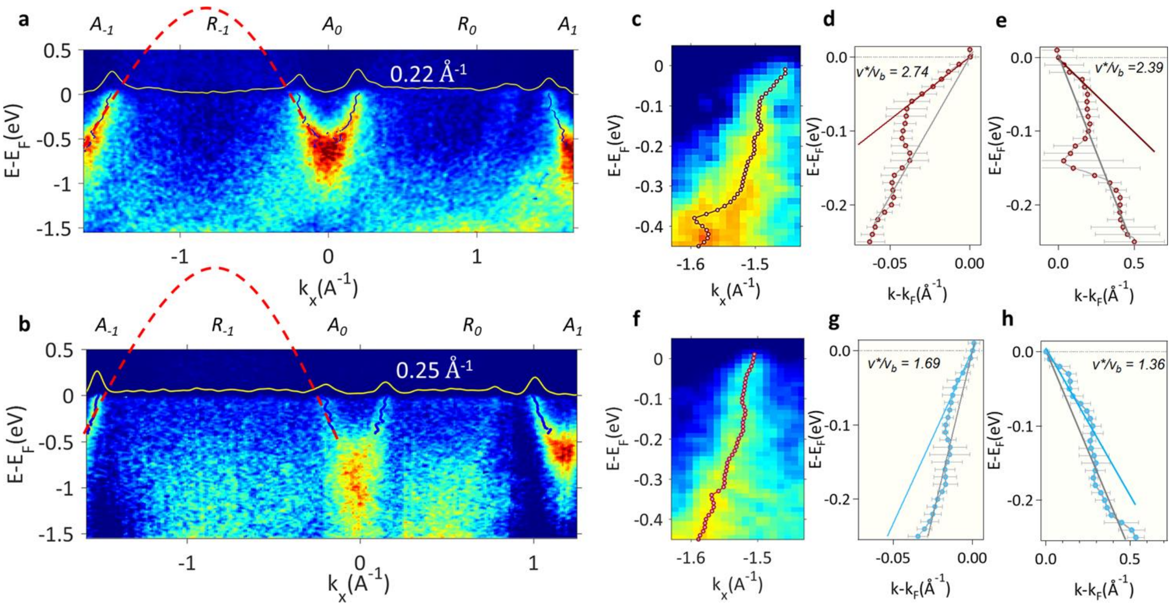

Fig. 1 (a, b) Angle-resolved photoelectron spectroscopy images recorded at the energy hv = 708 eV and p-polarized light along the RAR direction, probing the hole bands for LSMO surface (a), and for PZT|LSMO interface (b). The dots superimposed on each image are the momentum distribution curve (MDC) maxima, with the MDCs at E_F (yellow lines) used to extract the Fermi wavevector (k_F) values. (c) Zoom into the low-energy region of the experimental band structure around $Å^{-1}$ point for LSMO bare surface. (d, e) MDC maxima and their linear fits corresponding to the bare and renormalized dispersions in the kink region for LSMO surface interface around two different points of the Brillouin zone: A_{-1} (d) and A_1 (e). (f) Zoom into the low-energy region of the experimental band structure around A_{-1} point for PZT|LSMO interface. (g, h) MDC maxima and their linear fits corresponding to the bare and renormalized dispersions in the kink region for PZT|LSMO interface around two different points of the Brillouin zone: A_{-1} (g) and A_1 (h).

These results demonstrate that the FE polarization significantly depletes the holes at the LSMO|FE interfaces compared to bare LSMO surface. Such gradual decrease manifests the expected hole-depletion state, induced in the LSMO substrate by the **P**− state of the FE top layer, where the FE field is compensated by carriers from LSMO.

For the electron states, the effect of the FE polarization is clear from the ARPES data presented in Figure 2. The latter compares the ARPES images of the LSMO|PZT interface and of bare LSMO surface recorded at the Mn *2p* resonance along the ΓX direction. They represent band dispersions for the $e_g(3z^2\text{-}r^2)$ derived electron pockets centered at the Γ point through two BZs. The experimental k_F values and the corresponding electron densities, evaluated assuming approximately spherical shape of electron pockets show the increase when going from LSMO to the buried LSMO|PZT interface. Therefore, the FE polarization oriented inwards (P−) results in accumulation of additional electrons in the interfacial region of the LSMO|FE heterostructures compared to the LSMO surface. This in turn modulates the strength of the electron-phonon interaction, thus of the polaronic coupling for both the hole and electron bands. The effect is evident when computing the renormalized Fermi velocities of the hole band at the interface (Figure 1 g,h), showing a reduction of the effective mass by a factor of ~3 compared to the bare surface (Figure 1 d,e). The renormalization effect in the electron band is comparable (Figure. 2d,f) with that observed in the hole band.

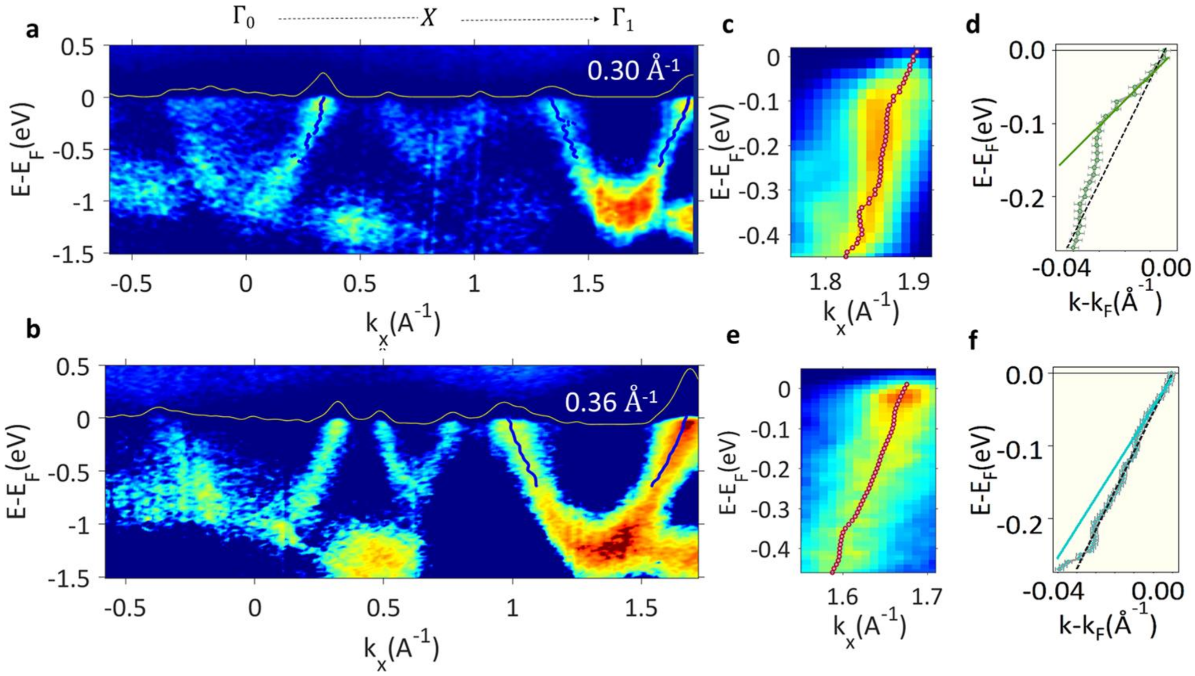

Fig. 2 Angle-resolved photoelectron spectroscopy (ARPES) images recorded with the energy hν = 643 eV and p-polarized light along the ΓX direction, probing the electron bands for LSMO (a) and PZT|LSMO interface (b). (c) Zoom-in of the ARPES images in the low-energy region, with the superimposed red dotted line showing the MDC maxima for LSMO surface. Low-energy MDC maxima and their linear fit corresponding to the bare and renormalized dispersions in the kink region for LSMO surface (d). (e) Zoom-in of the ARPES images in the low-energy region, with the superimposed red dotted line showing the MDC maxima for PZT|LSMO interface. (f) Low-energy MDC maxima and their linear fit corresponding to the bare and renormalized dispersions in the kink region for PZT|LSMO interface.

This finding shows that the light electron accumulation/depletion controlled by the FE state of the top material, and the accompanying better/weaker screening of the EPI is the key player in the modulated polaronic coupling at the FE/LSMO interface. This is because the distribution of the 3D electrons, deriving from a complex interplay between interface potential and mutual dynamic screening, presumably spread larger distances from the interface than the Thomas-Fermi length, providing static screening of slow lattice distortions even far from the interface. Our results thus open novel avenues towards realization of oxide electronic, spintronic, and superconducting devices based on the multifaceted effect of FE polarization on the orbital occupancy, band filling, electron correlations and electron-boson interaction.

References

1. MA Husanu, DG Popescu, F Bisti, LM Hrib, LD Filip, I Pasuk, R Negrea, MC. Istrate, L Lev, T Schmitt, L Pintilie, A Mishchenko, CM Teodorescu, VN Strocov, “Ferroelectricity modulates polaronic coupling at multiferroic interfaces”, *Communications Physics* 5, 209 (2022).

Microscopic Model for Ferroelectricity and its Statistical Treatment II: Variable Dielectric Constant Determined Self-Consistently

Cristian Mihail Teodorescu[a]
[a] National Institute of Materials Physics, 405A Atomiştilor, 077125 Magurele, Romania

Ferroic systems are characterized by long-range ordering of some individual entities. When these individual entities are magnetic moments, their long-range ordering manifests as ferromagnetism or antiferromagnetism. When these entities are electric dipoles, their long-range ordering yields ferroelectric (or anti-ferroelectric) behavior of the material. Elementary statistical physics starts always with a microscopic model expressing the interaction of an entity (moment) with its neighborhood. The Curie-Weiss theory of magnetization starts with the Heisenberg interaction between neighboring magnetic moments (indexed by 1 and 2 in the next equation), expressed in the form $-2J\boldsymbol{S}_1 \cdot \boldsymbol{S}_2$, where $\boldsymbol{S}_{1,2}$ are total atomic spins, connected to the atomic magnetic moment via the gyromagnetic factor (g) and the Bohr magneton (μ_{B}) $\boldsymbol{\mu}_j = -g\mu_{\mathrm{B}}\boldsymbol{S}_j$, and J is the exchange integral. The next step (the mean field theory) is to consider that one spin (say $\boldsymbol{S}_2$) can be replaced by the average spin in the material $\langle \boldsymbol{S} \rangle$, to simplify the problem for spin projections on a single spatial axis, and then to compute this average spin by using statistics, such that:

$$\langle S \rangle = \frac{\sum_{S_1} S_1 \exp\left(\frac{2JS_1\langle S\rangle + g\mu_{\mathrm{B}}S_1 B}{k_{\mathrm{B}}T}\right)}{\sum_{S_1} \exp\left(\frac{2JS_1\langle S\rangle + g\mu_{\mathrm{B}}S_1 B}{k_{\mathrm{B}}T}\right)} \equiv S_0 F\left(\frac{2JS_1\langle S\rangle + g\mu_{\mathrm{B}}S_1 B}{k_{\mathrm{B}}T}\right) \qquad (1)$$

where k_{B} is the Boltzmann constant and T the temperature. This yields an equation of state connecting the average value of the spin (and hence the atomic magnetic moment, *i.e.*, the magnetization) to the temperature and to the applied magnetic field of induction B. When the variable S_1 varies continuously, the ratio between the two sums may be expressed as the Langevin function $F(x) = L(x) = \coth x - 1/x$, when it takes only two values $\pm S_0$ it is $F(x) = \tanh x$, and when it varies between $-S_0$ to $+S_0$ in steps of unity $F(x)$ is the Brillouin function $B_{S_0}(x) = (2S_0 + 1)/(2S_0)\coth\{(2S_0 + 1)x/(2S_0)\} - 1/(2S_0)\coth\{x/(2S_0)\}$.

Until recently, ferroelectricity did not benefit from the existence of a microscopic model, allowing one to perform statistical physics and to derive the equation of state. Theorists affirmed even that the ferroelectric polarization is an ill-defined quantity, since in a polar material elemental dipoles may vary depending on how one performs the ‘pairing’ of positive and negative charges [1], then the only way to obtain some information about the polarization is to connect it to the ‘Berry phase’ accumulated by wavefunctions derived by density functional theory when the crystal evolves from a high symmetry to a low symmetry structure. Clearly, this is not tractable at all, not to speak about the difficulties to integrate in this model external applied fields or temperature effects. A few years ago the author proposed a first model for a microscopic energy usable to perform statistical physics. This is based on the fact that experimentally one observes that in single domain ferroelectric thin films charges are accumulated at external surfaces or interfaces of the film [2,3]. The sign of these accumulated charged layers are opposite to the sign corresponding to the termination of the polar material, thus these layers were denoted as ‘compensating’ for the depolarization field, because in their absence the depolarization field is oriented opposite to the sample polarization and would destroy it.

In Ref. [4] one starts from the hypothesis of the existence of elemental dipoles, attributed to a microscopic region of the material (e.g. the unit cell). The overall interaction of this dipole with all dipoles via the dipole-dipole interaction vanishes for an infinite material. Thus, what remains is the interaction of an elemental dipole with the charges accumulated at surfaces and interfaces of the material exhibiting single-domain ferroelectric ordering. The interaction energy may be written in the form $-Gp_1P/(\epsilon_0\kappa) = -Gp_1n_0\langle p\rangle/(\epsilon_0\kappa)$, where p_1 is the magnitude of the electrical dipole considered, $P = n_0\langle p\rangle$ the polarization, $\langle p\rangle$ the average value of the dipole moment, n_0 the dipole density (or the inverse of the volume of an unit cell), ϵ_0 the vacuum permittivity and κ the dielectric constant of the material. $G(\approx 0.5)$ is a 'geometric factor' introduced to take into account the dipole-dipole interactions in a material which is not infinite and which depends weakly on the tetragonality of the film and on its thickness. The above stabilization energy is on the same form as the Heisenberg interaction in the mean field theory. Then, the accumulated charges at surfaces or interfaces will be denoted as 'stabilizing' charges with the following meaning: '*As soon as a polarizable material or the heterostructure which comprises it may stabilize charges at its surfaces and interfaces, these charges are accumulated, producing the polarization of the material, such that the total energy of this system is lower than in the unpolarized state.*' [4]

Ref. [4] applied the Curie-Weiss theory starting with the above energy for a microscopic dipole and obtained results in good agreement with the experiment, provided the dielectric constant is of several hundreds. (One should add also the interaction of the elemental dipole with an applied external field $-p_1 E$, which is the equivalent of the interaction of an elemental magnetic moment with an applied magnetic field $-g\mu_{\mathrm{B}} S_1 B$). But in fact, recent works derived that the dielectric constant in a ferroelectric could be considerably lower [5]. Also, normally the dielectric constant is linked to the susceptibility of the material, which is obtained from the equation of state. One can then connect the dielectric constant to the static (or global) susceptibility, $\chi_g = P/(\epsilon_0 E)$, E being the applied electric field, or to the differential susceptibility, i.e. $\chi_d = {\epsilon_0}^{-1} \partial P/\partial E$, see Figure 1. It follows that permittivity of the material may be determined self-consistently [6].

The occurrence of the ferroelectric state is linked to the existence of a region of negative (global or differential) susceptibility in the origin, in order to obtain 'S–shaped' $P(E)$ curves which then may offer ferroelectric hysteresis (nonvanishing polarization in zero applied field). Ref. [6] treated several cases: (i) using the global susceptibility; (ii) using the differential susceptibility; (iii) using the differential susceptibility, and taking into account the poling history of the sample. Since only the last model offered reliable results, this will be detailed in the following. The 'poling history' implies that, in order to attain a given polarization at an external electric field $P(E)$, the sample is firstly polarized completely, at saturation (P_s), then the applied field is decreased at the desired value E. This is represented by arrows in Figure 1. Consequently, the stabilization energy corresponding to a given polarization P is written as:

$$\varepsilon_S = -\frac{Gp_0}{\epsilon_0}\left\{\int_0^{P_S} \frac{dP'}{1+\tilde{\chi}_g(P')} + \int_{P_S}^{P} \frac{dP'}{1+\chi_g(P')}\right\} \qquad (2)$$

where $\tilde{\chi}_g$ is the global susceptibility corresponding to the curve of first polarization (blue curve in Figure 1). A first consequence of this model is that the polarization curves do not pass through the origin, therefore there is a polarization imprint and also $\chi_g(0) = 0 \neq \chi_d(0)$. Also, the shape of $\tilde{\chi}_g$ needs not to be known. This model provides a solution with negative differential susceptibility in the origin, but the Curie temperature and the coercive fields derived by this model exceed by several orders of magnitude the usual experimental values. The only way to reconcile the model with experimental values is to consider a 'static permittivity' ϵ_1 exceeding by three orders of magnitude the vacuum permittivity. This can be related to the 'background dielectric constant' proposed some decades ago [7]. Then, a differential equation which may be solved by iterations allows one to derive hysteresis curves with reasonable coercive fields and Curie temperatures:

$$\frac{dE}{dP} = \frac{n_0 k_{\mathrm{B}} T}{{P_S}^2} \cdot \frac{dF^{-1}}{d\left(\frac{P}{P_S}\right)} - \frac{GE(P)}{P+\epsilon_1 E(P)} \qquad (3)$$

where one needs to take into account the bias field, i.e. $E(P=0) = E_0 < 0$. The solutions, however, are quite stable with respect to the choice of E_0 and the coercive fields E_c yield values in good agreement with the experiment. In particular, one obtains numerically a linear decrease of the coercive field with the temperature $E_c(T) \propto T_{\mathrm{C}} - T$, is in agreement with the available experimental observations and different from the result of the Curie-Weiss theory [4].

Hence, by using a few experimentally derived quantities, such as the coercive field at a temperature below the Curie temperature, the saturation polarization and the Curie temperature, one may compute the parameters of the model, in particular the dipole density and the background dielectric constant, and to check additionally the accuracy of the model. The small bias field introduced in the model seems also to have correspondence in reality.

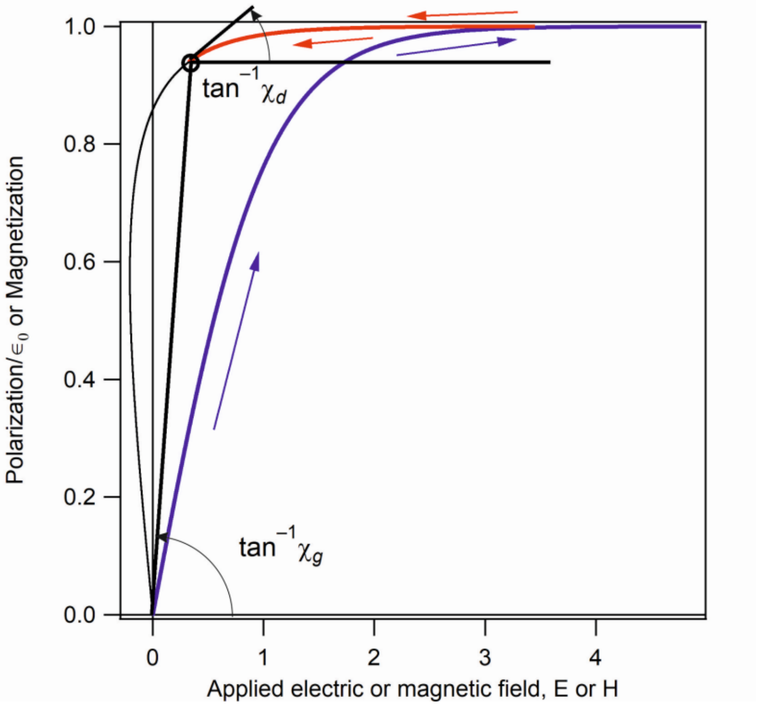

Fig. 1. Scheme to illustrate the global and differential susceptibility corresponding to one point in the $P(E)$ dependence, and the poling process passing through the first polarization curve (blue) and returning on the ‘real’ polarization curve (red).

References

1. NA Spaldin, “A beginner's guide to the modern theory of polarization”, *Journal of Solid State Chemistry* 195, 2–10 (2012).
2. LC Tănase, LE Abramiuc, DG Popescu, AM Trandafir, NG Apostol, IC Bucur, L Hrib, L Pintilie, I Pasuk, L Trupină, CM Teodorescu, “Polarization orientation in lead zirco-titanate (001) thin films driven by the interface with the substrate”, *Physical Review Applied* 10, 034020 (2018).
3. NG Apostol, MA Hușanu, D Lizzit, IA Hristea, CF Chirilă, L Trupină, CM Teodorescu. “CO adsorption, reduction and oxidation on Pb(Zr,Ti)O_3(001) surfaces associated with negatively charged gold nanoparticles”, Catalysis Today 366, 141–154 (2021).
4. CM Teodorescu, “Ferroelectricity in thin films driven by charges accumulated at interfaces”, *Physical Chemistry Chemical Physics* 23, 4085–4093 (2021).
5. CM Teodorescu, L Pintilie, NG Apostol, RM Costescu, GA Lungu, L Hrib, L Trupină, LC Tănase, IC Bucur, AE Bocîrnea, “Low energy electron diffraction from ferroelectric surfaces. Dead layers and surface dipoles in clean Pb(Zr,Ti)O_3(001)”, *Physical Review B* 96, 115438 (2017).
6. CM Teodorescu, “Self-consistently derived sample permittivity in stabilization of ferroelectricity due to charge accumulated at interfaces”, *Physical Chemistry Chemical Physics* 24, 5419–5430 (2022).
7. AK Tagantsev, “The role of the background dielectric susceptibility in uniaxial ferroelectrics”, *Ferroelectrics* 69, 321–323 (1986).

Lifetime Enhancement of Quasibound States in Graphene Quantum Dots *via* Circularly Polarized Light

Adrian Pena[a]

[a]National Institute of Materials Physics, 405A Atomiştilor, 077125 Magurele, Romania

In the recent few years, the electron trapping effects in a graphene quantum dot (GQD) were intensively studied and some methods to achieve them were proposed [1–4]. However, the electron trapping property of a GQD is permanently challenged by Klein tunneling, a striking relativistic process which manifests also in graphene [4]. The observed trapped electronic states, not being literally bound, were called "quasibound states". Generally speaking, a quasibound state is a resonance characterized by a finite lifetime and occur when an electron impacts a GQD, only for some well-defined parameters.

It was revealed that immersing a GQD in magnetic field is a good method to trap electrons [4]. However, the intensity of the magnetic field (B) should be appropriately adjusted in order to generate a quasibound state. The central point of this investigation is to find if a circularly polarized light irradiation may be helpful to induce trapping effects.

In order to study the way that an electromagnetic driving may enhance the electron trapping features of a GQD, a scattering analysis of an electron on a GQD has been performed. The process in question considers an incident electron propagating with energy E towards a GQD subjected simultaneously to a combination of magnetic field and circularly polarized light driving. As the electron interacts with the GQD, it is either reflected outside or transmitted inside the dot region. The analyzed system is schematically depicted in Figure 1.

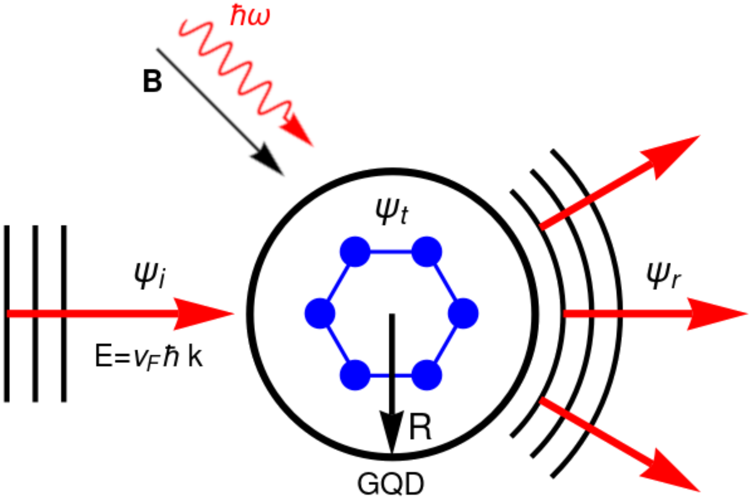

Fig. 1 Scattering of an electron on a GQD in the presence of combined magnetic field and circularly polarized light.

The incident electron which propagates towards the GQD is represented by a plane wave until the impact occurs. However, in a system with a circular geometry, an incident plane wave may be expressed as an infinite sum over all well-defined orbital angular momentum (OAM) states and the interaction with the GQD takes place with a different probability for each state of OAM. The scattering process is described in terms of *scattering modes,* where each scattering mode represents a state of a well-defined l OAM, with $l = -\infty,\ldots,-1,0,1,\ldots,\infty$.

The scattering process is firstly investigated in terms of *scattering efficiency (Q)* [5] which is defined as the scattering cross section divided by the geometric cross section and represents a measure of the interaction strength between the incident electron and the GQD. In the first step, the scattering analysis was performed in the presence of magnetic field, but in the absence of light, for an electron with E = 20 meV. It was observed that the scattering cross section exhibits *resonances* characterized by the existence of quasibound states, as shown in Figure 2 (left). A resonant scattering is described by high values of density inside the GQD, as depicted in the center panel, for l = 4 scattering mode [see green peak within inset (B) in the left panel]. On the other hand, in the case of non-resonant scattering, the incident wave function diffracts on the GQD (see right panel).

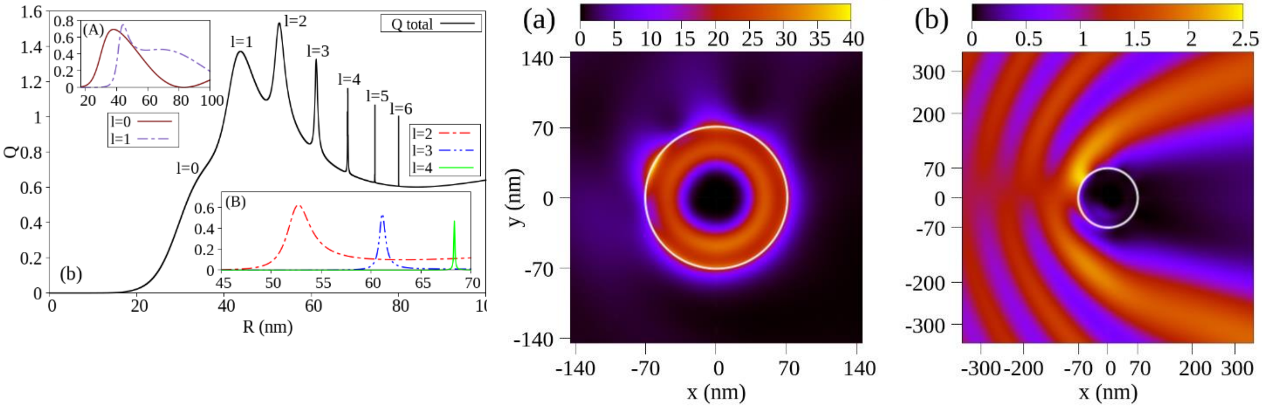

Fig. 2 Scattering analysis in the absence of light. *Left* – Q as a function of R, for B = 2.2 T. *Center* – Density for the case of resonant excitation of l = 4 scattering mode. *Right* – Density in the case of a non-resonant scattering.

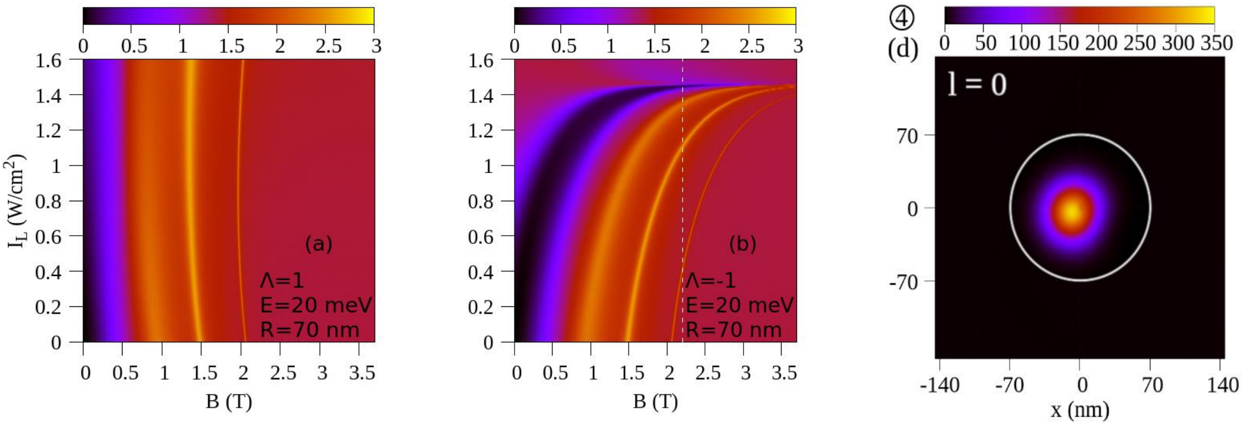

Fig. 3 Scattering analysis in the presence of magnetic field and circularly polarized light. *Left* – Scattering efficiency as a function of B and I_L, for the case of Λ = 1. *Center* – The case of Λ = -1. *Right* – Density in the near field of the GQD for l = 0 scattering mode.

First, a non-resonant configuration was chosen where R = 70 nm and E = 20 meV, in the absence of the light irradiation. In the next step, the light was switched on, in order to observe its effects. Figure 3(left panel) shows the scattering efficiency as a function of B and light intensity (I_L), for the case of positive helicity of the light (Λ = 1). Here, a series of “parallel” resonances may be observed, but the light intensity seems to not influence significantly the scattering. On the other hand, for the case of negative helicity (Λ = -1), the resonances are bending towards higher values of B, as the light intensity increases (see center panel). For instance, if B = 2.2 T, when Λ = 1 no resonance will be encountered. For the case of Λ = -1 an interesting effect happens. The white dashed line, corresponding to a constant B = 2.2 T, crosses one by one each resonance. This behavior translates in the possibility to choose which scattering mode is resonantly excited, by varying the light intensity. In the present case, the first crossed resonance is associated with l = 0 scattering mode and its corresponding density is shown in the right panel, where the trapping effect is obvious.

In the last step, since the scattering resonances are transient phenomena, the lifetime of the identified quasibound states was evaluated. In Figure 4 is presented the calculated lifetime for each resonance encountered at a given B. In both configurations, without light and in the presence of light driving, the trapping time is rising monotonously with B. However, when the light is present, the trapping times rise considerably, especially for large values of B.

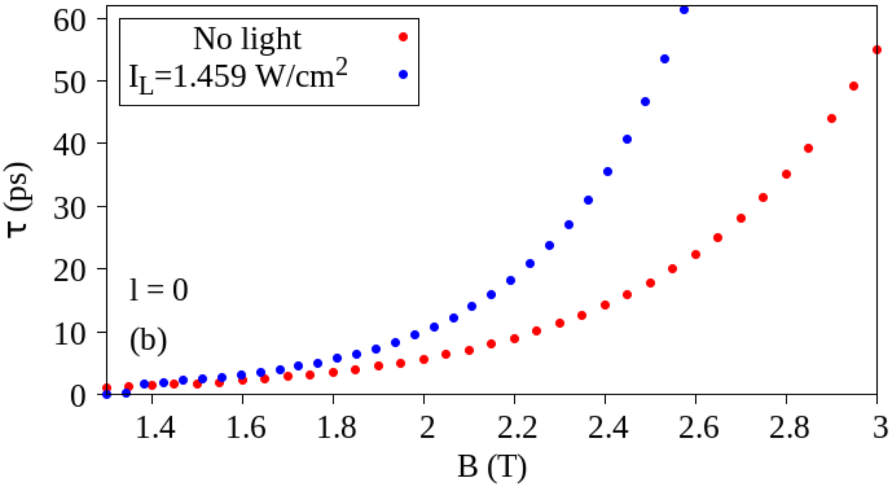

Fig. 4 Trapping time for each resonance identified at a given B.

References

1. J Lee, D Wong, J Velasco, Jr., JF Rodriguez-Nieva, S Kahn, HZ Tsai, T Taniguchi, K Watanabe, A Zettl, F Wang , LS Levitov, MF Crommie, “Imaging electrostatically confined Dirac fermions in graphene quantum dots”, *Nature Physics* 12, 1032 (2016).
2. C Gutiérrez, L Brown, CJ Kim, J Park, AN Pasupathy, “Klein tunnelling and electron trapping in nanometre-scale graphene quantum dots”, *Nature Physics* 12, 1069 (2016).
3. A Pena, “Electron trapping in twisted light driven graphene quantum dots”, *Physical Review B* 105, 045405 (2022).
4. A. Pena, “Electron trapping in magnetic driven graphene quantum dots”, *Physica E: Low-dimensional Systems and Nanostructures* 141, 115245 (2022).
5. MI Katsnelson, KS Novoselov, AK Geim, “Chiral tunnelling and the Klein paradox in graphene”, *Nature Physics* 2, 620 (2006).

The Ferromagnetic Nature of the Earth’s Innermost Solid Core

Cristian Mihail Teodorescu[a], Marius Adrian Hușanu[a]
[a]National Institute of Materials Physics, 405A Atomistilo, 077125 Magurele, Romania

The geomagnetic field screens the Earth’s surface from fluxes of charged particles from the cosmic radiation. This is essential for the development of complex organisms and for our actual electricity-based civilization. On long term, the Earth’s surface bombardment with charged particles could yield to the depletion of the atmosphere, as in the case of planet Mars, which does not benefit from a planetary magnetic field. It is also a proven fact that periodically the magnetic poles of the Earth are reversed [1]. More than one hundred field reversals during the last one hundred million years (My), and the last one that has occurred about 780,000 years ago. The duration of a field reversal is on the order of 1,000 to 8,000 years, which is low at the geological scale, but still enough to induce irreversible mutations in evolved species and to destroy all electronics on Earth, if during these reversals the geomagnetic field would considerably decrease. Apocalyptic scenarios related to the decrease of the geomagnetic field were discussed in wide audience books [2] and made the subject of large box office movies, such as *The Core* (Jon Amiel, Horsepower Films, 2003).

There is a general consensus that the geomagnetic field is produced by a complex rotation-convexion motion of the planet’s liquid core, supplied by the progressive solidification of the melt into the inner solid core, the so-called ‘geodynamo’ model [3–5]. Consistent efforts to develop this model and to use it in sophisticated simulations are motivated by the need to predict the next geomagnetic reversal, in order to mitigate its influence on our technology and even on the fate of complex organisms on Earth. It is, however, to be noticed that (i) during the last hundred field reversals complex organisms on Earth did not suffer sensibly (during the Jurassic, Cretaceous, Paleogene, Neogene or Quaternary periods) and (ii) the Cambrian explosion of life forms which occurred about 530–541 My ago seems to have been preceded by the formation of the Earth’s inner solid core, about 565 My ago [6]. From here, one can connect the occurrence of the geomagnetic field to the existence of the solid core of the planet and infer that probably no considerable decrease of its magnitude takes place during the reversals of the magnetic poles. Remark also that the Earth’s magnetic field is predominantly dipolar. These empirical statements were fundamented recently by a new theory of band ferromagnetism [7]. This new approach reconsiders Stoner’s theory, by taking into account the total electronic energy in the conduction band and not just their kinetic energy, knowing that in the case of a spin asymmetry the bottom of the conduction band is shifted towards lower energies for majority spin electrons and towards higher energies for minority spin electrons. As a consequence, for constant density of states (DOS), all metals have lower electronic energies in the state with maximum allowed spin asymmetry. In fact, DOSs from 3d metals are far from being constant, then a model with two peaks in the DOS was set up, the peaks being attributed to e_g or to t_{2g} states from crystal field theory, with the ordering of these peaks in energy depending on the crystal structure. This simple model allowed one: (*i*) To derive the most stable crystal structures amongst 3d metals. (*ii*) To derive a new criterion for ferromagnetism, written at zero temperature as:

$$\left(\frac{dg_0}{d\varepsilon}\right)(\varepsilon_\mathrm{F})\int_0^{\varepsilon_\mathrm{F}} g_0(\varepsilon)d\varepsilon < {g_0}^2(\varepsilon_\mathrm{F}) \qquad (1)$$

where $g_0(\varepsilon)$ is the paramagnetic DOS, *i.e.*, in absence of spin asymmetry. Note that the occurrence of spin asymmetry is solely dictated by the shape of DOS, there is no need to introduce another ordering term in the form of a Hubbard interaction, as in the Stoner model. (*iii*) To prove which phases are ferromagnetic, *i.e.* bcc Fe, hcp Co and fcc Ni among the stable phases, and also hcp Cr [8], fcc Mn [9] and bcc Co [10] amongst metastable phases. (*iv*) To explain the low coercive fields of metals by a sudden reversal of the role of majority and minority electrons in applied fields, induced by the conservation of electron number and knowing that at the Fermi level the DOS for majority and minority electrons are different for spin-split states. (*v*) Temperature dependence is easy to be implemented, and the model predicts Curie temperatures in agreement with experimental values for bcc Fe and hcp Co, which was not the case in the Stoner model. (*vi*) At very high temperatures, exceeding 5,000 K, metals (Fe, Co, Ni) become again ferromagnetic. We call this behavior *re-entrant ferromagnetism*.

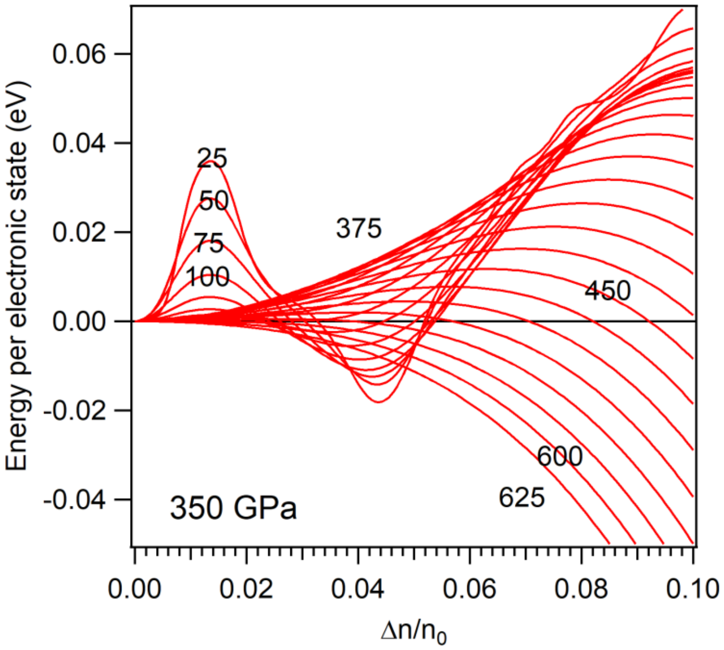

Fig. 1. Energy difference between the spin-polarized state and the spin-unpolarized state, as function of the asymmetry in the electron density between majority and minority spins, for 350 GPa pressure applied to the hexagonal close-packed iron and for several temperatures. The numbers on some curves represent $k_B T$, in milielectronvolts.

This re-entrant ferromagnetism, predicted with a model DOS, as described above, was reconsidered for ε-Fe (hcp structure) by using real DOS derived by ab-initio density functional theory (DFT) in Ref. [11], since it seems that this phase is the most stable in the Earth's inner solid core. DFT computations were performed at pressures up to 360 GPa, which is the stipulated pressure in the Earth's center. The result was in line with the predictions with the model DOS with two peaks (e_g, t_{2g} in order of increasing energy). Total energies can be easily computed starting with the computed DOS by integrating the DOS times the Fermi-Dirac distribution. Then, one may derive the energy difference between the spin-split state and the paramagnetic case and check whether this energy difference is negative, which implies that the ferromagnetic state is the most stable one. An example for such a computation for 350 GPa is given in Figure 1. From such computations, transition temperatures from the ferromagnetic (FM) to paramagnetic (PM) states (at lower temperatures, i.e. the Curie temperatures) can be derived, together with temperatures for PM → FM (re-entrant ferromagnetism) transitions. These are represented in Figure 2 as function of the pressure. By comparing the transition temperatures for the re-entrant ferromagnetism with the temperature profiles stipulated inside the Earth's core (and taking also into account the pressures), together with the magnitude of the atomic magnetic moments and then of the re-entrant magnetization, compared with the intensity of the magnetic field at the Earth's surface, one infers that in fact not the whole inner solid core (with estimated diameter 1,200 km) of the planet is ferromagnetic, but just a part of it (the 'innermost inner core' IMIC), with radius of about 200 km. The existence of the IMIC with a similar size was also inferred from the propagation asymmetry of seismic waves [12]. Note also that a similar (DFT + temperature dependence) calculation by using bcc Fe provided no re-entrant ferromagnetism, so maybe this structure has to be ruled out, at least when speaking about the IMIC.

There are then solid grounds to suppose that the Earth's inner core (or its IMIC) acts like a permanent magnet due to its extremely high temperature which favors the re-entrant ferromagnetism in the new theory of band ferromagnetism. Consequently, the reversal of the magnetic poles proceeds most probably by rotation of this ferromagnet, animated by effects of the outer liquid core and/or by external magnetic fields (solar eruptions, magnetic planetoids approaching the Earth, etc.). The amplitude of the geomagnetic field would not decrease during pole reversal, the Earth's surface will be still protected from the influence of charged particles, the atmosphere will not be depleted, complex life forms will not suffer, nor our electronics. We hope that these are good news, exceeding the community of planetary magnetism.

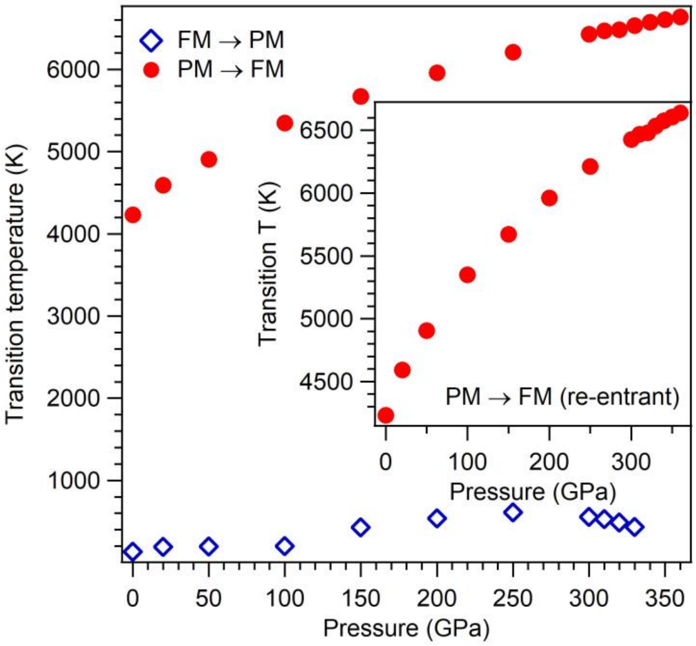

Fig. 2. Main graph: temperatures for the ferromagnetic → paramagnetic transition (Curie temperature), empty blue diamonds; and for the paramagnetic → ferromagnetic transition ('re-entrant ferromagnetism'), red full circles, for ε–Fe. The insert presents an enlarged view for the transition temperature for 're-entrant ferromagnetism'.

References

1. SC Cande, DV Kent, "Revised calibration of the geomagnetic polarity timescale for the Late Cretaceous and Cenozoic", *Journal of Geophysical Research: Solid Earth* 100, 6093–6095 (1995).
2. A. Mitchell, "The Spinning Magnet: The Electromagnetic Force That Created the Modern World – and Could Destroy It", Dutton, New York, 2018.
3. GA Glatzmaier, PH Roberts, "Rotation and magnetism of Earth's inner core", *Science* 274, 1887–1891 (1996).
4. GA Glatzmaier, RS Coe, L Hongre, PH Roberts, "The role of the Earth's mantle in controlling the frequency of geomagnetic reversals", *Nature* 401, 885–890 (1999).
5. BA Buffet, "Earth's core and the geodynamo", *Science* 288, 2007–2012 (2000).
6. RK Bono, JA Tarduno, F Nimmo, RD Cottrell, "Young inner core inferred from Ediacaran ultra-low geomagnetic field intensity", *Nature Geoscience* 12, 143–147 (2019).
7. CM Teodorescu, "Spin asymmetry originating from densities of states: Criterion for ferromagnetism, structures and magnetic properties of 3d metals from crystal field based DOSs", *Results in Physics* 25, 104241 (2021).
8. M Albrecht, M Maret, J Köhler, B Gilles, R Poinsot, JL Hazemann, JM Tonnerre, C Teodorescu, E Bucher, "Ferromagnetic hcp chromium in Cr/Ru(0001) superlattices", *Physical Review Letters* 85, 5344–5347 (2000).
9. Y Huttel, CM Teodorescu, F Bertran, G Krill, "Experimental evidence of long range magnetic order in the c(2×2) MnCu(100) surface alloy", *Physical Review B* 64, 094405 (2001).
10. M Izquierdo, ME Dávila, J Avila, H Ascolani, CM Teodorescu, MG Martin, N Franco, J Chrost, A Arranz, MC Asensio, "Epitaxy and magnetic properties of surfactant-mediated growth of bcc cobalt", *Physical Review Letters* 94, 187601 (2005).
11. CM. Teodorescu, MA Huşanu, "Re-entrant ferromagnetism at ultrahigh temperatures in epsilon–iron as possible origin of the geomagnetic field", *Physics of the Earth and Planetary Interiors* 326, 106856 (2022).
12. J Stephenson, H Tkalčić, M Sambridge, "Evidence for the innermost inner core: Robust parameter search for radially varying anisotropy using the neighbourhood algorithm". *Journal of Geophysical Research: Solid Earth* 126, e2020JB020545 (2021).

Interface Effects in 2D Topological Heterostructures

Bogdan Ostahie[a], **Alexandru Aldea**[a]
[a]National Institute of Materials Physics, 405A Atomistilor, 07715 Magurele, Romania,

Using two peculiar topological materials, Chern insulator and Weyl semimetal, the spectral and quantum transport properties of 2D heterostructures are theoretically analyzed. The specific behavior at the interfaces between different constituents of the heterostructure is provided by the external magnetic field and internal symmetries of the system. The combination of the topological edge state in the Chern insulator with the edge states originating from the Landau levels gives rise to a complex energy spectrum, and consequently to a multitude of new transport effects. Depending on the internal design of the system in a four terminal device the quantum Hall resistance may lack the negative plateaus, exhibit fractional values, include zero-value plateau.

In the quantum Hall regime, due to the interfaces constructed inside the finite lattice, the current streams not as it were along the borders, but moreover along the interfacing. In this way, one produces the alternate route of a few of the terminals connected to the finite lattice, and, as a result fragmentary levels of quantum Hall effect rise. Such a control of the edge states was gotten in graphene by applying an in-plane electrical bias [1]. Another strategy is to construct p/n junctions in quantum wells with inverted bands (HgTe/CdTe, InAs/GaSb) using local gates [2], [3], [4]. In this paper, we take after another situation by considering the lateral heterostructure interfacing that emerge by joining materials with distinctive topologies, to be specific the Chern insulator and Weyl semimetal. We approach the investigation of the heterostructure in the finite geometry with single or double junctions, which is closer for the point of view of experimental situations.

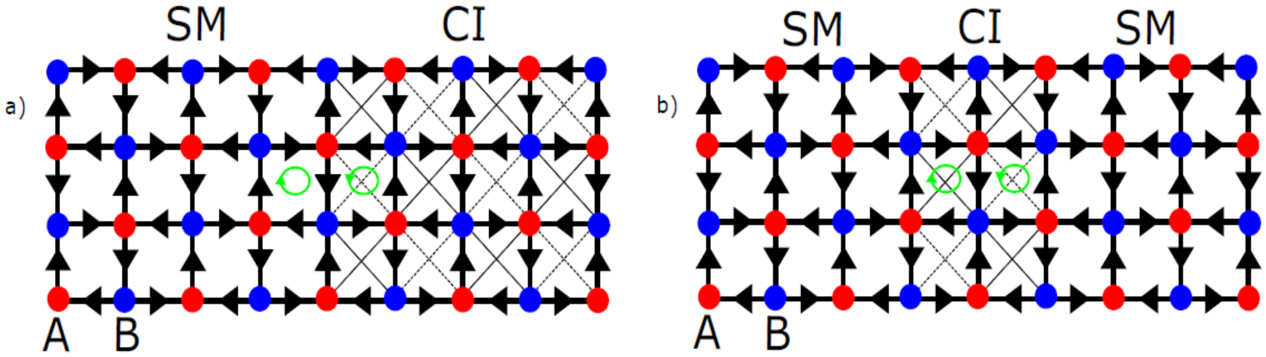

Fig. 1 Schematic representation of the diatomic lattice with two atoms per unit cell: A(red), B(blue): a) heterostructure consisting of semimetal (SM) and Chern insulator (CI) with a single interface and b) heterostructure with two interfaces consisting of SM/CI/SM. The arrows represent the phase associated with the hopping element t_1, and the green circles represent the sign of the local fluxes and the second-order hopping elements t_2 are represented vwith dotted and solid lines.

To better understand the formation of conduction channels near the edges and interfaces of the system, we analyzed the energy spectrum in the ribbon geometry. We studied the SM/CI heterostructure, considering that the upper part of the ribbon is in the Chern insulator phase and the lower part is in the Weyl semimetal phase. Such an approach involves imposing periodic conditions on the direction parallel to the interface between the two phases. Considering the two types of systems separately (semimetallic and Chern insulator) in perpendicular magnetic field we obtain the energy spectra in Figure 2. The energy spectrum of the semimetallic phase shows chiral symmetry, while in the presence of perpendicular magnetic field the Chern insulator phase loses this property. By joining the two types of ribbon in an SM/CI heterostructure we obtain an energy spectrum as in Figure 3, where reminiscences of the two initial spectra in Figure 2 can be observed.

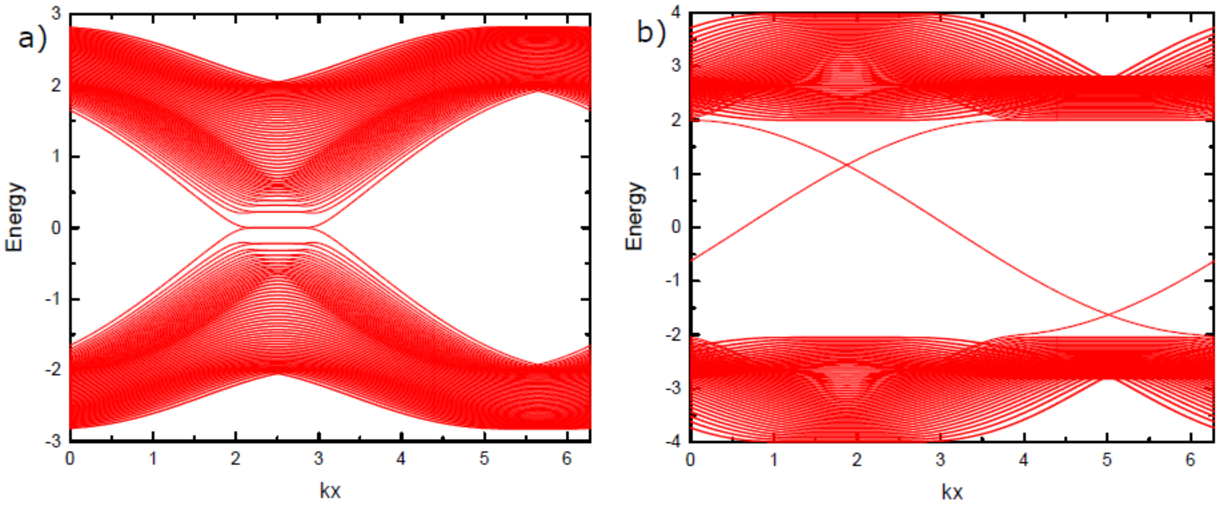

Fig. 2 Energy spectrum in ribbon geometry for a semimetal (a) and a Chern insulator (b) as a function of kx in the presence of the perpendicular magnetic field. In the case of figure (a), similarities with the energy spectrum of the graphene ribbon with armchair edges are observed. In the case of figure (b), the Chern-type edge states in the gap lose their electron-hole symmetry when the perpendicular magnetic field is applied.

Figure 3 shows the localization of the edge states for energy E=0.2. At this energy there are four edge states labeled A, B, C, D, and their localization at the edge of the system or at the interface is shown on the right side of the figure. In terms of chirality it is observed that edge states A and B have opposite chirality compared to states C and D. In direct space, the location and chirality of the current channels in the ribbon-type heterostructure are related with the localization of the edge states. In the case of a system with hard wall boundary the conduction channels must form closed circuits.

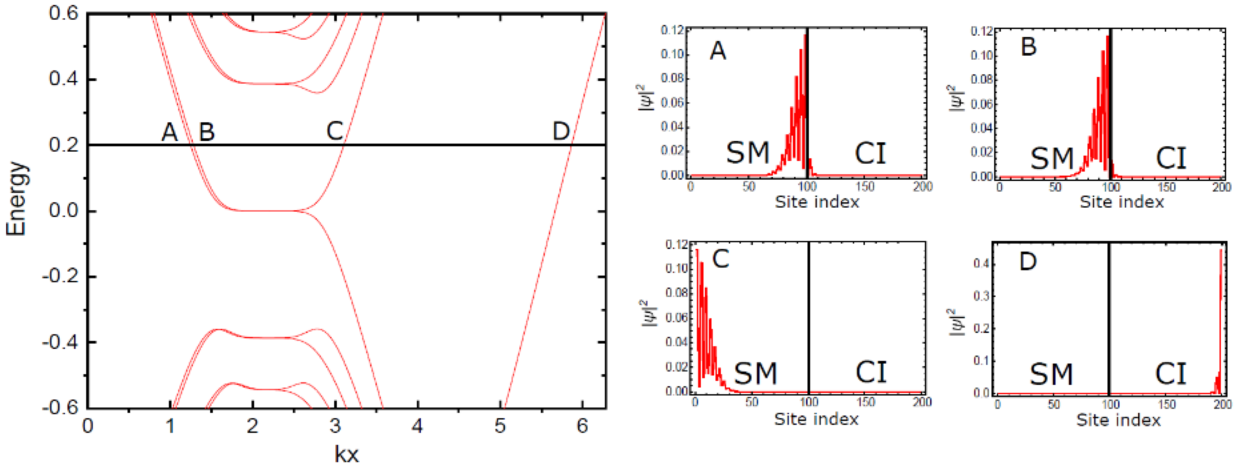

Fig. 3 The energy spectrum of the SM/CI ribbon in the perpendicular magnetic field as a function of kx (left). The black line at energy E=0.2 (chosen between Landau levels n=0 and n=1) intersects the spectrum at four points denoted by (A, B, C, D). The localization of the corresponding wave functions is shown on the right side according to the site index.

The numerical calculation of the transport properties is based on the Landauer-Büttiker formalism simulating a Hall device with four terminals. In the SM/CI heterostructure it is evident that the edge states populating the gaps of the heterostructure spectrum look different compared to those of the homogeneous material, resulting in strongly modified quantum transport properties. The case of a single junction is shown in Figure 4a, where new features of the quantum Hall resistance can be observed: (*i*) absence of negative plateaus; (*ii*) null value of the Hall resistance in the first gap of positive energies; and (*iii*) fractional values in all other gaps.

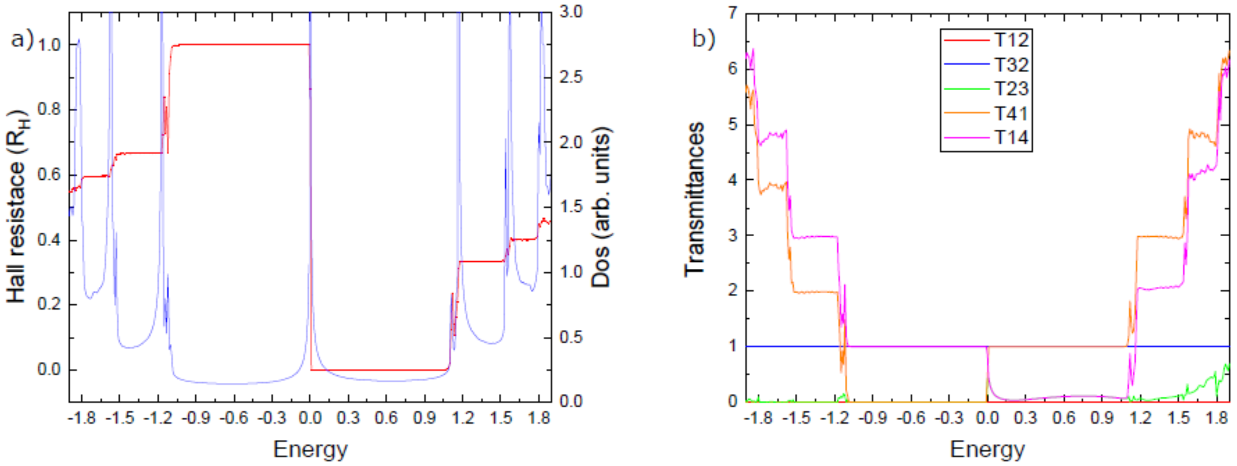

Fig. 4 (a) Hall resistance RH and the density of states Dos, (b) calculation of the transmission coefficients between various terminals.

Inspecting the spectrum in Figure 4a one notes that the vanishing of RH may be related to the edge states of alternating chirality. Also, the RH=0 due to the ridge in the middle of the system that cause vanishing of the transmission coefficients $T12$, $T21$, $T34$, $T43$. The absence of negative plateaus of the quantum Hall resistance can be understood by observing that, except for the spectral gap considered above, in all other gaps of the spectrum the edge states have the same chirality, which corresponds to a positive Hall resistance. The general expression of fractional values of the quantum Hall resistance can be understood using the numerical data of the transmission coefficients and constructing the transmission matrix [5].

References

1. B Ostahie, M Nita, A Aldea, “Electrical manipulation of edge states in graphene and the effect on quantum Hall transport”, Physical Review B 91, 155409 (2015).
2. GM Gusev, AD Levin, ZD Kvon, NN Mikhailov, SA Dvoretsky, “Quantum Hall effect in n-p-n i and n-2D topological insulator-n junctions”, *Physical Review Letters* 110, 076805 (2013).
3. MR Calvo, F de Juan, R Ilan, EJ Fox, AJ Bestwick, M Muhlbauer, J Wang, C Ames, P Leubner, C Brune, SC Zhang, H Buhmann, LW Molenkamp, D Goldhaber-Gordon, “Interplay of chiral and helical states in a quantum spin Hall insulator lateral junction”, *Physical Review Letters* 119, 226401 (2017).
4. M Karalic, C Mittag, T Tschirky, W Wegscheider, L Ensslin, T Ihn, “Lateral p-n junction in an inverted InAs/GaSb double quantum well”, *Physical Review Letters* 118, 26801 (2017).
5. B Ostahie, A Aldea, “Interface effects on the energy spectrum and quantum transport in two-dimensional topological heterostructures”, *Applied Surface Science* 587, 152769 (2022).

Chemically/Electrochemically Functionalization of Black Phosphorous Sheets with Diphenylamine and Poly(diphenylamine)

Mihaela Baibarac[a], Teodora Burlanescu[a], Malvina Stroe[a], Ion Smaranda[a], Catalin Negrila[a]
[a]Laboratory of Optical Processes in Nanostructured Materials, National Institute of Materials Physics, 405A Atomistilor, 077125 Magurele, Romania

The composites based on black phosphorus (BP) and organic or macromolecular compounds has allowed the development of new applications in the fields of information storage, delaying flame ignition, cancer therapy, rechargeable Li and Na batteries, photocatalysis, gas sensors and field effect transistors [1 and their references]. In this study [1], we report the synthesis of new composites which involve: a) the chemical functionalization of BP with diphenyl amine (DPA) by the solid-state interaction when the BP concentration in the mass of DPA/BPA mixture was varied from 0 wt.% to 0.5 wt.% and 1 wt.%; and b) the electrochemical functionalization of BP with poly(diphenylamine) (PDPA), by the electrochemical oxidation of 10^{-2} M DPA, 10^{-3} M $H_3PW_{12}O_{40}$ x H_2O (PTA) and 1M HCl in the semi-aqueous solution of dimethylformamide (DMF) and H_2O having the volumetric ratio of 1:1. The potential range used for recording the first five cyclic voltammograms was (+100; +960) mV *vs.* Ag/AgCl, the scanning rate of the potential being equal to 50 mV/s. Figure 1 shows the FTIR and PL spectra of DPA in initial state and after functionalization of BP sheets with DPA.

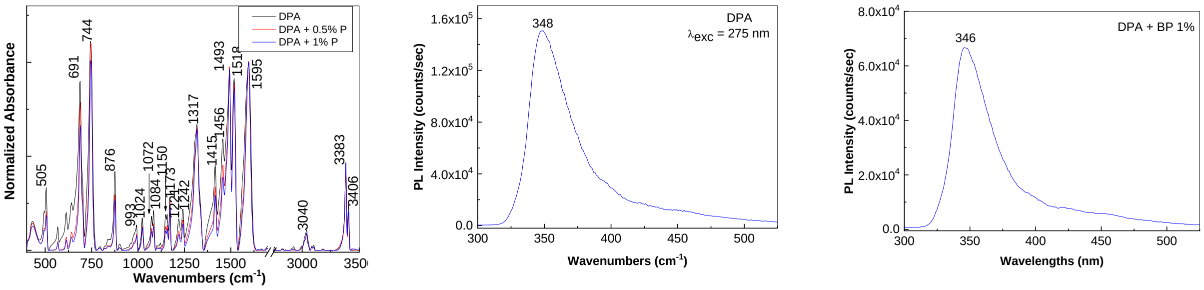

(a) (b) (c)

Fig. 1 (a) The IR spectra of DPA before (black curve) and after the interaction with BP; the BP concentration in the DPA/BP mixture being equal to 0.5 wt. % (red curve) and 1 wt.% (blue curve). The PL spectra of DPA before (b) and after the interaction with BP 1 wt.% (c), when the excitation wavelength is 275 nm [1].

The IR spectrum of DPA is characterized by bands with maxima at ~691−744, 876, 1173, 1242, 1317, 1415, 1456−1493−1518, 1595 and 3383 cm^{-1} (Figure 1a) attributed to the vibrational modes: out-of-plane deformation of benzene ring, deformation benzene ring, C−H bond, stretching of the C−N bond, C−H bond, N−H bond + C−H bond, C−C + C−H + N−H stretching, C−C bond stretching in the benzene ring and N−H bond, respectively [2]. In the presence of BP, a gradual decrease in the absorbance of the IR bands localized at 691−744 cm^{-1} and 876 cm^{-1} is observed. The PL spectra of DPA and DPA/BP are characterized by a band with a maximum at 348 and 346 nm with intensity equal to 1.51×10^6 counts/sec (Figure 1b) and 6.68×10^4 counts/sec (Figure 1c), respectively. The lower intensity of the PL spectra in Fig. 1c in comparison with Figure 1b indicates a quenching process of the DPA PL induced by BP sheets. The decrease in the absorbance of the IR bands localized at 691−744 and 876 cm^{-1} can be explained by the interaction of BP with DPA, when during the chemical interaction takes place a covalent functionalization of the BP layers with DPA, which leads to an intercalation of DPA between the BP layers, a part of BP layers being thus exfoliated. The reaction product corresponds to the iminophosphorene-type structure, this resulting according to Scheme 1.

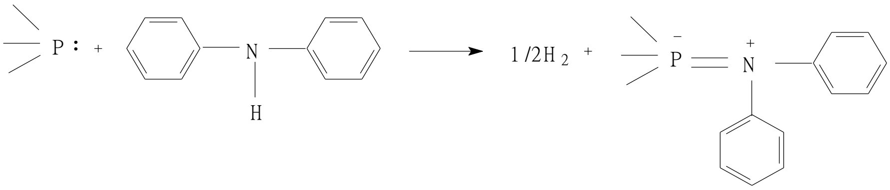

Scheme 1. The interaction of DPA with BP [1].

Figure 2 shows IR spectra of the composite resulted by the electrochemical oxidation of the DPA chemical functionalized BP sheets.

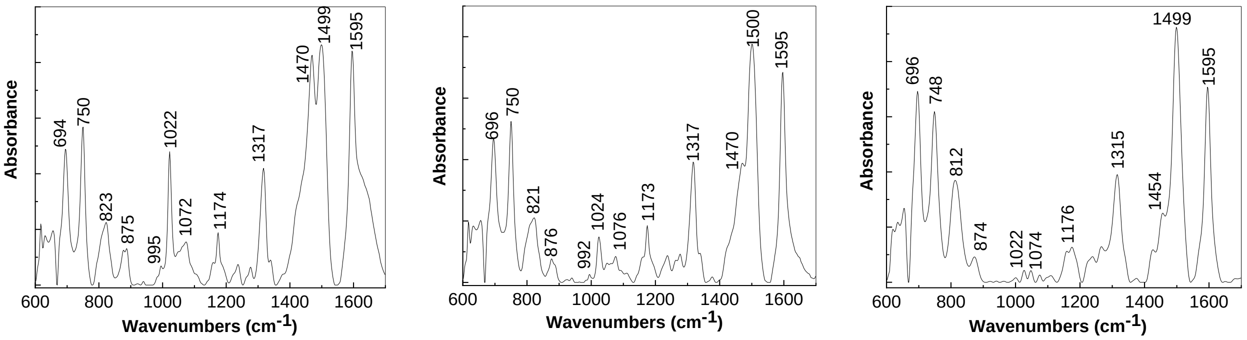

(a) (b) (c)

Fig. 2 IR spectra of the composite resulted by the electrochemical oxidation of the DPA chemical functionalized BP sheets when the concentration of BP in DMF in the synthesis mixture is 0.5 mg/mL (a),) and 0.1 mg/mL (b). Figure (c) shows the IR spectrum of PDPA doped with the PTA heteropolyanions [1].

Figures 6a,b highlight the following changes in the case of the composite resulted by the electrochemical oxidation of the DPA chemical functionalized BP sheets: (*i*) a shift of the maximum of the IR band from 812 to 823 cm^{-1}; (*ii*) an increase in the absorbance of the IR bands located at 1022 and 1072−1076 cm^{-1}; and (*iii*) a shift of the IR band from 1454 to 1470 cm^{-1} simultaneously with the change of the ratio between the absorbances of the IR bands from 1454-1470 and 1499 cm^{-1}. In Figure 6c, it can be seen that the IR spectrum of PDPA doped with the PTA heteropolyanions is characterized by the IR bands having maxima at 696, 748, 812, 874, 922, 1022, 1074, 1176, 1315, 1454, 1499 and 1595 cm^{-1}, these being attributed to the vibrational modes of the inter-ring deformation, ring deformation, $W-O_c-W$ (O_c corresponds to oxygen from the corner of the heteropolyanion structure), $W-O_e-W$ (O_e corresponds to oxygen from the side of the heteropolyanion structure), W=O, deformation of the quinoid ring, the stretching of the P−O−W bond, the C−H bond in the benzene (B) ring, $C_{aromatic}$ - N, the stretching of the C=N + C−H bond in the benzene ring, the stretching of the C−C bond in the benzene (B) ring + the stretching vibration of the C=C bond in the quinoid ring (Q) and the stretching of the C=C bond in the $-NH^+=Q=Q=NH^+-$ structure, respectively [3−5]. These variations can be explained taking into account the increase of the covalent bonds number between the BP sheets and DPA-type structural units, when effects of steric hindrance are induced to both the quinoid rings and the PTA heteropolyanions which compensates the existing positive charges on the PDPA macromolecular chain. In order to understand the chemical structure of composites resulted by the electrochemical oxidation of DPA chemical functionalized BP sheets, Scheme 2 will show the reactions which allows the macromolecular chain growth, *i.e.*, of dimers, tetramers and PDPA.

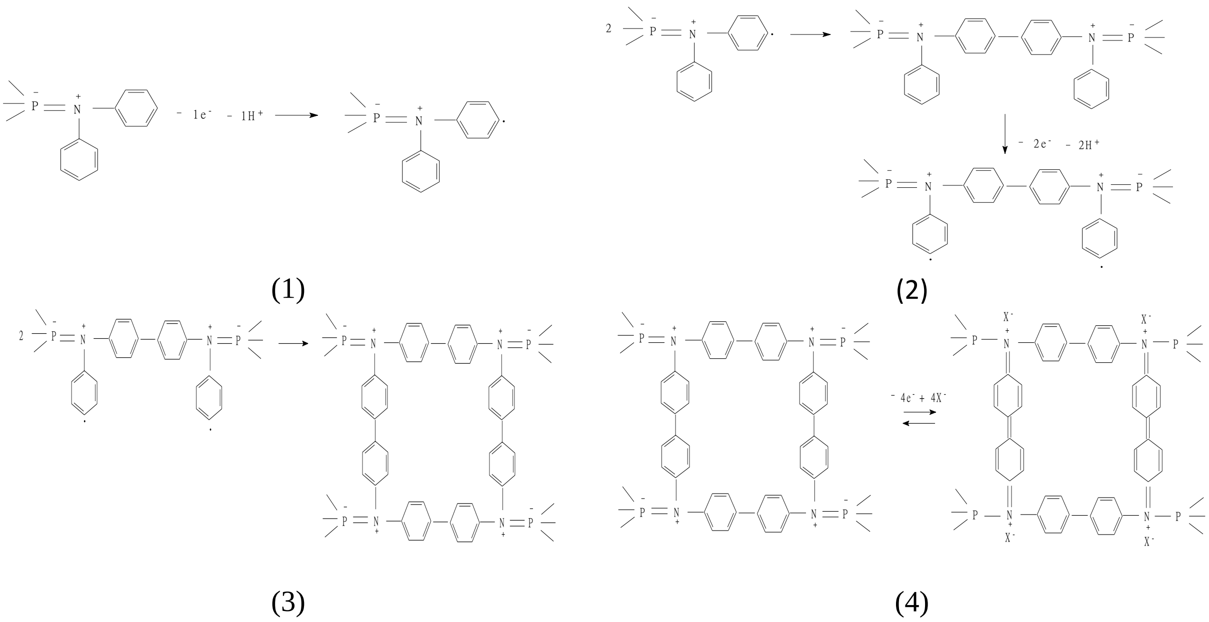

Scheme 2. The reactions describing the electrochemical oxidation reactions of the DPA chemical functionalized BP sheets, which leads to composites of the type pf BP sheets electrochemical functionalized with macromolecular compounds having repeating units of the type DPA doped with PTA heteropolyanions (X- corresponds to the PTA heteropolyanion) [1].

Summarizing these results, the IR spectroscopy and photoluminescence were two valuable tools to highlight the chemical and electrochemical functionalization of BP with DPA and PDPA, respectively.

References

1. M Baibarac, T Burlanescu, M Stroe, I Smaranda, C Negrila, "The photoluminescence and vibrational properties of black phosphorous sheets chemically/electrochemically functionalized in the presence of diphenylamine", *Polymers* 14, 4478 (2022).
2. J Kang, JD Wood, SA Wells, JH Lee, X Liu, KS Chen, MC Hersam, "Solvent exfoliation of electronic-grade, two dimensional black phosphorus", *ACS Nano* 9, 3596–3604 (2015).
3. S Quillard, G Louarn, S Lefrant, AG Macdiarmid, "Vibrational analysis of polyaniline: A comparative study of leucoemeraldine, emeraldine, and pernigraniline bases", *Physical Review B* 50, 12496–12508 (1994).
4. CT Kuo, WH Chiou, "Field-effect transistor with polyaniline thin film as semiconductor", *Synthetic Metals* 88, 23–30 (1997).
5. H de Santana, MLA Temperini, J Rubim, "*In situ* resonance Raman and reflectance spectroscopic study of the electrochemical oxidation of diphenylamine", *Journal of Electroanalytical Chemistry* 356, 145–155 (1993).

Correlated Studies of Photoluminescence, Raman scattering and FTIR Spectroscopy on Photodegradation of Pharmaceutical Compounds: Insights on the Photodegradation Mechanism

Mirela Paraschiv[a], Monica Dinescu[a], Ion Smaranda[a], Cristina Stefania Florica[a], N'ghaya Toulbe[a], Madalina Chivu[a], Mihaela Baibarac[a], Radu Cercel[a], Irina Zgura[a], Adelina Udrescu[a], Paul Ganea[a], Catalin Negrila[a], Cristina Bartha[a], Bogdan Chiricuta[b], Alexandru Trandabat[c], Corina M. Manta[d], Romeo Ciobanu[e]

[a]National Institute of Materials Physics, 405A Atomistilor, 077125 Magurele, Romania
[b]SC Apel Laser SRL, 25 Vanatorilor St, 077135 Mogosoaia, Romania
[c]SC Intelectro Iasi SRL, 700470 Iasi, Romania
[d]SARA Pharm Solutions S.R.L., 266 – 268 Calea Rahovei, 050912 Bucharest, Romania
[e] SC All Green SRL, 8 George Cosbuc Str., 700470 Iasi, Romania

This work reports the photodegradation of pharmaceutical compounds of the type losartan potassium (LP), pantoprazole sodium (PS), ampicillin (AM) and azathioprine (AZA) in the presence of various compounds such as NaOH and sodium thiosulfate (ST). In this order, correlated studies of photoluminescence (PL), Raman scattering and FTIR spectroscopy will be shown. Thus, Figure 1 shows the photoluminescence excitation (PLE), PL and FTIR spectra of LP interacted with NaOH under UV light.

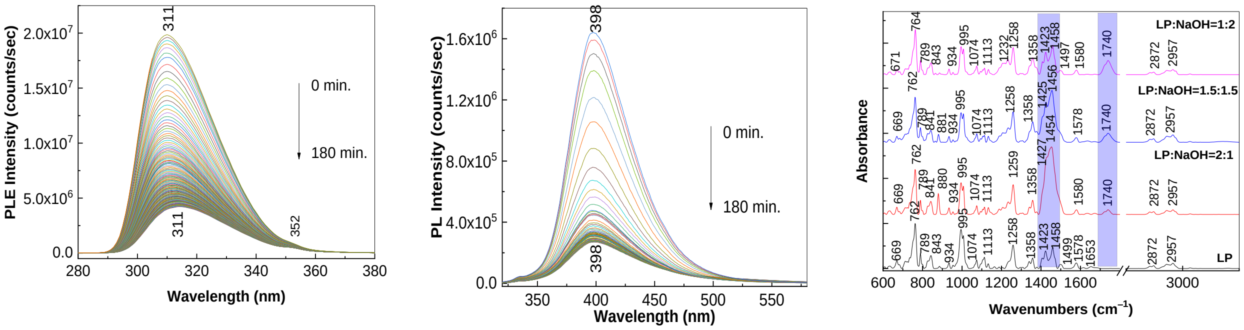

(a) (b) (c)

Fig. 1 (a) The evolution of PLE (a) and (b) PL spectra of NaOH-reacted LP under UV light, when the volumetric ratio of the LP (5mg/ml) and NaOH 1.5M is 1:2. (c) IR spectra of LP (black curve) and NaOH-reacted LP when the volumetric ratio LP:NaOH is 2:1 (red curve), 1.5:1.5 (blue curve) and 1:2 (magenta curve). [1].

The effect of UV light on the NaOH-reacted LP, time of 3 hours, consists in the decrease of the intensity of the PLE spectrum, from.98 × 10^7 counts/sec to 4.22 × 10^6 counts/sec (Figure 1a), and the PL spectrum, from 1.64 × 10^6 counts/sec to 2.65 × 10^5 counts/sec (Figure 1b). The reaction of LP with NaOH is proved by the following changes highlighted in Figure 1c: (*i*) the appearance of the IR band at 1740 cm^{-1}, which indicates the generation of a degradation product containing the functional groups having the C=O bonds [1], whose intensity increases with the NaOH volume in the LP : NaOH mixture; (*ii*) a variation of the ratio between the IR bands absorbance at (*a*) 995 and 1454–1458 cm^{-1}; and (*b*) 1258–1259 and 1454–1458 cm^{-1}, from 1.9 and 1.14 (Figure 1c, black curve) to 0.47 and 0.44 (Figure 1c, red curve), 0.57 and 0.58 (Figure 1c, blue curve) as well as 0.95 and 0.92 (Figure 1c, magenta curve); and (*iii*) a decrease of the ratio between the IR bands absorbance localized at 1423–1427 cm^{-1} and 1454–1458 cm^{-1}, associated to the vibrational modes: (*i*) C–N stretching in tetrazole ring and C–H wagging at imidazole ring and C–H scissor between benzoic and imidazole ring; and (*ii*) C–O–H bending and C–H scissor in the alkyl chain, respectively, from 0.83 (Figure 1c, red curve) to 0.77 (Figure 1c, blue curve) and 0.76 (Figure 1c, magenta curve), values which are smaller than that reported for LP (0.86, Figure 1c, black curve).

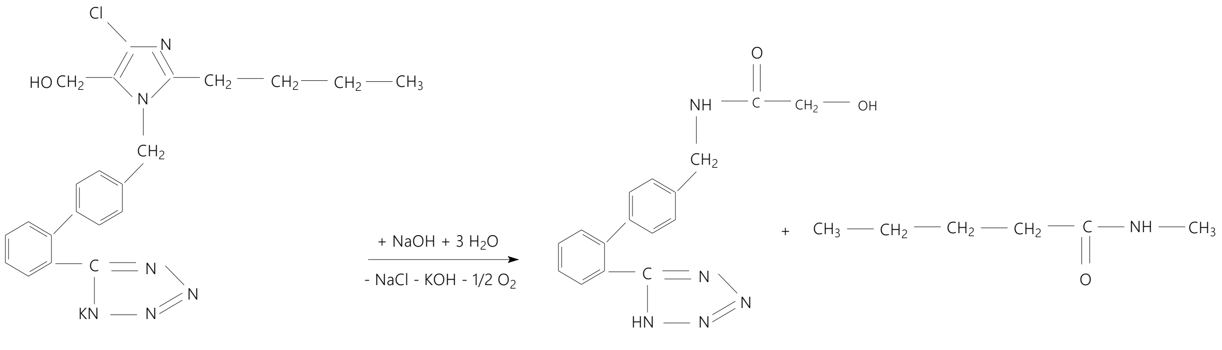

(1) (2) (3)

Scheme 1. The photodegradation reaction of LP in the presence of the NaOH aqueous solution.

Figure 2 shows the PL and Raman spectra of PS which has interacted with NaOH. The exposure of the NaOH reacted PS sample to UV light has as effect a diminution of the PL band intensity from 2.1×10^6 counts/sec to 2.72×10^5 counts/sec (Figure 2).

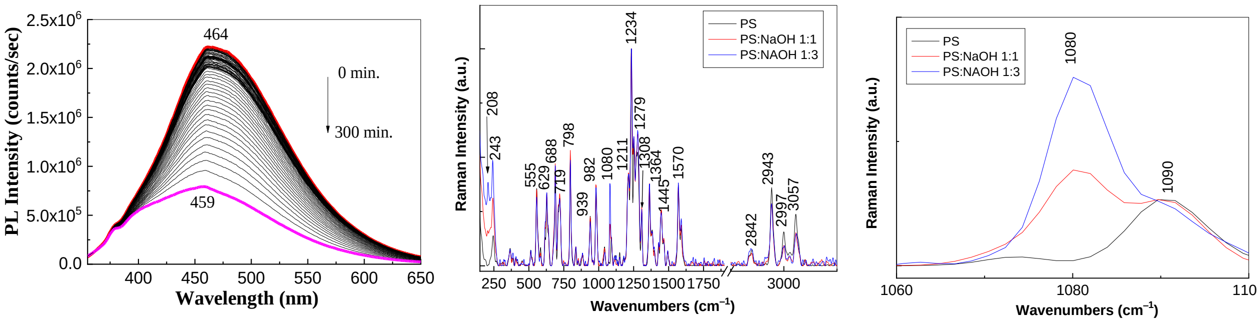

(a) (b) (c)

Fig. 2 PL spectra of PS interacted with NaOH (0.3M) when the volumetric ratio is equal to 1:2 (a).Raman spectra, in the 100–3500 cm^{-1} (b) and 1060–1100 cm^{-1} (c) spectral ranges, of PS (1) (curve black) and NaOH-reacted PS (1), when the weight ratio between PS (1) and NaOH was of 1:1 (red curve) and 1:3 (blue curve) [2].

The reaction of PS with NaOH, when the weight ratio of the two constituents is equal 1:1 and 1:3, leads to the appearance of a new line at 1080 cm^{-1}, the intensity ratio of the Raman lines peaked at 1080 and 1090 cm^{-1} is equal to 1.45 and 2.85, respectively. The Raman line at 1080 cm^{-1} is assigned to the alkoxide group vibrational mode [2]. This Raman line has been also reported in the sodium salt of carboxylic compounds [2]. As increasing the NaOH weight used in the NaOH-reacted PS, in Figure 2 a new line at 208 cm^{-1} is observed. This line not belongs to NaOH. The early studies have reported that NaOH shows a Raman line at 215 cm^{-1} [2]. We attribute the Raman line at 208 cm^{-1} to the ONa vibrational mode. The Raman line at 2842 cm^{-1} was reported to be attributed to the crystalline structure of PS dihydrate [2]. These changes indicate the emergence of the photo-degradation products were 5-difluoromethoxy-3H-benzimidazole-2-thione sodium and 2-oxy-methyl- 3, 4-dimethoxypyridine sodium salt.

Figure 3 shows the PL and Raman spectra of the AM reacted with NaOH. The PL spectrum of AM shows an emission band peaked at 450 nm having the intensity of 6.02×10^3 counts/sec. The UV exposure of the sample induce an increase in the PL band intensity up to 2.15×10^4 counts/s. The assignment of the Raman lines of AM (Figure 3b) were shown in Ref. [3]. The Raman spectrum of the AM: NaOH sample (Figure 3c) highlights that: (*i*) the most intense Raman line is peaked at 1004 cm^{-1}; (*ii*) the emergence of new Raman lines peaked at 1080, 1394 and 1630 cm^{-1}; (*iii*) a down-shift of the Raman line from 1188 cm^{-1} to 1184 cm^{-1}; (*iv*) a significand intensity decrease in the Raman line at 2939 cm^{-1} so that the intensities ratio of the Raman lines from 2941 to 2939 and 3064 to 3062 cm^{-1} ($I_{2941–2939}/I_{3064–3062}$) varies from 16.16 (Figure 3b) to 0.67 (Figure 3c); and (*v*) the disappearance of the Raman line at 781 cm^{-1}. These changes were explained considering the hydrolysis reaction of AM, when the following compounds are resulted: 2-amino-2-phenyl acetate sodium, 2-amino- 3,3-

dimethyl-7-oxo-4-thia-1-azabicyclo [3.2.0] heptane-2-carboxylic acid and α-aminobenzylpenicilloic acid sodium salt [8].

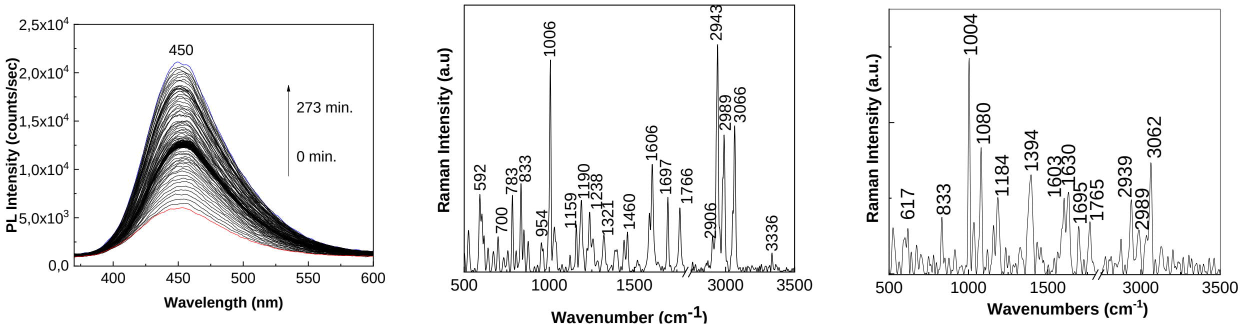

(a) (b) (c)

Fig. 3 PL spectra of AM reacted with NaOH, when the volumetric ratio AM: NaOH is equal to 1:2 (a). Raman spectra of AM (b) and NaOH-reacted AM (c). The insert of (b, c) shows the Raman spectra after the baseline correction.

Figure 4 shows the PL and FTIR spectra of AZA interacted with ST. After exposure of the AZA:ST sample, time of 10 h, one observe a shift of the PL band from 503 to 531 nm and an increase in the intensity of PL band from 1.18×10^4 counts/s to 8.3×10^4 counts/s. The AZA photodegradation in the presence ST is highlighted in Figure 4 b by a downshift of the IR band of AZA from 1336 to 1331 cm^{-1}, attributed to the N–C–N deformation vibrational mode in the purine ring is a consequence of the transformation of the -N=CH–NH- bonds into the -NH–C(O)–NH- bonds.

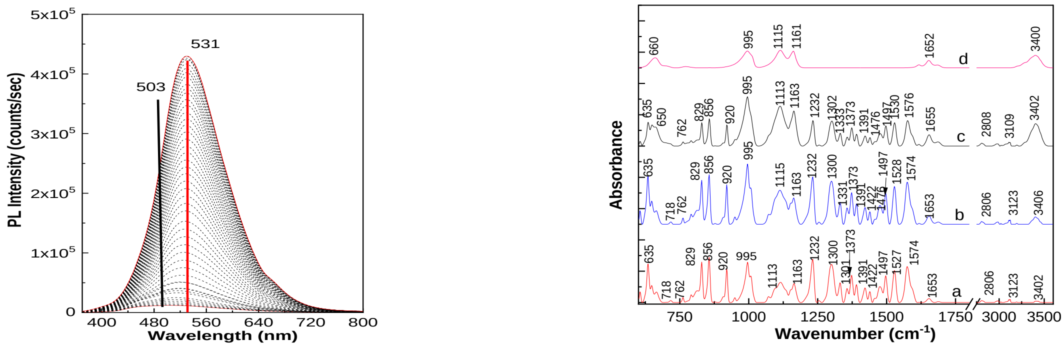

(a) (b)

Fig. 4 PL spectra of the AZA:ST sample with a ST concentration of 75 wt.% (a), recorded at λ_{exc} = 300 nm. Blue and red curves indicate the PL spectra of samples in dark conditions and after an UV exposure time of 600 min. Black curves correspond to PL spectra collected after every 130 s of UV irradiation. IR spectra of the ST-reacted AZA samples with ST concentrations in the reaction mixture of 25 wt.% (b, curve a), 50 wt.% (b, curve b) and 75 wt.% (b, curve c), as well as ST (b, curve d).

The results above shown indicate that the photoluminescence, Raman scattering and FTIR spectroscopy are valuable tools for the assessing of the drug photodegradation processes.

References

1. M Paraschiv, I Smaranda, I Zgura, P Ganea, M Chivu, B Chiricuta, M Baibarac, "Degradation of losartan potassium highlighted by correlated studies of photoluminescence, infrared absorption spectroscopy and dielectric spectroscopy", *Pharmaceutics* 14, 2419 (2022).
2. M Baibarac, M Paraschiv, R Cercel, I Smaranda, C Bartha, A Trandabat, "Correlated studies of photoluminescence, vibrational spectroscopy and mass spectrometry concerning the pantroprasole sodium photodegradation", *Scientific Reports* 12, 9515 (2022).
3. R Cercel, M Paraschiv, CS Florica, M Daescu, A Udrescu, RC Ciobanu, C Schreiner, M Baibarac, "New aspects concerning the ampicilline photodegradation", *Pharmaceuticals* 15, 415 (2022).
4. N Toulbe, I Smaranda, C Negrila, C Bartha, CM Manta, M Baibarac, "Photodegradation of azathioprine in the presence of sodium thiosulfate", *International Journal of Molecular Sciences* 23, 3975 (2022).

Molecular Dynamics of Alkyl Benzoate Liquid Crystals in the Bulk State and in their Composites with Oxide Nanopowders

Ligia Frunză[a], Irina Zgură[a], Constantin Paul Ganea[a], Andreas Schönhals[b]
[a]Laboratory of Optical Processes in Nanostructured Materials, National Institute of Materials Physics, 405A Atomistilor, 077125 Magurele, Romania
[b]Federal Institute of Materials Research and Testing (BAM), D-12205 Berlin, Germany

In this study [1] the results obtained on monotropic nematic liquid crystals 4-pentylphenyl 4'-alkyl benzoate (5PnB) (n = 3 or 5 carbon atoms in the alkyl chain) are presented. The mesophases of 4-pentylphenyl 4-alkyl benzoate (5PnB) liquid crystal are revealed by the polarized optical microscopy (POM) images. Figure 1 presents some images by POM taken during cooling at several temperatures around the I-to-N transition temperature.

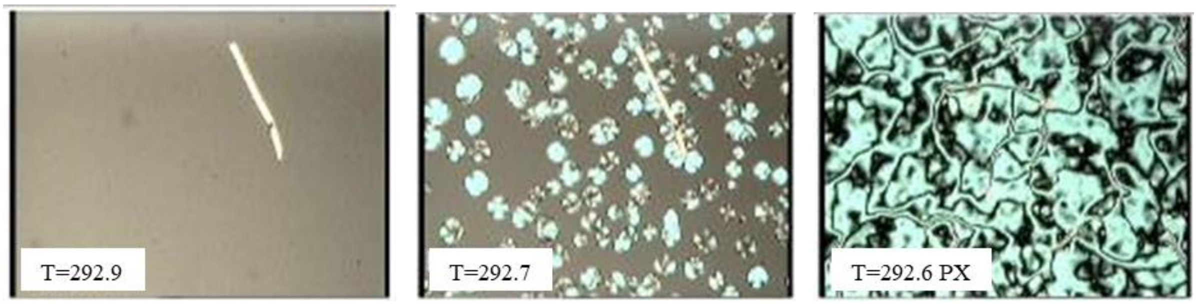

Fig. 1 Optical images at different temperatures around the I-to-N transition, for the bulk samples 5P3B; PX-Crossed polarizers (see ref. [1]).

Molecular dynamics in the bulk samples or in composites prepared with Aerosil A380 was investigated by broadband dielectric spectroscopy over a large temperature range. The dielectric spectra (Figure 2a,b) of bulk LCs (5P3B and 5P5B) present two relaxation processes in the temperature range of the nematic phase, and at least one extended process in the isotropic region.

The dielectric behavior changes at the phase transition. Two processes indicated by peaks in ε'' are observed in the dielectric spectra in the temperature range of the bulk liquid crystal phase. They are due to the anisotropic structure of the material. The process at lower frequencies is due to rotational fluctuations of the molecule around its short axis, while the relaxation at higher frequencies occurs due to different modes of flipping around the long axis.

The dielectric properties of the composites (Figure 2c,d) are essentially different from those of the bulk liquid crystal. In the case of composites, a single relaxation process is observed indicated by a peak of the dielectric loss while two relaxation processes were observed in the bulk. The dielectric loss maximum shifts to higher temperatures with increasing temperature. The relaxation process observed for the composites is attributed to the molecular mobility of the 5PnB molecules adsorbed on the aerosil particles in a surface layer.

Thus, from the dielectric spectroscopy measurements on the composites, it became clear that there is only one main relaxation process at much lower frequencies compared to those obtained on the bulk material, this being attributed to the dynamics of the molecules in the surface layer.

The relaxation rate, $f_p(T)$ is much lower for the composites than that in the bulk (Figure 3), in both the nematic and the isotropic state and no discontinuities in the temperature dependent of the relaxation rates at the phase transition of bulk are observed.

The composites with silica/LC ratio higher than 7 do not show phase transition showing in addition the preparation homogeneity. This is the signature of the monolayer. No discontinuities in the temperature dependence of the relaxation rates are observed at the phase transition of corresponding bulk.

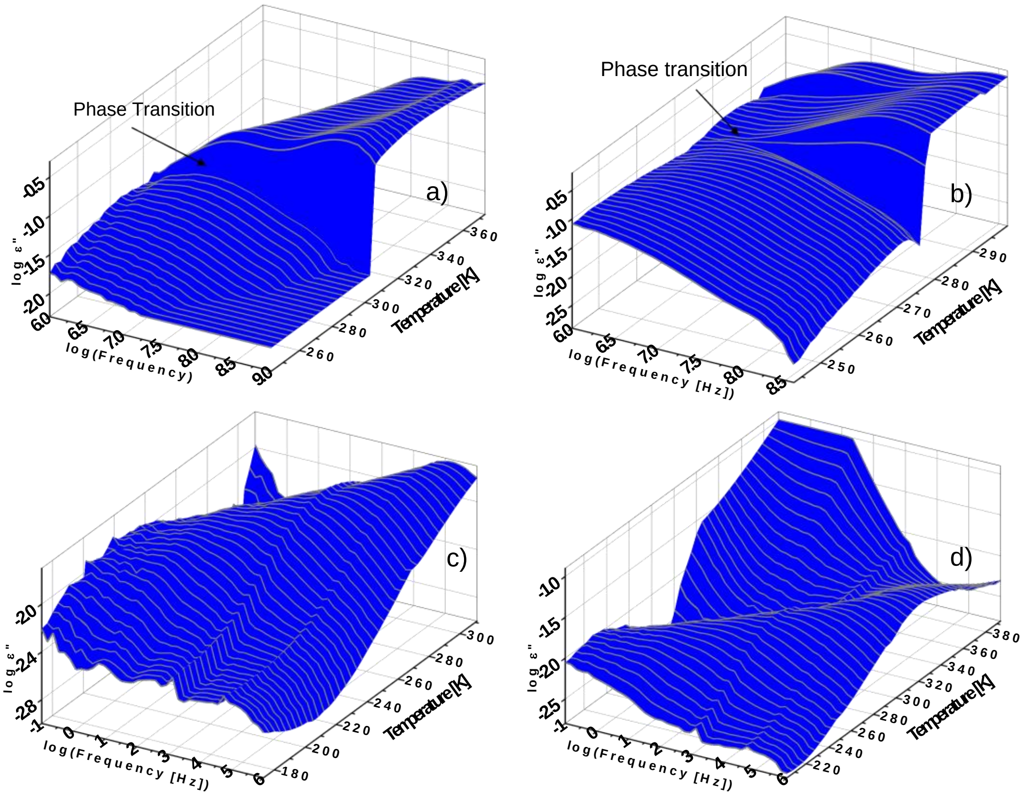

Fig. 2. Dielectric loss spectra as ε'' *vs.* frequency and temperature for the samples: (a) bulk 5P3B; (b) bulk 5P5B; in the high frequency domain; (c) composite 5P3B/A380(12); and (d) composite 5P5B/A380(12), in the low frequency domain. (see ref. [1]).

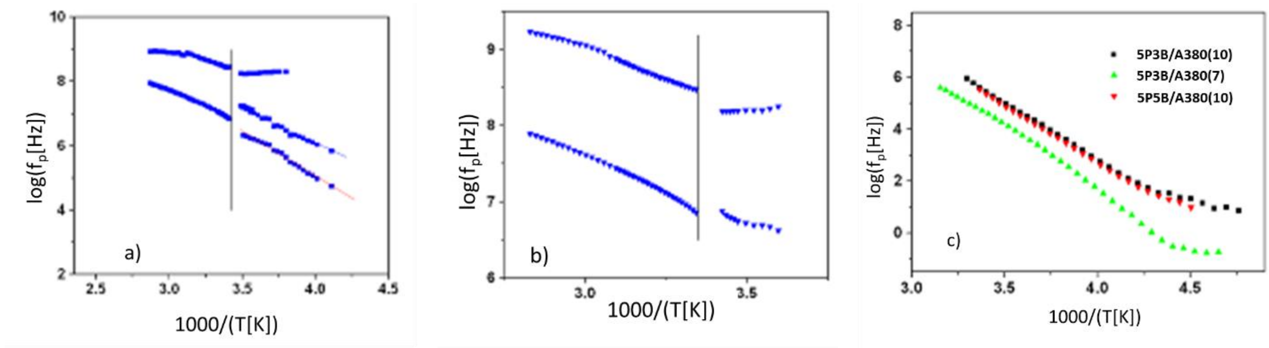

Fig. 3 Temperature dependence of the characteristic frequencies for: (a) bulk 5P3B; (b) bulk 5P5B; and (c) composites. The vertical lines show the found transition temperatures (see ref. [1]).

This relaxation process is assigned to the molecular dynamics of 5PnB molecules adsorbed in a surfaces layer onto the silica particles. FTIR spectra indicate that phenyl benzoate molecules strongly interact with the aerosil surface *via* hydrogen bonds involving the ester C=O groups.

References

1. L Frunza, I Zgura, CP Ganea, A Schönhals, “Molecular dynamics of alkyl benzoate liquid crystals in the bulk state and in the surface layer of their composites with oxide nanopowders”, *Journal of Molecular Liquids* 359, 119374 (2022).

Europium (II)-Doped CaF_2 Nanocrystals in Sol-Gel Derived Glass-Ceramic: Luminescence and EPR Spectroscopy Investigations

Corina Elisabeta Secu[a], Catalin Negrilă[a], Arpad Mihai Rostas[a,b], Mihail Secu[a]
[a]National Institute of Materials Physics, 405A Atomistilor, 077125 Magurele, Romania
[b]National Institute for Research and Development of Isotopic and Molecular Technologies, 67-103 Donat, 400293 Cluj-Napoca, Romania

The optical performances of Eu^{2+}-activated phosphors have attracted significant attention because of the remarkable properties related to the broad and intense luminescence of Eu^{2+} ions ([1] and references therein) and related applications in lighting and display areas, scintillator detectors, X-ray storage phosphors for digital imaging applications and persistent phosphors [1]. The optical performances are related to the broad and intense Eu^{2+} ion fluorescence, which is due to the 5d-4f parity allowing transition and is strongly dependent on the host lattice. In particular, there is an increased and renew interest in CaF_2:Eu^{2+} nanophosphor, optical properties and related applications: scintillators, particles detectors, and dosimetry [2]

Among the physico-chemical preparation methods of the nanophosphors, sol-gel chemistry offers a flexible and controllable approach for the synthesis of RE^{3+}-doped nanocrystalline materials and in particular oxyfluoride nano-glass ceramics, where the optically active fluoride nanocrystals are embedded within an amorphous silicate glassy matrix. Through a controlled nucleation and crystallization processes of the initial xerogel, the partition of the optically active RE^{3+}-ions into the precipitated fluoride nanocrystals is reached, accompanied by high transparency and remarkable luminescence properties ([3,4] and references therein). Up to now, the research efforts of oxyfluoride glass-ceramics were focused only on optical properties of the trivalent RE^{3+}-doped luminescent fluoride nanocrystals ([3] and references therein) and the optically active bivalent RE^{2+} -ions (such as Eu^{2+} and Sm^{2+}) has just only recently been reported in the literature [5].

In the present case we have prepared Eu^{2+}/ Eu^{3+}-doped $95SiO_2$–$5CaF_2$ sol-gel derived oxyfluoride glass ceramics by using metal alkoxides and trifluoroacetic acid as in-situ fluorination agent [6]; nanocrystalline phase precipitation is obtained during calcination at 800 °C [5,6].

The X-ray diffraction (XRD) patterns of Eu^{3+}-doped ($95SiO_2$–$5CaF_2$) glass-ceramics showed extra-diffraction peaks assigned to the CaF_2 nanocrystalline cubic phase precipitation in the glass matrix [5,6] (not shown). The lattice parameter a = 5.515 Å is different from a = 5.465 Å of the undoped glass-ceramic or CaF_2 crystal indicating the expansion of the crystalline lattice.

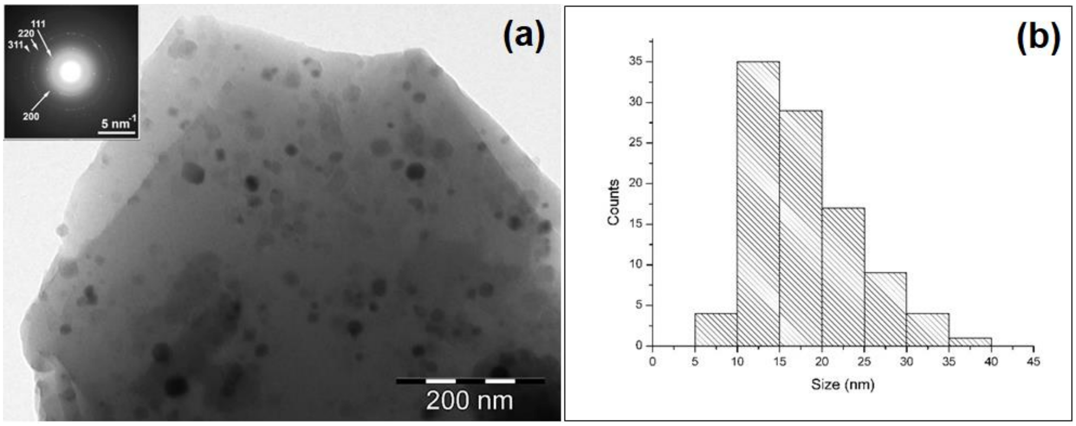

Fig. 1 TEM image of a glass grain containing embedded CaF_2 nanocrystals and the corresponding SAED pattern (a) and the histogram showing the size distribution of the embedded CaF_2 nanocrystals (b) (ref. [6]).

The transmission electron microscopy (TEM) image of a sample grain containing embedded nanocrystals is shown in the Figure 1a; the corresponding Selected Area Electron Diffraction (SAED) pattern proves the formation of the CaF_2 cubic phase (*a*=0.546 nm). The nanocrystals size distribution (Figure 1b) shows a lognormal shaped curve, with a mean size value of about 17 nm [6].

The photoluminescence (PL) spectrum recorded on glass-ceramic annealed in air shows strong, and structured Eu^{3+}-related luminescence $^5D_0 \rightarrow {}^7F_{0-4}$ peaks at 576, 590, 611, 648, 690 nm accompanied by a weaker, broad, blue luminescence at 425 nm due to the silica glass matrix.

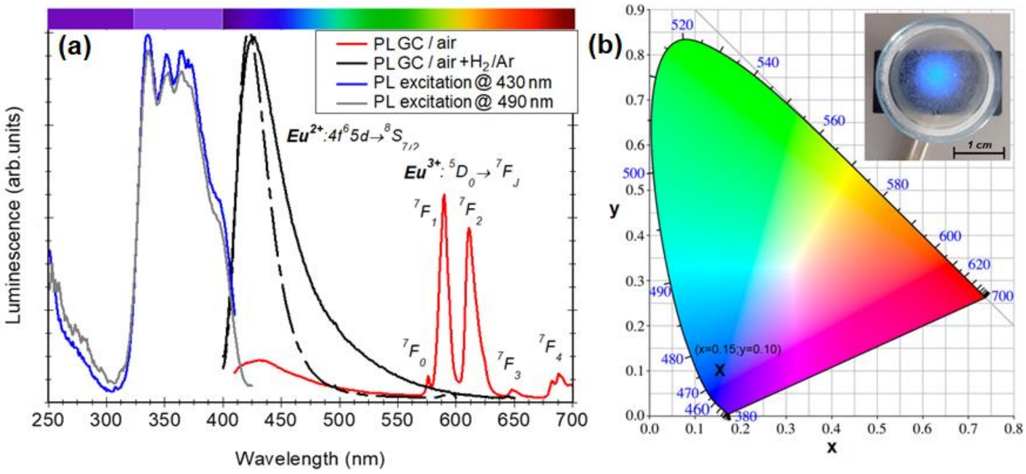

Fig. 2 PL and PL excitation spectra of Eu^{2+}/ Eu^{3+}-doped SiO_2-CaF_2 glass-ceramic (a) and the chromaticity diagram of the sample annealed in a reducing atmosphere; The inset shows the luminescent powder glass image.

The PL spectrum recorded in the glass-ceramic additionally annealed in a reducing atmosphere show new features; the Eu^{3+}-related luminescence peaks disappear and are replaced by a broad blue luminescence peaking at 425 nm accompanied by a weak and long tail in the visible region (Figure 2). As the 425 nm luminescence band is similar to the one reported for Eu^{2+} doped CaF_2 crystals [7] it was assigned to the Eu^{2+} ions that have replaced the Ca^{2+} ions in the cubic fluorite structure of the precipitated CaF_2 nanocrystals. This assumption is confirmed by the comparison between the corresponding excitation spectrum and the reported absorption spectrum [7], showing a typical "staircase" pattern between 310-425 nm, originating from transitions from the $4f^7(^8S_{7/2})$ ground state to the lowest crystal-field level of the $4f^65d$ configuration [1] from which the Eu^{2+} radiative de-excitation is observed. The excitation spectra of the 425 nm or 490 nm (luminescence on the visible tail) are quite similar, showing a broad and structured band between 310 and 410 nm due to the crystalline field splitting. The visible *"tail"* luminescence indicates a second type of Eu^{2+} ions in different locations/sites inside the CaF_2 nanoparticles with slightly perturbed coordination. In the CaF_2 crystalline structure, the excess positive charge caused by the Eu^{3+} doping is compensated by the interstitial fluorine ions or by substitutional oxygen ions in a neighboring fluorine site. Hence, we suppose that interstitial fluorine ions and oxygen ions (from the silica matrix [6]) behave as perturbation factors of the Eu^{2+} luminescence, and the broadening effect is consistent with several sites present in the nanoparticles with different site symmetries. The Eu^{2+} luminescent ions species are produced due to the Eu^{3+} to Eu^{2+} reduction reaction occurring during thermal processing using the hydrogen-based reducing atmosphere: Eu^{3+} ion gains an electron from the hydrogen that loses (or "donates") that electron and transforms to Eu^{2+}. The X-Ray Photoelectron Spectroscopy (XPS) spectra (not shown) have revealed the presence of both Eu^{2+} and Eu^{3+} ion species, in the fluoride nanocrystals and in the glass matrix, respectively. However, the Eu^{3+} ions luminescence cannot be observed in the PL spectra (Figure 2) because their luminescence signal is very weak being covered by the much stronger Eu^{2+} luminescence.

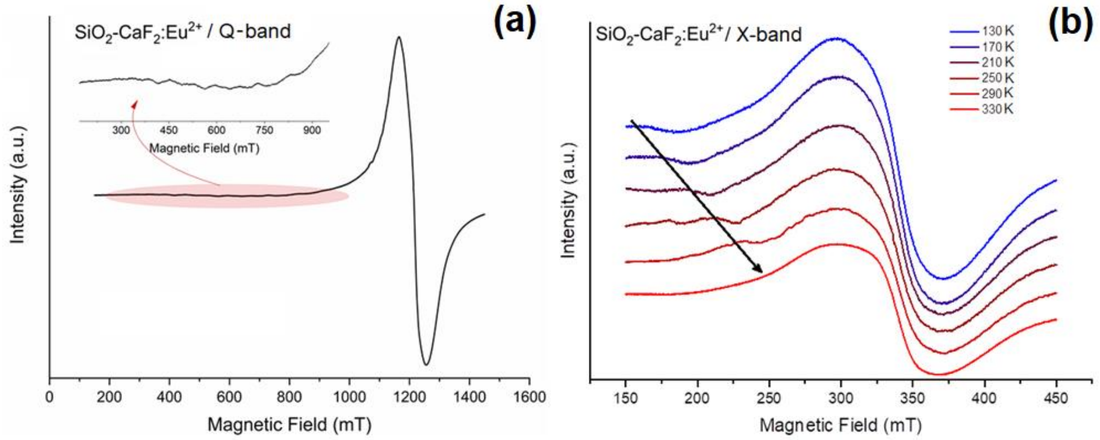

Fig. 3 Q-band EPR spectrum of the Eu^{2+}-doped SiO_2-CaF_2 glass-ceramic annealed in a reducing atmosphere (a) and the X-band EPR spectra recorded in the temperature ranging from 130 to 330 K with 40 K steps (b).

The electron paramagnetic resonance (EPR) spectrum recorded on Eu^{2+} -doped glass-ceramics annealed in a reducing atmosphere shows a comprehensive signal, with an isotropic g-value of 1.9972 and a peak-to-peak linewidth of ~ 91 mT (Figure 3a). As the spectrum is similar to that recorded on Eu^{2+} doped CaF_2 single crystal that shows fine structure centered at $g = 1.99$ [8], and PL measurements showed the Eu^{2+} luminescence in doped CaF_2 crystals, we assign the EPR signal to the Eu^{2+} ions incorporated in the precipitated CaF_2 nano-crystals in the glassy matrix. Low-intensity resonances depicted in the inset are due to the fine structure of a Eu^{2+} ion but is hardly visible due to the high Eu^{2+} concentration (1%), which results in a strong spin–spin exchange interaction. The X-band EPR measurements performed in in the temperatures range from 140 to 330 K (Figure 3b) revealed a new EPR resonance in the low field region supposed to be related to the Eu^{2+} too. The signal shifts towards $g \sim 2$ with increasing temperature (the arrow), consistent with a strong spin–lattice and spin–spin interaction.

In conclusion, the presented approach can be used to obtain other new oxy-fluoride glass-ceramic materials doped with divalent ions such as Sm^{2+}, Yb^{2+} for related applications: X-ray storage phosphor for digital imaging, persistent spectral hole burning for high-density optical memories, red broadband persistent luminescence, and white light sources.

References

1. D Poelman, PF Smet, “Europium-doped phosphors for lighting: The past, the present and the future”. In *Proceedings of the 2011 International Workshop on Advanced Nanovision Science*, Ghent Belgium (2011)
2. F Nakamura, T Kato, G Okada, N Kawaguchi, K Fukuda, T Yanagida, “Scintillation and dosimeter properties of CaF_2 transparent ceramic doped with Eu^{2+}”, *Ceramics International* 43, 604–609 (2017).
3. M Secu, C Secu, C Bartha, “Optical properties of transparent rare-earth doped sol-gel derived nano-glass ceramics”, *Materials* 14, 6871 (2021).
4. G Gorni, JJ Velázquez, J Mosa, R Balda, J Fernández, A Durán, Y Castro, “Transparent glass-ceramics produced by sol-gel: a suitable alternative for photonic materials”, *Materials* 11, 212 (2018).
5. C Secu, AM Rostas, M Secu, “Europium (II)-doped CaF_2 nanocrystals in sol-gel derived glass-ceramic: luminescence and EPR spectroscopy investigations”, *Nanomaterials* 12, 2016 (2021).
6. M Secu, CE Secu, C Ghica, “Eu^{3+}-doped CaF_2 nanocrystals in sol–gel derived glass–ceramics”, *Optical Materials* 33, 613–617 (2011).
7. T Kobaiashi, SJ Mroczkowski, F Owen, L Brixner, “Fluorescence lifetime in Eu^{2+}-doped chlorides and fluorides”, *Journal of Luminiscence* 21, 247–257 (1980).
8. JM Baker, B Bleaney, W Hayes, “Paramagnetic resonance of *S*-state ions in calcium fluoride”, *roceedings of the Royal Society of London. Series A. Mathematical and Physical Sciences* 247, 141–151 (1958).

Effect of Aluminum Nanostructured Electrode on the Properties of Organic Heterostructures with Bulk Heterojunction Layer

Oana Rasoga[a], Carmen Breazu[a], Marcela Socol[a], Ana-Maria Solonaru[b], Loredana Vacareanu[b], Gabriela Petre[a,c], Nicoleta Preda[a], Florin Stanculescu[c], Gabriel Socol[d], Mihaela Girtan[e], Anca Stanculescu[a]

[a]National Institute of Materials Physics, 405A Atomistilor, 077125 Magurele, Romania
[b]Petru Poni Institute of Macromolecular Chemistry, 41A Gr. Ghica Voda Alley, 700487 Iasi, Romania
[c]Faculty of Physics, University of Bucharest, 405 Atomistilor, 077125 Magurele, Romania
[d]National Institute for Laser, Plasma and Radiation Physics, 409 Atomistilor, 077125 Magurele, Romania
[e]Laboratoire LPHIA, Université d'Angers, LUNAM, 2 Bd. Lavoisier, 49045 Angers, France

The mixed layers (bulk heterojunctions) have been proposed as an alternative for improving the performance of solar cells, but very quickly they started to be considered for applications in many types of organic devices, such as Organic Field Effect Transistors, organic phototransistors, organic photodetectors and organic photodiodes for visible light communication. The optimization of the devices' performances can be obtained by the selection of adequate donor: acceptor pairs to assure an homogeneous mixture at nanometer scale. In this way it is maximized the interfacial area between the two components for an efficient generation of the charge carries, their transport to and collection by the electrodes. In addition, the manipulation of light generated by the nanostructuring of interfaces could be considered as a means to improve the optical/electrical properties of the organic heterostructures. Recently we have investigated the properties of the organic heterostructures with new mixed layer for optoelectronic applications [1] and the effect of the periodic patterning of the metallic electrode surface on the properties of small molecule organic bi-layer heterostructures [2], bulk-heterojunction-based organic heterostructures [3] and nucleobase thin films for optoelectronic applications [4]. This study [5] presents some results of the comparative investigations on the organic heterostructures Al/donor: acceptor/ ITO, realized with mixed layers, deposited by Matrix Assisted Pulsed Laser Evaporation, containing an arylenevinylene-based polymer containing carbazole units substituted at 3,6- (AMC30) or 2,7-(AMC31) positions as donor and a fullerene derivative, [6,6]-phenyl C_{61} butyric acid butyl ester (PCBB) or non-fullerene perylene tetracarboxidiimide derivative (AMC14) as acceptor, deposited on both Al flat and nanostructured electrode (Figure 1a,b).

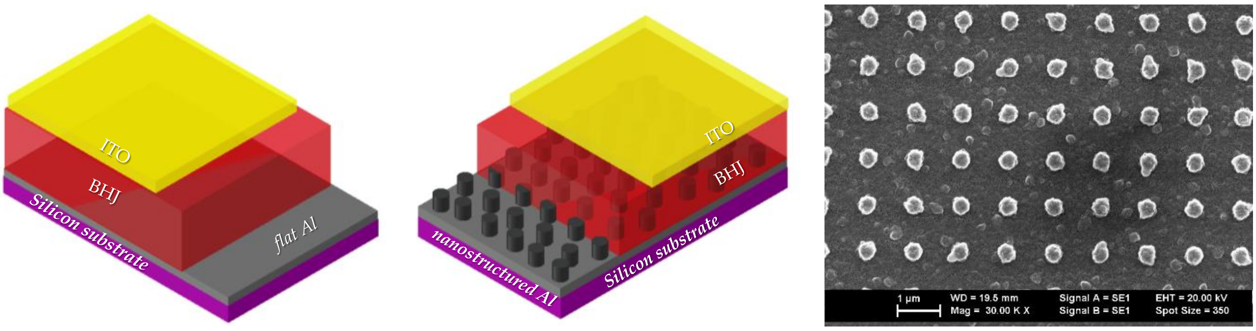

(a) (b) (c)

Fig.1 Representation of the organic heterostructure with bulk heterojunction AMC30/AMC31:PCBB/AMC14 on: Al_{flat} electrode (a) [5]; Al_{nano} electrode (b) [5]. SEM images of nano-patterned Al layer (c) [5].

A two-dimensional (2D) periodic structure with a cylindrical pillar-like shape with a periodicity of ~1.1 µm was realized in a polymeric layer using UV-Nanoimprint Lithography [5]. Subsequently, the Al layer was deposited on these nanostructures by vacuum evaporation, increasing the height and slightly changing the shape of the pillars which became irregular, and generating a morphology showing hillocks with an inflorescence-like aspect (Figure 1c) [5].

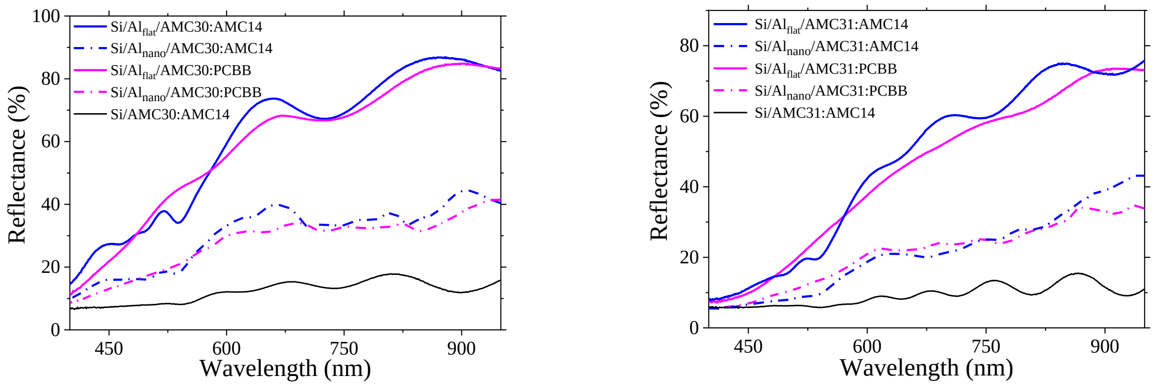

(a) (b)

Fig. 2 Reflectance spectra of AMC30/AMC31:PCBB/AMC14 mixed layers [5].

The reflectance of the mixed layers deposited on Al$_{nano}$ was affected by the light trapping through multiple scattering inside the gaps delimited by the pillars [5] (Figure 2). Because the 2D array is characterized by a low density of nanostructures, the reflectance spectra of the mixed layers showed broad and shallow oscillations compared to the same layer deposited on Al$_{flat}$ [5].

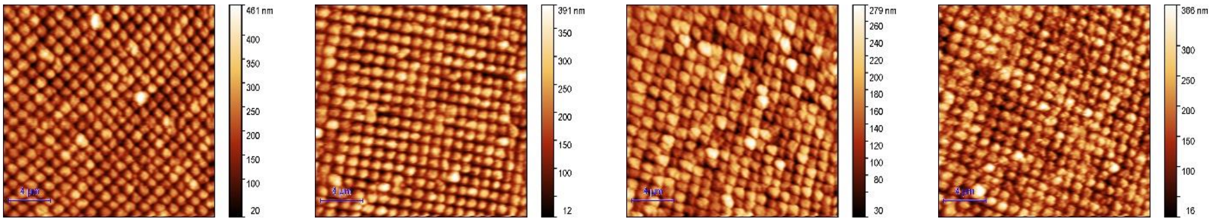

AMC30:PCBB AMC30:AMC14 AMC31:PCBB AMC31:AMC14

Fig. 3 2D AFM images of the AMC30/AMC31:PCBB/AMC14 mixed layers deposited on Al$_{nano}$ [5].

Independently of acceptor, the mixed layer preserved the nano-patterning of Al layer (Figure 3) [5] determining the light trapping by multiple scattering of radiation [5]. The roughness of the mixed layer deposited on Al$_{nano}$ is higher than the roughness of the layer deposited on Al$_{flat}$ and is correlated with lower reflectance [5].

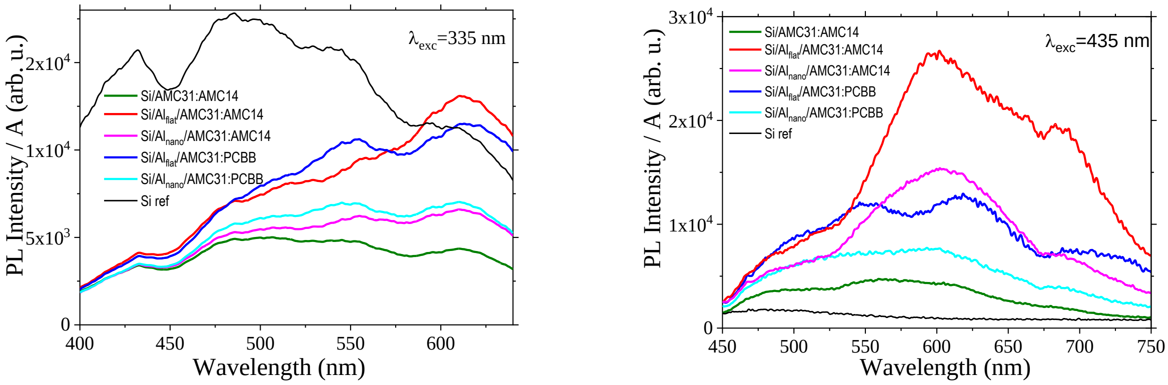

(a) (b)

Fig. 4 Photoluminescence spectra of AMC 31: fullerene/non-fullerene layers at UV (a) [5] and Vis (b) [5] excitation.

Heterostructures deposited on Al$_{nano}$ with the mixed layer containing non-fullerene acceptor showed a decrease in the emission intensity at both UV and Vis excitation (Figure 4a,b) [5]. The emission of the mixed layer containing fullerene derivative is also weak at excitation with visible light because of the luminescence quenching mechanism (Figure 4b) [5].

All the heterostructures showed a slightly non-linear injection contact behavior [5]. The nano-patterning of the Al electrode has induced an increase in the current in the heterostructures with a mixed layer containing as donor the shorter-conjugation-length polymer (AMC30) and characterized by high roughness, independently of the type of acceptor (Figure 5a,b) [5].

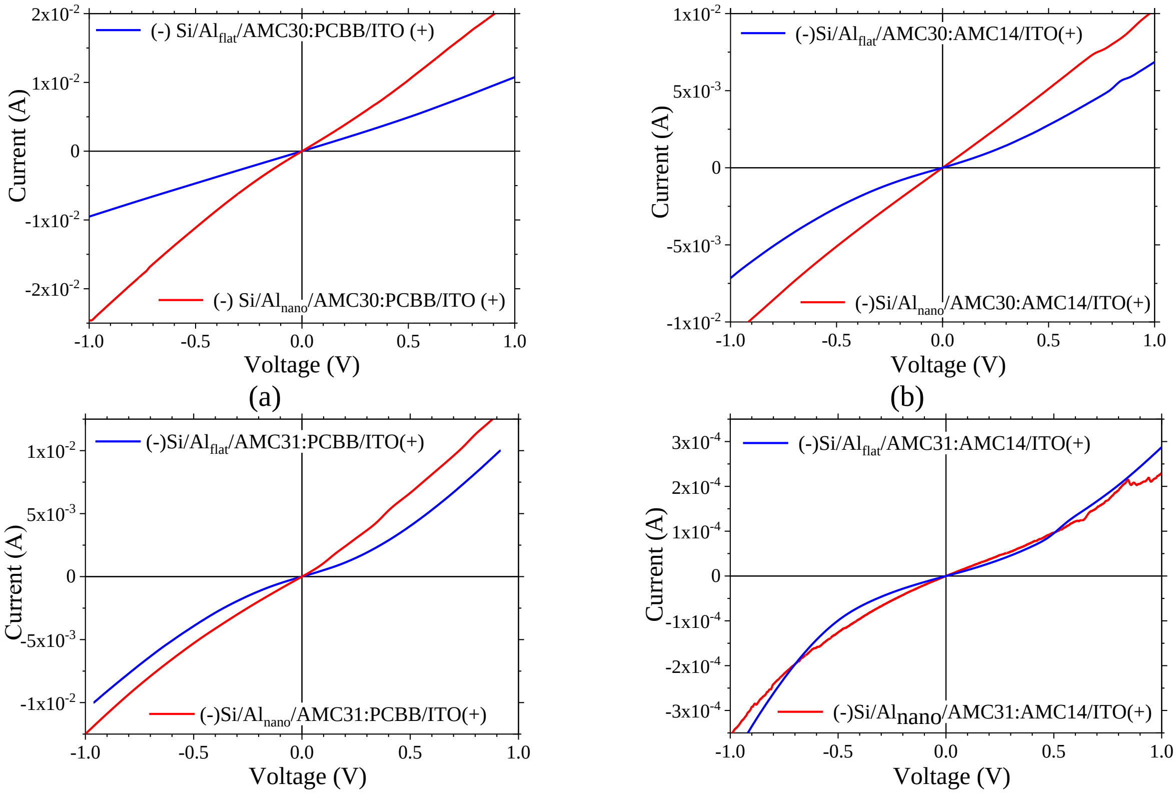

(a) (b)

(c) (d)

Fig. 5 I-V characteristics of the investigated heterostructures [5].

Therefore, this type of heterostructure with nanostructured metallic electrode, Al$_{nano}$/short-conjugation-length arylenevinylene polymer:fullerene derivative or perylene diimide derivative/ITO could be used as a charge injection element in organic electronics [5].

References

1. G Petre, A Stanculescu, M Girtan, M Socol, C Breazu, L Vacareanu, NPreda, O Rasoga, F Stanculescu, AS Doroshkevich, “Organic heterostructures with Indium-free transparent conductor electrode for optoelectronic application”, *Physica Status Solidi A* 219, 2100521 (2022).
2. C Breazu, M Socol, N Preda, E Matei, O Rasoga, M Girtan, R Mallet, F Stanculescu, A Stanculescu, “On the properties of organic heterostructures prepared with nano-patterned metallic electrode”, *Applied Surface Science* 443, 592 (2018)
3. A Stanculescu, C Breazu, M Socol, O Rasoga, N Preda, G Petre, AM Solonaru, M Grigoras, F Stanculescu, G Socol, G Popescu Pelin, M Girtan, “Effect of ITO electrode patterning on the properties of organic heterostructures based on non-fullerene acceptor prepared by MAPLE”, *Applied Surface Science* 509, 145351 (2020).
4. C Breazu, M Socol, N Preda, O Rasoga, A Costas, G Socol, G Petre, A Stanculescu, “Nucleobases thin films deposited on nanostructured transparent conductive electrodes for optoelectronics applications”, *Scientific Reports* 11, 7551 (2021).
5. O Rasoga, C Breazu, M Socol, AM Solonaru, L Vacareanu, G Petre, N Preda, F Stanculescu, G Socol, M Girtan, A Stanculescu, “Effect of aluminum nanostructured electrode on the properties of bulk heterojunction based bheterostructures for electronic”, *Nanomaterials* 12, 4230 (2022).

HRTEM Investigations on Microstructural Ordering in $NaMn_{0.2}Fe_{0.2}Co_{0.2}Ni_{0.2}Ti_{0.2}O_2$ High-entropy Sodium Oxide as Candidate Cathode Material for Na-ion Batteries

Corneliu Ghica[a], **Katarzyna Walczak**[b], **Anna Plewa**[b], **Wojciech Zając**[b], **Anita Trenczek-Zając**[b], **Marcin Zając**[c], **Janusz Toboła**[b], **Janina Molenda**[b]
[a]National Institute of Materials Physics, 405A Atomistilor, 077125 Magurele, Romania
[b]AGH University of Science and Technology, 30 al. Mickiewicza, 30-059, Krakow, Poland
[c]National Synchrotron Radiation Centre Solaris, 98 ul. Czerwone Maki, 30-392, Krakow, Poland

In a complex geopolitical context affecting the exploitation and trading of raw materials for applications in strategic sectors such as energy or transport industries, developing alternative materials with comparable figures of merit is one of the nowadays most challenging quests addressed by materials science researchers. Given the wide availability and low price of sodium compared to lithium, Na-ion batteries (SIBs) represent today a potential alternative to Li-ion batteries (LIBs) that now dominate the market due to their high energy and power density. This summary refers to an in-depth microstructural investigation of high-entropy $NaMn_{0.2}Fe_{0.2}Co_{0.2}Ni_{0.2}Ti_{0.2}O_2$ layered oxide as potential cathode material for SIBs in relation with the Na^+ intercalation/deintercalation mechanism [1].

Na-based layered transition metal oxides, with the general formula of Na_xMO_2 where M stands for one or more transition metal ions, are very good candidates for cathode material in NIBs due to the low Na^+ diffusion barrier. The crystal structure can be described as a packing of layers of edge-connected MO_6 octahedra that can host Na-ions in positions with a prismatic (P) or octahedral (O) symmetry. The transition metal ions M are reduced and oxidized during the Na intercalation / elimination processes (sodiation and desodiation) upon battery discharging/charging cycles. The lateral shifting of the adjacent MO_2 layers and the stacking sequence can determine a large variety of local structures (*e.g.*, P2 and O3 types) which can be modified during the charging/discharging cycles, in function of the chemical composition. In high-entropy oxide materials for SIB cathodes, three or more transition metal ions in equal proportions are randomly distributed in equivalent Wyckoff positions. The high-entropy configuration contributes to an increased stability of the crystal structure (entropy-stabilized structures) [2].

The $NaMn_{0.2}Fe_{0.2}Co_{0.2}Ni_{0.2}Ti_{0.2}O_2$ oxide has been prepared by high-temperature solid-state reaction starting from Na_2CO_3, $MnCO_3$, $CoCO_3 \cdot H_2O$, $Ni(CH_4COO)_2 \cdot 4H_2O$, Fe_2O_3 and TiO_2 precursors, in oxygen atmosphere at 950 °C. The atomic-resolution transmission electron microscopy investigations illustrated hereafter have been performed on a JEM ARM 200F analytical instrument operated at 200 kV.

The TEM image in Figure 1a shows a large thin crystal grain exhibiting a streaky diffraction contrast as dark stripes running parallel to the long side of the crystal, characteristic to a high density of planar defects. The corresponding SAED pattern (Figure 1b) has been indexed according to the rhombohedral structure (trigonal axes) of $NaFeO_2$ that perfectly fits the interplanar distances calculated from the diffraction pattern. The analyzed SAED patterns confirm that the as-prepared high-entropy oxide has adopted the layered structure of $NaFeO_2$, with Mn, Fe Co, Ni and Ti sharing the ionic position of Fe in $NaFeO_2$. Therefore, the grain orientation is [01-1], having the [111] axis perpendicular to the observation direction and the (111) planes parallel to the long sides of the crystal grain.

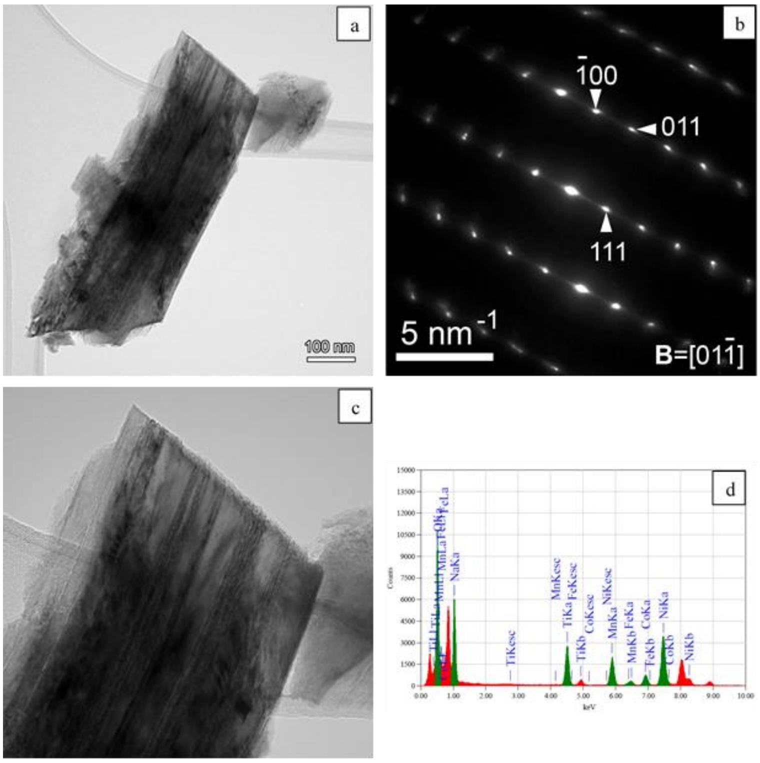

Fig. 1 (a) TEM image and (b) the associated SAED pattern of a $NaMn_{0.2}Fe_{0.2}Ni_{0.2}Co_{0.2}Ti_{0.2}O_2$ grain in [01-1] zone axis orientation. (c) Enlarged TEM image revealing structural domains with a high density of (111) planar defects. (d) EDS spectrum of the grain in (a).

The enlarged image in Figure 1c confirms the presence of structural domains separated by planar defects running along the (111) crystallographic planes.

The EDS spectrum in Figure 3d reveals the presence of all the expected elements. However, the measured Na/Mn/Fe/Ni/Co/Ti atomic concentrations are slightly different from the 1/0.2/0.2/0.2/0.2/0.2/2 nominal values, being actually around 1/0.3/0.02/0.7/0.3/0.4, not considering the atomic concentration measured for oxygen. The large variety of ionic species in the composition creates the premises for nanoscale structural modifications such as phase segregation, precipitation or chemical ordering. The formation of the layered oxide structure along the [111] trigonal axis can be confirmed by crystal grains in particular orientations, only, namely those orientations where the [111] axis is perpendicular to the observation direction.

The [01-1] zone axis orientation satisfies this condition, which allowed us to perform a high-resolution analysis in this respect. The atomic structure of the crystal grain in Figure 1 is revealed by the HRTEM images acquired in several adjacent locations. Local FFT diagrams of the HRTEM image in Figure 2 show that different crystallographic orientations may be observed within the same grain. The dominant orientation is given by the FFT diagram corresponding to area denoted A. The local FFT reveals the same crystallographic orientation given by the SAED pattern obtained on the entire grain (Figure 1b), namely the [01-1] zone axis, with the [111] crystallographic direction in the grid plane. The enlarged cropped area shows the typical HRTEM pattern for this orientation, where the alternating Na/TM crystallographic planes with a periodicity of 0.52 nm along [111] are clearly visible.

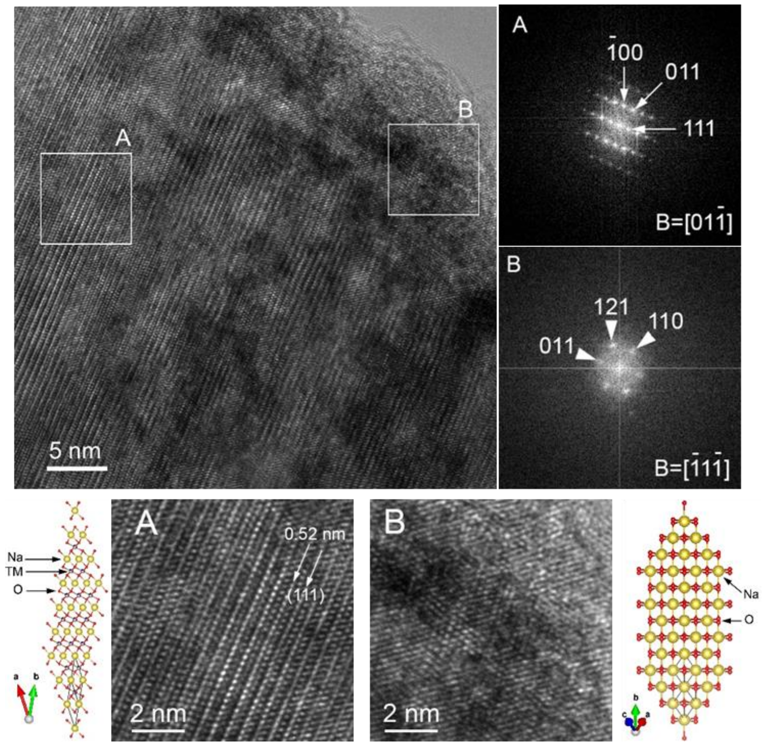

Fig. 2. Large area HRTEM image showing the atomic structure of the grain in Figure 1. The two areas denoted with A and B show a different local structure, as pointed by the local FFT patterns next to the micrograph. The enlarged HRTEM patterns from the two areas show the atomic structure of likely two different structural orientations corresponding to the two attached structural models [1].

The atomic structural model in the same [01-1] orientation is figured next to the enlarged HRTEM pattern from area A. The FFT diagram from the neighboring area B reveals a different local crystalline structure resulting in the extinction of the -100, 111 and the equivalent peaks observed in area A. Similar extinctions could be noticed within the stripe domains observed at lower magnification in Figure 1. This can be explained either by a local structural disorder such that the Na/TM stacking order becomes no longer visible. Alternatively, however, these areas could represent domains with a different crystallographic orientation, with similar interplanar distances, but where the [111] direction is no longer perpendicular to the observation direction. One such possibility is presented in Figure 2 by the structural model obtained along the [-11-1] zone axis of the same structure used to describe area A. This orientation fits the FFT pattern obtained for area B, but it does not allow evidencing the chemical ordering along [111]. Further analytical microstructural investigations are on the way in order to elucidate the role of the chemical ordering on the electrical properties of this high-entropy oxide.

References

1. K Walczak, A Plewa, C Ghica, W Zajac, C Trenczek-Zajac, M Zajac, J Tobo, J Molenda, “$NaMn_{0.2}Fe_{0.2}Co_{0.2}Ni_{0.2}Ti_{0.2}O_2$ high-entropy layered oxide - experimental and theoretical evidence of high electrochemical performance in sodium batteries”, *Energy Storage Materials* 47, 500–514 (2022).
2. A Sarkar, Q Wang, A Schiele, M R Chellali, S S Bhattacharya, D Wang, T Brezesinski, H Hahn, L Velasco, B Breitung, “High-entropy oxides: Fundamental aspects and electrochemical properties”, *Advanced Materials* 31, 1806236 (2019).

EPR and Microstructural Study of Black TiO_2 Nanoparticles with Efficient Photocatalytic Performance for Degradation of Pharmaceuticals

Daniela Ghica[a], Mariana Stefan[a], Catalina G. Mihalcea[a], Aurel-Mihai Vlaicu[a], Luminita Andronic[b], Smagul Karazhanov[c]

[a]Laboratory of Atomic Structures and Defects in Advanced Materials, National Institute of Materials Physics, 405A Atomistilor, 077125 Magurele, Romania

[b]Product Design, Mechatronics and Environment Department, Transilvania University of Brasov, 29 Eroilor, 500036 Brasov, Romania

[c]Solar Energy Department, Institute for Energy Technology, 2027 Kjeller, Norway

Defective black TiO_2 nanomaterials have emerged as an interesting class of highly efficient photocatalysts, providing a successful resolution to the issues posed by the UV region limited light absorption and high recombination rate of the photogenerated charge carriers in the “white” TiO_2. Responsible for the improved absorption of solar radiation is the bandgap narrowing induced by the presence of defects such as Ti^{3+} and oxygen vacancies on the surface and the crystallographic lattice disorder, which also promotes the charge separation of electrons and holes [1,2].

We have investigated by electron paramagnetic resonance (EPR) the nature and distribution of the defects in several nanostructured black TiO_2 polymorphs, in correlation with microstructural studies by X-ray diffraction (XRD) and analytical transmission electron microscopy (TEM) [3]. The synthesis of the black TiO_2 nanostructures was a cost-effective process in two stages, consisting of (*i*) the synthesis of white TiO_2 nanopowders with anatase, rutile and anatase-rutile mixture structures by a sol-gel method followed by annealing at different temperatures, and (*ii*) the chemical reduction of the white TiO_2 with sodium borohydride ($NaBH_4$). According to the XRD and (HR)TEM investigations (Figures 1, 2), the 400°C white and black (chemically reduced) samples consist of anatase nanoparticles with crystallite size of 15 nm and 12 nm, respectively.

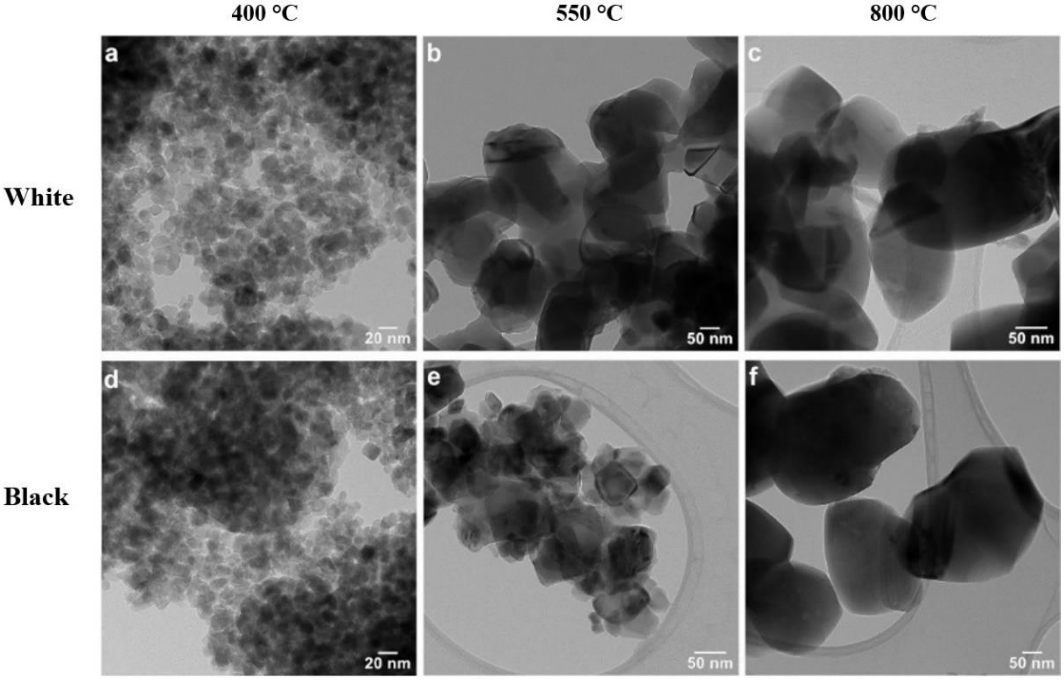

Fig. 1 TEM images revealing the size and morphology of the TiO_2 samples annealed at the indicated temperatures.

The 550 °C samples consist of a mixture of anatase (16%) and rutile (84%) phases, with the average crystallite size for anatase three times larger than for the 400 °C samples, while for the rutile phase it decreases from 127 nm to 75 nm after chemical reduction. The 800 °C white and black samples consist of rutile particles with an average crystallite size of 130 nm.

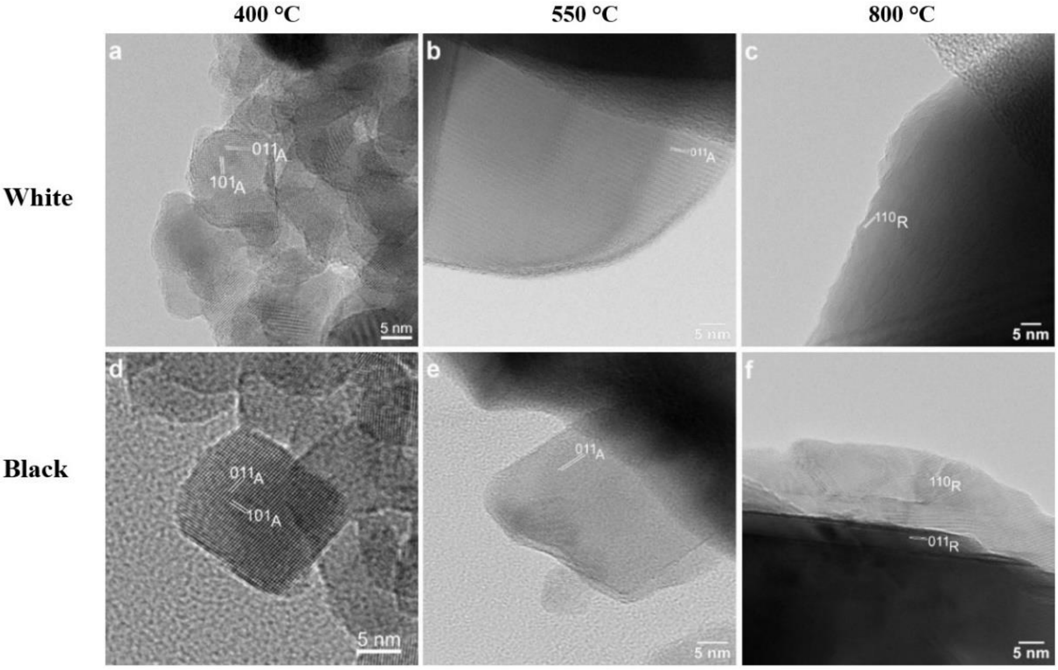

Fig. 2 HRTEM images revealing the morphology of the white and black TiO_2 samples annealed at the indicated temperatures. Interplanar distances are marked with A and R for the anatase and rutile phases, respectively.

The EPR investigations revealed the main effect of the chemical reduction treatment, namely the formation of a large quantity of Ti^{3+} defects in all the black samples (Figures 3, 4). Oxygen vacancies associated defects (F^+ center = singly charged oxygen vacancy) are observed only in the anatase samples (Figure 3 – the narrow EPR line in both white - W and black - B 400 °C samples).

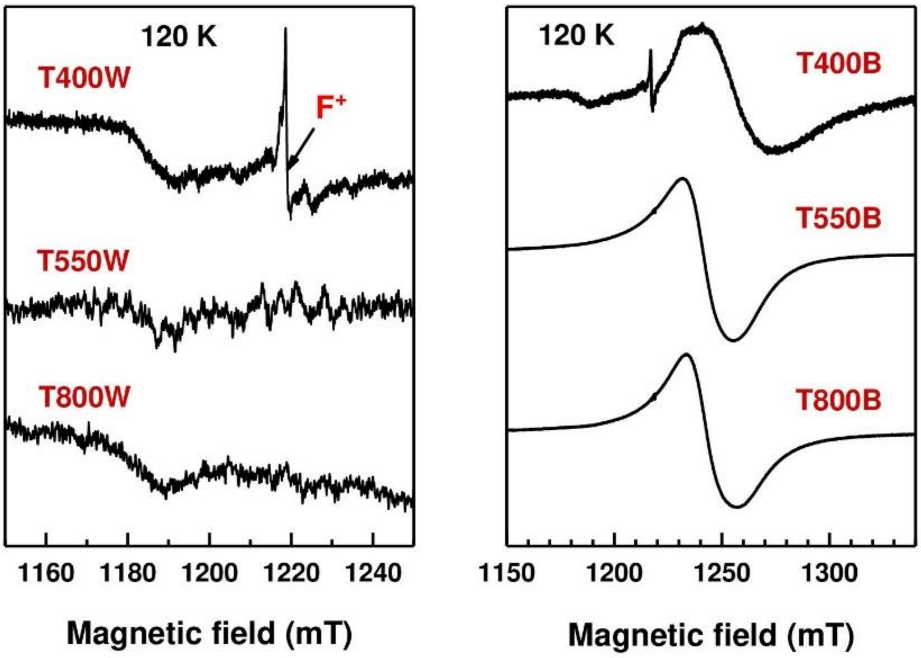

Fig. 3 Q-band EPR spectra of the white (W) and black (B) samples recorded at 120 K.

The quantitative analysis of the EPR spectra of the three black samples shows that in the 400 °C anatase sample ~90% of the Ti^{3+} ions are localized on the nanoparticles surface, forming the $Ti^{3+}{}_A(s)$ centers (Figure 4). For the other two samples, where rutile was the dominant/only phase, the majority of the Ti^{3+} ions are found in bulk interstitial or substitutional sites, denoted as the $Ti^{3+}{}_{R}(i)$ and $Ti^{3+}{}_{R}(b)$ centers, respectively (Figure 4). Therefore, higher surface reactivity and photocatalytic efficiency are expected for the black anatase sample, where most of the Ti^{3+} ions are localized on the nanoparticles surface.

Indeed, the black anatase sample exhibits the highest photocatalytic degradation and mineralization activity of amoxicillin, due to its specific structure, the small size of the nanoparticles and the localization of the Ti^{3+} defects predominantly on the surface of the photocatalyst [3].

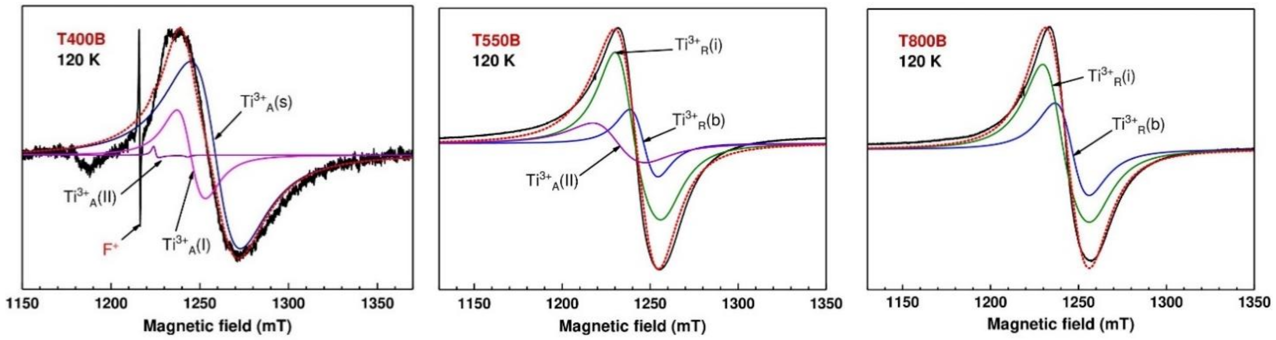

Fig. 4 Experimental (solid black line) spectra of the black samples at 120 K. The simulated spectra (red dot lines) are the sum of the calculated spectra of the different Ti^{3+} centers.

Acknowledgments: CERIC-ERIC Consortium proposal no. 20212076, Contract POC 332/390008/29.12.2020-SMIS 109522.

References

1. A. Naldoni, M. Altomare, G. Zoppellaro, N. Liu, Š. Kment, R. Zbořil, P. Schmuki, “Photocatalysis with reduced TiO_2: From black TiO_2 to cocatalyst-free hydrogen production”, *ACS Catalysis* 9, 345–364 (2019).
2. L. Andronic, A. Enesca, “Black TiO_2 synthesis by chemical reduction methods for photocatalysis applications”, *Frontiers in Chemistry* 8, 565489 (2020).
3. L. Andronic, D. Ghica, M. Stefan, C.G. Mihalcea, A.M. Vlaicu, S. Karazhanov, “Visible-light-active black TiO_2 nanoparticles with efficient photocatalytic performance for degradation of pharmaceuticals”, *Nanomaterials* 12, 2563 (2022).

Microstructure and Conduction Electrons Quantum Properties of Small Diamond Cubic α-Sn Nanocrystals Embedded in Cubic Boron Nitride Crystals

Sergiu V. Nistor[a,b], Leona C. Nistor[a], Mariana Stefan[a], Alexandra C. Joita[a,b]
[a]Laboratory of Atomic Structures and Defects in Advanced Materials, National Institute of Materials Physics, 405A Atomistilor, 077125 Magurele, Romania
[b]University of Bucharest, Faculty of Physics, 405 Atomistilor, 077125 Magurele, Romania

Cubic boron nitride (cBN) with zinc blende structure is a wide band-gap (~6.4 eV) semiconductor, industrially prepared as a crystalline superhard powder by the temperature gradient method, at high pressure and high temperature (HT-HP). Due to the extreme difficulty of preparing enough large, good quality single crystals with controlled impurity content, the presence, distribution and atomic properties of the impurities incorporated in its crystal lattice are little known. One such native impurity is Sn, evidenced by correlated analytical high resolution scanning transmission electron microscopy/transmission electron microscopy [a-(HR)STEM/TEM] and multifrequency electron spin resonance (ESR) investigations carried out on dark cBN crystallites from a batch of large grained, BORAZON CBN Type 1, 60/70 FEPA B251 superabrasive powder [1].

The a-(HR)STEM/TEM investigations revealed nano-sized aggregates of Sn atoms, as quasi-spherical nanocrystals (NCs) with undistorted diamond cubic α-Sn single phase structure, incorporated in the cBN crystallites (Figure 1), predominantly of small average diameter $d_m = 2.5$ nm, as well as a few larger ones. The stabilization in the cBN lattice of the cubic α-Sn NCs above the bulk α-β transition temperature $T_c = 13.2$ °C is supported by the HRTEM images (Figures 1b,c), which reveal clear interfaces with no separating layer, and is explained by the interplay between interface and pressure effects. Further investigations of cBN crystallites submitted to annealing at 950 °C in vacuum ($P < 10^{-4}$ mbar) for 4 h revealed the dissolution of the α-Sn NCs, with ejection and oxidation of the Sn atoms and formation of nanocrystalline SnO_2.

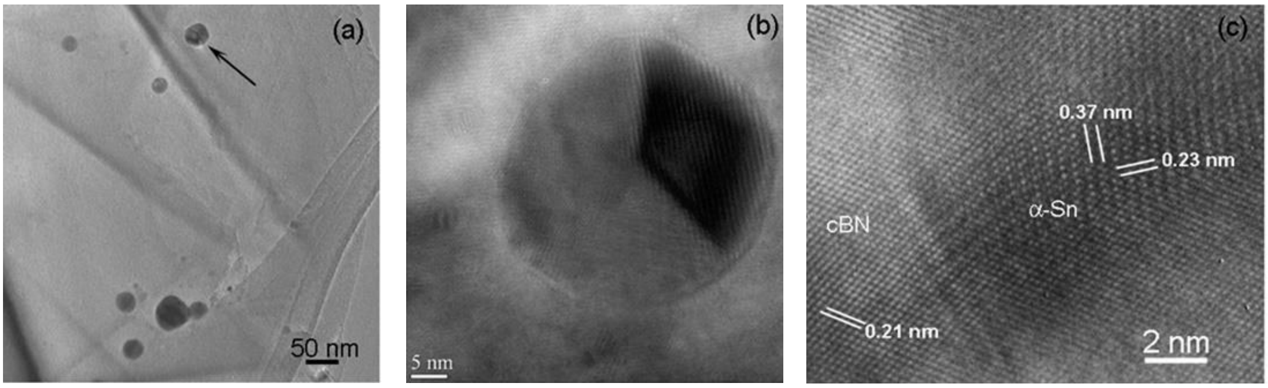

Fig. 1 Low magnification TEM image (a) and HRTEM images (b) and (c) along the [011] zone axis, showing Sn precipitates embedded in a dark cBN crystalline flake.

The X- and Q-band ESR investigations of the as received cBN revealed the presence of a symmetrical, narrow Lorentzian shaped line with a g-value $g_1 = 2.0028$ that did not vary in the 20 to 295 K temperature range (Figure 2a). For the annealed cBN crystallites this line, called **Sn1**, was strongly diminished in intensity, pointing to its association with the α-Sn NCs. The particular temperature variations of the ΔB_1 linewidth, A_1 amplitude and $I_1 = A_1 \times (\Delta B_1)^2$ intensity of the **Sn1** line (Figures 2b–d) could be explained, as further discussed, by the presence of two energy levels above and below the magnetic doublet level responsible for the **Sn1** line, with an average separation $\Delta_{QC}/k_B = 125$ K. The **Sn1** line was attributed to the conduction ESR (CESR) of the small α-Sn NCs with metal-like properties, in agreement with its temperature and microwave frequency independent g_1 factor and its very small $\Delta g = 0.0005$ shift from the free electron $g_e = 2.0023$ value. The analysis of the **Sn1** linewidth ΔB_1 variation at low temperature demonstrated that the specific conditions for the quantum confinement (QC) of conduction electrons in small metallic colloids [2] are accomplished at $T < 125$ K for the small ($d_m = 2.5$ nm) α-Sn NCs in the cBN crystallites.

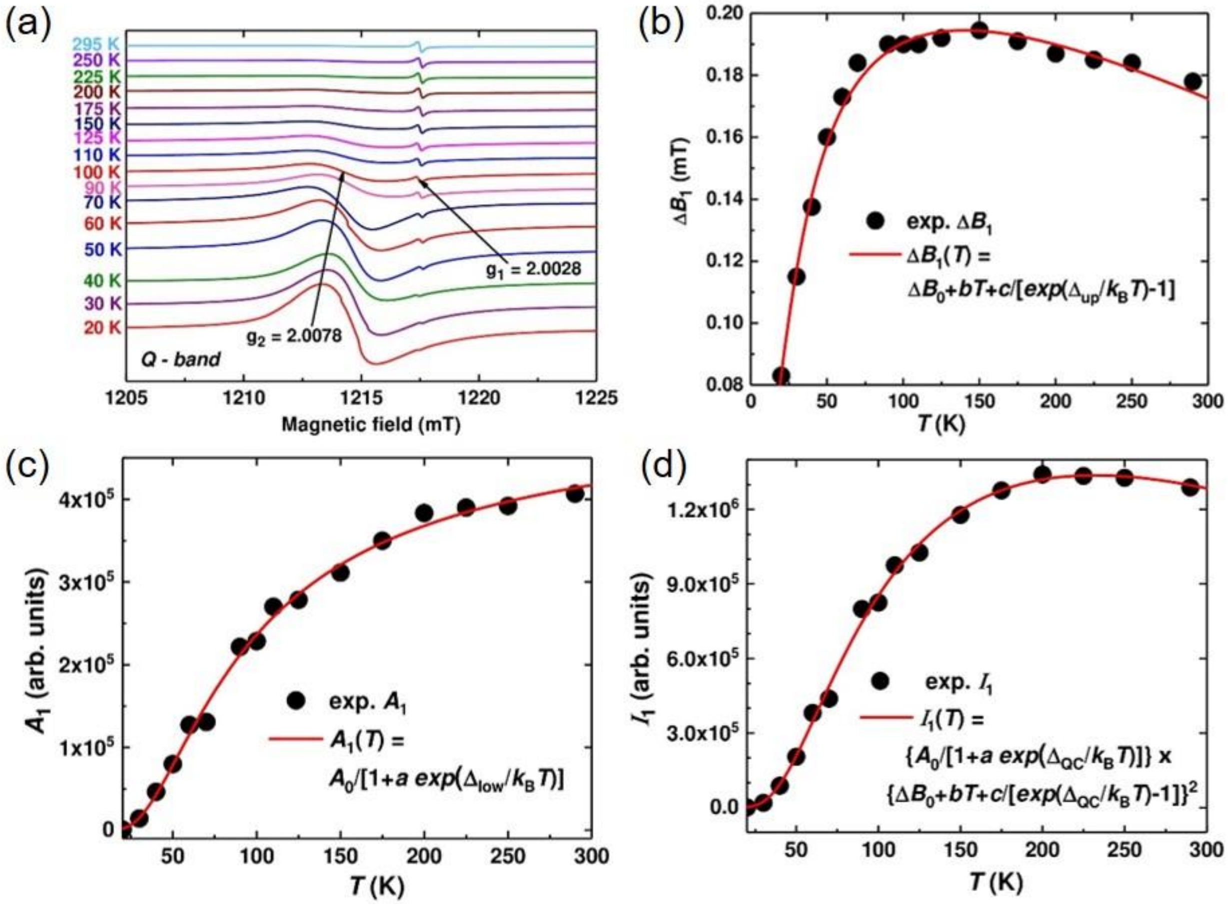

Fig. 2 (a) Q-band ESR spectra of the cBN crystallites at different temperatures. Temperature variation of the (b) ΔB_1 linewidth, (c) A_1 amplitude and (d) I_1 intensity of the Q-band Sn1 line. Dots: experimental points. Red lines: fitting with the functions displayed in figure legends, where $\Delta_{up}/k_B = 120$ K; $\Delta_{low}/k_B = 130$ K and $\Delta_{QC}/k_B = 125$ K.

The small, frequency independent g–shift of the **Sn1** line, suggesting an almost pure s-type conduction electrons ground state, as well as the presence of discrete conduction electron energy levels with Δ_{QC}/k_B average separation, were tentatively explained with the theoretically predicted electron quantum properties of small, unstrained α-Sn NCs, in comparison with the bulk α-Sn electron properties [3]. Indeed, first principles calculations of the electronic properties of small ($d < 12$ nm) α-Sn NCs demonstrated that for such α-Sn NCs a band gap Δ_G opens at E_F^n, with a change from the bulk $\Gamma_{7v} < \Gamma_{6c} < \Gamma_{8v}$ states order to the nano $\Gamma_{7v} < \Gamma_{8v} < \Gamma_{6c}$ order induced by lifting the Γ_{6c} state above the Γ_{8v} state (Figure 3). The resulting band inversion, called topological phase transition, promotes mainly the Sn 5s-states above the gap in the conduction band, which explains the observed temperature and frequency independent, small g-shift and the metal like character of the α-Sn NCs incorporated in the cBN crystallites.

The QC induced conduction electrons discrete energy levels of the α-Sn NCs in the cBN crystallites, consisting of two energy levels situated above and below the main magnetic doublet level responsible for the **Sn1** line, could be attributed to a restricted set of allowed electronic states selected from a basis set that incorporates the orbital motion boundary conditions.

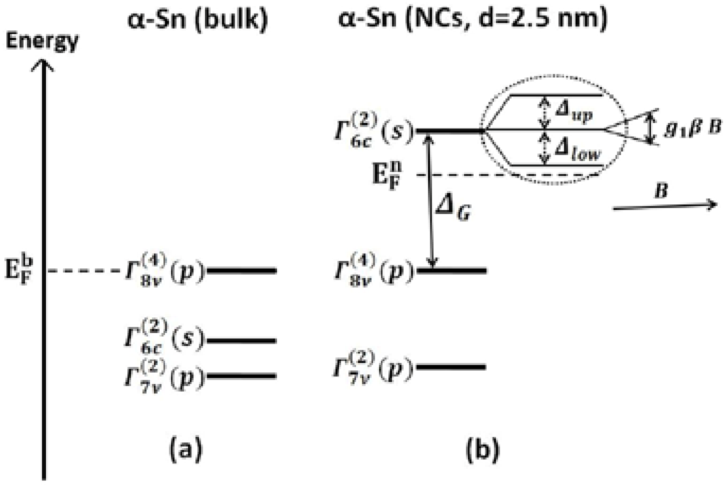

Fig. 3 Suggested energy band structure along the Γ direction in the reciprocal space, for: (a) bulk α-Sn [3] and (b) small α-Sn NC (ref. [3] and the present ESR data). The upper indices denote the spin degeneracy order of the respective states. Part of the energy levels fine structure of the conductive Γ_{6c} band, attributed to QC of the conduction electrons orbital motion in the α-Sn NCs [2] with its Δ_i/k_B ~125 K spacing, is presented in an expanded view (dashed circle) on the top, right side of the diagram. The position of the Fermi energy level $E_F{}^n$ with respect to the lowest energy level of the Γ_{6c} band fine structure is suggested based on the thermally activated properties of the **Sn1** line.

References

1. SV Nistor, LC Nistor, M Stefan, AC Joita, “Microstructure and conduction electron quantum properties of small diamond cubic α-Sn nanocrystals embedded in cubic boron nitride crystals”, *ACS Omega* 7, 41981–41996 (2022).
2. R Kubo, A Kawabata, S Kobayashi, “Electronic properties of small particles”, *Annual Review of Material Science* 14, 49–66 (1984) and references cited therein.
3. S Kuefner, J Furthmuller, L Matthes, M Fitzner, F Bechstedt, “Structural and electronic properties of α-tin nanocrystals from first principles”, *Physical Review B* 87, 235307 (2013).

Ethanol Dehydration to Ethylene Catalyzed by Mn-modified Hollow Silica Spheres – The Importance of the Acidity

Mihaela Florea[a], Amelia Bocîrnea[a], Ștefan Neațu[a], Andrei Kuncser[a], Mihaela-Mirela Trandafir[a], Florentina Neațu[a]
[a]National Institute of Materials Physics, 405A Atomistilor, 077125 Magurele, Romania

Ethylene is the most widely produced petrochemical in the world, and any ethylene feedstocks that do not rely on oil are a desirable alternative [1]. Ethanol (EtOH) dehydration to ethylene takes place in the presence of zeolites, metal oxides, and heteropolyacids [2-4] and requires temperatures between 180–500 °C. For such a process, it is crucial not only the presence of acid sites, but also the existence of certain types and strengths of acids sites. Mesoporous hollow silica spheres hold great potential (HMS) as new materials with great accessibility to the active sites that can enhance the catalytic process. Moreover, hollow silica-alumina spheres demonstrated the existence of Brönsted acidity that promotes the acid-base catalytic reaction, like the dehydrogenation of ammonia borane [5]. This study focused on the catalytic acidity in ethanol dehydration of zirconia-modified silica hollow spheres with Mn-Me (1:1 molar ratio) bimetallic nanoparticles in the inner cavity, where Me=Fe, Ni, Zn [6].
SEM pictures have indicated that the hollow spheres had been successfully shaped; the spheres' exterior shells were composed of a heterogeneous mixture of silica, zirconia, and $SiZrO_4$ oxides. For Ni- and Zn-containing materials, the distribution of sphere sizes is greater, with the maximum values reaching (400–500 nm), whereas for Fe-containing materials, the distribution of sphere sizes was significantly smaller (300 nm) (Figure 1).

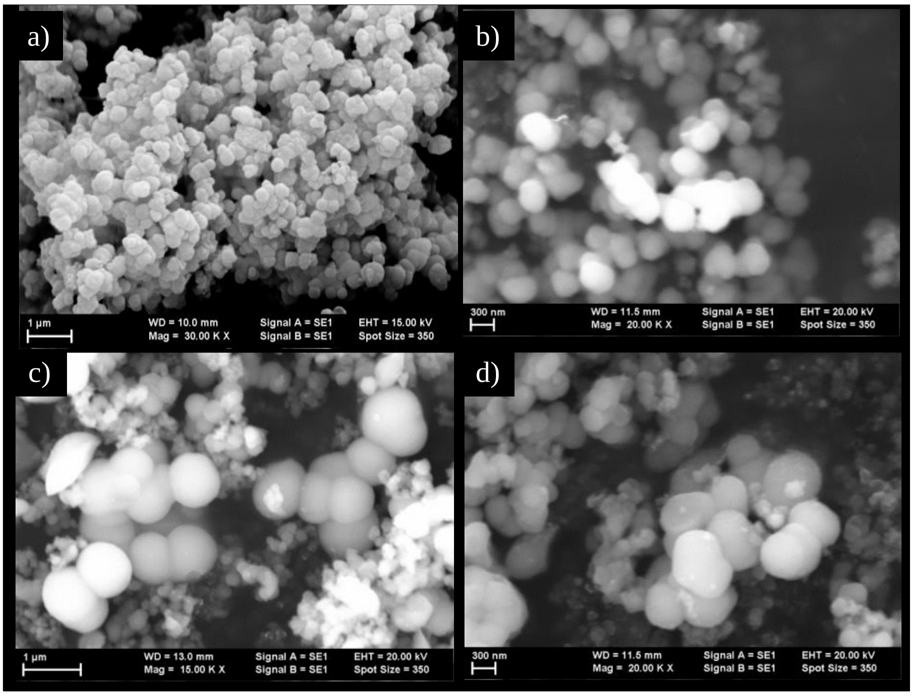

Fig. 1 SEM images of: (a) MnNi@C; (b) MnFe@SiZr; (c) MnNi@SiZr; and (d) MnZn@SiZr samples.

The oxidation states of Mn and the oxides that make up the shell of the hollow spheres were both affected by the degree to which the Mn core was modified with Zn, Fe, and Ni, as evidenced by XPS data. Thus, Mn^{3+} predominates (70%) in the MnZn-containing material, whereas Mn^{2+} predominates (63%) in the MnFe-containing material. The MnNi@SiZr sample consists of a mixture of Mn^{2+}/Mn^{3+} with a ratio of 1.3, as well as a trace amount of Mn^{4+}. The acidity, as assessed by NH_3-TPD, was correlated with the changes observed after manganese was modified with the metal transition (Fe, Zn, Ni); thus MnNi@SiZr has the highest surface area and the highest amount of total number of acid sites, of which 47% are weak acid sites, 53% are medium acid sites, and none are strong acid sites.

Moreover, double-mixed Mn-Me oxides do not present any strong acid sites in the samples. The large concentration of Lewis acids found in Mn@Si likely explains the material's preferential catalytic behavior toward acetaldehyde. Mn@SiZr catalyst with high activity and selectivity for ethylene was developed by modifying the hollow spheres' outer shell with zirconia to boost the acidity, leading to an ethylene yield of 56%.

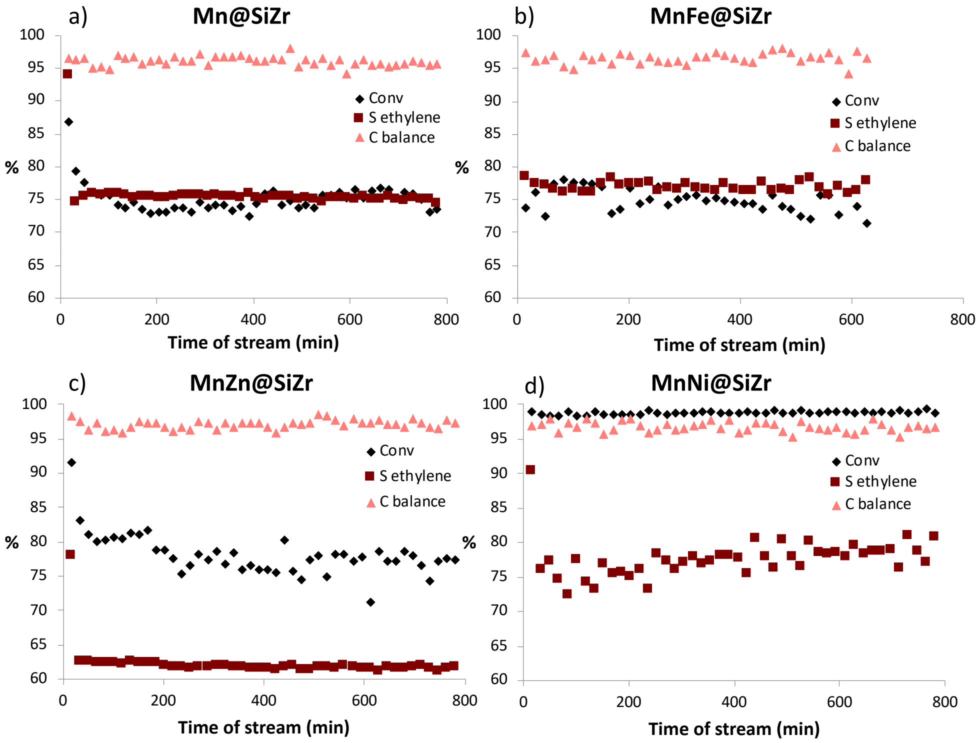

Fig. 2 Dependence of ethylene yield with acidity and ZrO_2:Si–O–Zr ratio, at 350 °C, WHSV 1.4 h^{-1}, 50 mg catalyst, 30 min.

Adding transition metal to the Mn@SiZr material, the activity and selectivity of the new catalysts formed have increased importantly (Figure 2). With an ethylene yield of 75%, Ni performs best among the three transition metals utilized to boost the MN@Si Zr catalyst. Based on the acidity of these materials and the observed findings, we can infer that acidity is a critical factor in the production of ethylene from ethanol. It's not just the total acidic site count that matters, but also the acidic site types.

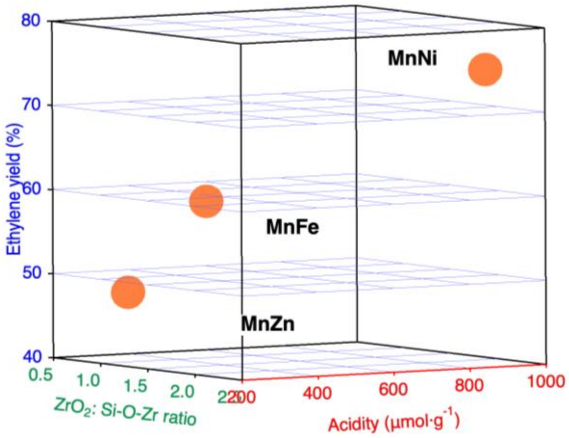

Fig. 3 Dependence of ethylene yield with acidity and ZrO_2:Si–O–Zr ratio, at 350 °C, WHSV 1.4 h^{-1}, 50 mg catalyst, 30 min.

While Ni alone in the center of a Si-Zr hollow sphere shows extremely low activity, adding Mn to the center of the spheres has a synergistic effect that boosts ethylene production. In contrast with Fe and Zn, Mn coupled with Ni produced a very stable material with stream time, with no reductions in the activity being seen at any time. High activity and selectivity to ethylene can only be achieved by including an appropriate quantity of Mn^{3+} (41%) within the material, which is only present in MnNi@SiZr. XPS findings, for which we determined the highest ratio ZrO_2:Si–O–Zr, corroborate well with the superior catalytic activity of MnNi@SiZr (Figure 3).

Considering the above data, and the fact that it was assumed that the active sites present in the MnZn@SiZr catalyst were insufficient to transform DEE into ethylene, it is reasonable to conclude that the formation of ethylene through ethanol dehydration occurs via a parallel series mechanism, as shown in Scheme 1.

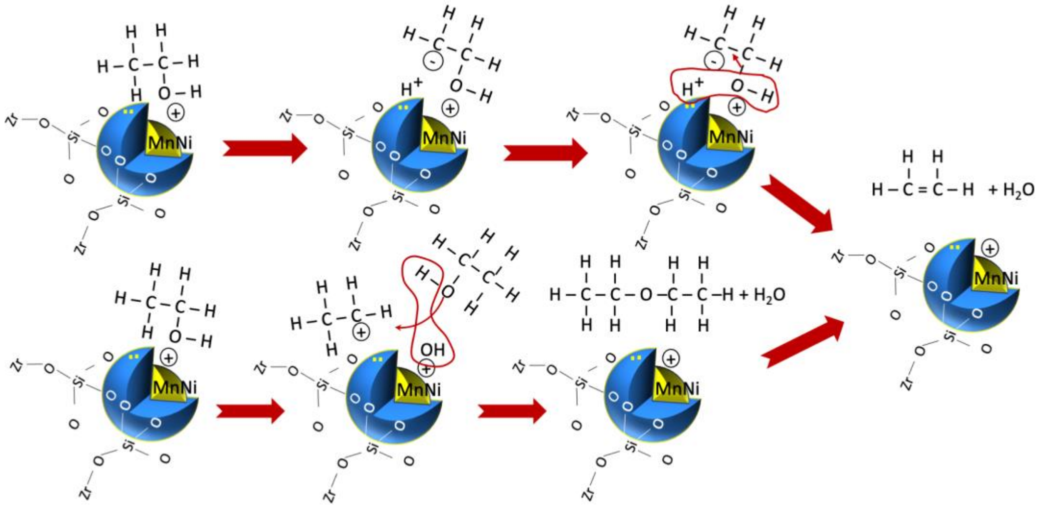

Scheme 1 Proposed mechanism for the MnMe@SiZr catalysts for ethanol dehydration.

To sum up, for MnMe@SiZr hollow spheres: (*i*) the number of acid sites is directly proportional to the activity of the material; (*ii*) the presence of strong acid sites does not play important role in the ethylene formation, but is rather related with the acetaldehyde formation; and (*iii*) the ratio between the weak/medium sites is very important in achieving high selectivity and activity, with the presence of medium sites being a prerequisite. We conclude that these results point to promising new directions for the discovery of efficient and stable catalysts for ethylene synthesis from ethanol. Since the newly synthesized structures were shown to be quite stable at relatively high temperatures and were not impacted by carbon deposition, they can be applied to various acid-base processes in flow, avoiding deactivation.

References

1. K Weissermel, HJ Arpe, "Industrial Organic Chemistry", Wiley (2008).
2. T Okuhara, N Mizuno, M Misono, "Catalytic chemistry of heteropoly compounds", *Advances in Catalysis* 41, 113–252 (1996).
3. W Alharbi, EF Kozhevnikova, I V Kozhevnikov, "Dehydration of methanol to dimethyl ether over heteropoly acid catalysts: The relationship between reaction rate and catalyst acid strength", *ACS Catalysis* 5, 7186 (2015).
4. J Schnee, A Eggermont, EM Gaigneaux, "Boron nitride: A support for highly active heteropolyacids in the methanol-to-DME reaction", *ACS Catalysis* 7, 4011 (2017).
5. T Umegaki, R Ogawa, S Ohki, M Tansho, T Shimizu, Y Kojima, "Control of pore size in shell of hollow silica–alumina composite spheres for hydrolytic dehydrogenation of ammonia borane", *Journal of Porous Materials* 26, 611 (2019).
6. M Florea, A Bocîrnea, S Neațu, AM Kuncser, MM Trandafir, F Neațu, "Tuning the acidity by addition of transition metal to Mn modified hollow silica spheres and their catalytic activity in ethanol dehydration to ethylene", *Applied Catalysis A: General* 646, 118860 (2022).

Towards applications

Visible-Light Photodetectors Based on Self-Connected CuO-ZnO Core-Shell Nanowire Arrays

Andreea Costas[a], Nicoleta Preda[a], Camelia Florica[a], Cristina Besleaga[a], Andrei Kuncser[a], Ionut Enculescu[a]
[a]National Institute of Materials Physics, 405A Atomistilor, 077125 Magurele, Romania

In the last decades, semiconductor nanowires have received considerable research interest being considered the new building blocks for the next generation optoelectronic devices. Lately, metal oxide core-shell nanowires based on CuO and ZnO, have been used frequently for applications in fields such as photocatalysis, photodetectors, light emitting diodes, *etc* due to their novel functionalities given by the *p-n* staggered gap heterojunction between the two components.

The current study proposes a novel visible-light photodetector system based on self-connected CuO–ZnO core-shell nanowire arrays fabricated on metallic interdigitated electrodes. The photodetector system was developed employing a stepwise preparation route. Firstly, metallic interdigitated electrodes were fabricated on Si/SiO_2 wafer by a conventional photolithography process and a Cu layer was electrodeposited on top of them. CuO nanowire arrays (core) were obtained using thermal oxidation in air and a ZnO thin film shell was deposited by RF magnetron sputtering, covering the entire surface of the CuO nanowires. Thus, Figure 1 displays the TEM measurements of a single CuO nanowire and of a single CuO–ZnO core-shell nanowire, evidencing a diameter of 50 nm for the CuO nanowire that grows along the (200) direction of monoclinic structure with an interplanar spacing of d(200) = 0.23 nm. Moreover, a 90 nm diameter was found for the CuO–ZnO core-shell nanowire and the *p–n* heterostructure of the CuO–ZnO core-shell nanowires was proved by EDX elemental mappings of a single CuO–ZnO core-shell nanowire.

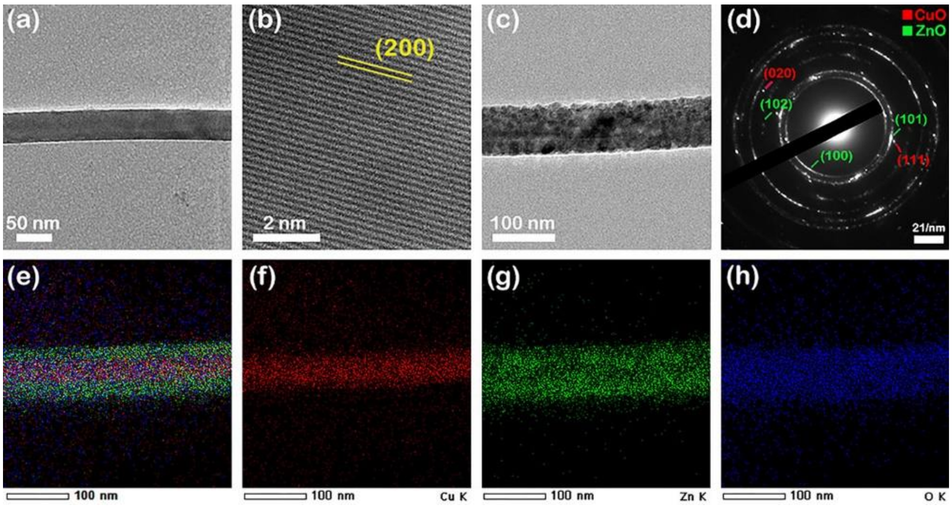

Fig. 1 (a) TEM image and (b) HRTEM image of a single CuO nanowire; (c) TEM image and (d) SAED pattern of a single CuO-ZnO core-shell nanowire, (e) – (h) EDX elemental mapping of a single CuO-ZnO core-shell nanowire and of its Cu, Zn and O as individual elements.

The FESEM images (Figure 2a,b,d,e) revealed that the metallic interdigitated electrodes are uniformly covered by nanowire arrays, both type of nanowire arrays having a cylindrical shape and a high aspect ratio. In addition, it can be noticed an average diameter of about 50 nm for the CuO nanowires and of 90 nm for the CuO–ZnO core-shell nanowires, in accordance with the TEM investigations. The XRD patterns of the samples (Figure 2c,f) show a monoclinic phase for the CuO nanowires and a hexagonal wurtzite phase for the ZnO film shell.

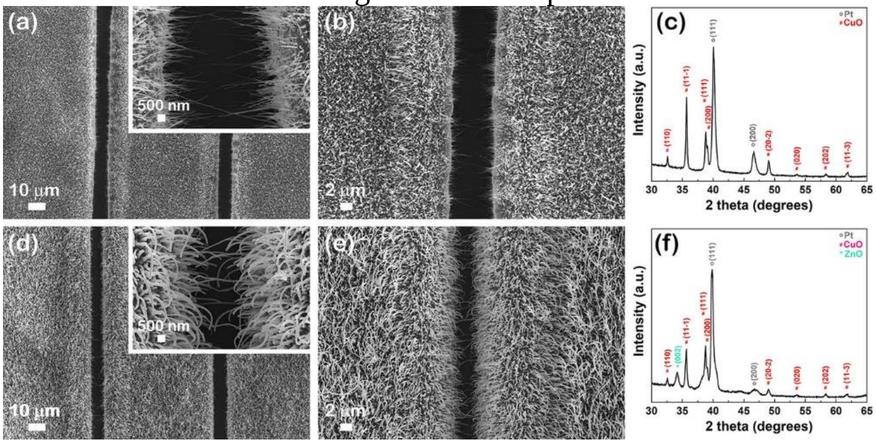

Fig. 2 FESEM images of the obtained array of nanowires: (a) CuO and (b) CuO-ZnO core-shell; (c), (d) XRD patterns and (e), (f) Kubelka-Munk function representations for (c), (e) CuO nanowires and (d), (f) CuO-ZnO core-shell nanowires.

Figure 3a displays a schematic representation of the band diagram for the CuO–ZnO core-shell heterojunction. The semilogarithmic plot of the current-voltage characteristic for the photodetectors reveal a non-linear shape, evidencing a rectifying behavior that originate from the *p-n* radial heterojunction formed at the CuO/ZnO interface in the CuO–ZnO core-shell nanowires. Furthermore, the time-dependent photoresponse measurements (Figure 3c,d) recorded at 2 SUN with light ON/OFF cycles at 0.5 V for the CuO–ZnO core-shell nanowires photodetector system shows a rise and decay time of 0.5 s and a photocurrent gain of 6.5 μA.

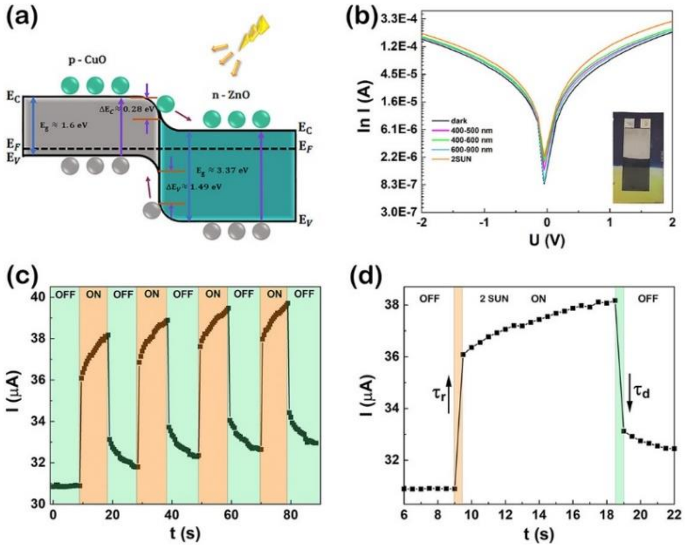

Fig. 3 (a) Schematic representation of the band diagram for CuO-ZnO core-shell heterojunction; (b) Current-voltage semilogarithmic plot of the core-shell nanowire photodetector system under dark (black) and under illumination with different spectral intervals: 400 – 500 nm (magenta), 400 – 600 nm (green), 600 – 900 nm (cyan) and 2 SUN (orange); (c) Time-dependent photoresponse and (d) Rise and decay time at 0.5 V of the photodetector system.

The results confirm that such photodetector system based on self-connected CuO–ZnO core-shell heterojunction nanowire arrays can have a potential impact on the development of the future nanoscale optoelectronic devices.

References

1. A Costas, C Florica, N Preda, C Besleaga, A Kuncser, I Enculescu, “Self-connected CuO–ZnO radial core–shell heterojunction nanowire arrays grown on interdigitated electrodes for visible-light photodetectors”, *Scientific Reports* 12, 6834 (2022).

Nanostructured Materials for Sensing Molecular Metabolic Biomarkers of Cell Cultures

Madalina M. Barsan[a], Daniela Oprea[a]; Caroline G. Sanz[a], Daniel N. Crisan[a], Ricardo J.B Leote[a], Melania Onea[a], Anca Aldea[a], Teodor Adrian Enache[a]
[a]Laboratory of Functional Nanostructures, National Institute of Materials Physics, 405A Atomistilor, 077125 Magurele, Romania

Integration of cell lines with sensing devices is an important approach for the investigation of cellular response and behavior during various treatments and/or stimulus. Utilization of (bio)sensors to test and evaluate cell culture can bring great value in divers applied fields as biology research, biotechnology with direct application in medicine, pharmaceutical industry and many others [1]. Electrochemistry represents a suitable method for monitoring biological targets due to its low-cost and easy operation procedure, expanding the investigation of crucial cellular processes of *in vitro* experimentation [1].

Monitoring the process of the rat adrenal medulla pheochromocytoma PC-12 differentiation, divers neurogenic characteristics may be observed and this may include studying the level of secreted neurotransmitters, studying neuron morphology before and after neurite outgrowth, can be as well observed and characterized the expression of ion and neurotransmitter receptors [2]. Under normal conditions of cultivation, PC-12 cells manifest all the characteristics of the adrenal gland cells, dividing and generating more adrenal gland type of cells. In the case of applying nerve growth factor (NGF) treatment to the culture, PC 12 cells initiate differentiation process and begin to manifest morphological and functional characteristics of sympathetic ganglion neurons but a special attention should be given to the support material since the surface properties influence and control the differentiation process.

Using NGF and a thin gold layer deposited on a glass strip and modified with collagen, as cell culture support, the differentiation of PC 12 cells was achieved, as can be observed on Figure 1. Since the support surface is a conductive one and, at the same time, a good working electrode material for electrochemical application on further studies the differentiated PC12 will be assessed through electrochemical methods.

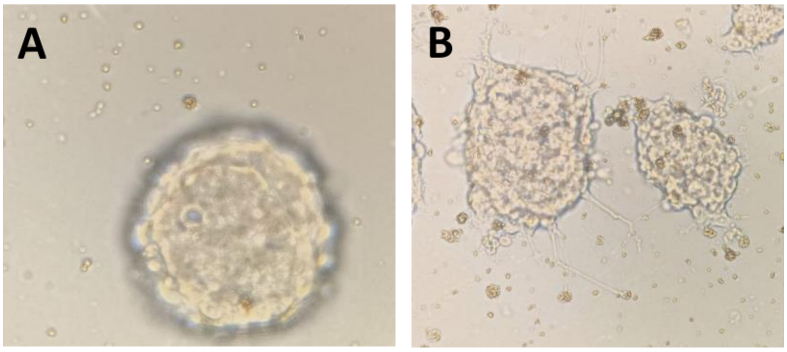

Fig. 1 PC 12 cells (A) before and (B) after differentiation process occurring at collagen modified surface.

The biocompatibility properties of gold thin film were also investigated using the melanoma B16 cell line. For this, the viability of the B16 cells at the gold electrode surface was evaluated and compared with the cells growth on biocompatible glass surface using florescence (Figure 2) and scanning electron microscopy. At both surfaces the cells presented the typical morphology, with well-defined nucleus and a few prolongations. Comparing the results obtained it was observed that the gold surface showed a high biocompatibility, highlighted by the number of cells and the specific morphology which are similar to the cells grown on the glass slide.

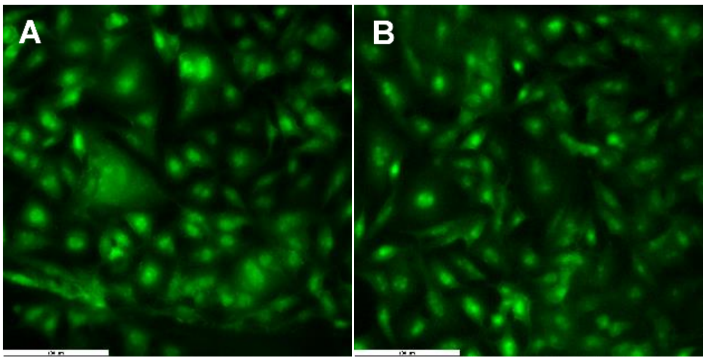

Fig. 2 Fluorescence microscopy images of B16 cells grown 48 h on (A) biocompatible glass and (B) gold surface. Scale bar: 100 µm.

Taking advantages on the conductive properties of the gold surface, the effect of oxidative stress on the B16 cell culture induced by hydrogen peroxide or proton beam irradiation was investigated by the means of cyclic voltammetry and through the evaluation of open circuit potential [3]. The results showed a modification of the electrochemical signal after the exposure of the cells to the hydrogen peroxide or proton beam irradiation. For both oxidative stress agonists, i.e. H_2O_2 and proton radiation, the cyclic voltammetry showed a main oxidation peak at +0.55 V which may correspond to the oxidation of H_2O_2 at the gold surface while the OCP measurements revealed a decrease of the values with the increase of oxidative stress of the cells (Figure 3). These findings were accomplished and confirmed by fluorescence and field effect scanning electron microscopy.

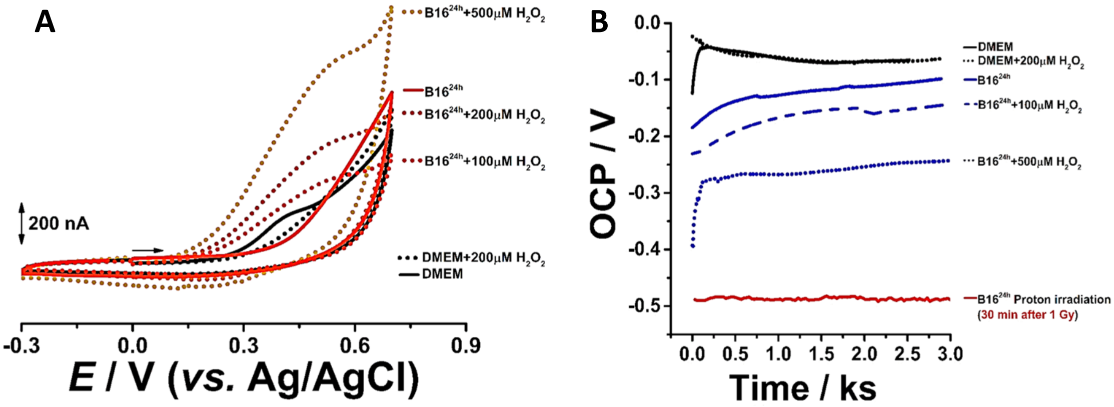

Fig. 3 (A) Cyclic voltammetry and (B) OPC before and after proton irradiation of B16 cells.

Enzyme immobilization for increased sensitivity and stability in time, is key to the development of successful and useful biosensors. Incorporation of enzymes as bioelements of recognition at the conductive polymeric substrate further provides increased selectivity towards the targeted analyte, whilst optimal enzymatic performance can be achieved through modelling of the (bio)sensing surface in terms of enzyme immobilization procedure and overall enzyme loading. Thus, novel and disposable biosensors based on superoxide dismutase (SOD) immobilized on gold nanoparticles or metallized polycaprolactone electrospun polymeric fibers (PCl/Au) has been proposed for the determination of $O_2^{\bullet -}$ in cell culture media.

Gold nanoparticles (AuNP) were synthesized via the citrate reduction method and modified with mercaptocarboxylic acid ligands. A long aliphatic ligand in the form of 11-mercaptoundecanoic acid (MUA), and a short aromatic ligand in the form of 4-mercaptobenzoic acid (MBA) were investigated as model ligands for functionalized AuNP for enzyme immobilization. The thiol group in the ligands are used for binding due to the high affinity to gold while the carboxylic acid functional group can be used to bind amine groups present in enzymes [4].

The morphology of the citrate stabilized $AuNP_{CIT}$ and the functionalized $AuNP_{MUA}$ and $AuNP_{MBA}$ was investigated and while the size of the Au core was generally similar (~20 nm), the particle distribution was significantly different. While $AuNP_{CIT}$ was dispersed into individual or small clusters of particles, $AuNP_{MUA}$ aggregates into a tightly packed monolayer while $AuNP_{MBA}$ aggregates into a porous multilayered structure. These features can explain some of the observed properties of the biosensors obtained by enzyme immobilization [4].

Enzyme immobilization was carried out by activation of the ligands' carboxylic acid groups using EDC/NHS and linking through enzyme's amine side-chain groups. The obtained bionsensors' performance was evaluated in terms of sensitivity and stability. Since the sensitivity is directly correlated with the distance between the enzyme and the electroactive gold core, $AuNP_{CIT}$ showed the best sensitivity, but in the absence of covalently attached ligands, the stability of the biosensor is low. The long aliphatic chains of MUA offer increased flexibility and steric freedom to stabilize the enzyme, but the increased distance from the enzyme to the gold core leads to a decreased sensitivity. The MBA ligand is rigid so there is little steric freedom to accommodate the ligand, but it still allows for covalent immobilization so the stability is greatly increased compared to $AuNP_{CIT}$. The shorter distance to the gold core as well as the aromatic ring which allows electron transfer mechanisms, give $AuNP_{MBA}$ increased sensitivity over the MUA functionalized nanoparticles, thus serving as a compromise between stability and sensitivity [4].

Nevertheless, high performances can be achieved using electrode substrates made of metallized electrospun polymeric fibers, versatile for sensing applications [5]. The electrochemical characterization of the conductive fiber scaffold was initially assessed through cyclic voltammetry (CV). SOD enzyme was employed as bioelements of superoxide recognition, for which three immobilization procedures were investigated: (*i*) crosslinking with EDC/NHS at a cysteine self-assembled monolayer ($PCl/Au/SOD_{CYS}$); (*ii*) biopolymer encapsulation with chitosan ($PCl/Au/SOD_{CHI}$); and (*iii*) cross-linking with glutaraldehyde ($PCl/Au/SOD_{GA}$). Scanning electron microscopy (SEM) was used to characterize the biosensor surface morphology; at the $PCl/Au/SOD_{CYS}$ biosensor, the enzyme can be easily seen in close proximity to the fiber scaffold. Fixed potential amperometry was conducted at −0.3 V and + 0.3V in 0.1 M PB pH 8.0 with successive additions of 20 μM of $O^{2\bullet-}$, in the absence of oxygen, at three SOD biosensors. At negative potentials, the working principle of the biosensors is based on the reduction of H_2O_2, generated in the enzymatic catalyzed dismutation of $O_2^{\bullet-}$ by SOD [6]. The working principle of the biosensors at +0.3 V can be attributed to the oxidation of the catalytic center of the enzyme itself, since, upon interaction with $O2^{\bullet-}$, the copper present at the active site is (bio)chemically reduced and then directly oxidized at the applied potential. In this case, the biosensor response in the presence of dissolved oxygen is identical to that recorded in the absence of oxygen, which is favorable for the final applicability of the device to monitor released superoxide from stressed/damaged cells. The biosensors analytical performance is directly dependent on the applied potential and the signal transduction mechanism during the amperometric monitoring of $O_2^{\bullet-}$. At −0.3 V, the PCl/Au/SODCHI presented superior analytical parameters, with highest sensitivity value of 40.1 μA mM^{-1} cm^{-2} to $O_2^{\bullet-}$, LOD of 0.9 μM and 3.0% deviation between measurements (Figure 4). At +0.3 V, the PCl/Au/SODCYS presented the highest sensitivity value of 16.1 μA mM^{-1} cm^{-2}, with a limit of detection of 1.9 μM and a 3.2% deviation between measurements (Figure 5). For the latter, the recognition of the active site of the enzyme is more efficient than peroxide recognition in negative potentials given the proximity of the enzyme active center to the electrode substrate, in addition to avoiding signal from the chemical dismutation of superoxide in aqueous media.

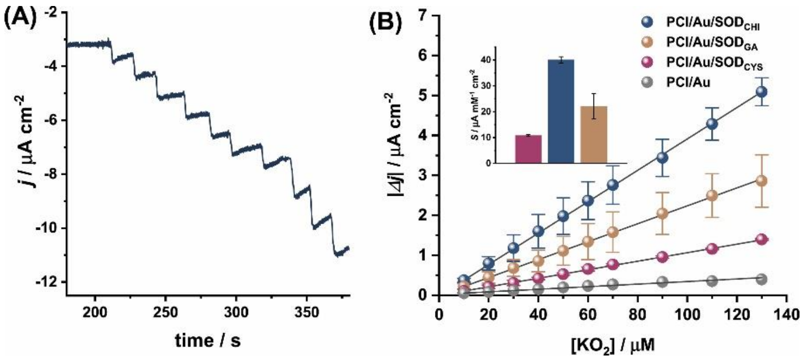

Fig. 4 (A) Typical fixed potential chronoamperometric response obtained in 0.1 M PB pH 8.0 at −0.3 V using PCl/Au/SODCHI with successive additions of KO2 and (B) Calibration curve constructed from amperograms obtained at −0.3 V for each SOD biosensor construction; (inset-corresponding sensitivity values).

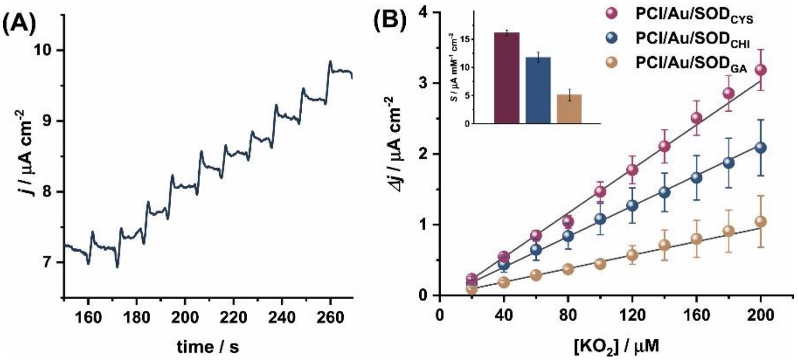

Fig. 5 (A) Typical fixed potential chronoamperometric response obtained in 0.1 M PB pH 8.0 at +0.3 V using PCl/Au/SODCHI with successive additions of KO2 and (B) Calibration curve constructed from amperograms obtained at +0.3 V for each SOD biosensor construction and PCl/Au (inset-corresponding sensitivity values).

The PCl/Au/SOD$_{CYS}$ biosensor showed no significant interference in the presence of common biological compounds and was further applied for monitoring $O_2^{\bullet-}$ in cell culture media at +0.3V. The sensitivity value was 14.5 µA mM^{-1} cm^{-2}. High recovery values over 92% were obtained for each $O_2^{\bullet-}$ addition. Thus, the overall performance of the developed biosensor shows the promising applications for the on-line monitoring of superoxide in cell cultures grown directly on the biosensor itself.

References

1. D Oprea, CG Sanz, MM Barsan, TA Enache, "PC-12 cell line as a neuronal cell model for biosensing applications", *Biosensors 12,* 500 (2022).
2. Q Liu, C Wu, H Cai, N Hu, J Zhou, P Wang, "Cell-based biosensors and their application in biomedicine", *Chemical Reviews* 114, 6423–6461 (2014).
3. M Onea, M Bacalum, AL Radulescu, M Raileanu, L Craciun, TR Esanu, TA Enache, "Electrochemical evaluation of proton beam radiation effect on the B16 cell culture", *Scientic Reports* 12, 2261 (2022).
4. CG Sanz, DN Crisan, RJB Leote, M Onea, MM Barsan, "Bioconjugates of mercaptocarboxylic acids functionalized AuNP and superoxide dismutase for superoxide electrochemical monitoring", *Microchimica Acta* 189, 245 (2022).
5. RJB Leote, M Beregoi, I Enculescu, VC Diculescu, "Metallized electrospun polymeric fibers for electrochemical sensors and actuators", *Current Opinions in Electrochemistry* 34, 101024 (2022).
6. CG Sanz, M Onea, A Aldea, MM Barsan, "Disposable superoxide dismutase biosensors based on gold covered polycaprolactone fibers for the detection of superoxide in cell culture media", *Talanta* 241, 123255 (2022).

Electrochemical Sensing of Oxidative Stress Initiators and their Interactions with DNA and Cells

Victor C. Diculescu[a], Teodor Adrian Enache[a], Monica Enculescu[a], Madalina M. Barsan[a], Caroline G. Sanz[a], Alexandru Evanghelidis[a], Mihaela-Cristina Bunea[a], Daniela Oprea[a], Ricardo J.B. Leote[a]

[a]Laboratory of Functional Nanostructures, National Institute of Materials Physics, 405A Atomistilor, 077125 Magurele, Romania

Oxidative stress denotes the imbalance between the concentration of free radicals resulting from metabolic reactions and the organisms' ability to neutralize these radicals and has a significant role in the aging process and in the pathophysiology of age-related diseases. This imbalance is usually caused by endogenous factors such as reactive oxygen species resulting from intracellular redox reactions or from exogenous factors such as exposure to medical treatment. Oxidative stress affects the normal biological processes through interactions with cellular components, including lipids, DNA and proteins, leading to medical anomalies [1]. From this, point of view the development of devices and methodologies capable to detect and identify oxidative stress initiators as well as their interaction with cellular components, especially DNA, is necessary.

Quantification of oxygen in 2D constructs of human valvular interstitial cells

The study aims the design and application of a new 2D model for human heart valve based on gold covered electrospun polycaprolactone (PCL/Au) fibers populated with valvular interstitial cells (VIC), which are found inside the valve leaflets, and in the case of a tissue implantation, their oxygen supply is minimum; therefore, information regarding the oxygen levels will be valuable for developments in the tissue engineering of valves. The model contains the PCL/Au as an oxygen electrochemical sensor for the monitoring of cell oxygenation in the cellular matrix grown directly on the surface of the sensor (Figure 1).

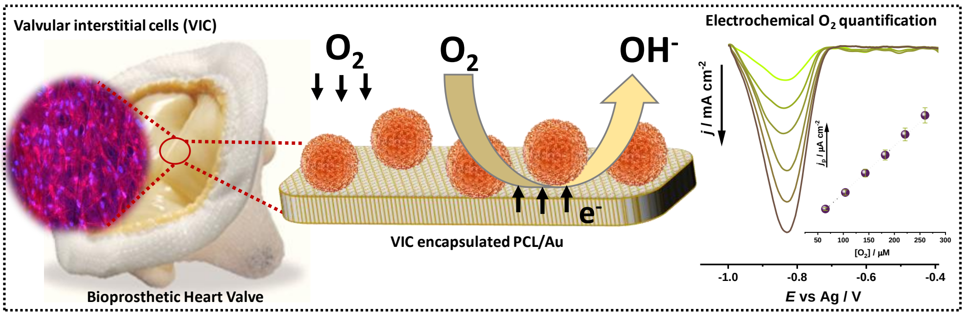

Fig. 1 Illustration of the 2D model for human heart valve based on PCL/Au fibers populated with VIC, with the PCL/Au serving as oxygen electrochemical sensor. From reference [2].

In this work the PCL fibers with diameters between 0.5-0.8 µm (Figure 2A) were fabricated by electrospinning a PCL polymeric solution and covered with Au by DC magnetron sputtering. Before the cell growth on the PCL fibers the obtained PCL scaffolds were sterilized by UV light exposure followed by permeabilization in the culture medium. Finally, the human VIC were cultured on the scaffolds and let to grow for 2 days, ensuring cell proliferation up to 2 cell cycles.

The evaluation of PCL and PCL/Au biocompatibility was done by LDH cytotoxicity assay, with culture dishes serving as control. A small 7.7% decrease in LDH activity for the cells grown on PCL fibers was indicative for an increase in cells viability grown on PCL/Au compared to those grown in conventional culture dishes. Moreover, the morphology of cells on PCL/Au fibers investigated after 7 days of culture by fluorescence microscopy (Figure 2B) show the homogeneously distribution of VIC with the formation of cell networks.

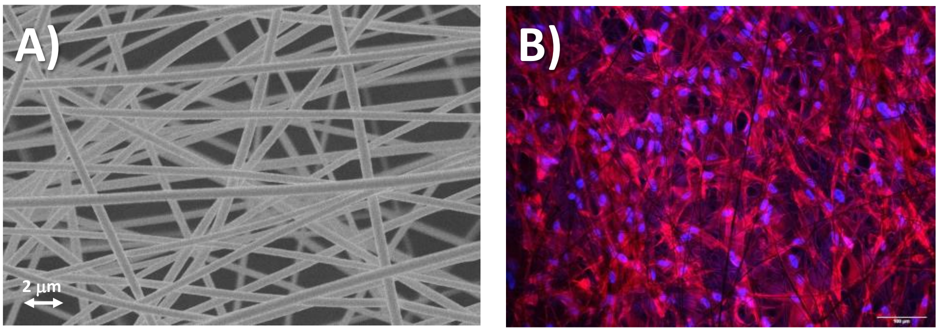

Fig. 2 (A) SEM images of PCL/Au obtained at 10k magnification and (B) VIC morphology encapsulated in 2D-membranes of PCL/Au at day 7 of culture as determined by phalloidin labelled F-actin (red) and DAPI nuclear staining (blue) at a scale bar 100 µm (20x). Adapted from reference [2].

The electrochemical response of PCL/Au was then evaluated in sodium phosphate buffer solution (NaPB pH 7.5) and in the culture medium (DMEM), with the cyclic voltammetric response showing clearly the oxygen reduction in the negative region at potential values close to -0.6 V vs. Ag. As expected, upon cell encapsulation within the PCL/Au fiber network, the capacitance currents decrease.

Since electrochemical impedance spectroscopy (EIS) is a sensitive technique for processes occurring at the electrode interface, it was employed to quantify O_2 in cellular media at the PCL/Au/cells sensor, at the potential of -0.65 V vs Ag required for the O_2 reduction observed in the CV study.

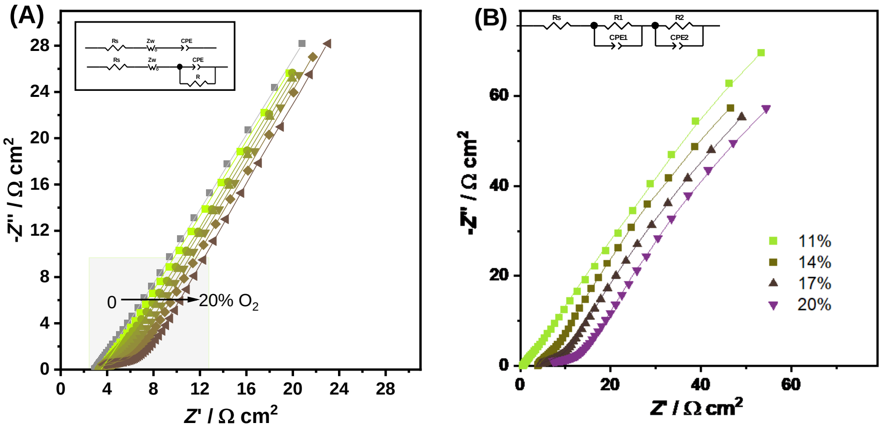

Fig. 3 Complex plane impedance plots recorded at -0.65 V vs. Ag in cellular media at (A) PCL/Au for at O_2 concentration between 0 and 20% and (B) PCL/Au/cells for O_2 concentration between11 and 20% (insets are the equivalent circuits used to fit the spectra). Adapted from reference [2].

The first step was to calibrate the PCL/Au sensor by recording EIS at controlled O_2 concentration (Figure 3A) which was achieved by placing the electrochemical cell in a hypoxistation. The levels of O_2 were varied between 5 and 20%, corresponding to a dissolved O_2 concentration in cellular media between 65 to 260 µM. The spectra were fitted using an equivalent circuit, with one circuit element, the diffusional Warburg resistance (Z_W), having a linear dependency with the O_2 concentration. The real impedance (Z') and impedance magnitude ($|Z|$) at 10 Hz lead to similar sensitivity values towards O_2 sensing, with good linear correlation factor R^2 of 0.993 and 0.996. Following, EIS spectra were recorded at PCL/Au/cells (Figure 3B) the change in the EIS profile being in agreement with the CV data and indicating the encapsulation of the cells in the fiber network., with partial coverage of the PCL/Au with the cells. Best linearity dependence with the oxygen concentration were obtained using *Z*’ and |*Z*|, with similar sensitivities of 78 and 76 Ω cm^2 mM^{-1}, respectively, and linear correlation factors above 0.996.

Influence of the Photodegradation of Azathioprine on DNA and Cells

Azathioprine is an immunossupresive drug which can present dangerous side effects due its photosensitivity. These aspects led to the development of numerous spectrophotometric and electrochemical studies regarding the degradation of azathioprine and its interaction with DNA and cells. The main purpose of the study consisting in the evaluation of interaction between UV degradation products of azathioprine and DNA through electrochemical methods, before and after photodegradation, and in studying their effects on the fibroblast cells L929. The photodegradation effects of AZA on DNA and the fibroblast cells L929 it was investigated using UV–Vis spectrophotometry and differential pulse voltammetry, while the interaction of AZA and its metabolites, before and after photodegradation, with an L929 cell culture was investigated by point of view of cell viability and fluorescence microscopy.

Each sample was degraded by exposure to the Solar simulator (SS) for a period of time at one Sun. All the samples of AZA and its metabolites were investigated by UV spectrophotometry in the presence and absence of dsDNA before and after exposure for different times to the solar simulator (SS). The results obtained through the spectrometric investigations revealed the formation of 6-mercaptopurine and 1-methyl-4 nitro-imidazole after the degradation of azathioprine and their interaction with DNA.F or the evaluation of potential damages produced by the UV degradation of immunossupresive drug and its metabolites DP voltammetry measurements were realized for monitoring the oxidation currents of the purine bases within the dsDNA (Figure 4). The voltammetric measurements confirmed the formation of adducts between the guanine residues from dsDNA and AZA metabolites, highlighting the degradation of DNA and formation of oxidative products.

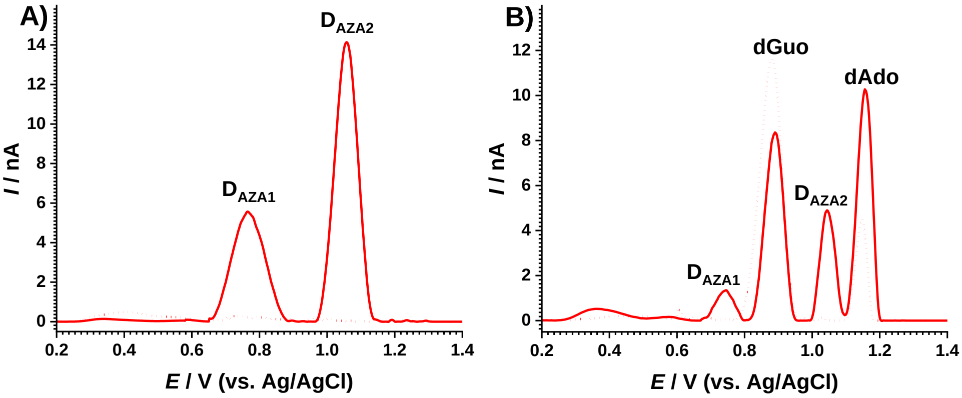

Fig. 4 DP voltammograms of 60 µM AZA: (A) before and (B) after incubation with 10 µg mL^{-1} dsDNA | in pH 7.0 0.1 M phosphate buffer, during (dotted curve) 0 and (full line) 180 min exposure to the solar simulator. From reference [3].

The interaction mechanism was obtained by studying the interaction of dsDNA and AZA metabolites 1-methyl-4 nitro-imidazole and 6-mercaptopurine. These studies revealed that the degradation products of 6-mercaptopurine were responsible for the interaction with adenine segments, while 1-methyl-4 nitro-imidazole metabolites led to the formation of adducts with guanine residues.

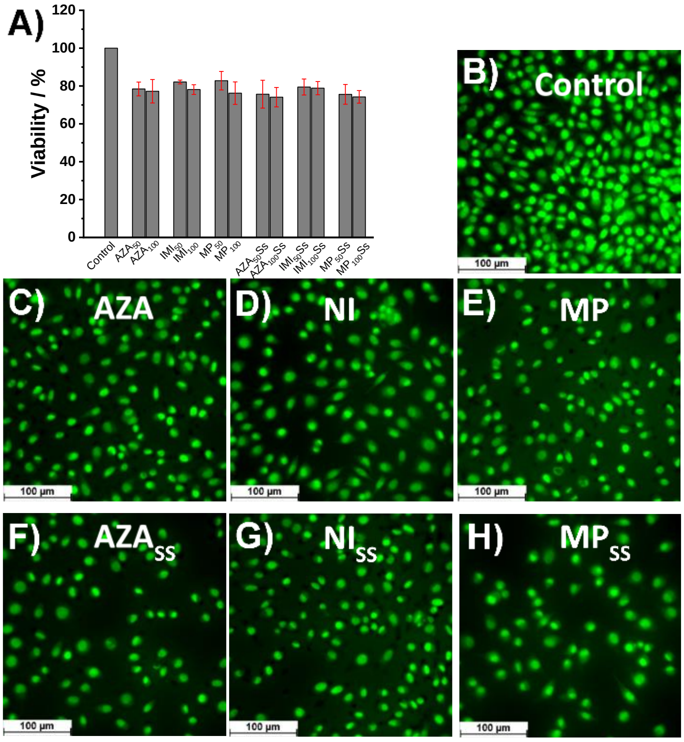

Fig. 5 (A) Cell viability and (B–H) fluorescence microscopy images obtained for L929 cells.

The evaluation of L929 cells viability was realized using the MTS assay (Figure 5). The *in vitro* assays carried out on L929 cells in the presence of AZA and its metabolites revealed a maximum decrease around of 20% attributed to the AZA and MP samples, showing that the cells were not affected.

Electrochemical characterization of shikonin and in-situ evaluation of interaction with DNA

Shikonin, a natural compound with pharmaceutical properties, has attracted interest due to its anti-oxidant properties, potential anti-cancer activity and activity over several biological pathways, such as dsDNA transcription/replication of cancer cells and inhibition of pyruvate kinase M2. The electrochemical behavior of shikonin in aqueous media was investigated at glassy carbon electrodes by cyclic and differential pulse voltammetry. The electrochemical mechanism of shikonin was attributed to the redox processes of the substituents of the naphthazarin structure (Schemes 1A and 1B). The reduction occurs at the quinone functional group present in the naphthazarin moiety, following a mechanism involving a total of 2 electrons and 2 protons. In the presence of oxygen, the semiquinone radical intermediate is involved in an electrocatalytic reaction with oxygen, and the formation of superoxide occurs concomitantly with the regeneration of the initial quinone functionality (Scheme 1A). In the anodic potential region, the one-step oxidation process involves 2 electrons and 2 protons of the dihydroxy moiety at the naphthazarin structure. A reversible behavior was observed at lower values of pH and for faster scan rates, suggesting that the oxidation of shikonin in aqueous media follows an electrochemical-chemical (EC) redox mechanism, characteristic to catechol derivatives (Scheme 1B).

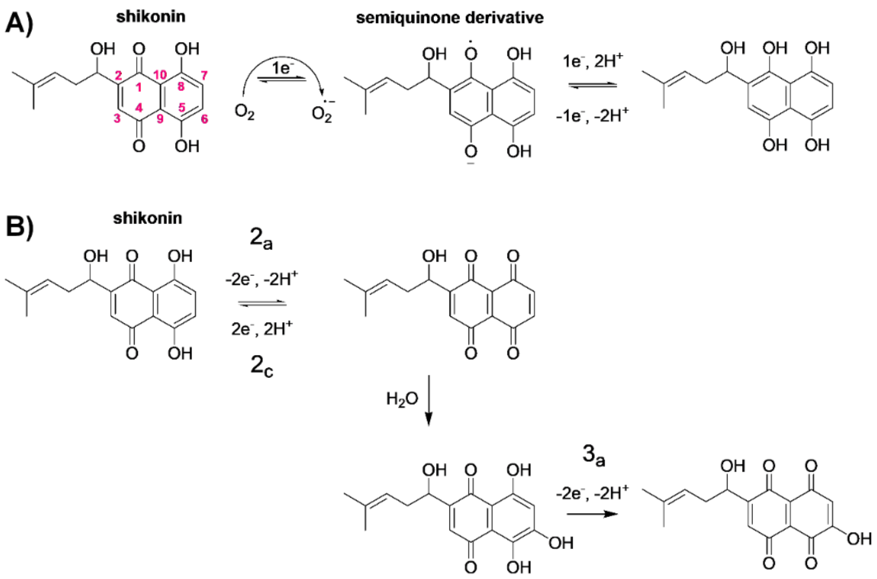

Scheme 1 Proposed (A) reduction and (B) oxidation mechanisms of shikonin. From reference [4].

The interaction between the redox products of shikonin and dsDNA was in-situ evaluated with the dsDNA-electrochemical biosensor. The procedure involved two steps. First, the dsDNA-electrochemical biosensor was incubated in a solution of shikonin. Then, the dsDNA-electrochemical biosensor was transferred to the electrochemical cell that contained only pure acetate buffer electrolyte, where a conditioning potential of -0.20 V or +0.60 V was applied during 600s in order to reduce the quinone functionality or oxidize the dihydroxy moiety of shikonin molecules bound to the dsDNA layer, respectively. This procedure was carried out both in the absence and presence of dissolved oxygen (Figure 6).

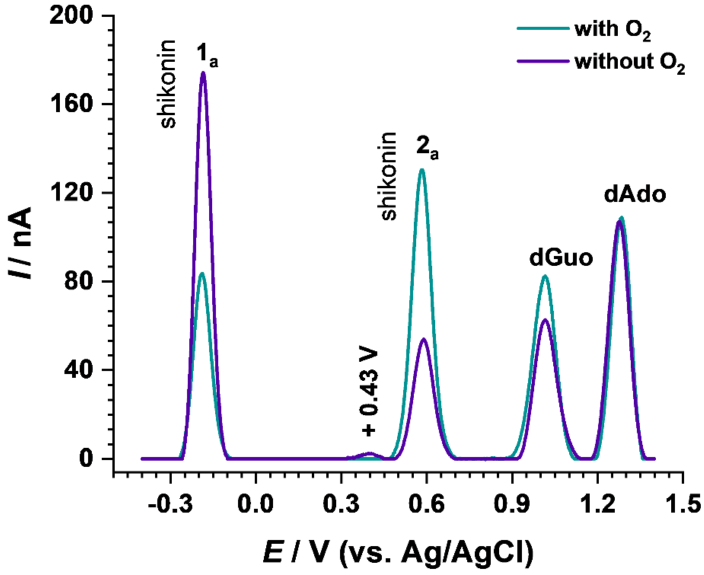

Figure 6. DP voltammograms obtained with the dsDNA-electrochemical biosensor in 0.1M acetate buffer pH 4.5 after incubation during 5 min at -0.20 V in 10 µM shikonin in the absence and presence of oxygen. From reference [4].

The oxidative damage to DNA produced by the *in-situ* reduction of shikonin is explained taking into consideration the shikonin reduction mechanism. Briefly, shikonin is reduced at potential values below -0.20 V resulting in a semiquinone intermediate. In the absence of oxygen, the stabilization of the semiquinone intermediate occurs with the transfer of 1 e^- and 1 H^+ to fully reduced shikonin. In the presence of oxygen, the stabilization of the semiquinone intermediate occurs with the generation of superoxide and regeneration of the initial quinone functionality (Scheme 1). Therefore, it is proposed that when the conditioning potential of -0.20 V is applied in the absence of oxygen to the DNA-electrochemical biosensor previously incubated in a shikonin solution, the semiquinone intermediate is *in-situ* formed, and its stabilization occurs with the transfer of electrons from a dGuo residue resulting in a guanine cation radical (Scheme 2).

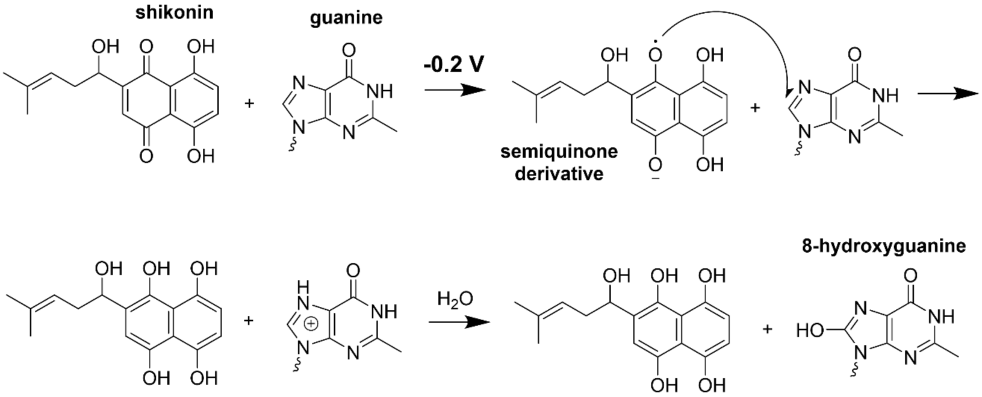

Scheme 2 Proposed mechanism for the in-situ damage to DNA by shikonin redox product. From reference [4].

In these conditions, the fast hydrolysis of the generated guanine cation radical occurs with the formation of 8-hydroxyguanine (Scheme 2) similar to previous reports on adriamycin and other naphthoquinone derivatives. At the same time, shikonin is fully reduced leading to an increased 1_a oxidation peak on DP voltammograms (Figure 6).

References

1. TA Enache, E Matei, VC Diculescu, “Electrochemical sensor for carbonyl groups in oxidized proteins”, *Analytical Chemistry* 91, 1920–1927 (2018).
2. CG Sanz, AC Mihaila, A Evanghelidis, VC Diculescu, E Butoi, MM Barsan, “Quantification of cell oxygenation in 2D constructs of metallized electrospun polycaprolactone fibers encapsulating human valvular interstitial cells”, *Journal of Electroanalytical Chemistry* 905, 116005 (2022).
3. MC Bunea, VC Diculescu, M Enculescu, D Oprea, TA Enache, “Influence of the photodegradation of azathioprine on DNA and cells”, *International Journal of Molecular Sciences* 23, 14438 (2022).
4. RJB Leote, CG Sanz, VC Diculescu, “Electrochemical characterization of shikonin and in-situ evaluation of interaction with DNA”, *Journal of Electroanalytical Chemistry* 921, 116663 (2022).

Solutions for Combatting Implant Bacterial Infection Based on Silver Nano-Dispersed and Gallium-Incorporated Bioactive Phosphate Glass Magnetron Sputtered Films

George E. Stan[a], Adrian-Claudiu Popa[a], I. Zgura[a], Bryan W. Stuart[b], Matthew J. Carrington[b], David M. Grant[b], Marius Necsulescu[c]

[a]Laboratory of Complex Heterostructures and Multifunctional Materials, National Institute of Materials Physics, 405A Atomistilor, 077125 Magurele, Romania
[b]Advanced Materials Research Group, Faculty of Engineering, University of Nottingham, University Park, NG7 2RD, Nottingham, United Kingdom
[c]Army Centre for Medical Research, 010195 Bucharest, Romania

The coating of endo-osseous dental and orthopedic implants with thin-films based on bioactive glasses incorporating various metal-based antimicrobial agents has recently emerged as a potent solution against the recent rise of resistant bacterial strains [1], furthermore as a decline in the efficacy of conventional antibiotic treatments as a prophylactic measure for preventing post-surgery infections was stressed [2]. In this respect, the physical vapor deposition techniques, markedly the magnetron sputtering-based ones, are particularly attractive due to their propensity to generate high quality mechanically adherent and conformal thin films. Thereby, premises are settled to supersede the longstanding industrial standard of plasma sprayed thick implant-type coatings. Phosphate-based bioactive glasses (PBG) were already shown to be effective therapeutic carriers by incorporating and subsequently releasing osteogenic elements such as Ca, P, and Mg to stimulate bone regeneration [3]. The complementary incorporation of anti-microbial metal agents could expand its application range.

Consequently, in a joint-venture inter-institutional effort [4], the University of Nottingham (UK) and the National Institute of Materials Physics (Romania), advanced two independent antibacterial strategies based on magnetron sputtered PBG sacrificial layers for the future prevention of implant infections: (*i*) the dispersion of silver nanoparticles into the glass matrix by co-sputtering from two targets resulting in a composite coating; and (*ii*) control over the duration of the antimicrobial efficacy by changing the thickness of the sacrificial Ga-doped PBG deposited layer [5]. The manufacturing routes proposed herein (*i.e.*, thin Ag:PBG composite layers or thicker Ga incorporated PBG coatings) use the capacity of the additional constituting glass elements (*i.e.*, Ca, Mg, Na, and Fe) to modify the cross-linking of phosphate glass units, endowing a suitable degradation timescale capable of facilitating the fast release of (*i*) Ag in its metallic form (known to possess lower systemic toxicity with respect to its ionic form [6]) from the composite layers or (*ii*) Ga^{3+} ions from the glass coatings, within a required window of 6 – 24 h, period when pathogens are still metabolically inactive, and thereby easier to eradicate.

Dual target consecutive co-sputtering was uniquely employed to produce a 46 nm Ag:PBG (P_2O_5–MgO–CaO–Na_2O–Fe_2O_3) composite observed by high resolution TEM to consist of uniformly dispersed ≈5 nm metallic Ag nano-particles in a glass matrix (Figure 1 a–e). Ga^{3+} was integrated into a phosphate glass preform target (P_2O_5–MgO–CaO–Na_2O–Ga_2O_3) which was sputtered to film thicknesses of ≈400 or 1400 nm (Figure 1f,g). The XPS analysis probed the major metallic chemical status of the embedded silver-based nano-particles.

The antimicrobial efficacy of Ag:PBG and Ga-PBG PVD layers was assessed by quantification of viable colony forming units (CFU) of *Staphylococcus aureus* (Figure 2a) and *Escherichia coli* (Figure 2b) after 6 and 24 h of culture. When culturing on the uncoated titanium (Ti) substrate, a progressive proliferation of bacteria (up to 3-log increase at 24 h) was observed, irrespective strain type. The bactericidal effect of Ag:PBG and Ga-PBG layers was evidenced for both types of bacteria. Similar antimicrobial trends were shown at both time points for all films in relation to Gram-negative *E. coli*, where CFUs were reduced by 2 log (after 6 h) and 2.5 log (after 24 h) with respect to the initially seeded CFUs. In comparison to the uncoated Ti substrate, a 3.5-log and 5-log *E. coli* reduction was recorded at 6 and 24 h, respectively. In the case of Gram-positive *S. aureus*, the antibacterial efficacy increased in the order Ag:PBG-PVD < Ga-PBG-PVD≈400 nm < Ga-PBG-PVD≈1400 nm, at all-time points. The proliferation of *S. aureus* was drastically reduced for the Ga-containing coatings, whereby 5 and 6 log-reductions were recorded after 24 h in the case of Ga-PBG-PVD≈400 nm and Ga-PBG-PVD≈1400 nm, respectively, relative to the uncoated substrate. Thus, it is suggested that the intensity of the effect can be controlled by varying the Ga-PBG-PVD film thickness (and thereby, the amount of therapeutic ions to be released).

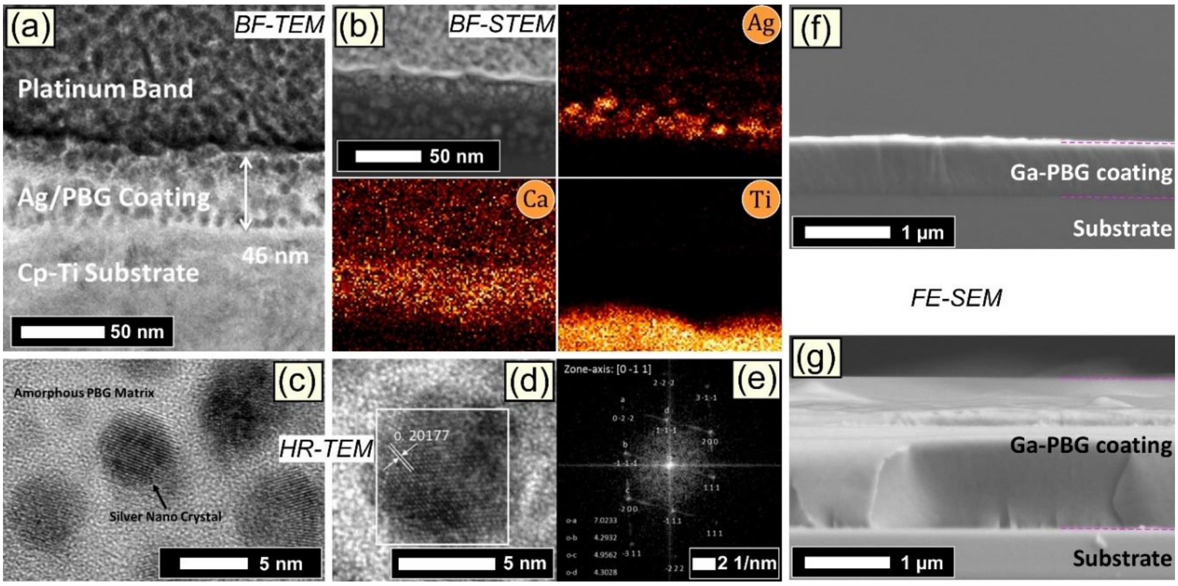

Fig. 1 (a) Cross- BF-TEM micrograph of the Ag:PBG-PVD/Ti thin film (thickness of ~46 nm); (b) Cross-sectional BF-STEM image of the Ag:PBG-PVD/Ti specimen accompanied by EDXS elemental distribution maps of Ag, Ca, and Ti. (c) HR-TEM image of an Ag:PBG-PVD/Ti thin film FIB lamella, highlighting the even dispersion of Ag nano-crystals within an amorphous PBG matrix. (d) HR-TEM image of a single Ag nano-crystal, where (e) illustrates the associated FFT of the region marked in (d). The FFT presented in (e) indexes to Ag [0 –1 1]. (f,g) Representative cross-FE-SEM images of the Ga-PBG-PVD/Si coating at a thickness of (f) ≈400 and (g) ≈1400 nm.

A human mesenchymal stem cell (hMSC) line was used to test the cytocompatibility of the PBG-based coatings. The hMSCs grown on PBG implant-type coatings presented a morphology typical for the cell line, retaining their shape, being well-spread on the surfaces, and having healthy lamellipodia and filopodia and a normal distribution of actin microfilaments in the cytoskeleton (Figure 2 c–e). Only rare cells undergoing division were rounded. The nuclei had typical ovoid shape, with normal dimension and condensation of chromatin. The MTS tests suggested cellular proliferation on both Ag and Ga containing PBG layers (Figure 2f). However, a delayed hMSCs proliferation was noticed for the Ag:PBG-PVD when compared to the bare Ti and Ga-PBG-PVD≈1400 nm. Overall, the morphological analysis of cells grown on these layers in conjunction with the cell proliferation data showed that these films are cytocompatible. Regarding the potential toxicity of the antimicrobial agents (Ag and Ga) in some systems (*e.g.*, nephrotoxicity, hemotoxicity), it should be highlighted that the PBG films leached a very small amount of Ag (~9 ppm) and Ga (max. ~27 ppm) in total. Even in the event of total dissolution of the films, the amount of Ga released for a dental fixture (typically 3.75 mm thick and 11 mm long) covered with ≈1400 nm and ≈400 nm of Ga-PBG-

PVD film would be approximately 200000 – 700000 times less than the Ga amount in the case of a course of Ga nitrate treatment for hypercalcemia that has been shown to be a major risk in causing renal function impairment.

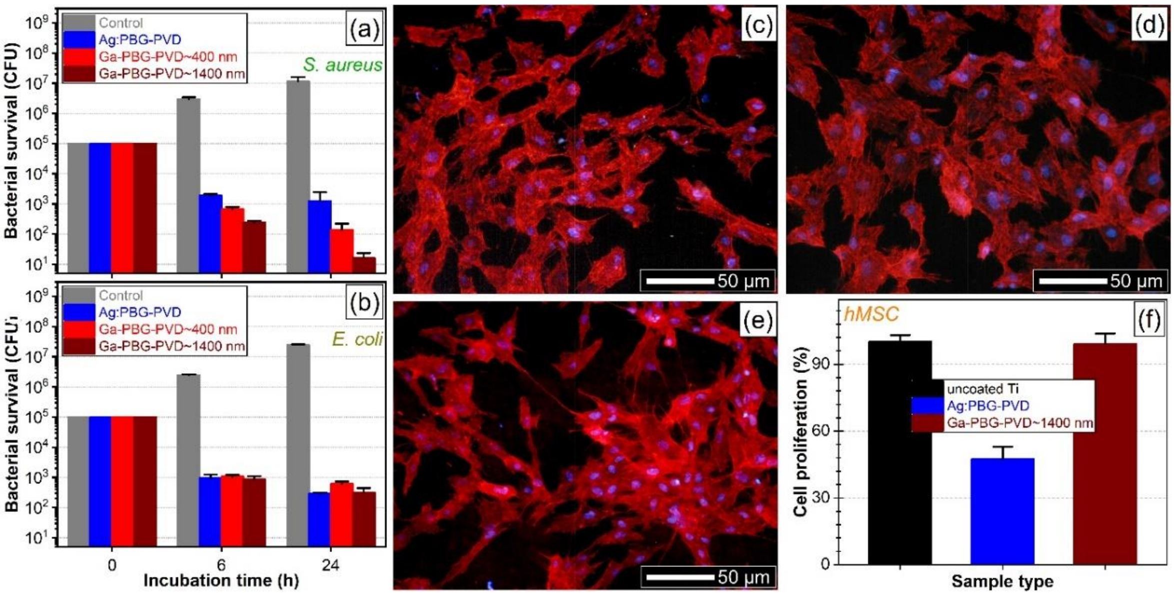

Fig. 2 (a, b) Time evolution of the antibacterial activity of the Ag:PBG-PVD and Ga-PBG-PVD implant-type coatings against (a) *S. aureus* and (b) *E. coli.* The data are represented as logarithmic values of CFU mL^{-1} of bacterial cells. (c–f) Cell cultures tests: (c–e) Morphology of hMSCs grown for 24 h on the (c) uncoated and (d) Ag:PBG-PVD and (e) Ga-PBG-PVD≈1400 nm coated cp-Ti. Actin microfilaments were stained with Phalloidin-AlexaFluor596 (red), whilst the cell nuclei were counterstained with DAPI (blue). (f) hMSCs proliferation at 24 h, as assessed by MTS.

The combined preliminary antibacterial – cytocompatibility studies showed that both magnetron sputtering PBG-based coating solutions have the potential to be used as sacrificial layers to counteract implant infection due to surface contamination. The results within this study could contribute to paving the way for the development of fully tailorable therapeutic films with widespread applicability in next generation endo-osseous implants such as hip stems or dental implants. Our future research studies will continue on the basis of these established premises.

References

1. L Drago, M Toscano, M Bottagisio, "Recent evidence on bioactive glass antimicrobial and antibiofilm activity: A mini-review", *Materials* 11, 326 (2018).
2. B Li, TJ Webster, "Bacteria antibiotic resistance: new challenges and opportunities for implant-associated orthopedic infections", *Journal of Orthopaedic Research* 36, 22–32 (2018).
3. HR Fernandes, A Gaddam, A Rebelo, D Brazete, GE Stan, JMF Ferreira, "Bioactive glasses and glass-ceramics for healthcare applications in bone regeneration and tissue engineering", *Materials* 11, 2530 (2018).
4. BW Stuart, GE Stan, AC Popa, MJ Carrington, I Zgura, M Nesculescu, DM Grant, "New solutions for combatting implant bacterial infection based on silver nano-dispersed and gallium incorporated phosphate bioactive glass sputtered films: A preliminary study", *Bioactive Materials* 8, 325–340 (2022).
5. GE Stan, AC Popa, C Besleaga, OSIM patent RO 134819 (2022).
6. ABG Lansdown, "A pharmacological and toxicological profile of silver as an antimicrobial agent in medical devices", *Advances in Pharmacological and Pharmaceutical Sciences* 2010, 910686 (2010).

Anharmonic Phonon Properties and Memristive Characteristics of SnSe Nanoflakes

Angel T. Buruiana[a], Amelia E. Bocirnea [a], Andrei C. Kuncser[a], Teddy Tite[a], Elena Matei [a], Claudia Mihai[a], Aurelian C. Galca[a], Alin Velea[a], Natalia Zawadzka[b], Katarzyna Olkowska-Pucko[b], Łucja Kipczak[b], Adam Babiński [b], Maciej R. Molas[b]
[a]National Institute of Materials Physics, 405A Atomistilor, 077125, Magurele, Romania,
[b]Institute of Experimental Physics, Faculty of Physics, University of Warsaw, 5 Pasteura, 02-093 Warsaw, Poland

Non-volatile resistive switching, known as memristor effect, where an electric current switches the resistance of a two-terminal device between a high resistance state and a low resistance state is an important feature that is crucial in the development of high density information storage, computing and reconfigurable systems. The ability to encode the biasing history makes the memristor suitable for the potential application as a storage class memory. Unlike dynamic random access memory (DRAM) or static random access memory (SRAM), the storage class memory, usually based on floating gate transistors or magnetic storage, operates at a slower speed but has a higher density and non-volatility. To surpass the performance of the floating gate transistors and the magnetic storage, the size of the memristor element is preferred to be less than 10 nanometers to achieve high density integration, thus bringing it in the bidimensional materials domain. The device should be able to retain its state for years, even decades, and possess large write-erase endurance at a reasonable switching speed. The device switching energy per operation should be as low as possible to be energy efficient and compatible with the circuits that are to be driven, which are comprised of advanced CMOS technology nodes. Although it is challenging to demonstrate all the best figures of merit in a single material system, the memristor has shown a great potential which makes it a strong candidate as the next generation storage class memory.

An important aspect that needs to be considered when fabricating such devices is the thermal and electrical transport in materials which are related to the anharmonic phonon effect. Since phonons are the dominant heat carrier in semiconductors it is important to understand their temperature dependent behavior in order to correlate the thermal transport properties with their anharmonic bonding. The thermal lattice conductivity can be determined by the anharmonic phonon coupling process between different phonons. Hence, characterizing the temperature effect on the lattice is of high importance to understand the limitations to charge carrier mobility and thermal conductivity. A common method to achieve this is using the high-resolution and non-destructive Raman Spectroscopy since it provides important information about the crystal structure, vibration of chemical bonds, phonon dispersion and electron-phonon interaction.

Tin selenide is a p-type semiconductor that has an orthorhombic crystal structure in space group Pnma (62) with atoms arranged in two adjacent double layers of tin and selenium that are held together by weak van der Waals interactions. It has a wide range of applications due to its narrow bandgap and can be synthesized relatively easily through chemical/physical methods.

A technique that is easy to implement in industry and has already shown its efficiency in obtaining 2D materials is the Physical Vapor Transport [1, 2], for which the schematic diagram is presented in Figure 1. As a thermodynamic process, it has been found recently that physical vapor transport (PVT) is able to produce high-quality 2D crystals with more stable atomic structures, and thereby in near future could be a pinnacle technique to obtain 2D materials to be considered for optoelectronics applications. When the thermodynamic conditions are reached, the precursor SnSe powder evaporates and recrystallizes on the cold surface of the substrate, while the thickness and morphology of the nanoflakes (NF) are dependent on the deposition parameters.

The chemical composition and structure of the samples are shown in Fig. 2. The morphology of the as-synthesized NFs was investigated through optical microscopy and AFM, which showed that the rectangular shape is due to the orthorhombic structure. Optical microscopy indicates a uniform contrast suggesting a constant thickness of the flake (Figure 2a). Figure 2b presents an AFM image with the corresponding line profile of a typical synthesized SnSe NF, revealing a thickness under 100 nm which is controllable through the growth parameters used in the synthesis experiment.

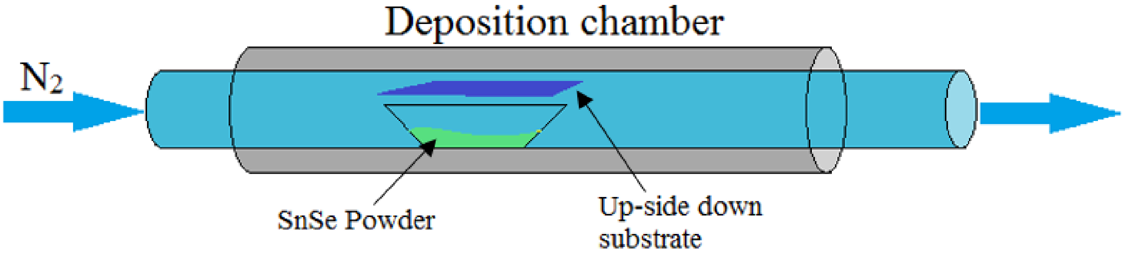

Fig. 1 Schematic diagram of the PVT equipment used in the synthesis of SnSe nanoflakes.

The HR-TEM image, Figure 2c, of a typical rectangular NF shows lattice fringes with lattice spacing of about 3.04 Å, corresponding to reflections on (0 1 1) planes. The SAED pattern, Figure 2d, observed along the [1 0 0] zone axis has been associated with the orthorhombic phase of the SnSe system (COD ID: 1537675). The SEM image of a SnSe NF and the corresponding EDX elemental mapping is shown in Figures 2e–h. EDX shows a uniform distribution of the elements on the surface of the entire nanoflake with an average quantified concentration of 47.46 % Sn and 52.54% Se.

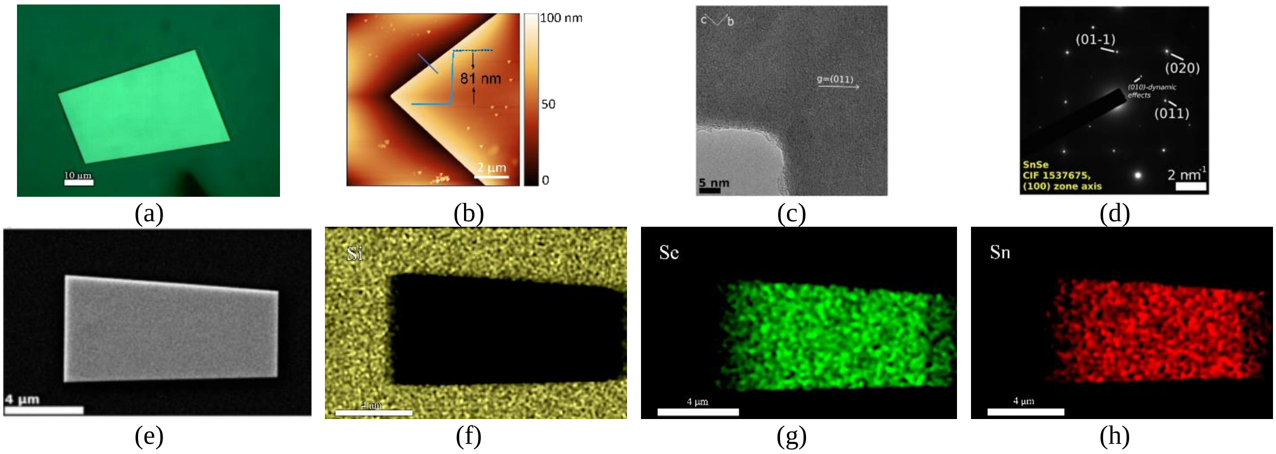

Fig. 2 Characterization of tin selenide nanoflakes: (a) Optical image of a synthesized NF on Si/SiO_2 (300 nm) substrate; (b) AFM image of a typical tin selenide nanoflake showing a thickness of 81 nm; (c) HR-TEM of a SnSe nanoflake; (d) The corresponding SAED pattern observed along the [1 0 0] zone axis, confirming the single crystalline orthorhombic nature; (e) SEM image and EDX elemental mapping of a SnSe NF: (f) Si, (g) Se, (h) Sn.

In order to investigate the anisotropic structure of the NF, measurements of the polarization-resolved Raman scattering were performed and the polar plots of the integrated intensities are presented in Figure 3 as a function of the detection angle. In the co-linear configuration, the polarization axes of all the A_g modes are oriented in the same direction at 37° while the polarization axes of the B_{3g} modes are at 81°. The A_g modes display 2-fold symmetry with an angle period of 180° while the B_{3g} modes present 4-fold symmetry with and angle period of 90° with the same intensity of perpendicular arms. In the cross-linear configuration, the results are similar for the modes of the same symmetry while the polarization axes of the Raman modes are shifted by about 45°. The analysis of the temperature evolution of the Raman spectra from 300 K down to 5 K of a SnSe NF showed that the strength of phonon anharmonicity varies for different phonon modes [3]. The modes A_g and B_{3g} have a strong temperature dependence of Raman shift and linewidth. This combined with the angular dependence of phonon modes exhibited by the polarization-resolved Raman spectra suggests a strong anisotropy of the SnSe nanoflakes.

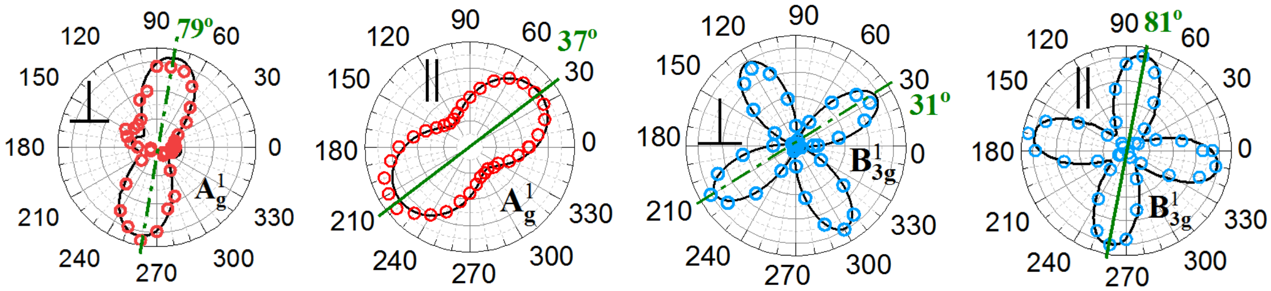

(a) (b) (c) (d)

Fig. 3. Polar plots of the integrated intensities of two representative phonon modes measured at T = 5 K under 1.96 eV excitation: (a) A_g^1 in cross-linear configuration; (b) A_g^1 in co-linear configuration; (c) B_{3g}^1 in cross-linear configuration; (d) B_{3g}^1 in co-linear configuration.

Furthermore, a two terminal device was built using the obtained SnSe nanoflakes which shows memristive behavior, presented in Fig. 4. The inset shows a SnSe nanoflake transferred on Ti/Au contacts. The transfer was made as in [1]. The switching in the memristor is due to the migration of the charged defects toward grain boundaries. Superior electrical conductivity of b and c axes is responsible also for the low threshold voltage (3 V) of the built lateral device. By comparing the SnSe memristor with similar devices from literature one can notice that this type of memristor has a lower power consumption.

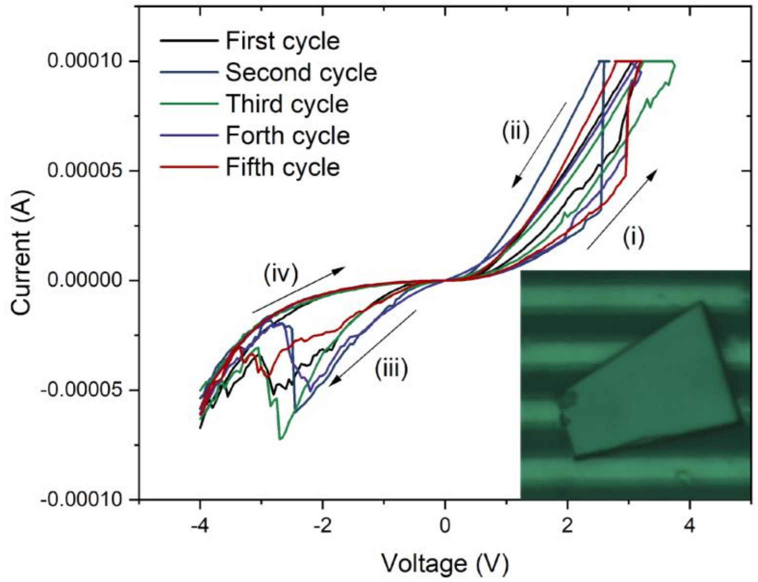

Fig. 4. Non-volatile memory switching of SnSe memristor. The inset shows an optical image of the built device.

References

1. AT Buruiana, F Sava, N Iacob, E Matei, AE Bocirnea, M Onea, AC Galca, C Mihai, A Velea, V Kuncser, Micrometer "Sized hexagonal chromium selenide flakes for cryogenic temperature sensors", *Sensors.* 21, 8084 (2021).
2. AT Buruiana, F Sava, E Matei, I Zgura, M Burdusel, C Mihai, A Velea, "Simple and clean method for obtaining Sn nanoparticles for hydrophobic coatings", *Materials Letters* 278, 128419 (2020).
3. AT Buruiana, AE Bocirnea, AC Kuncser, T Tite, E Matei, C Mihai, N Zawadzka, K Olkowska-Pucko, Ł Kipczak, A Babiński, MR Molas, A Velea, AC Galca, "Layered SnSe nanoflakes with anharmonic phonon properties and memristive characteristics", *Applied Surface Science* 599, 153983 (2022).

Facile Synthesis of Low Toxicity Iron Oxide/TiO_2 Nanocomposites with Hyperthermic and Photo-Oxidation Properties

Traian Popescu[a], Christien Oktaviani Matei[b], Daniela Cristina Culita[c], Valentin-Adrian Maraloiu[a], Arpad Mihai Rostas[a], Lucian Diamandescu[a], Nicusor Iacob[a], Tudor Savopol[b], Monica Cristiana Ilas[a], Marcel Feder[a], Andreea-Roxana Lupu[d], Alexandra Corina Iacoban[a], Ioana Dorina Vlaicu[a], Mihaela Georgeta Moisescu[b]

[a]National Institute of Materials Physics, 405A Atomistilor, 077125 Magurele, Romania
[b]Biophysics and Cellular Biotechnology Department, Excellence Centre for Research in Biophysics and Cellular Biotechnology, “Carol Davila” University of Medicine and Pharmacy, 8 Eroii Sanitari Blvd., 050474 Bucharest, Romania
[3]“Ilie Murgulescu” Institute of Physical Chemistry, Romanian Academy, 202 Splaiul Independentei, 060021, Bucharest, Romania
[4] “Victor Babes” National Institute of Pathology, 99–101 Splaiul Independentei, 050096 Bucharest, Romania

Magnetic hyperthermia (MHT) [1–3] and semiconductor photodynamic therapy (SCPDT) [4,5] represent two cancer therapeutic approaches in which nanoparticles (NPs) with magnetic and semiconductor properties exert direct antitumor activity by the generation of heat and reactive oxygen species (ROS) into the tumor tissue, respectively.

The present study aimed to assess the feasibility of developing low-cost multipurpose iron oxide/TiO_2 nanocomposites (NCs) for use in combined antitumor therapies and water treatment applications [6]. Three types of iron oxide nanoparticles (Figure 1) were used to synthesize nanocomposites with different Fe/Ti ratios (Figure 2).

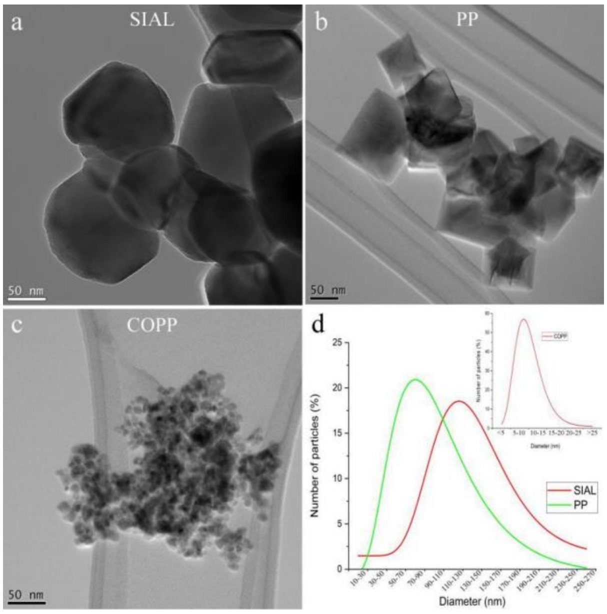

Fig.1 CTEM images of the initial iron oxide nanoparticles (a–c) and their size distributions fitted with a log-normal function (d).

The larger size (≈100 nm) iron oxide nanoparticles (IONPs) formed magnetic core-TiO_2 shell structures at high Fe/Ti ratios (Figure 2) and solid dispersions of IONPs embedded in TiO_2 matrices when the Fe/Ti ratio was low (Figure 3a,b). When the size of the iron phase was comparable to the size of the crystallized TiO_2 nanoparticles (≈10 nm), the obtained nanocomposites consisted of randomly mixed aggregates of TiO_2 and IONPs (Figure 3c,d).

The best inductive heating (Figure 4) and ROS photogeneration (Figure 5) properties were shown by the NCs synthesized at 400 °C which contained the minimum amount of α-Fe_2O_3 and sufficiently crystallized anatase TiO_2.

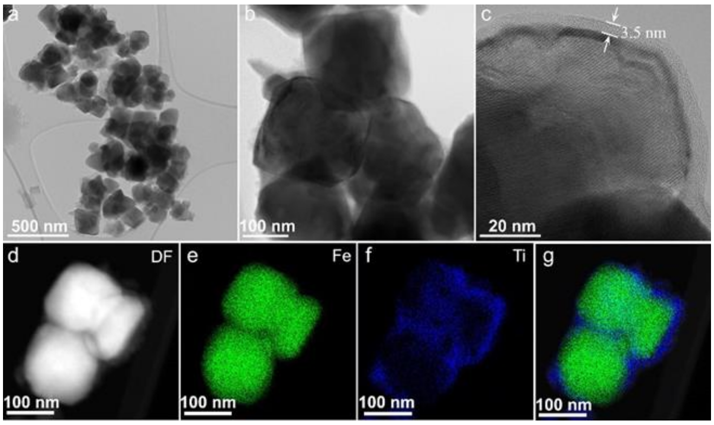

Fig .2 CTEM (a,b) and HRTEM (c) images of SIAL nanocomposites - iron oxide/TBT 500 mg/ml treated at 200 °C (NC-SIAL-500/200); dark field (DF)-STEM image of nanocomposites (d), elemental maps of Fe (e) and Ti (f) and the overlay of the two maps (g).

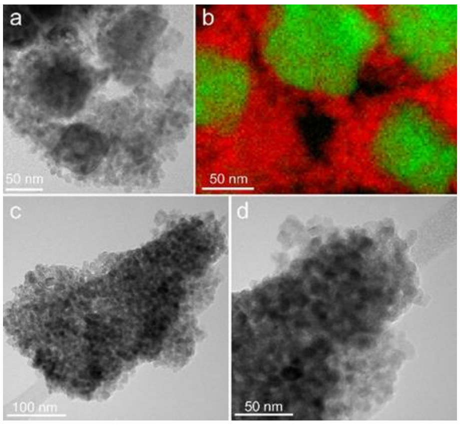

Fig. 3 CTEM image (a) and overlay (b) of EELS elemental maps of Fe (green) and Ti (red) for PP nanocomposites - iron oxide/TBT 200 mg/ml treated at 400 °C (NC-PP-200/400); CTEM images (c,d) for COPP nanocomposites (NC-COPP-200/400).

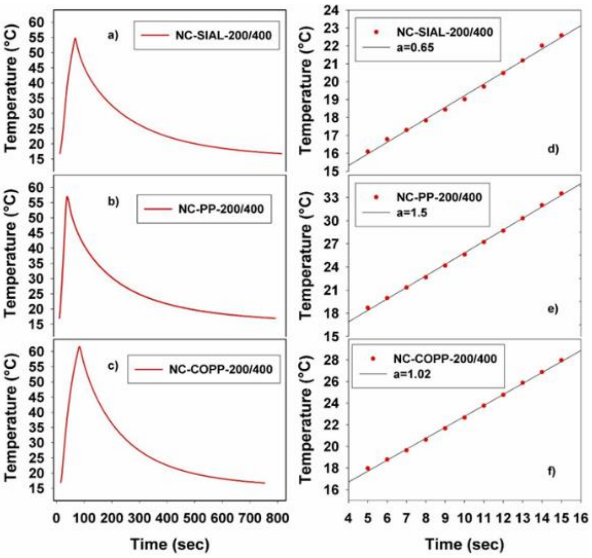

Fig. 4 Heating-cooling curves (a–c) and linear fits with slopes "a" (d–f) for nanocomposites (200 mg iron oxide/ml TBT synthesized at 400 °C) exposed to an alternating magnetic field of 175 Oe.

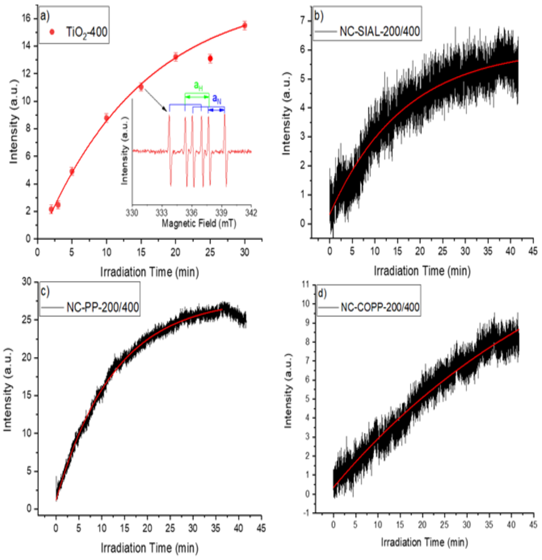

Fig. 5 ROS photogeneration kinetics (UV 365 nm) for: (a) TiO_2-400 (inset: EPR spectrum); (b) NC-SIAL-200/400; (c) NC-PP-200/400; (d) NC-COPP-200/400.

Their cytocompatibility was assessed on cultured human and murine fibroblast cells and analyzed in relation to the adsorption of bovine serum albumin from the culture medium onto their surface (Figures 6 & 7). The tested nanocomposites showed excellent cytocompatibility to human fibroblast cells. The results also indicated that the environment (*i.e.*, phosphate buffer or culture medium) used to disperse the nanomaterials prior to performing the viability tests can have a significant impact on their cytotoxicity.

The overall results indicate that it is feasible to synthesize multipurpose iron oxide-TiO_2 magnetic nanocomposites with engineered morpho-structural, AC magnetic heating, ROS photogeneration and biocompatibility properties, convenient for their use in various biomedical and environment-related applications. The produced nanocomposites are appropriate for further functionalization with organic photosensitizers, therapeutic molecules or pollutant-binding compounds.

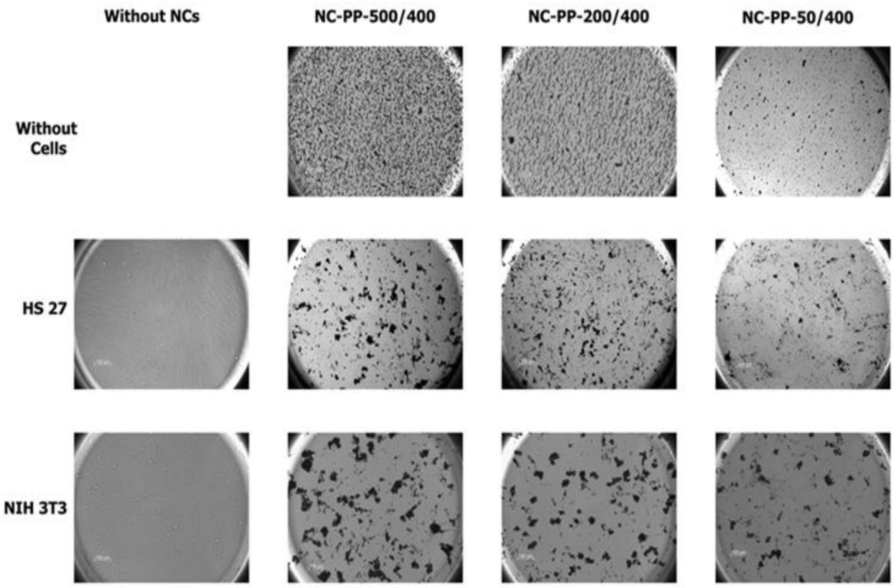

Fig .6 Bright field microscopic images (20× objective) of NCs suspensions (150 µg/ml) in the absence of cells (top raw) and of cells incubated for 24 h with nanocomposites (NC-PP-500/400, NC-PP-200/400 and NC-PP-50/400) ultrasonicated in supplemented DMEM (NCs final concentration was 100 µg/ml): Hs27 cells (middle raw), NIH-3T3 cells (bottom raw).

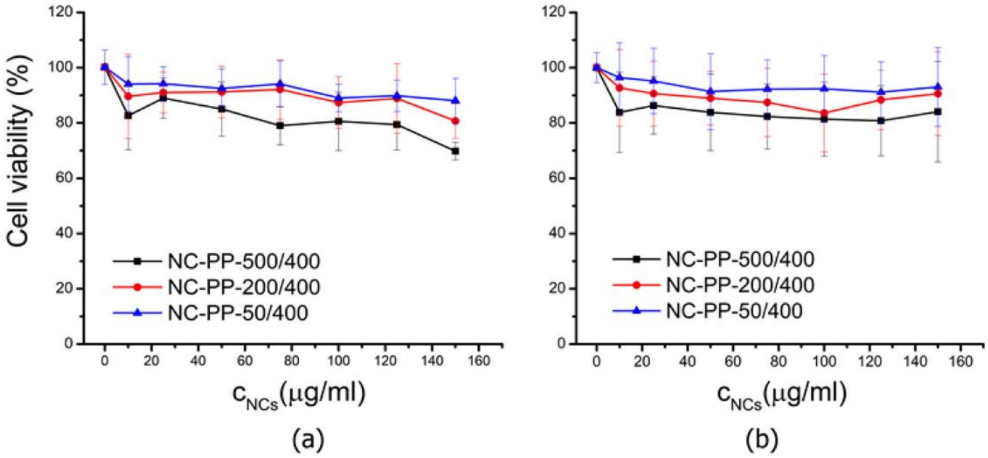

(a) (b)

Fig. 7 Cell viability of cells incubated for 24 h with nanocomposites (NC-PP-500/400, NC-PP-200/400 and NC-PP-50/400) ultrasonicated in supplemented DMEM: (a) HS 27 cells, (b) NIH-3T3 cells.

References

1. AR Lupu, T Popescu, M Stojanović, "Therapeutic use of inorganic nanomaterials in malignant diseases", in: Environmental Nanotechnology (N Dasgupta, S Ranjan, E Lichtfouse, Eds.), Springer International Publishing/Springer Nature, Switzerland, pp. 47–87 (2020).
2. RE Rosensweig, "Heating magnetic fluid with alternating magnetic field" *Journal of Magnetism and Magnetic Materials* 252, 370–374 (2002).
3. JL Roti, "Cellular responses to hyperthermia (40-46 degrees C): cell killing and molecular events", *International Journal of Hyperthermia* 24, 3–15 (2008).
4. L Colombeau, S Acherar, F Baros, P Arnoux, A Mohd Gazzali, K Zaghdoudi, M Toussaint, R Vanderesse, C Frochot, "Inorganic nanoparticles for photodynamic therapy", In: Light-Responsive Nanostructured Systems for Applications in Nanomedicine. Topics in Current Chemistry (S Sortino, Ed.), vol. 370, pp. 113–134 (2015).
5. M Sivasubramanian, YC Chuang, LW Lo, "Evolution of nanoparticle-mediated photodynamic therapy: From superficial to deep-seated cancers", *Molecules* 24, 520 (2019).
6. T Popescu, C Oktaviani Matei, DC Culita, VA Maraloiu, AM Rostas, L Diamandescu, N Iacob, T Savopol, MC Ilas, M Feder, AR Lupu, AC Iacoban, ID Vlaicu, MG Moisescu, "Facile synthesis of low toxicity iron oxide/TiO_2 nanocomposites with hyperthermic and photo-oxidation properties", *Scientific Reports* 12, 6887 (2022).

Revealing the Performances Toward Gas Sensing with NiO-based Gas Sensors – The Influence of Chemical Synthesis and Calcination Temperature

Adelina Stanoiu[a], Corneliu Ghica[a], Catalina Gabriela Mihalcea[a,b], Daniela Ghica[a], Simona Somacescu[c] , Ovidiu Gabriel Florea[a] Cristian Eugen Simion[a]

[a] Laboratory of Atomic Structures and Defects in Advanced Materials, National Institute of Materials Physics, 405A Atomistilor, 077125 Magurele, Romania

[b]Faculty of Physics, University of Bucharest, 405 Atomistilor, 077125 Magurele, Romania

[c]"Ilie Murgulescu" Institute of Physical Chemistry, Romanian Academy, 202 Splaiul Independentei, 060021 Bucharest, Romania

Metal oxide-based gas sensors have been used extensively towards the detection of various explosive and harmful gases [1]. It is known that both chemical synthesis route and calcination temperature have a strong influence over the grain morphology and consequently on the gas sensing properties. Herein, nickel oxide (NiO) was prepared via different hydrothermal chemical routes and calcined at 400 °C and 500 °C. Due to the difference in the calcination temperature it was found from the TEM investigations (Figure 1) that NiO calcined at 400 °C has an average crystallite size of 11±2 nm while the NiO calcined at 500 exhibits an average crystallite size of 19±2 nm.

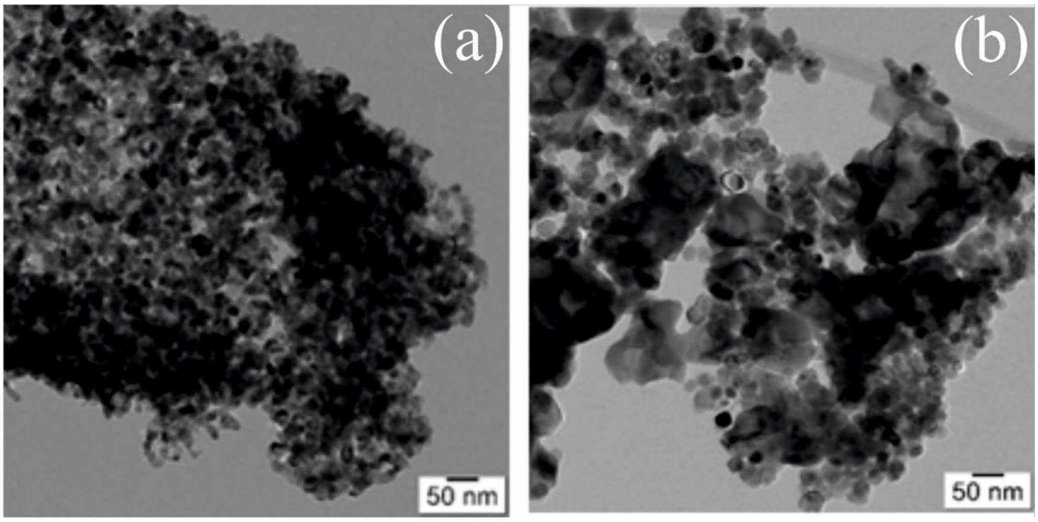

Fig. 1 TEM images of NiO calcined at (a) 400 °C and (b) 500 °C.

From the point of view of the morphological aspects, NiO calcined at 400 °C shows particles with quasi-spherical shape while the one calcined at 500 °C exhibit well defined facets [2].
Sensor signal was defined as the ratio Rgas/Rair, for carbon monoxide (CO) as reducing gas; where Rgas is the sensor electrical resistance in the presence of CO diluted in air with well-defined relative humidity (RH) and Rair is the electrical resistance under synthetic air with RH. Since NiO is a p-type semiconductor, the sensor resistance increases the presence of CO. The investigated sensitive materials showed a bell-like behavior (Figure 2) of the sensor signal (S) with respect to the operating temperature. Such behavior is observed for most of the semiconductor metal oxide based gas sensors and can be explained by the balance between the rate of the adsorption/desorption processes [3]. The maximum of the sensor signal occurs at 250 °C when sensors are exposed to 50 ppm of CO under 50% RH.

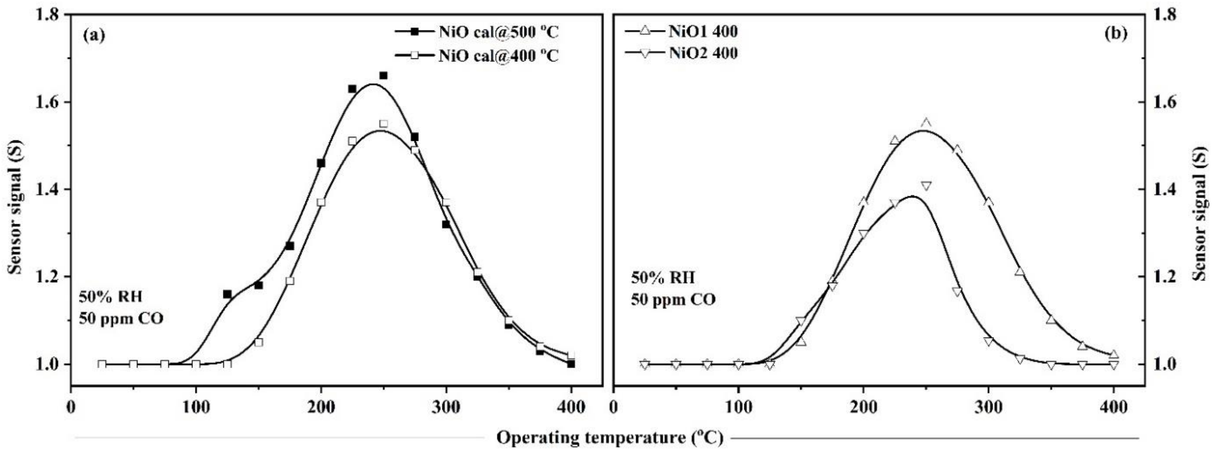

Fig. 2 Sensor signal dependence with respect to the operating temperature for (a) NiO calcined at 400 °C and 500 °C and (b) NiO prepared *via* two different chemical routes.

It is known that the presence of relative humidity in the target gas atmosphere, affects the overall sensing performances of gas sensors. This is due to the formation of hydroxyl groups at the surface which exhibits a competition effect for the same reaction sites as the target gas molecules [4]. This is the main reason why the presence of RH downgrades the sensing performances. As can be seen in Figure 3, in the case of NiO based gas sensors, the presence of RH (10%, 30% and 50%) does not affect the base electrical resistance nor the electrical changes in the presence of different CO (15, 30, 50, 70, 100 ppm) concentrations.

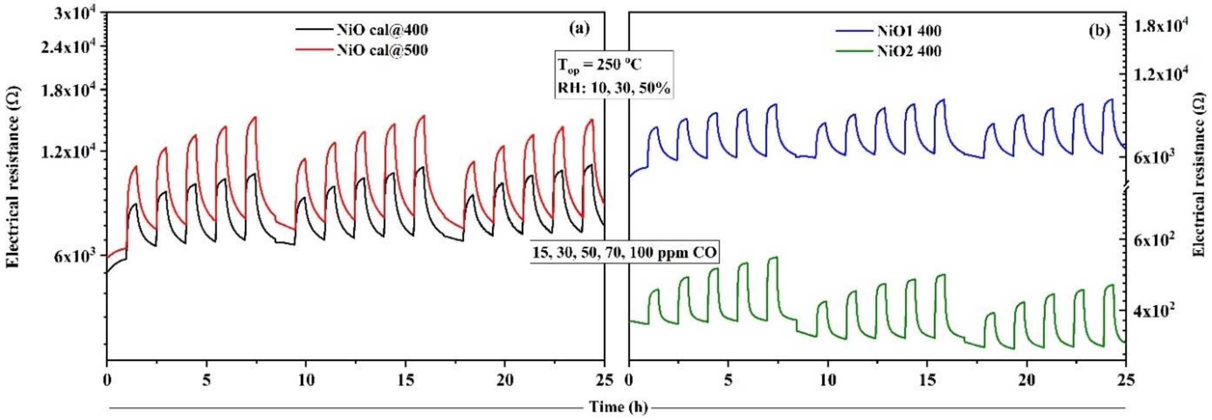

Fig. 3 Electrical resistance time dependence for (a) NiO calcined at 400 °C and 500 °C and (b) NiO prepared *via* two different chemical routes.

From the simultaneous contact potential difference and electrical resistance changes we extract the energetic changes in terms of work function, surface band bending and electron affinity. The insights about the possible gas sensing interaction mechanisms have been addressed. Thus, CO prefers the direct reaction with the surface OH species for the case of NiO calcined at 400 °C:

$$CO^{gas} + OH^{-} \rightarrow CO_2^{gas} + H^{+} + e^{-}$$

While the NiO calcined at 500 °C undertakes a two-step reaction mechanism above and below 15 ppm of CO namely: with the surface hydroxyl groups (up to 15 ppm CO) followed by CO-oxygen interaction above 15 ppm CO:

$$CO^{gas} + OH^{-} + O_{latt} \rightarrow CO_2^{gas} + OH^{\delta-} + e^{-}$$

$$CO^{gas} + O^{-} \rightarrow CO_2^{gas} + e^{-}$$

In the case of NiO sensitive materials prepared via two chemical reaction routes the following interaction mechanisms have been proposed. In the case of NiO1 400 the increase in the sensor response was explained by the CO interaction with both pre-adsorbed oxygen species and surface hydroxyl groups:

$$CO^{gas} + (Ni_{latt}^{+} - OH^{-}) + O_{latt} \rightarrow CO_2^{gas} + Ni_{latt} + (OH)_{latt}^{+} + e^{-}$$

While for the NiO2 400 one fold CO interaction mechanism with the surface oxygen species explain the observed sensitivities:

$$CO^{gas} + O^{-} \rightarrow CO_2^{gas} + e^{-}$$

References

1. A Staerz, U Weimar, N Barsan, “Current state of knowledge on the metal oxide based gas sensing mechanism”, *Sensors & Actuators, B: Chemical* 358, 131531 (2022).
2. A Stanoiu, C Ghica, CG Mihalcea, D Ghica, S Somacescu, OG Florea, CE Simion, “Effects of calcination temperature on CO-sensing mechanism for NiO-based gas sensors”, *Chemosensors* 10, 191 (2022).
3. S Xue, S Cao, Z Huang, D Yang, G Zhang, “Improving gas-sensing performance based on MOS nanomaterials: A review”, *Materials* 14, 4263, (2021).
4. A Stanoiu, C Ghica, CG Mihalcea, D Ghica, CE Simion, “The role of the synthesis routes on the CO-sensing mechanism of NiO-based gas sensors”, *Chemosensors* 10, 466 (2022).

CO_2 Sensitivity Exploration of $Sn_{1-x}Gd_xO_{(4-x)/2}$ Under In-Field Conditions – The Detection Mechanism Associated with the Morphological Features Induced by the Doping Level

Corneliu Ghica[a], Catalina G. Mihalcea[a,b], Cristian E. Simion[a], Ioana D. Vlaicu[a], Daniela Ghica[a], Ion V. Dinu[a], Ovidiu G. Florea[a], Adelina Stanoiu[a]

[a]Laboratory of Atomic Structures and Defects in Advanced Materials, National Institute of Materials Physics, 405A Atomistilor, 077125 Magurele, Romania

[b]Faculty of Physics, University of Bucharest, 405 Atomistilor, 077125 Magurele, Romania

Carbon dioxide (CO_2) is currently the main GHG alongside methane, secondary nitrous oxides and fluorinated gases. Besides its effect on global warming, CO_2 is recognized to be hazardous to human health [1]. Therefore, obtaining low-cost, simple and selective chemo-resistive CO_2 gas sensors is a current challenge, especially as current devices consist of high prices or complicated operation modes such as electrochemical cells and capacitive or nondispersive infrared sensors.

In line with the current interest in CO_2 monitoring, our study explores the CO_2 sensitivity of $Sn_{1-x}Gd_xO_{(4-x)/2}$ powders, for x ranging from 0 to 1 [2]. The nanostructured powders were prepared by a wet chemical co-precipitation method. Investigations regarding the morphology, structure, elemental composition, distribution of Gd in the SnO_2 matrix and nanoparticle size distribution of the $Sn_{1-x}Gd_xO_{(4-x)/2}$ powders were performed with respect to pure SnO_2 and Gd_2O_3 (Figure 1), using JEOL JEM-2100 and JEOL ARM 200F transmission electron microscopes, both equipped with X-ray detectors used to acquire EDS spectra and maps, for the elemental characterization.

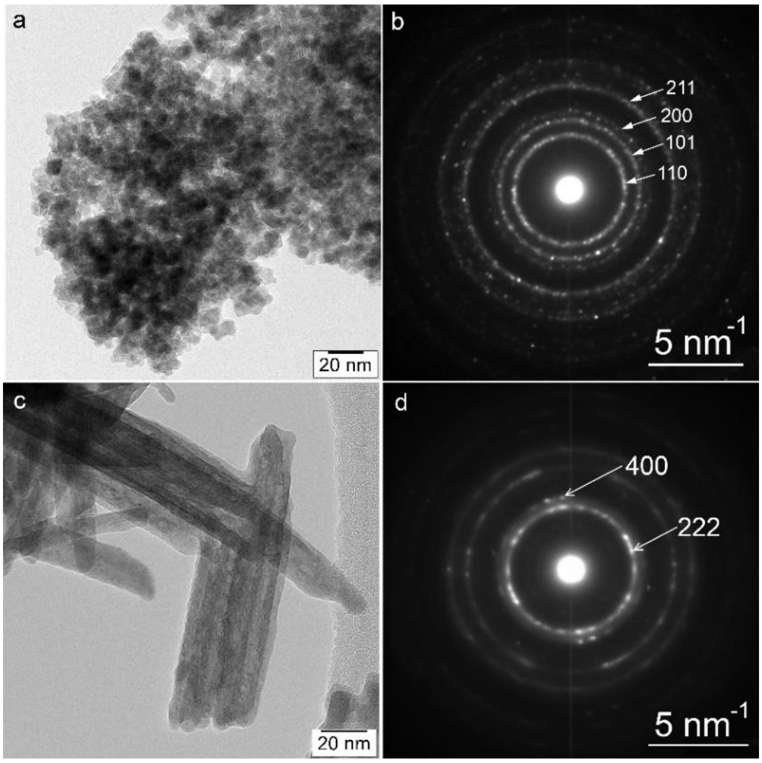

Fig. 1 (a) TEM image of a cluster of as-prepared SnO_2 nanoparticles; (b) SAED pattern of the nanoparticles cluster in (a) showing the formation of the tetragonal SnO_2 phase; (c) TEM image of as-prepared Gd_2O_3 sample; (d) the corresponding electron diffraction pattern.

From the microstructural point of view, our goal is to determine a concentration limit regarding the Gd integration as a doping ion before the chemical segregation of a secondary phase. The STEM-EDS compositional maps show the uniform distribution of Gd with respect to Sn for the samples with a nominal doping concentration up to 5% (Figure 2).

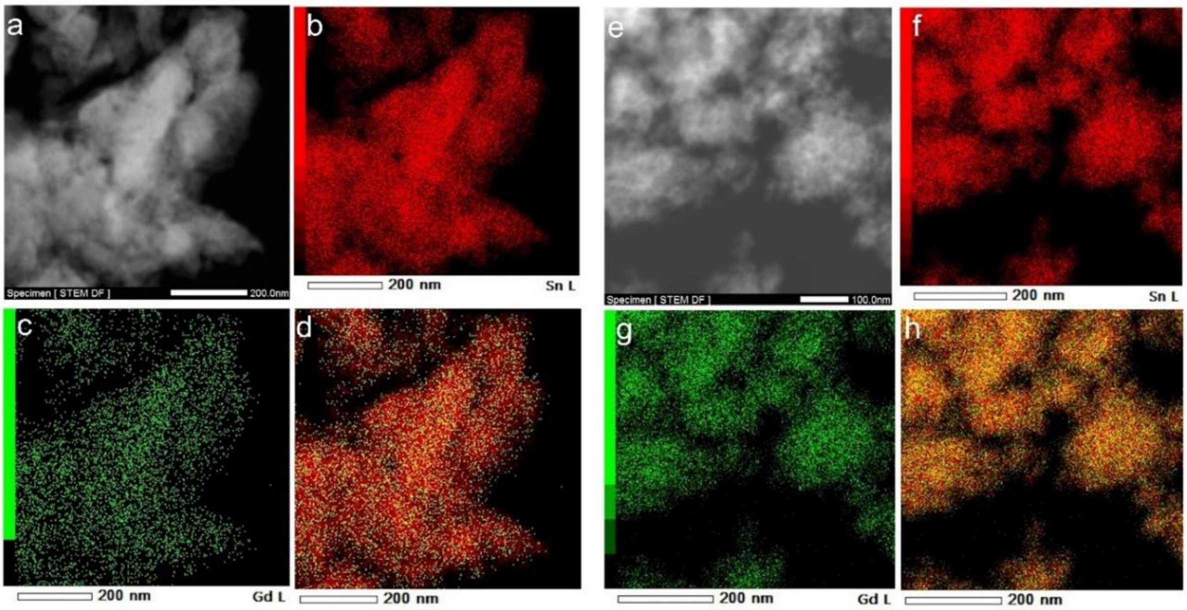

Fig. 2 STEM ADF images, Sn/Gd individual elemental maps and overlapped chemical maps obtained for SnO_2:Gd1% (a-d), and SnO_2:Gd5% (e-h) suggesting a homogeneous sample doping.

A certain trend for chemical segregation of Gd has been observed in the case of the 10% doped sample where the chemical maps have revealed some compositional inhomogeneities consisting of isolated areas with higher Gd content and is obvious for the 20% Gd-doped sample, as demonstrated by STEM-EDS mapping. The corroborated results of the analytical TEM/STEM investigations confirm the Rietveld refinement of the XRD patterns, pointing to a homogeneous Gd doping of the nanostructured SnO_2 powders for low doping concentrations and the formation of a nanocomposite based on SnO_2 as main phase and cubic Gd_2O_3 as secondary phase for the highly doped samples.

The $Sn_{1-x}Gd_xO_{(4-x)/2}$ powders were ground in order to eliminate the possible agglomerations and subsequently mixed with α-terpinol. The obtained paste was screen-printed onto commercial Al_2O_3 substrates provided with interdigitated Pt electrodes and heater. A temperature calibration procedure Temperature = f (applied voltage on the heater) using a LumaSens IN 5-L plus Pyrometer has been implemented for tuning up the gas-sensitive performances.

Gas sensing properties of previously obtained sensors have been evaluated under dynamic in-field conditions ensured by a fully computer-controlled Gas Mixing System (GMS). The in-field conditions were provided by the total flow through the system consisting of mixed user-defined gas type and kept constant at 200 ml/min. CO_2 (400 - 3000 ppm) has been dosed in dry synthetic air (purity 5.0) with variable RH (0 - 50%). Real-time data acquisition of the electrical resistance changes was acquired with Keithley Electrometer 6517A. Knowing that the surface temperature causes specific chemical interactions, the preliminary evaluation of the samples was made for a fixed concentration of CO_2. After exposure, the sensor signal was computed as the relative variation of the electrical resistance between reference synthetic air and air containing 3000 ppm CO_2 (Figure 3a). To determine the sensing mechanism, the content of Gd, the RH level (0÷50%RH) and the CO_2 concentration (400 - 3000 ppm) for the optimum operating temperature T_{op} = 300 °C have been also considered (Figure 3b).

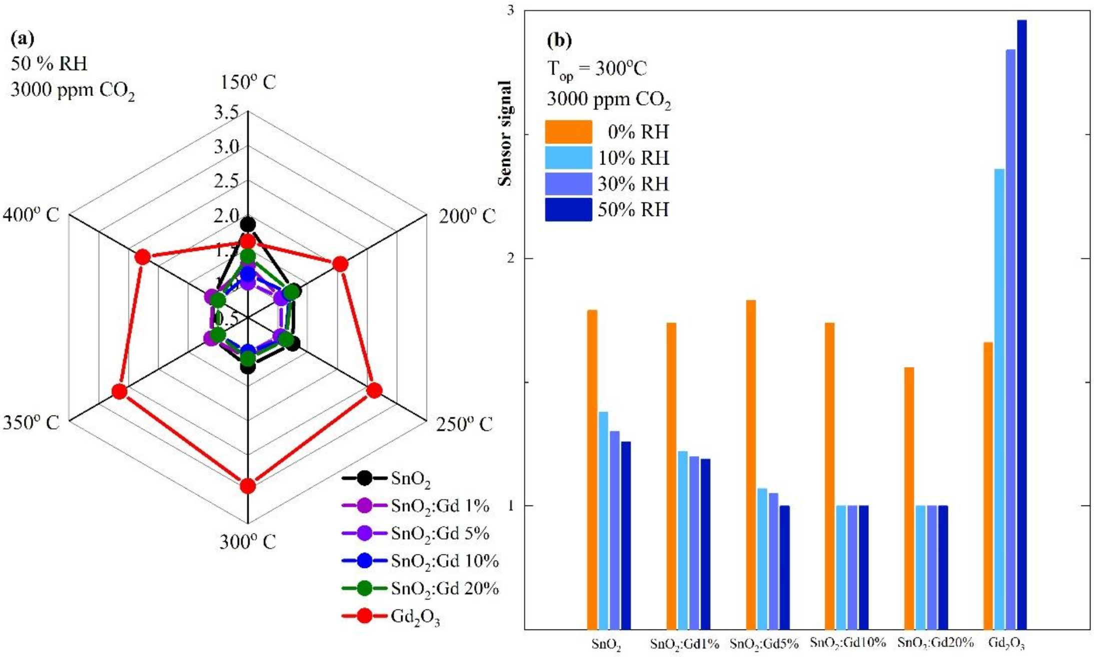

Fig. 3 Sensor signal behavior in relation to the content of Gd and variable RH.

By increasing the Gd content, the influence of RH level decreases, remaining obvious the difference between dry and humid atmospheres. The behavior induced by RH is Gd_2O_3 different for Gd_2O_3. Therefore, in order to understand the CO_2 detection mechanism, operando DC electrical resistance and Contact Potential Difference (CPD) measurements were performed by Mc-Allister KP-6500 Kelvin Probe connected to the GMS. The results allowed decoupling of the dipolar from the ionosorption processes under in-field conditions (50% RH). Thus, according to Peng and Merz Jr. [45] the possible chemical interaction for the case of SnO_2 is described by eq. (1):

$$CO_2{}^{gas} + OH^- \rightarrow HCO_3^- \tag{1}$$

For Gd_2O_3 belonging to the class of rare earth oxides which have extremely polar surfaces according to Külah *et al.* [32], the chemical interaction involves H^+ as described by eq. (2):

$$CO_2{}^{gas} + 2e^- + 2H^+ \rightarrow CO + H_2O \tag{2}$$

It is worth emphasizing that our study highlights the ability of Gd_2O_3 to sense CO_2 between 400 and 3000 ppm, recommending it for in-field applications.

References

1. NL Sireesha, “Correlation amongst indoor air quality, ventilation and carbon dioxide”, *Journal of Scientific Research* 9, 179–192 (2017).
2. C Ghica, CG Mihalcea, CE Simion, ID Vlaicu, D Ghica, IV Dinu, OG Florea, A Stanoiu, “Influence of relative humidity on CO_2 interaction mechanism for Gd-doped SnO_2 with respect to pure SnO_2 and Gd_2O_3”, *Sensors and Actuators B: Chemical* 368, 132130 (2022).
3. Z Peng, KM Merz Jr., “Theoretical investigation of the $CO_2 + OH^- \rightarrow HCO_3^-$ reaction in the gas and aqueous phases”. *Journal of the American Chemical Society* 115, 9640–9647 (1993).
4. E Külah, L Marot, R Steiner, A Romanyuk, TA Jung, A Wäckerlin, E Meyer, “Surface chemistry of rare-earth oxide surfaces at ambient conditions: reactions with water and hydrocarbons”, *Scientific Reports* 7, 43369 (2017).